Lanthanide Luminescent Self-Assembly Complexes: From Solution Studies to Mechanical Sensing on Gold Surfaces

Niamh S. Murray
October 2008

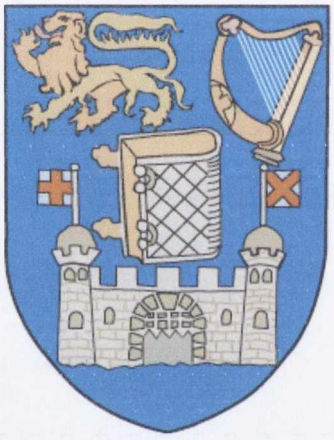

University of Dublin
Trinity College

Based on research carried out under the direction of
Prof. T. Gunnlaugsson (TCD) and Prof. S. Jarvis (UCD)

A Thesis Submitted to the School of Chemistry, University of Dublin, Trinity College for the degree of Doctor of Philosophy

Declaration

This thesis is submitted for the degree of Doctor of Philosophy to the University of Dublin, Trinity College. It has not been previously submitted for any degree or examination to this, or any other University. Except where acknowledged, all work described herein is original and has been carried out by the author. Permission is granted so that the library may lend or copy this thesis upon request. This permission covers only single copies made for study purposes, subject to normal conditions of acknowledgement.

Acknowledgements

I would like to begin by thanking my two supervisors, Prof. Thorri Gunnlaugsson and Prof. Suzi Jarvis. I am very grateful for all the help, support and enthusiasm I have received from both of them in many different ways through the duration of my PhD. I will always appreciate what you have done for me.

I would like to thank the members of the TG group, past and present; Aline, Andrew, AnnMarie, Brian, Celia, Celine, Christophe, Cidalia, Claire, Danni, Debbie, Doireann, Emma, Eoin, Gary, Flo, Jen, Joe, Julie, Julien, Lin, Lisa, Rebecca, Rob, Sally, Sam, and Susan, as well as our newbies, Elaine, Laura and Steve! Thank you all so much for the many lunchtimes filled with laughter, and especially for all your help in the last few months. I would also like to thank the members of the Jarvis group, past and present; Alan, Anika, Camilla, Cristiano, Davy, Geraldine, Gil, Gillian, Jason, Khizar, Liz, Maarten, Mads, Mick, Michael, Paula, Siu Hong, Takeshi, Urs and Venkata, and also our sometime member Prof. John Sader, thank you all.

Thank you to all the technical and administrative staff in the School of Chemistry for their assistance through the years; John, Manuel, Martin, Fred, Patsy, Brenden, Mark, Peggy, Teresa, Corinne, Helen, Maria, and Tess. Thank you to Neal Leddy from the CMA in Trinity, and Padraig in the workshop in the Conway Institute, UCD for their help with various aspects of my many projects.

Special thanks goes to Celia, Cidalia, Aline, and Steve for patiently reading the drafts of this thesis, I will always be grateful! Also, to Jason for the many hours spent helping and guiding me through some of the more complex aspects of AFM, as well as for the company and friendship throughout our many "all-nighters" in Trinity's SFI labs. To Camilla, thank you for looking after me and the rest of the group so well during your time with us. To Gary, thank you for your friendship over the last four years, and for being someone who will always appreciate just how good South Africa was. To my bench buddies Danni, Doireann, Amila, and recently, Christophe, your friendship and laughs made the whole experience so much more fun.

Thank you to all my friends outside of Trinity, especially the HCK girls. You have been a constant source of tea, chats, and bottles of wine, nights out, nights in, and most importantly, friendship for the last eighteen (!) years. I don't know what I would do without you.

Finally, the biggest thanks go to my family; John, Jane, Sinead, Johnny and Andrew. Your love, encouragement and support are what have brought me this far, and to you I dedicate this work.

List of Abbreviations

α	coefficient of thermal expansion
Abs	absorbance
AFM	atomic force microscopy
AuPs	Gold nanoparticles
β	overall stability constant
bipy	bipyridine
CBS	Cantilever-based Sensors
CD	circular Dichroism
$CHCl_3$	Chloroform
CH_2Cl_2	Dichloromethane
CH_3CN	Acetonitrile
CH_3OH	Methanol
COSY	Correlation Spectroscopy
CPL	Circularly polarized luminescence
Cyclen	1,4,7,10-tetraazacyclododecane
χ	chi
[ ]	concentration
δ	chemical shift
d	doublet
DMF	Dimethylformamide
DOTA	1,4,7,10-tetraazacyclododecane-*N,N',N'',N'''*-tetraacetic acid
DPA	2,6-Pyridinecarboxylic acid
DTPA	Diethylenetriamine pentaacetic acid
ε	relative strain
E	Young's modulus

EDCI	1-(3-Dimethylaminopropy)-3-ethyl-carbodiimide hydrochloride
EDTA	ethylenediamine tetraacetic acid
ES-MS	Electro spray mass spectrometry
Et_2O	diethyl ether
EtOH	Ethanol
FIB	focused ion beam
FITC	Fluorescein isothiocyanate
GaAs	gallium arsenide
h	hour
HEMA	2-hydroxyethyl methacrylate
HEPES	4-(2-Hydroxyethyl)piperazine-1-ethanesulfonic acid
HNO_3	Nitric acid
HPLC	High performance liquid chromatography
HOBt	Hydroxybenzotriazolehydrate
IR	Infrared
isc	intersystem crossing
J	coupling constant
K	apparent stability constant
k	spring constant
KBr	Potassium bromide
kHz	kilo hertz
KOH	potassium hydroxide
L	unspecified ligand
λ	wavelength
Ln	Lanthanide
log	logarithm (base 10)

m	multiplet
M	unspecified metal
MEMS	microelectromechanical systems
MMA	Methyl methacrylate
ms	milli seconds
m/z	mass to charge ratio
μ	micro (x 10^{-6})
n	nano (x 10^{-9})
N	Newton
ν	Poisson ratio
NMR	nuclear magnetic resonance
NOE	Nuclear Overhauser Effect
OLED	Organic light emitting diode
PET	photo induced electron transfer
pH	-log[H3O^{+}]
ppm	parts per million
QCM	Quartz crystal microbalance
σ_s	total surface stress
σ_0	residual surface stress
ρ	density
S^0	singlet ground state
S^1	first excited singlet state
SAM	Self assembled monolayer
SEM	scanning electron microscopy
T	temperature
T^1	first excited triplet state

TCPD	di(4-tertbutylcyclohexyl)peroxydicarbonate
THF	tetrahydofuran
tlc	Thin Layer Chromatography
TMACl	Tetramethylammonium chloride
TPEN	tetrakis(2-pyridylmethyl)ethylenediamine
UV	ultra violet
ω	frequency

Abstract

This thesis entitled "Lanthanide Luminescent Self-Assembly Complexes: From Solution Studies to Mechanical Sensing on Gold Surfaces" is divided into five Chapters. Chapter 1 gives a detailed account of lanthanide-based supramolecular systems as sensors within the literature. It highlights the principles and advantages of lanthanide luminescent sensing, and a review of lanthanide templated complexes and assemblies is given. A review of some of the ways that lanthanide complexes have been incorporated onto solid substrates is then presented, along with some preliminary work on lanthanides on gold.

Chapter 2, details the synthesis, characterisation, and photophysical studies of two chiral ligands and their corresponding Eu^{III} complexes in organic solvents. Several techniques are used to characterise these complexes, including NMR, CD, CPL, IR, UV-Vis and luminescence spectroscopy, as well as mass spectrometry. Titrations using NMR, UV-Vis and luminescent spectroscopies are used to investigate the formation of the EuL_3 species two solvent systems. The analysis of the data presented examines the effect of solvent polarity, the chirality of the ligands and the timescale of the experiment on the formation of the EuL_3 complex.

Chapter 3 describes the characterization and qualitative analysis of a lanthanide-based chemosensor on a flat gold substrate. This Chapter is designed as a link between two different topics, as it is hoped that by combining the optical properties of lanthanide-based sensors, and the mechanical properties of cantilever sensors, a self-verifying dual function sensor can be developed. To the best of the author's knowledge, there are no examples in literature of lanthanide luminescence on a flat gold surface. It has been widely considered that gold quenches lanthanide luminescence by means of vibrational deactivation. However, this effect is distance dependent, and so by maintaining a certain distance between the lanthanide center and the gold surface, it is possible to observe lanthanide luminescence. Luminescence and IR spectroscopies as well as AFM imaging were used to characterise and analyse these samples. All of the results presented are qualitative and designed as a "proof of principle" study.

Chapter 4 discuss some of the theoretical considerations of using mechanical microcantilever mass sensors, and gives an experiment to verify the proposed theory that attempts to correlate the effect of surface stress on the stiffness of cantilever plates. These sensors are at their most sensitive when used dynamically, *i.e.* monitoring the change in resonant frequency, and not the deflection of the cantilever. However the theory that is

commonly used to describe these systems is inadequate, and often contradictory to the results obtained. These Chapters attempt to verify the theory first proposed by Lagowski in 1975 (Lagowski, J.; Gatos, H. C.; E. S. Sproles, Jr., *Applied Physics Letters* **1975,** 26, (9), 493-495) and more recently by Sader *et al.* in 2007 (Lachut, M. J.; Sader, J. E., *Physical Review Letters*, **2007**, 99, 206102-4), describing the effect of surface stress on the stiffness of a microcantilever. Finally, Chapter 5 outlines the experimental procedures used in Chapters 2, 3, and 4.

TABLE OF CONTENTS

PAGE

3. LANTHANIDE-BASED SENSORS ON GOLD: FROM FLAT GOLD TO FUNCTIONALISED CANTILEVERS

4. AN EXPERIMENTAL STUDY OF THE EFFECT OF SURFACE STRESS ON THE STIFFNESS OF CANTILEVER PLATES

5. EXPERIMENTAL

Chapter 1
Introduction

1. Introduction

1.0 Introduction

The focus of this thesis is on lanthanide metals and their application as highly efficient chemical sensors. Currently the majority of research into lanthanides focuses on their behavior in solution, which is an interesting and dynamic area of research. However it requires specialised equipment and has limited application outside of a laboratory. By immobilising these sensors on a solid substrate, it would open them up to use in practical, user-friendly devices.

This Chapter begins by discussing the properties that make them unique and allow for their use as chemical sensors, and as supramolecular self-assembly templates. This will be followed by a review of work done by several research groups that are currently examining the use of lanthanide metal complexes on solid substrates, to exploit lanthanides to their full potential. Recently, researchers have begun to immobilise lanthanide complexes on nanoparticles. As they are soluble, and so at the interface between solid and solution phase studies, this topic will be reviewed next, giving examples of several types of nanoparticles that have been synthesised, and their uses. Several examples of lanthanides immobilised on a variety of substrates will then be detailed. There have not been many of these published to date, so in this section, some other examples of functional self assembled monolayers (SAMs) will also be discussed with a view to incorporating lanthanide chemistry into such systems. Chapter 1 finishes by discussing some of the other types of sensors currently in use and under research, and how incorporation of more than one sensing technique into a single device can produce a more effective device, with less potential errors.

1.1 Introduction to Lanthanide Metals

The lanthanides correspond to the first period of the f-block elements starting at lanthanum, and ending at lutetium. There is a gradual filling of the 4f electron shell, which is shielded by the outer $5s^2 5p^6$ subshells. Lanthanides have the general electronic configuration $[Xe]4f^n 5d^1 6s^2$ with n = 0 (La) to 14 (Lu) and their most stable oxidation state is 3+ with an $[Xe]4f^n$ configuration.[1, 2] Ln^{III} ions display large and variable co-ordination numbers (CN = 6 – 12) with 8 and 9 being the most common. In solution, the coordination number can be difficult to predict because the Ln^{III} ion will fulfill its co-ordination sphere, unless a ternary donor for

example, bipyridine or phenanthroline is added,[1] by binding small molecules or anions (such as water, hydroxide, chloride, *etc.*) if the number of available binding sites offered by the host is too low.[3] Lanthanides may be classified as 'hard' acids and therefore prefer to bind to 'hard' bases, such as nitrogen, oxygen, or fluorine, rather than 'soft' bases such as phosphorous, sulphur, or iodine,[2] and they bind mainly through electrostatic interactions.

The 4*f* electrons of lanthanide metals imperfectly shield each other from the increased positive charge of the nucleus, so that the effective nuclear charge attracting each electron steadily increases through the lanthanide elements, resulting in successive reductions of the atomic and ionic radii. The lanthanum ion, La^{III}, has a radius of 1.061 angstroms, whereas the heavier lutetium ion, Lu^{III}, has a radius of 0.850 angstroms. This is known as the *lanthanide contraction.*

Lanthanides have unique photophysical properties, the details and advantages of these will be discussed in the next section.

1.1.1 Photophysics of Lanthanide Metals

"Luminescence" is a term used to describe a whole range of phenomena which involve decay from an electronically excited state by emission of a photon[4]. There are two types of luminescence discussed within this introduction: fluorescence and phosphorescence. Fluorescence is a spin-allowed process that occurs in the time frame 10^{-6} - 10^{-12} s^{-1} whereas, phosphorescence involves a change in spin multiplicity and is a slower process, taking from 10^{-6} s to as much as several seconds. For convenience, the term 'luminescence' will be used here to describe both fluorescence and phosphorescence.[4]

Lanthanide *f-f* transitions are Laporte forbidden and therefore very weak, with extinction coefficients of the order of 0.5-3 $dm^3mol^{-1}cm^{-1}$. However, this can be advantageous, as once the excited state has been populated, the *f-f* downward transition forces a longer excited state lifetime (into ms).[5] This makes lanthanides particularly useful for *in vivo* sensing of biological analytes as many of these fluoresce (known as autofluorescence), which can interfere with recording the signal from other types of luminescent sensor. Also, Lanthanides have longer lifetimes, this allows for the use of time resolved techniques that can overcome the problem of autofluorescence and light scattering. This involves a process called time gating, which is illustrated in Figure 1.1. By delaying the time between excitation and detection of the emission, the short-lived background signals can be avoided.[6]

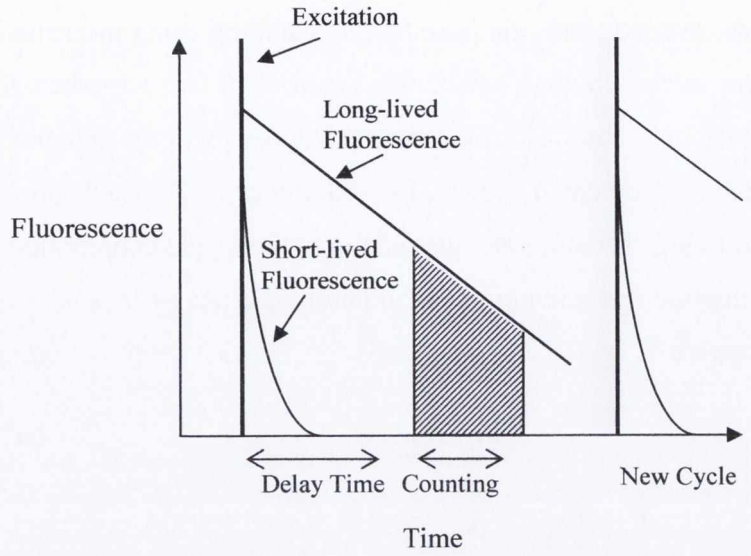

Figure 1.1 Illustration of Time Gating. There is a time delay between excitation and recording of the emission, to avoid detection of the short-lived autofluorescence.

Direct excitation of the Ln^{III} ion is difficult and as such, they are in general photophysically inert due to their low molar absorptivities and large energy gaps present between the emissive and ground states.

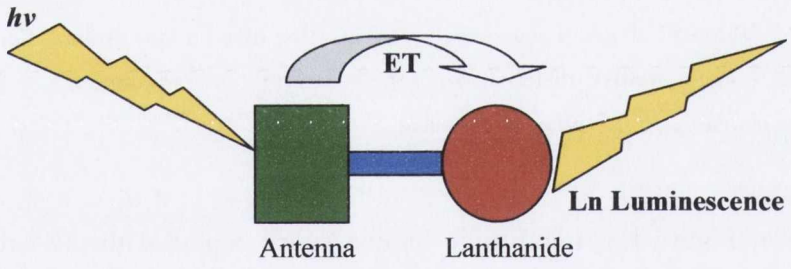

Figure 1.2 Diagram explaining the antenna effect. Indirect excitation of the lanthanide metal can occur *via* an energy transfer from the antenna to the metal centre, resulting in lanthanide emission.

However, the excited states can also be populated by using a sensitising chromophore or antennae (known as the *antenna effect*, see Figure 1.2) if the triplet excited state of the antenna is sufficiently long-lived and if the triplet (T_1) energy of the antenna is close to that of the Ln^{III} ion, $^5D_0$ (E = 17200 cm^{-1}) and $^5D_4$ (E = 20500 cm^{-1}) for Eu^{III} and Tb^{III} respectively.[7] By attaching a sensitizing chromophore, or antenna to the ligand coordinated to the lanthanide ion, we allow for this indirect excitation of the lanthanide ion by means of an intramolecular energy transfer process[7-10].

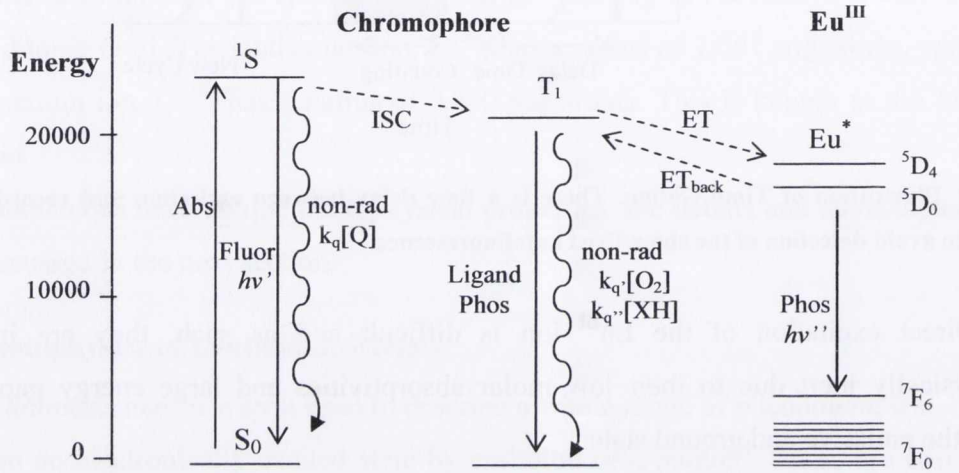

Figure 1.3 Simplified Jablonski diagram showing the sensitisation of a Ln ion. Fluor = fluorescence, Abs = absorption, non-rad = non-radiative deactivation, ISC = intersystem crossing, ET = energy transfer, ET_{back} = back energy transfer, Phos = phosphorescence

As shown in Figure 1.3, Lanthanide luminescence begins with the excitation of the antenna from the ground state, S_0, to the singlet-excited state, S_1. Following the formation of this excted state, deactivation to the ground state S_0, with concomitant ligand fluorescence emission (*hν'*), can occur. It is also possible for this excited state to be quenched by various radiationless deactivations ($k_q[Q]$) back to the ground state S_0. A triplet excited state, T_1 can be populated by intersystem crossing (ISC). At this point T_1 can be lost by quenching from singlet oxygen, ($k_{q'}[O_2]$). It is also possible to transfer the excited state of the antenna T_1 to the lanthanide excited state ($^5D_4$ and $^5D_0$ for Tb^{III} and Eu^{III} respectively) by way of an energy transfer process, resulting in Ln*.[11] At this point deexcitation can occur resulting in an Ln^{III} emission (*hν''*).[2]

Two possible mechanisms exist for the transfer of energy from the T_1 of the antenna to the lanthanide centre ($^3Ar \rightarrow {}^*Ln$); The Förster[12] and the Dexter[13] energy transfer mechanisms, respectively.

The Förster energy transfer mechanism involves the overlap of energy levels and it is described in terms of an interaction between the transition dipole moments. The energy transfer occurs through space and has an r^{-6} distance dependence, where r is the distance between the excited chromophore/antenna and the metal ion. As such, the energy transfer process is made more efficient by minimizing the distance between the lanthanide ion and its antenna.[12]

The Dexter mechanism involves electron transfer that occurs as a result of exchange between the excited chromophore and the metal ion in a through-bond interaction. It has an e^{-r} dependency, so, as with the Forster mechanism, the process is more efficient with minimum value of r.[13]

From this, we can conclude that once the lanthanide ion is excited, ϕ, or quantum yield, *i.e.* its luminescent efficiency, depends on a number of factors:

a) **The efficiency of the $S_1 \rightarrow T_1$ intersystem crossing**
b) **The efficiency of the energy transfer from $T_1 \rightarrow Ln^*$ (the lanthanide centre)**
c) **The radiation efficiency of the lanthanide complex, Φ_{Ln}**
d) **The degree of quenching by non-radiative means**

The most significant of these in determining the quantum yield of the lanthanide complex is the non-radiative quenching processes. This usually occurs through quenching by solvent molecules, when they have access to the lanthanide ion. This is something that should generally avoided, however many groups have used this process to their advantage and this will be discussed further later in this chapter and in chapter 3.[14-16] One benefit of this quenching process is that it allows for the calculation of the number of water molecules within the first coordination sphere of the lanthanide.

1.1.2 Lanthanide Quenching by H_2O and q-Values

Non-radiative deactivation can occur through energy transfer to vibrational modes that match the energy of the excited state of the lanthanide ion.[17] In aqueous solution, the main quenching process occurs through dissipation of the energy of the lanthanide excited state by

high frequency vibrations from solvent water molecules. This process is dependent on the proximity of the O-H oscillator to the lanthanide ion.

Assuming that only the O-D oscillations contribute to deactivation, and that all other quenching pathways are the same in water and in deuterated water, the number of metal-bound-water molecules can be calculated by measuring the lifetime of the complex in H_2O and D_2O. The *q*-value is calculated using equations derived by Horrocks *et al.*[18-20] with refinements made by Parker *et al.*[17, 21] that take into account deactivation by N-H and C-H oscillators as well as that by O-H oscillators, **Equation 1.1** and **Equation 1.2**.

A is a proportionality constant that gives a value for the sensitivity of the corresponding lanthanide ion to quenching by metal-bound-water molecules. A = 1.2 and 5.0 ms for Eu^{III} and Tb^{III}, respectively.

$$q^{EuIII} = A\left[\left(\frac{1}{\tau_{H2O}} - \frac{1}{\tau_{D2O}}\right) - 0.25 - 0.075x\right] \qquad \textbf{Equation 1.1}$$

$$q^{TbIII} = A\left[\left(\frac{1}{\tau_{H2O}} - \frac{1}{\tau_{D2O}}\right) - 0.06\right] \qquad \textbf{Equation 1.2}$$

The correction terms -0.25 and -0.06 represent quenching by second sphere water molecules, and -0.075*x* is the quenching by N-H oscillators, where *x* is the number of these oscillators directly bound to the Ln ion in a given complex.[17] The value of *q* is measured with an error of ± 0.5.

As well as it providing information on the efficiency of lanthanide luminescence, knowledge of the number of water molecules coordinated to a metal ion is of great importance in understanding the nature and reactivity of metal complexes in solution.

All of these photophysical properties make lanthanide metals useful for many purposes, in particular, as chemical sensors. This will be discussed in the next section.

1.1.3 Lanthanide Metals as Chemosensors

A chemical sensor can be defined as a device capable of delivering real time information about an analyte in a sample.[22] A sensor consists of a reporter linked to a receptor that can bind to the target analyte and will induce a change in the properties of the reporter, which can be visually or instrumentally detected. The receptor must be able to bind selectively and reversibly for the sensor to be useful.

Luminescence is a highly sensitive detection technique, potentially capable of detecting a single molecule. However, it can be an unreliable method, as luminescent molecules are in general very susceptible to influence from variables other than what you want to sense. That is, luminescent sensors are commonly used in *in vivo*, or *in vitro* sensing but, as much biological matter luminesces to some degree, the signal from the sensor can be lost in the background noise (autofluorescence). So in order to make good use of luminescent sensors we must find a luminescent signalling system that has a long enough lifetime to avoid this autofluorescence. The choice of receptor and fluorophore decide these two key components.

1.1.4 Efficient Ligands for Lanthanide Complexation

In addition to the features discussed above with respect to energy-transfer processes and minimization of non-radiative deactivation, when designing ligands for lanthanide complexation, it is important that they are both kinetically inert and thermodynamically stable toward metal dissociation, and have a saturated co-ordination sphere[23]. This is particularly necessary for use in *in vivo* sensing as lanthanide ions are toxic to biological systems due to their essentially non-directional electrostatic bonding, so they are fairly easily accommodated without distorting binding sites. They are also known to substitute isomorphously for calcium in some metalloproteins and to activate certain Ca-based systems in the absence of calcium, and so they are very toxic for bones.[2, 24] A number of Gd^{III}-based MRI contrast agents have recently been withdrawn from use due to worries over their stability *in vivo*, and therefore their toxicity to humans.[25] This is a challenge for synthetic chemists, given the high lability of lanthanide ions and their need for high co-ordination numbers.

In aqueous solutions, the enthalpy and entropy changes upon complex formation between Ln^{III} cations and many ionic ligands are predominantly influenced by changes in hydration of both the Ln^{III} ion and the ligand(s). Complexation results in a decrease in hydration, yielding a positive change in entropy favourable to the complexation process. The

dehydration process is endothermic and, since contribution from bond formation between the cation and the ligand(s) often does not compensate, the overall complexation process is generally entropy driven.[23] Therefore, it is advantageous to use preorganised, polydentate ligands to provide the coordination environment around the lanthanide ion. These polydentate ligands can be linear or cyclic and there are many examples of each. Some of these will be discussed in the following sections.

1.1.4.1 Acyclic Lanthanide Complexes

It is possible to use one or more polydentate linear ligands when complexing lanthanide metals, to shield the metal and prevent quenching from proximate oscillators.

Complexes of the type $[Ln(EDTA)(H_2O)_x]^{2-}$ or $[Ln(DTPA)(H_2O)]^{2-}$ can be readily prepared by heating the desired lanthanide oxide with sodium hydroxide and EDTA **1**, or DTPA, **2**. Complexes such as this, with Gd^{III} $[Gd(DTPA)(H_2O)]^{2-}$ have been investigated as contrast agents for diagnostic imaging in MRI scanners, to assist *in vivo* tissue analysis. The use of the chelating ligand DTPA (Diethylenetriamine pentaacetic acid) leads to the formation of a very stable (log $K \sim 22$) complex with low toxicity, that can be excreted by the kidneys intact (the EDTA complex is quite toxic, log $K \sim 17$).[2]

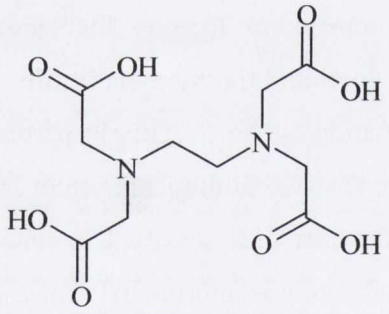

1

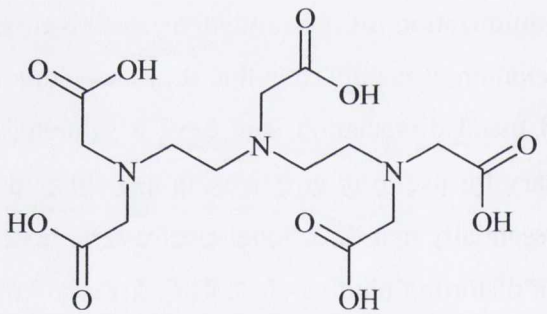

2

Receptor **3**, by Monalti *et al.* [26] consists of a P=O unit and two bipy subunits, which form a stable complex with both Eu^{III} and Tb^{III}, with the bipy acting as an antenna. When nitrate is added to an acetonitrile solution of either **Eu.3** or **Tb.3** an increase in emission intensity occurs. Addition of chloride produced a similar, although less pronounced effect, and fluoride and acetate were far less pronounced again. The changes that were observed in the emission were attributed to a sequential substitution of ligands by nitrate anions. The initial increase in intensity was due to the displacement of solvent molecules by one nitrate anion, followed by coordination of a second nitrate anion that displaced one of the bipy arms leading

to an increased efficiency of the ligand-to-metal energy transfer process between the remaining bipy arm and the lanthanide centre. The overall effect was that of an increase of 11% in emission intensity.

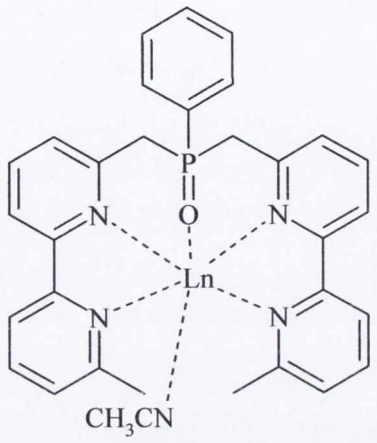

3

The Eu^{III} and Tb^{III} complexes of the tripodal pyridine-based ligands **4** and **5** were studied in acetonitrile.[27] In this case, the pyridine moieties functioned as antennae for lanthanide sensitization. The **Eu.4** complex gave the most striking result with nitrate, where addition of three equivalents gave rise to substantial changes in the phosphorescence spectrum and a 4.9 fold enhancement of the luminescence. Chloride and acetate both produced small changes, but no other anion had any significant effect. The **Tb.4** complex produced significant changes upon addition of chloride, with a 5.4 fold enhancement after the addition of three equivalents of anion. Measurements taken with the achiral analogue, **5**, produced similar results, but with much less sensitivity.

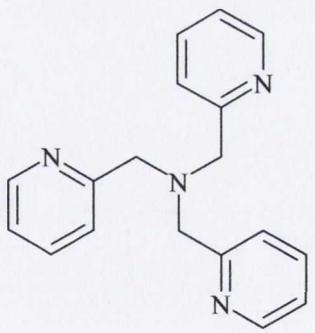

4

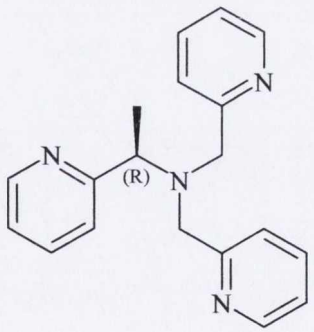

5

The tetrapodal ligand **6** by Bünzli *et al.*[1] is fitted with 8-hydroxyquinoline pendant arms, and the spacer has an amide group and a specific length designed to achieve a tight coordination around the Ln ion, fulfilling its first coordination sphere. Ligand **6** forms trivalent

complexes with lanthanide ions in water, yielding stable 1:1 podates with pLn values in the range of 15 – 16. Several species are present in equilibrium, however the 1:1 species was largely dominant in the pH range 6 - 8.

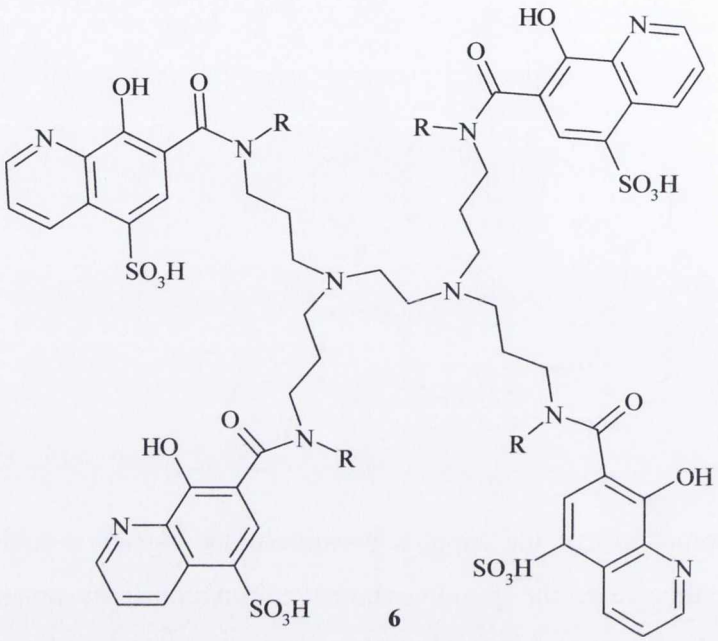

a: R = H

b: R = Me

6

Hanaoka *et al.*[28] designed a ligand using a DTPA framework and bis-picolyl coordinating unit, to produce ligand **7**. It was observed that in the presence of Zn^{II} the Tb^{III} emission was enhanced as the coordination of the Zn^{II} ion brought the two bis-picolyl units closer to the metal centre, thereby promoting a better sensitisation of the Ln-centred luminescence.

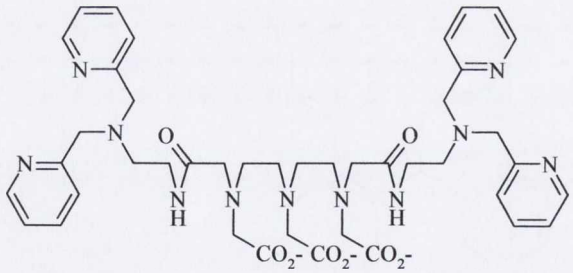

7

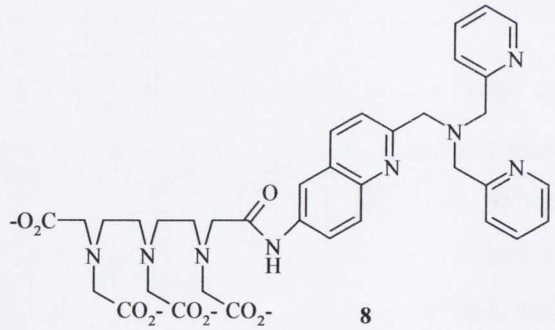

8

However, the poor luminescence intensity of the system and the short excitation wavelength (λ_{ex} = 260 nm) prompted the authors to develop **8**.[29] It consisted of the same

DTPA framework, but with only one Zn^{II} coordinating unit. This was separated from the DTPA by a quinolyl group that acted both as chromophore and as an acceptor for Zn^{II}.

The sensor has been shown to bind the Zn^{II} through the tetrakis(2-pyridylmethyl)ethylenediamine (TPEN) moiety see Figure 1.4. This sensor can bind to group I, II and transition metal ions in a pH independent manner between pH *ca.* 4-9. The emission was most significantly enhanced in the presence of Zn^{II}.

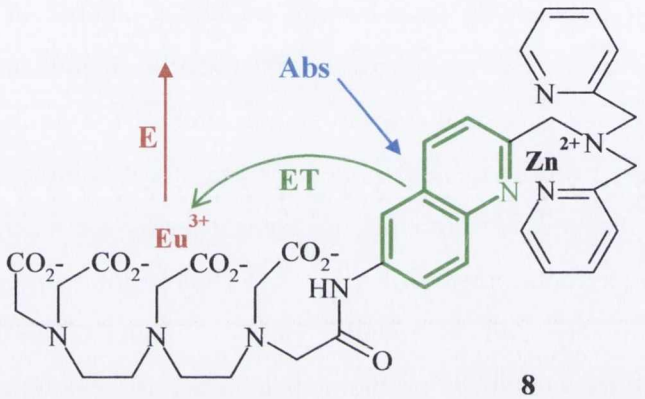

Figure 1.4 Abs = Absorption, ET = Energy Transfer, E = Emission. This Figure shows the binding mechanism of the Zn^{II} to the (TPEN) moiety of ligand 8. It also shows the energy transfer from the quinolate to the Eu^{III} centre and the resultant emission.

Acyclic complexes have many uses; however in general, cyclic structures provide more stable chelation sites. Some examples of cyclic lanthanide complexes will be discussed in the section that follows.

1.1.4.2 Cyclic Lanthanide Complexes

Since the publication of the crystal structure of the lanthanide complex with EDTA, the aminocarboxylate complexing unit has been grafted on numerous scaffolds, including macrocycles (for example, cyclen: 4,7,10-tetraazacyclododecane). Stability of these complexes comes from the combination of large entropic effects due to de-solvation of the water molecule, charge compensation occurring upon complexation, and the formation of strong ionic bonds with the carboxylate units, including the formation of stable five-membered chelate rings.

The coordination chemistry of lanthanides with crown ethers and their cyclic and acyclic analogues has been studied since the late 1970's. As a result there are many suitable macrocyclic ligands for complexing lanthanides, a few of which are detailed below.

Macrocycles utilise a specific version of the chelate effect, which suggests that complexes of bidentate or polydentate ligands are more stable than those composed of several monodentate ligands with similar donor atoms. A macrocycle has donor atoms arranged in fixed positions so there is less of an entropic effect in the binding energy of macrocycles than in monodentate or polydentate ligands with an equal number of donor atoms. Thus the *macrocyclic effect* means that complexes of macrocyclic ligands are more stable than those with linear polydentate ligand analogues of similar strength (or similar donor atoms).[30]

Ligands based on the cyclen framework are ideal complexation agents for trivalent lanthanide ions.[31] As well as stabilising the complexes by the macrocyclic effect, they fulfil the high co-ordination requirement of Ln^{III} ions.[32] The resulting structures are both, very stable and, thermodynamically and kinetically inert, in aqueous solution and are therefore particularly useful for analytical or biomedical uses, for example as magnetic resonance imaging contrast agents,[24] or as catalysts for the specific cleavage of RNA and DNA[33-35]. There are many examples of the use of cyclen as a lanthanide chelating ligand from the Gunnlaugsson group, and some of these will be discussed later in this section.

Additionally, a sensitising chromophore can easily be attached to one of the amine functionalities of the cyclen macrocyclic core as pendant arms, which, as described earlier, allows for the tuning of the photophysical properties of the resulting complex.

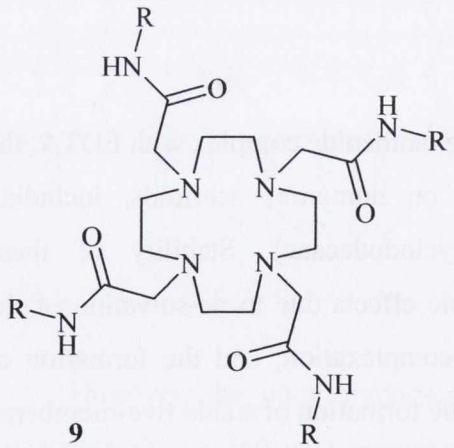

9

a: R =

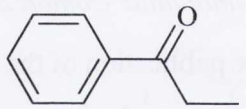

b: R =

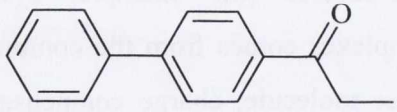

The ligand cyclen has been used extensively for binding Eu^{III} and Tb^{III}. Many examples have been synthesised by the Bünzli group.[36] Both ligands **9a** and **9b**, form highly luminescent 1:1 complexes in water with a stability constant of log K = 12.89 ± 0.15 at 298 K, for **Eu.9a**. Additionally, **Tb.9b** was the first reported X-ray structure of a Tb^{III} cyclen complex. The X-ray structure showed that the metal ion was nine coordinate; bound to the four nitrogen atoms of the macrocycle, the four oxygen atoms of the amide functions, and to one water molecule, giving overall nine coordination sites and square anti-prismatic geometry around the Tb^{III} ion.

Complexes **10** and **11** were developed by Parker *et al.*[37] and also utilise an organic chromophore as the fluorescence of *N*-alkylated phenanthridium is known to be quenched by the presence of halide ions in aqueous media.[38] It is thought that quenching occurs through electron transfer from the halide to the singlet excited state of the electron-poor cation. This property had been exploited in the design of biologically relevant assays for chloride, and this subunit was incorporated as an antenna into receptors **10** and **11**.[37] The europium complex shows a decrease in phenanthridium fluorescence intensity upon addition of halides to aqueous solution, as expected. This was accompanied by a decrease in the Eu^{III} luminescence, and the effect has been shown to be independent from additions of Na_2CO_3, $H_2PO_4^-$, lactate, and citrate. Hydroxide ions have been shown to attack the *N*-methylphenanthridium groups at C6 in a reversible reaction, resulting in a decrease in Eu^{III} emission intensity. The europium emission intensity can therefore be considered to be pH independent from pH 2 – 9, but emission falls in intensity by a factor of up to 200 as the pH goes beyond 13.

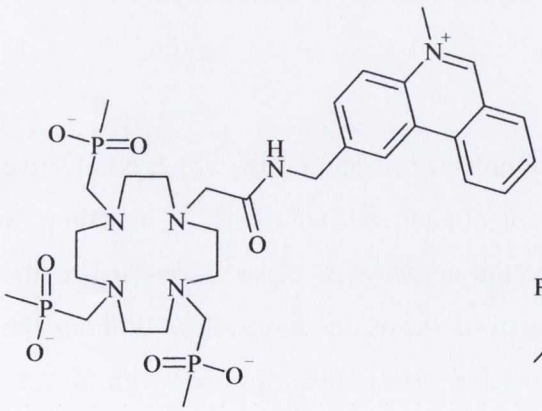

10

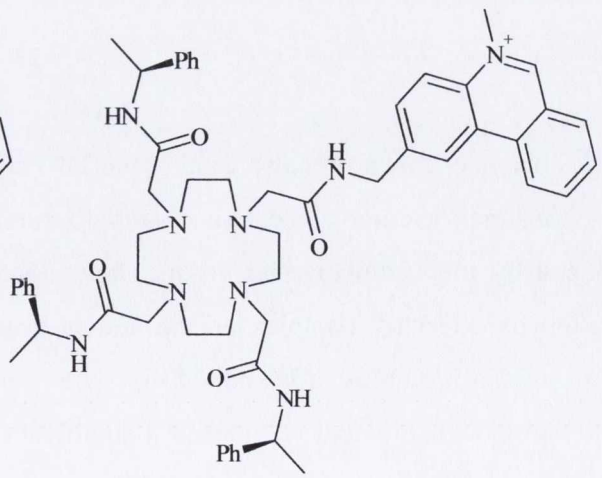

11

As mentioned previously, it is possible to use the radiationless deactivating powers of solvent molecules that are bound within the first coordination sphere of the lanthanide, to create an *OFF – ON* sensor. The Eu^{III} and Tb^{III} complexes of ligands **12a** and **12b**, synthesised by Dickins *et al.*[16], and Bruce *et al.*[15] use the reversible displacement of water molecules coordinated to the lanthanide centre as a probe for anion sensing. For example, **Eu.12a**, **Eu.12b**, **Tb.12a**, and **Tb.12b**, all have two metal-bound water molecules, and showed an enhancement in its emission intensity in the presence of fluoride, acetate and sulphate. No change was observed with any other halides or nitrates. However, hydrogen carbonate and carbonate both displaced the water molecules and showed a significantly higher emission intensity than fluoride, acetate, or sulphate, and gave rise to longer excited state lifetimes for all four complexes.

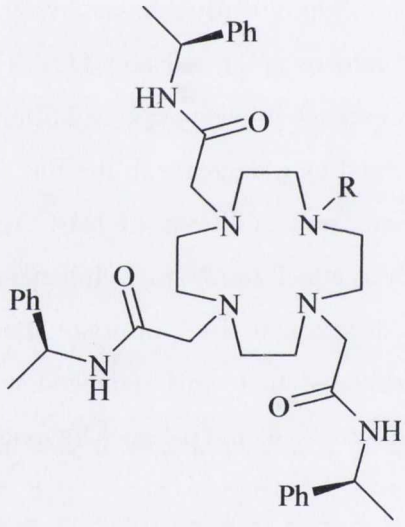

a: R = H

b: R = Me

12

This mechanism was also used in the Tb^{III} complex of receptor **13a,** which is selective for *p-N,N*-dimethylaminobenzoate and salicylate anions in aqueous solutions.[39] This complex developed by the Gunnlaugsson group, shows that the addition of these anions led to the formation of a ternary complex as the anions displaced the water molecules. Without the anions, neither complex **13a** nor **13b**, were emissive. However, titration with *p-N,N*-dimethylaminobenzoic acid resulted in a significant "*switching on*" of the emission, with an enhancement of the luminescence of *ca.* 680.

The principal quenching mechanism in this system involves vibrational energy transfer to the bound OH oscillators (H_2O molecules). When these are removed, *i.e.* the water molecules are displaced, the OH quenching no longer occurs and so the emission is enhanced. The Tb^{III} complex of **13b** resulted in a similar behaviour, although with slightly less enhancement of the emission (approximately 220 times). A range of similar guest anions did not induce a significant luminescent response. Titrations were performed with *p-N,N*-dimethylaminobenzoic acid in the presence of other guests, and they showed that receptors **13a** and **13b** displayed selectivity of this molecule over other suitable guests.

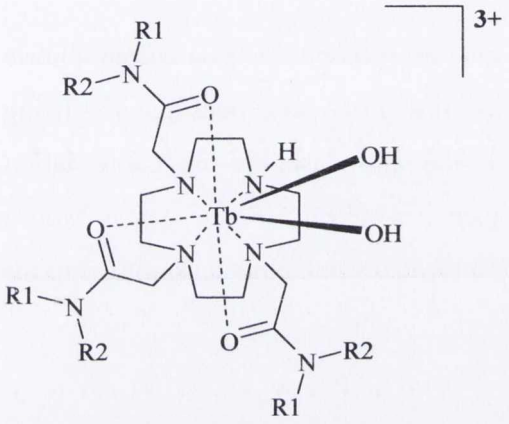

13

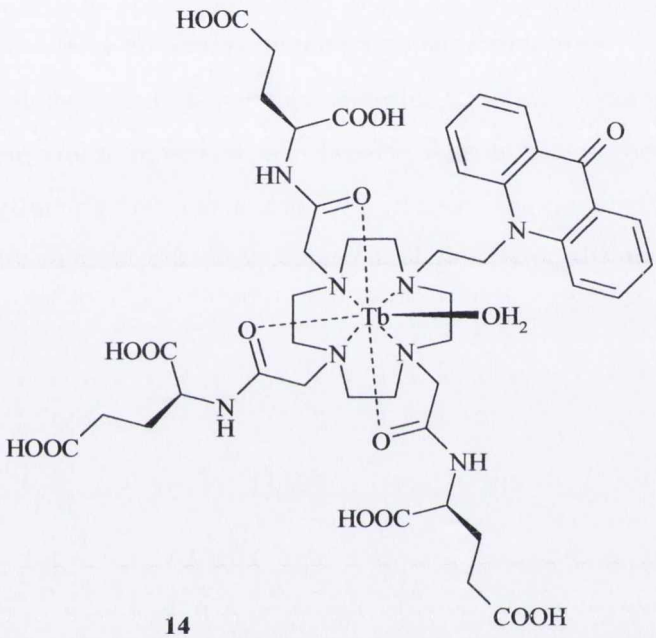

14

It is possible to use cyclen-based lanthanide sensors for *in cellulo* detection. Bretonniere *et al.*[40] developed a series of cyclen-based sensors using acridone as the sensitising chromophore. The most successful of these was **14**, which contains the acridine sensitiser and three glutarate residues. Complex **Eu.14** exhibited a 69% change in the intensity ratio of the 615/588 nm emission bands over the concentration range of 5 – 15 mM of HCO_3^- (the intracellular range) in a cell lysate medium.

Parker *et al.*[7] have synthesised an extensive series of luminescent lanthanide chelates with derivatized cyclens which act as sensors for pH, pO_2, and selective anion analysis and as stains for cell imaging. Several of the latter probes for *in cellulo* work have quantum yields in the range 5% - 10% in water and can be excited at the start of the visible range (> 340 nm).

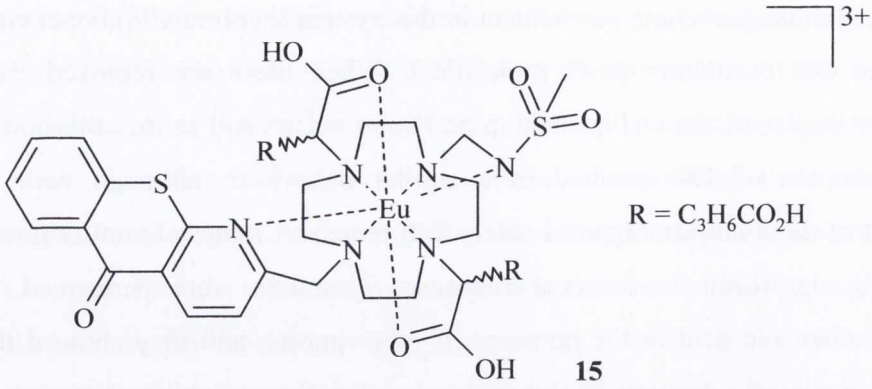

$R = C_3H_6CO_2H$

15

In the bifunctional anionic complex **15.Eu** the azathiaxanthone acts as a chromophoric antenna while the sulphonamide substituent binds the metal in a pH-dependent manner, being coordinated at high pH and uncoordinated at low pH. In the latter case, the free coordination position is occupied by a water molecule which partly quenches the Eu^{III} luminescence. Mouse skin fibroblasts NIH-3T3 cells uptake the complex which localizes in the nucleus, allowing for its selective staining.[41]

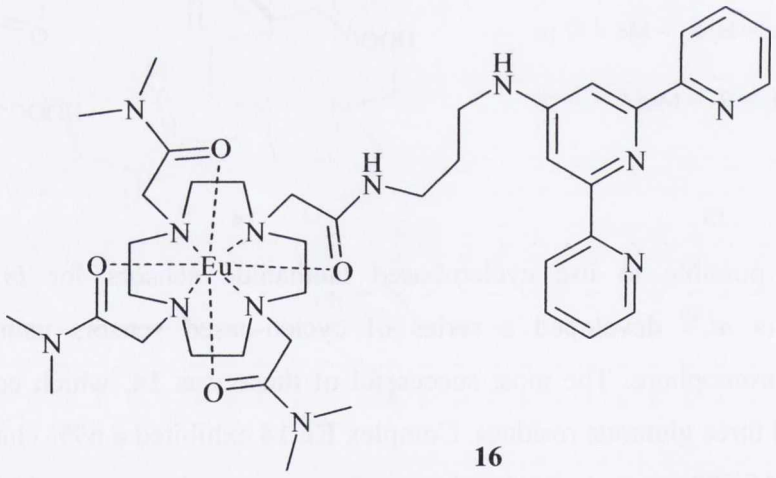

16

Ligand **16** was designed with a view to forming a mixed *d-f* assembly, where the terpyridine coordinates the d-metal, and populates the lanthanide through the *antenna effect*.[42] The addition of transition metal ions such as Fe^{II} at pH 7.4 in buffered aqueous solution, to **Eu.16** resulted in *ca.* 95% quenching of $^5D_0 \rightarrow {}^7F_J$. This near complete quenching gives an indication of the sensitivity of the Eu^{III} emission to the coordination of the chelating antenna. The process could also be followed by UV-Vis absorption measurements, with the appearance

of a long wavelength absorption band signifying the presence of the MLCT state. Here, the Eu^{III} luminescence quenching is most likely due to energy transfer occurring from the lanthanide excited state to the ^{3}MLCT state of the Fe^{II} terpyridine complex. These changes were fully reversible upon addition of EDTA (ethylenediaminetetraacetic acid).

Following on from the last section, ligand **17** also forms a *d-f* complex. It is a cyclic ligand that was designed as an improvement of **7** and **8** by Pope *et al.*[43] It consists of a cyclen unit linked to the DTPA Zn^{II} coordinating unit. The luminescence of the resulting Eu^{III} complex was responsive to Zn^{II} ions, the presence of which modulated the emission intensity and the lifetimes, through a change in the hydration number from 0 to 2 in the absence and presence of Zn^{II}, respectively.

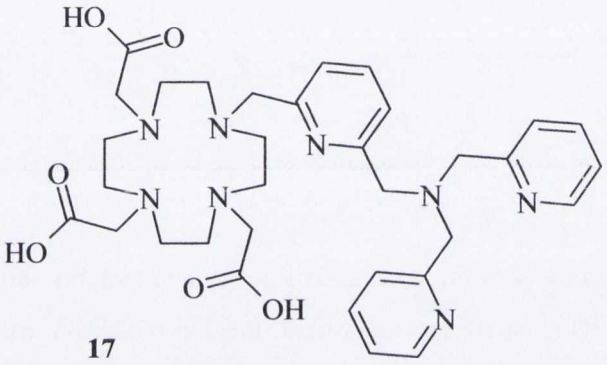

17

So far we have looked at several examples of lanthanide complexation into a pre-organized structure. These structures were specifically designed to accommodate a lanthanide metal, by possessing specific size, charge and number of coordination sites. However, lanthanide ions can bind to ligands that are not pre-organised in this manner. This will be discussed in the next section.

1.1.4.3 Metal induced Self-Assembly

Lanthanides and indeed other metals can induce self-assembly, an action in which carefully tailored particles spontaneously assemble around the selected guest.[32] Application of these processes in lanthanide coordination chemistry is relatively recent, but has already produced an array of two and three-dimensional functional architectures.[44] In coordination chemistry, self-assembly of the host cavity not only relies on the strong ion–dipole bonds to spatially organize the ligands, but also on the presence of programmed weak non-covalent interactions between these strands.[32]

Reinhoudt *et al.*[45] have recently described the Eu^{III} and Tb^{III} complexes of an EDTA-linked β-cyclodextrin dimer **18**, which operate in H_2O at pH 7.0 as luminescent sensors for aromatic carboxylates. EDTA is commonly used in lanthanide self-assemblies. However, it does not satisfy the high coordination requirements of the Ln^{III} ion. Consequently, sensitizing guests having both hydrophobic binding sites for β-cyclodextrin and a Ln^{III}-coordinating functionality are of particular interest.

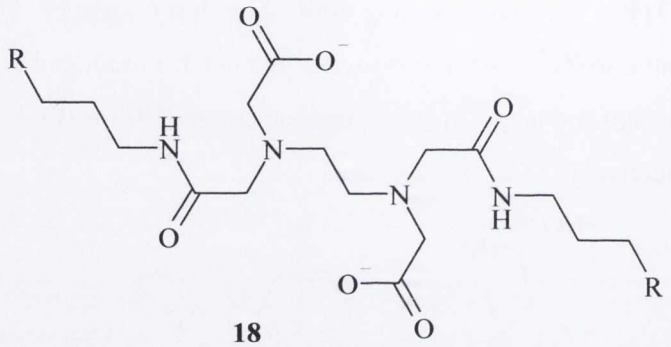

18

R = β-Cyclodextrin

Ligand **18** does not contain a sensitising antenna, so no lanthanide emission was observed initially. However, when **19** was added, the luminescence intensities of both **18.Eu** and **18.Tb** increased by a factor of 350 and 310, respectively, upon excitation of the antenna, **19** at 250 nm. The antenna molecule **19** has both a guest site (the *p-tert*-butylphenyl moiety) for binding to β-cyclodextrin and a Ln^{III}-coordinating carboxylate group. This allowed for coordination to the Ln^{III} centre of the **Ln.18** complex and thus led to efficient energy transfer from the antenna to the lanthanide centre.

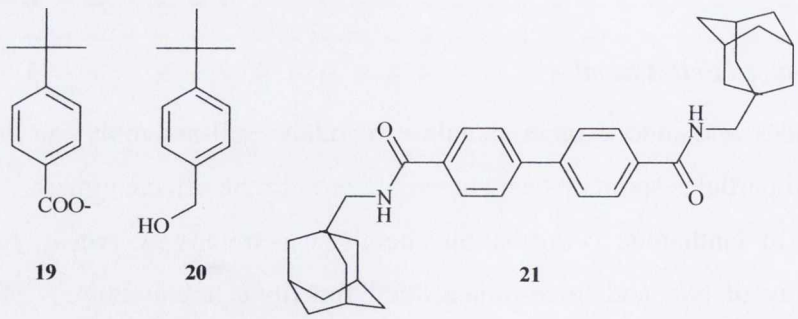

19 **20** **21**

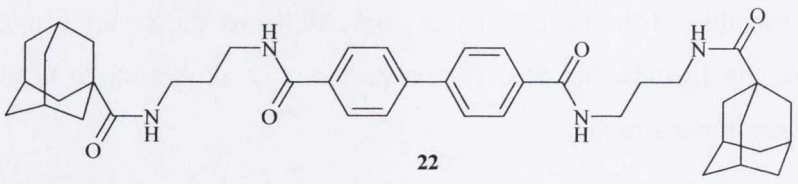

22

p-tert-Butylbenzyl alcohol **20**, complexes as strongly to the β-cyclodextrin as **19**, but lacks a Ln^{III} coordinating site, and so it was used as a reference. The triplet state energy of **20** was assumed to be comparable to that of **19**, and therefore suitable as a sensitiser for both Eu^{III} and Tb^{III} luminescence. The stability constant of $K = 5.0 \times 10^4\ M^{-1}$ was reported for complex **Eu.18.19**. As expected, the addition of the benzyl alcohol **20**, led to much smaller enhancements of *ca.* 2 fold. This indicated that it was necessary for the antenna to be closely bound to the Ln^{III} centre to sensitise it efficiently.

The interaction between **Eu.18** and bisadamantyl biphenyl sensitizers **21** and **22**, was also investigated. Once again, upon excitation of the sensitisers at 285 nm, large increases in the Eu^{III} luminescence was observed, *ca.* 300 and 360 fold for **21** and **22** respectively, in D_2O. A 1:1 binding stoichiometry was observed for both self-assemblies with very high association constants, which suggest that both the β-cyclodextrin cavities of **18** were involved in the binding of the bisadamantyl biphenyl sensitizers **21** and **22**.[46]

Lanthanide assemblies can also contain more than one lanthanide centre. Bünzli *et al*,[44] built a series of dimetallic structures that were soluble in organic solutions, in order to minimize the desolvation energy of the Ln^{III} ions. The resulting helicates formed bimetallic *4f–4f* helicates self-assembled in water. The complex of **23c** is highly stable, with a pEu ≈ 21 as compared to 25 for $[Eu(DOTA)]^-$, (where $pLn = -\log[Ln^{III}(aq)]^{3+}$ when $[Ln^{III}]_t = 10^{-6}$ M and $[DOTA] = 10^{-5}$ M, at pH = 7.4).[47] The Ln^{III} ions are well protected from water interaction, resulting in quite long lifetimes of the excited $Eu(^5D_0)$ and $Tb(^5D_4)$ levels (2.1 and 2.5 ms, respectively). The quantum yield of the metal luminescence amounts to 24% for the Eu helicate, but is much smaller for the Tb complex because of a back transfer process. However, Sm^{III} and Yb^{III} (emitting in the NIR range) are also sensitized.

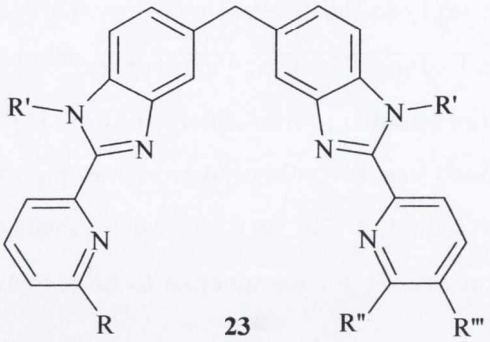

23

a: R = R" =

R' = CH_2CH_3

R"' = H

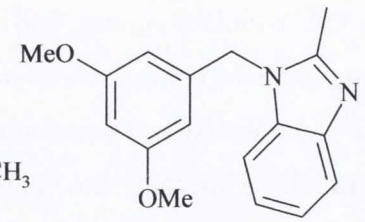

b: R = R" =

R' = CH_2CH_3

R"' = H

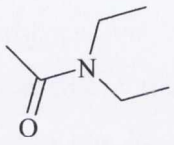

c: R = R" =

R' = CH_2CH_3

R"' = H

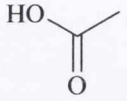

d: R =

R' = CH_3

R" = H

R"' = H

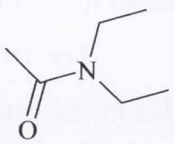

Piguet *et al.*[48] showed that in the absence of coordinating anions, **24** complexes lanthanides such as (Ln = La^{III}, Nd^{III}, Eu^{III}, Gd^{III}, Tb^{III}, Ho^{III}, Yb^{III}, and Lu^{III}) to give $[\mathbf{Ln.24_n}]^{3+}$ (n = 1-3) in acetonitrile, where three, six, and nine heterocyclic nitrogen atoms respectively, are coordinated to the metal ion.

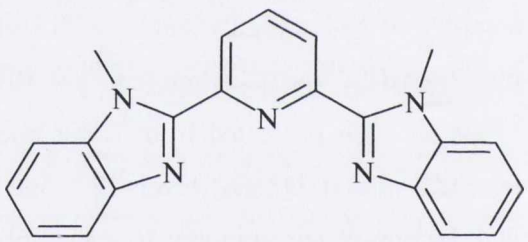

24

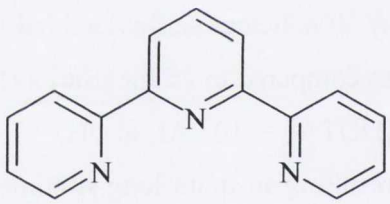

25

Unfortunately, the reported X-ray crystal structure of its analogue, $[\mathbf{Eu.(25)_3}]^{3+}$ is not accurate enough to allow a detailed comparison, but detailed luminescence and NMR studies in acetonitrile solution have firmly established that $[\mathbf{Eu.(25)_3}]^{3+}$ exhibits coordinated and uncoordinated equilibria at one of the nine pyridine rings, giving a predominantly eight-coordinate solution structure. In the same conditions, such decomplexation processes are not observed for $[\mathbf{Eu.(24)_3}]^{3+}$, which is the only species in solution. This increase in stability on going from $[\mathbf{Eu.(25)_3}]^{3+}$ to $[\mathbf{Eu.(24)_3}]^{3+}$ can be assigned to the intramolecular stacking interactions in the cations, which we expect to be significantly increased when pyridines were replaced by more extended aromatic benzimidazoles. The luminescent properties of the

complexes are consistent with this. They show the Ln^{III} ions are fully protected by the ligands, except in solution where some solvent interaction seems to occur.[48]

One ligand unit that has been used many times and is known to bind lanthanide metals very efficiently is the pyridine-2,6-dicarboxylic acid unit. Le Borgne *et al.*[49] synthesised a series of semi-rigid tridentate binding units derived from pyridine, beginning with **26a**.[50] The group demonstrated that the connection of symmetrical tertiary amide side arms at the 2- and 6-positions of the central pyridine rings provided a library of versatile tridentate binding units for the complexation of Ln^{III}. The increased steric congestion brought by the replacement of diethylamide **26a** with diisopropylamide in **26b** and dibenzylamide in **26c** decreases the affinity of the tridentate cavity for Ln^{III}, but 1:1 $[Ln(L)]^{3+}$ and 1:2 $[Ln(L)_2]^{3+}$ complexes can be obtained at submilimolar concentrations in acetonitrile for the three ligands. From this, it is clear that the triple-helical complexes $[Ln(L)_3]^{3+}$ are more sensitive to steric effects because of the location of a large number of terminal amide groups along the three-fold axis.

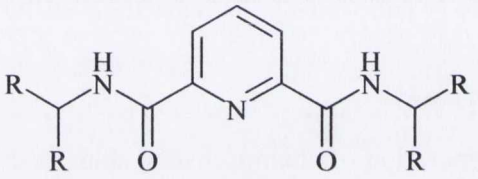

a. R = C_2H_5
b. R = $CH(CH_3)_2$
c. R = CH_2-C_6H_5

26

The associated formation constants are thus reduced by 3–4 orders of magnitude when going from $[Ln(\mathbf{26a})_3]^{3+}$ to $[Ln(\mathbf{26b})_3]^{3+}$, and they become too small to be determined for $[Ln(\mathbf{26c})_3]^{3+}$ which eventually establishes that peripheral interstrand interactions can control the wrapping process, a crucial point for generating size-discriminating effects. As far as 1:2 complexes $[Ln(\mathbf{26b})_2(H_2O)_2(CF_3SO_3)]^{2+}$ and $[Ln(\mathbf{26c})_2(H_2O)_2(CF_3SO_3)]^{2+}$ are concerned, very similar structural and photophysical behaviour was observed which indicates insignificant electronic coupling between the terminal alkyl or aryl groups and the tridentate bis-carboxamidopyridine core. However, two noticeable differences should be mentioned.

(1) A slightly improved **26c.Ln** (Ln = Eu, Tb) energy transfer process increases quantum yields in solution for complexes with **26c**, but the light-conversion process remains modest because of the inefficient ligand-centred sensitisation.

(2) The dynamics of solvent exchange in the first coordination sphere is faster for $[Ln(\mathbf{26c})_2(H_2O)_2(CF_3SO_3)]^{2+}$, thus leading to an average C_{2h} or D_2 symmetry on the NMR time scale while $[Ln(\mathbf{26b})_2(H_2O)_2(CF_3SO_3)]^{2+}$ exhibits C_2 symmetry.

It is thought that hydrophobic effects resulting from the four benzyl groups may be responsible for restricted access of the first coordination sphere together with weaker interactions with solvent molecules in $[Ln(\mathbf{26c})_2(H_2O)_2(CF_3SO_3)]^{2+}$.

This section has reviewed just a small selection of the lanathanide chelates that have been studied. There are several detailed reviews by Bünzli,[23, 51] Piguet,[3] Gunnlaugsson,[46, 52, 53] and Parker,[7, 54] that give many more examples.

Although, lanthanides make excellent sensors, their utility is somewhat restricted as they are predominantly studied in solution. By immobilising them on a solid substrate they could be developed into devices that could be used outside of a specialist laboratory. The next section deals with some examples of lanthanides, and some other functional metal complexes, that have been immobilised on a variety of substrates to increase their utility.

1.2 Lanthanides on Solid Substrates

For practical reasons, the incorporation of chemosensors, such as those that have been discussed in the previous section, into materials is highly desirable as it gives a platform for these sensors allowing for their development into easy to use, practical devices. Of special interest is the development of such chemosensors for ions and biomolecules.[55] For the reasons previously outlined, lanthanide-based chemosensors are ideal biological sensors and so it is of importance to design and synthesise a lanthanide-based sensor that can be immobilised on a substrate. In this section, several examples of lanthanides functioning on a variety of substrates will be reviewed.

1.2.1 Nanoparticles

Design and production of functional nanomaterials is of current interest due to a variety of potential applications ranging from chemistry to biological sciences. While the poor water-solubility, difficult surface conjugation chemistry and possible toxicity *in vivo* of quantum dots are still under investigation,[56, 57] metal and semiconducting nanoparticles are being extensively researched as they exhibit interesting size- and shape-dependent properties that combine with the intrinsic functionalities of organic and biomolecular systems. This is

done by incorporating them on the surface of nanoparticles, to yield hybrid materials with novel properties and functions.[58] As nanoparticles are water soluble, they provide a convenient first step towards the functionalisation of substrates with lanthanides.

Fluorescence spectroscopy is not commonly used as a tool for examining metal nanoparticles as it is generally believed that gold nanoparticles quench the singlet excited state of the chromophore when it is attached to their surface. However, several groups have shown that as long as the chromophore is situated sufficiently far away from the surface of the nanoparticle, and they are densely packed on the surface, no quenching is observed.[14, 58]

Thomas *et al*,[58] functionalised gold nanoparticles (AuNPs) with monothiol derivatives of 2,2'-dipyridyl **27**. The average size of the metal core is around 4 nm, with a shell of ~ 340 bipyridine ligands around the Au nanoparticle, **AuNP-28**.

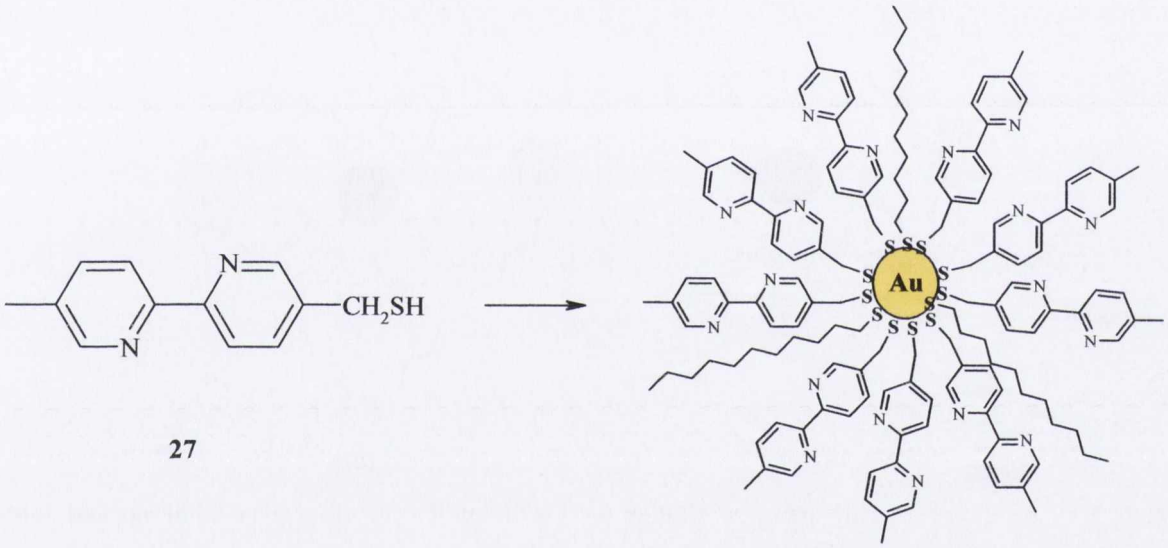

27 **28**

The complexation ability of **AuNP-28** with Eu^{III} and Tb^{III} ions was further investigated by following the changes in the absorption spectrum. The thiol derivative of bipyridine, **27**, in acetonitrile exhibits two absorption maxima one at 249 nm and the other at 295 nm. Upon addition of increasing concentrations of Eu^{III}, a decrease in the intensity of the σ–σ^* absorption band (295 nm) of **27** along with the concomitant emergence of a new band around 325 nm was observed. The emergence of a new band for **AuNP-28** at 325 nm upon addition of Eu^{III}/Tb^{III} ions is attributed to the polarization resulting from the metal ion coordination and the conformation change of the ligand to the *cis* form.

Absorption isotherms and Job's method of continuous variation (see Chapter 2) indicated a 1:3 (M:L) stoichiometry. A 1:3 complexation allows for two modes of interaction: (a) bipyridines bound on the same Au nanoparticle coordinating with Eu^{III}/Tb^{III} ions and (b) bipyridines from different nanoparticles coordinating to a given lanthanide ion (see Figure 1.5). Transmission Electron Microscopy (TEM) was used to investigate which mode occurred. The images of the Au-nanoparticles without any Eu^{III} showed random distribution throughout the grid, whereas self-assembly was observed in the presence of Eu^{III} ions. This aggregation suggests that mode (b) occurs.

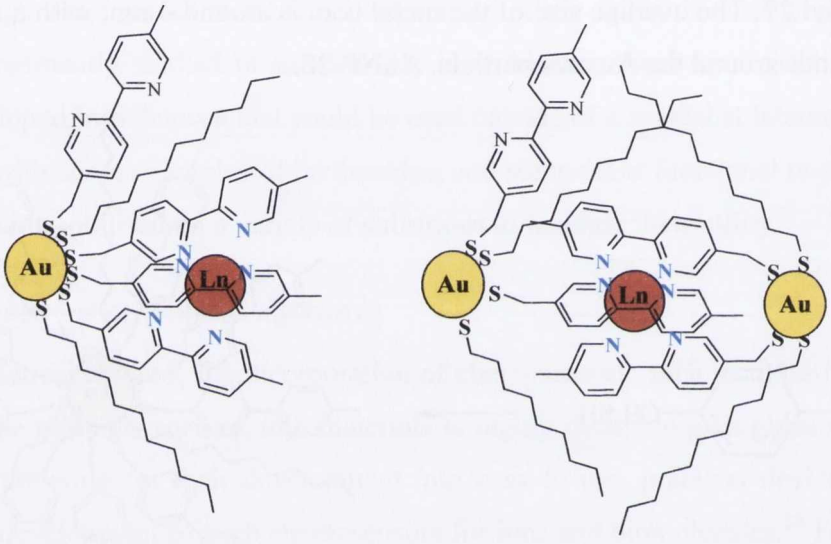

(a) (b)

Figure 1.5 Two of the possible modes of binding for Eu.28 and Tb.28. Absorption isotherms and Job's method continuous variation indicated a 1:3 M:L stoichiometry.

The **AuNP-28.Eu** was found to have a lifetime of 0.36 ms, while the terbium analogue, **AuNP-28.Tb** had a lifetime of 0.7 ms. Interestingly, the luminescence lifetimes of lanthanide complexes were not influenced by linking them onto gold nanoparticles.

The ability of **AuNP-28.Eu** to sense alkali metal ions (Na^+, K^+), alkaline earth metal ions (Ca^{2+}, Mg^{2+}) and transition metal ions (Cu^{2+}, Zn^{2+}, Ni^{2+}), was investigated. A dramatic decrease in the luminescence was observed upon addition of alkaline earth metal ions (Ca^{2+}, Mg^{2+}) and transition metal ions (Cu^{2+}, Zn^{2+}, Ni^{2+}), most likely due to the displacement of the Eu^{III} ions by these ions, whereas the luminescence intensity was not influenced by the addition of Na^+ and K^+ ions.

A recent example from the Gunnlaugsson group shows a lanthanide-based sensor immobilized on a gold nanoparticle that effectively senses biologically relevant phosphate anions such as flavin monophosphate.[14] This was achieved by synthesising **29**, a heptadendate macrocycle conjugate possessing an alkyl thiol group, which enables the adsorption of **Eu.29** onto the surface of gold nanoparticles, and results in the formation of water soluble gold nanoparticles **AuNP-29.Eu**, this complex is the subject of Chapter 3. The switching "*on*" of the Eu^{III} emission, upon formation of **AuNP-29.Eu.30** from **AuNP-29.Eu** was monitored by luminescence titrations using **30,** with λ_{ex} = 336 nm. The corresponding emission was indicative of the direct coordination of **30** to the Eu^{III} centre and the displacement of the two metal-bound water molecules, as the hypersensitive $\Delta J = 2$ transition centered at 616 nm, gave rise to the greatest changes in the Eu^{III} emission. The formation of a ternary complex, or a self-assembly, between **AuNP-29.Eu** and the antenna **30**, at pH 7.4 (0.1 M HEPES) formed the stable complex **AuNP-29.Eu.30**, which was highly luminescent upon excitation of the antennae. The binding was a 1:1 stoichiometry between each gold conjugated **Eu.29** and **30**, so it was possible to estimate the number of bound Eu^{III} complexes per AuNP as *ca.* 230. These luminescent AuNPs can be used to sense flavin monophosphate, **31**, through the displacement of **30** by **31**.

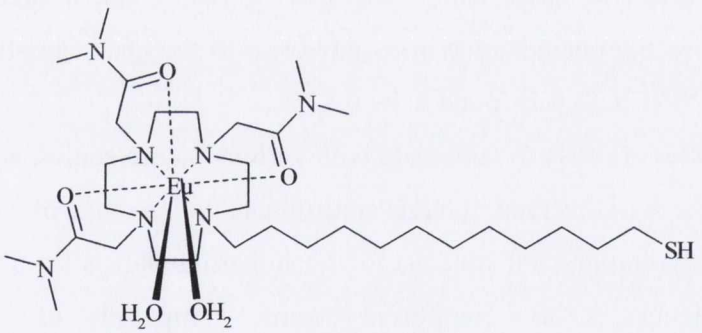

29

30:

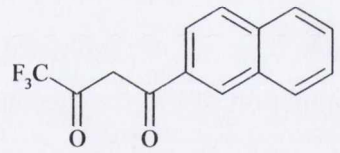

31:

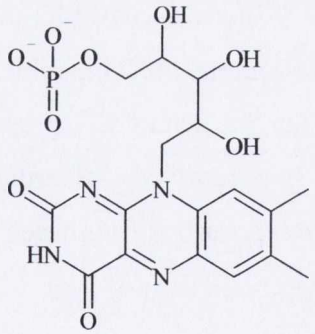

Pikramenou *et al.*[59] synthesised a ligand with a rigid structural framework, based on DTPA (See Figure 1.6). The design of **32** incorporates a binding core composed of oxygen and nitrogen that gives thermodynamically stable (log $K \approx 15$), neutral lanthanide complexes, that are soluble in polar solvents. The pendant arms sensitised the lanthanide centre and had thiol groups that could bind to soft transition metals.

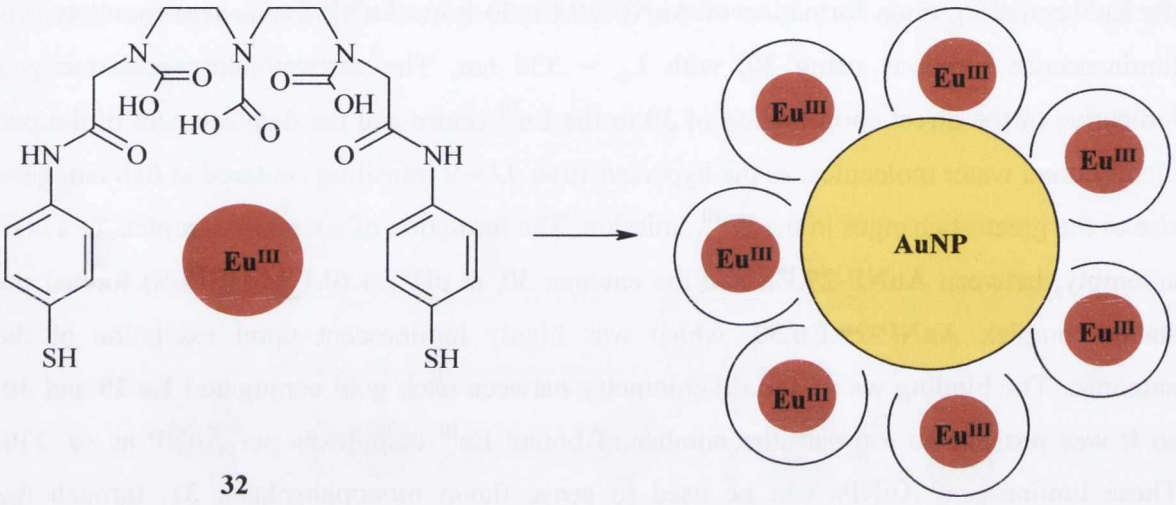

32

Figure 1.6 A schematic of the binding mechanism of complex AuNP- Eu.32.[59]

TEM analysis showed that the functionalised nanoparticles **AuNP-Eu.32** were monodisperse, unaggregated and spherical in shape with a diameter of 10–15 nm. Indirect population of the Eu^{III} excited state *via* the phenylamide arms gave rise to the characteristic Eu^{III} emission, and the lifetime of **AuNP-Eu.32** was found to be 0.8 ms.

The surface of SiO_2 nanoparticles are easy to conjugate with various biomolecules, are water-soluble, biocompatible, and the size of this type of NP is controllable with a range of 5 – 200 nm.[60] Chen *et al.*[60] prepared highly luminescent aqueous Eu^{III} nanoparticle labels for use in time-resolved fluorometric assays. The complexes were composed of a polyaminocarboxylate-based chelator binding the Eu^{III} and a coumarin 120 dye as the antenna.

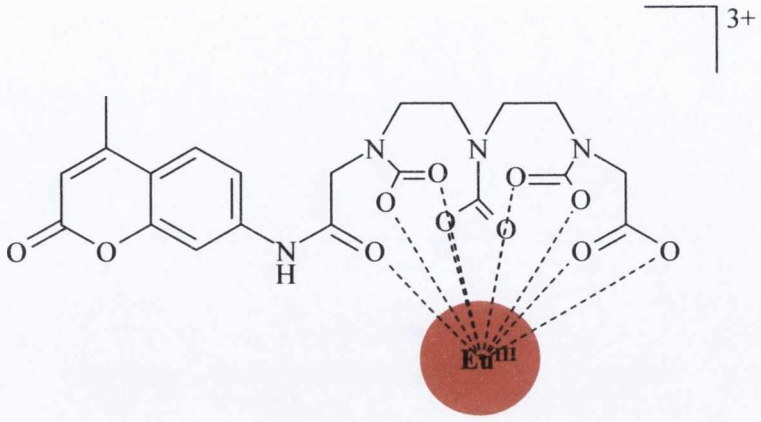

33

Figure 1.7 Ligand 33 binding to Eu^{III}

Polyaminocarboxylates have high water-solubility and a high binding constant for lanthanides. SiO_2 nanoparticles containing many of these luminescent complexes were prepared by the reverse microemulsion method. TEM and scanning electron microscopy (SEM) images show that the **Eu.33** (see Figure 1.7) nanoparticles are 55 ± 3 nm size and spherical. Preliminary DNA assays showed that **Eu.33** could be applicable to time-resolved fluorometric assays, and that the detection sensitivity was improved 50-fold compared with the conventional dye fluorescein isothiocyanate (FITC).

1.2.2 Other Substrates

The concept of monolayers was introduced in 1917, when Langmuir studied the spreading of amphiphiles on water and realised that this film was one molecule thick.[61] Later, Blodgett was able to transfer this monolayer from the air-water interface onto a solid support (Langmuir-Blodgett (LB) films).[62] However these layers were thermodynamically unstable, so temperature change or exposure to solvents could ruin their structure.[63] The spontaneous formation of monolayers was first demonstrated in 1946 by Zisman *et al.*[64] who showed that alkylamines form self-assembled monolayers (SAMs) on platinum substrates. Since this time, a large variety of SAMs have been created, for example thiols on gold,[65] alkyltrichlorosilanes on glass,[66] and fatty acids on metal oxide surfaces,[67] see Figure 1.8.[63]

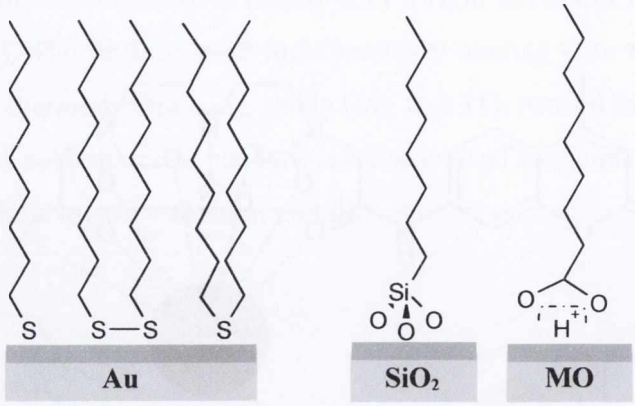

Figure 1.8 SAMs on gold, glass and metal oxides.[63]

A common feature of these systems is the strong interaction between the functional group of the adsorbate and the bare substrate. Also, van der Waals interactions among the adsorbate molecules give rise to a dense packing on the monolayer.[63] Research in this topic has been increasingly directed towards applications of molecularly defined surfaces, with the possibility of introducing the desired optical, electrical, and chemical properties in monolayers making them very attractive as photoresists, lubricants, optoelectronics, or sensing devices.

The following sections are designed to review a few examples of how metal complexes have been immobilised on a variety of substrates to produce functional devices. Where possible, examples using lanthanide metals have been used.

1.2.2.1 Organic Light Emitting Diodes

Organic light emitting diodes (OLEDs) are devices that can be used in many applications for example in television screens, or computer displays. OLEDs typically emit less light per area than inorganic solid-state based LEDs which are usually designed for use as point-light sources. A significant benefit of OLED displays over traditional liquid crystal displays (LCDs) is that OLEDs do not require a backlight to function. Thus they draw far less power and, when powered from a battery, can operate longer on the same charge. Because there is no need for a backlight, an OLED display can be much thinner than an LCD panel, see Figure 1.9. This area of research has recently been reviewed by de Bettencourt-Dias.[68]

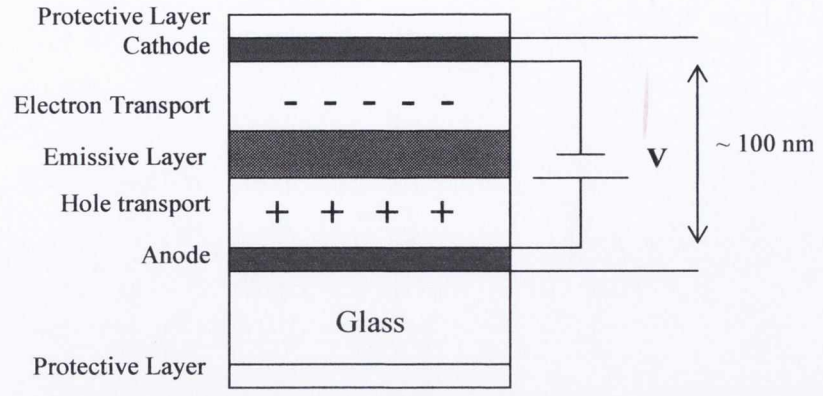

Figure 1.9 Diagram of an organic light emitting diode (OLED).[47] A voltage bias is applied to the iron tin oxide (ITO) electrodes. The voltage bias is not large, but since the layers are very thin (typically a few nm thick), the electric field is in the range of 10^5 - 10^7 Vcm^{-1}.

Lanthanides are highly effective for use in OLEDs due firstly, to their line-like emission bands and secondly, to their excitation process. Lanthanides can be excited *via* an intramolecular energy transfer, so there can be very high internal quantum efficiency, as opposed to only ca. 25% for organic fluorophores that lose energy through thermal deactivation processes, without the emission of photons.[69]

Okamoto *et al.*[70] developed two lanthanide-based OLEDs, **34** and **35**, both of which gave sharp emission bands and a characteristic bright Ln^{III} luminescence was observed at low voltages.

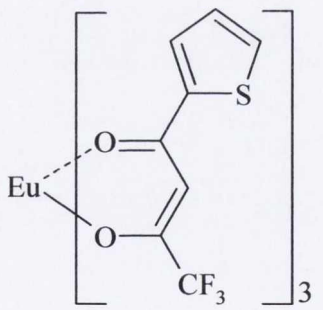

34

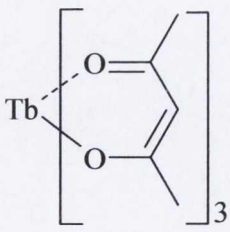

35

A major challenge in OLEDs is the design of efficient, white-emitting diodes. One approach to designing such devices is by doping 2.5% dendritic Eu^{III} diketonates such as [Eu(TCPD)(Phen)] **36** into *4,4'- N, N'*-dicarbazole biphenyl (CBP).[71] CBP is known for being an excellent host for phosphorescent dopants as it possesses a high-energy triplet state

(21000 cm^{-1}) and its ambipolar charge-transporting ability. This technique produced a very efficient, white light emitting OLED.

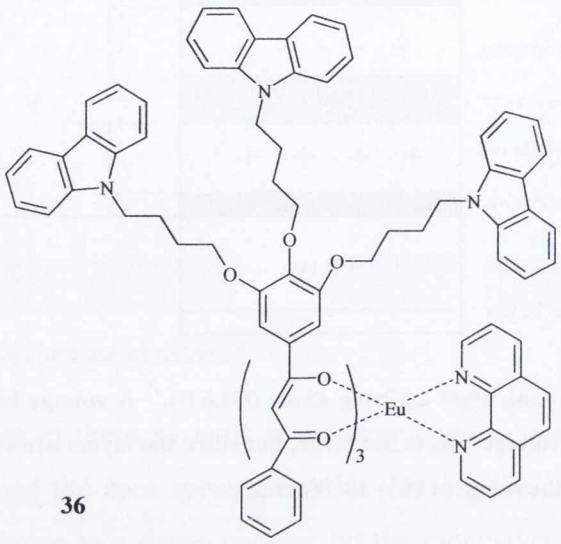

36

1.2.2.2 Glass

Sol–gel glass is an optically transparent, porous and homogeneous material, favouring its use as a sensor matrix. Moreover, it is more chemically inert and photostable than organic polymers and the controlled preparation of thin films of defined porosity is relatively well understood.[66]

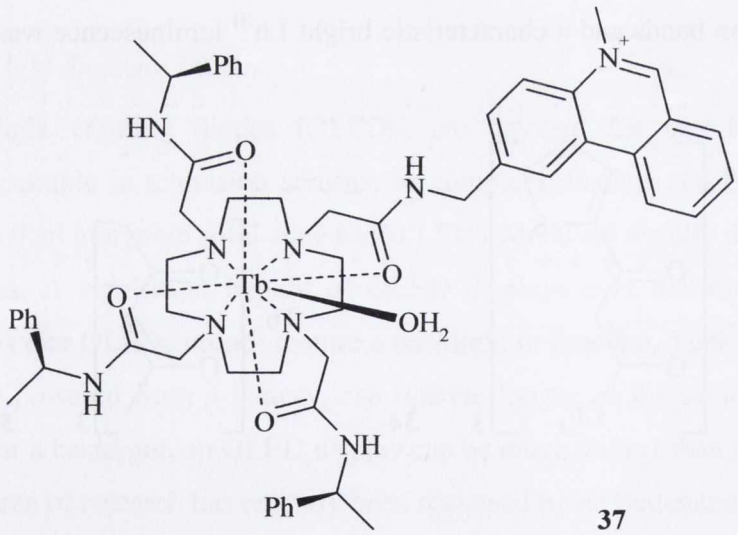

37

Molecular oxygen is known to quench lanthanide emission (see Figure 1.3). Using this phenomenon, Blair *et al.*[66] recently incorporated cationic Tb^{III} complexes, [**Tb.37**]$^{4+}$ bearing an *N*-methylphenanthridinium chromophore in sol–gel thin films and analysed their response

characteristics with respect to variations in dissolved oxygen concentration. Analysis of the emission lifetime decay curves (547 nm) led to a linear calibration model, defined over an oxygen concentration range from zero to 0.5 mM (in H_2O, 295 K).

The sol–gel film prepared with a H_2O/Si ratio of 4, incorporating **[Tb.37]**$^{4+}$, exhibits good sensitivity to dissolved oxygen and represents the first example of lanthanide luminescence being used to signal changes in dissolved oxygen concentration in an operational sensor.[66]

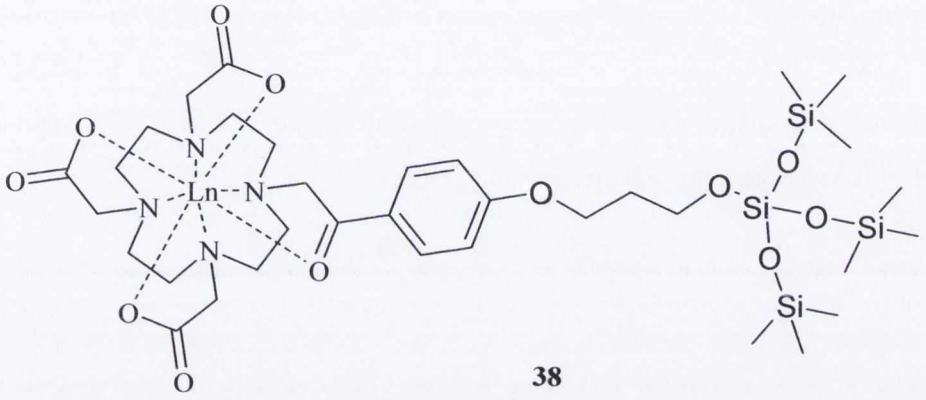

38

Accorsi *et al.*[72] synthesised highly stable **Eu.38** and **Tb.38** complexes, and anchored them onto a single SiO_2 transparent layer, yielding *ca.* 40 nm thick films, and thereby allowing for high loading of these complexes within the films (4.8 nm^3 of film volume per chromophore) which resulted in uniform and easily colour-tunable luminescent layers. To avoid heterogeneous dispersion of the lanthanide complexes, they covalently bound them to the silica matrix. This procedure yielded highly homogeneous, transparent, and red-luminescent SiO_2 films. These were very stable and could undergo thermal processing up to 200 °C for hours with no appreciable consequences.

1.2.2.3 Hydrogels

Hydrogels are three-dimensional, hydrophilic, polymeric networks that swell, but do not dissolve in water.[73] They were first used as biomaterials back in 1960 by Wichterle and Lim.[74] Polymeric structures are termed hydrogels when the amount of water retained is between 20 – 100% of the total weight. They have many similar properties to human tissue, and are generally accepted when implanted *in vivo*, and so are ideal for use in tissue regeneration. Hydrogels are non-toxic, non-antigenic, non-irritable, and chemically very

stable. They are also permeable to small molecules such as oxygen, and other nutrients. So far, they have been used in many biomedical applications, such as artificial organs, contact lenses, and surgical sutures.[75, 76] Lanthanide-based systems have been incorporated into hydrogels, with the aim of developing luminescent sensors into medical and pharmaceutical monitoring devices. In the Gunnlaugsson laboratory, the Eu^{III} complex of **39** was incorporated into a hydrogel matrix of poly[methylmethacrylate-co-2-(hydroxyethylmethacrylate)].[55] In previous, solution studies, **39** was found to behave as a pH switch in aqueous solution, that can monitor pH changes from *ca.* 2.5 to 8. The control hydrogel matrices were prepared using methylmethacrylate (MMA) and 2-(hydroxyethyl-methacrylate) (HEMA) in three different ratios: 1:1 (MMA:HEMA, w/w), 1:3 (MMA: HEMA, w/w) and 100 % HEMA. All the hydrogels demonstrated Eu^{III} emission upon excitation of the antenna. Not surprisingly, this process was much slower than that observed in solution.[46]

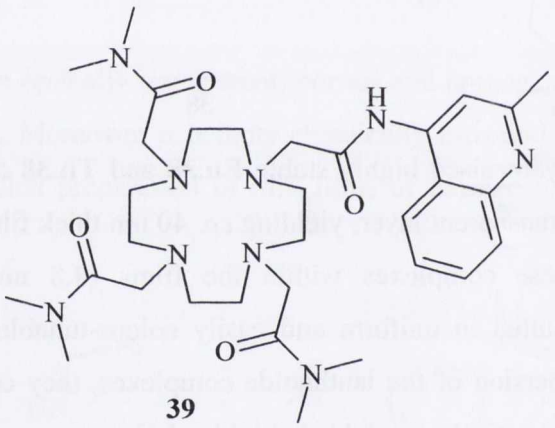

39

The hydrogel's photophysical properties were examined by confocal laser-scanning microscopy (CLSM) and steady-state luminescence. The emission was modulated by soaking the films in alkaline or acidic solution for 1 hour. Luminescence emission micrographs clearly showed that at pH 2, the hydrogel incorporating 0.05% w/w of **Eu.39** showed a typical red emission of Eu^{III}, whereas at pH 11, the red emission was almost entirely quenched, see Figure 1.10.[55]

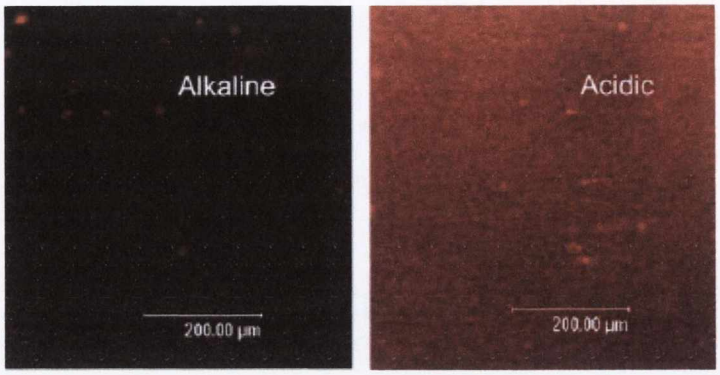

Figure 1.10 CLSM image of a section of hydrogel (MMA/HEMA, 1:3) incorporating 0.05% w/w Eu.39 in acidic and basic media.[55]

Lianos *et al.*[77] formed a hydrogel from poly(*N,N*-dimethylacrylamide) and complexed it with terpyridine and lanthanide metal ions, Eu^{III} and Tb^{III}. The hydrogel can be formed in three different phases: swollen with water, lyophilized (*i.e.*, dried by freeze-drying), where it loses the solvent but preserves the swollen configuration, and dried in the air where it shrinks. The three hydrogel phases affect the type of complex formed between terpyridine and the metal ion. So, in the swollen and lyophilized phases, emission from the metal is observed, and occurs *via* energy transfer from the excited ligand. In the shrunken phase, an intense green fluorescence is emitted, which is ligand-centred and independent of the complexed metal ion. In the absence of any metal ion, the ligand emits blue luminescence, independently of the hydrogel phase.

1.2.2.4 Gold

Gold is a relatively inert metal: it does not form a stable oxide surface and it resists atmospheric contamination for a reasonable period of time. It has a strong specific interaction with sulphur that allows the formation of monolayers in the presence of many other functional groups, and long-chain alkanethiols can form a densely packed, crystalline or liquid-crystalline monolayer on gold.[78] It is also a good starting material as it minimises uncertainties over the effects of surface roughness and sensor density.

There are many examples of molecular self-assemblies, and sensor systems on gold, however there is very little detailing lanthanides on gold. This is because gold strongly quenches luminescence from nearby molecules, and consequently there are only a few reports of the detection of luminescence on gold.[79] It is possible however, to overcome this problem by putting a spacer, for example an alkyl chain, between the gold substrate and the

luminescent molecule. It has been found by Kittredge *et al.* that a minimum chain length of 7 carbon atoms is required to avoid quenching by the surface.[80]

The start of this section will give two examples of functional SAMs on gold, and finish with an example of lanthanide chelates on a gold substrate. To the best of the author's knowledge, this is one of only a few examples of such a system in the literature.

Electrochemical methods are a popular choice for the detection of binding events on a SAM functionalised substrate. Many experimental techniques can be used to probe these interactions such as cyclic voltammetry,[81-83] or impedance spectroscopy.[84, 85]

Studies have been performed by Reinhoudt *et al.*[86] on the selective binding of metal ions to crown ether SAMs by impedance spectroscopy. As the metal ions bind to the crown ethers, the capacitance of the monolayer increased, and a very large increase in the charge transfer resistance was observed. The simultaneous monitoring of these two effects allowed for the determination of association constants for the interaction of various metal ions with SAMs of 12-crown-4, 15-crown-5, and 18-crown-6 adsorbates. 12-crown-4 showed the strongest affinity for Na^+, with a $K[M^{-1}]$ of 15800, while 15-crown-5, **40**, had a $K[M^{-1}]$ of 27100 for K^+. 18-crown-4 had the best result for K^+, however this was not significantly larger than for Li^+, Na^+, or Cs^+. High surface density of the crown ether, leads to the sandwich complexation of the metal ion, see Figure 1.11.

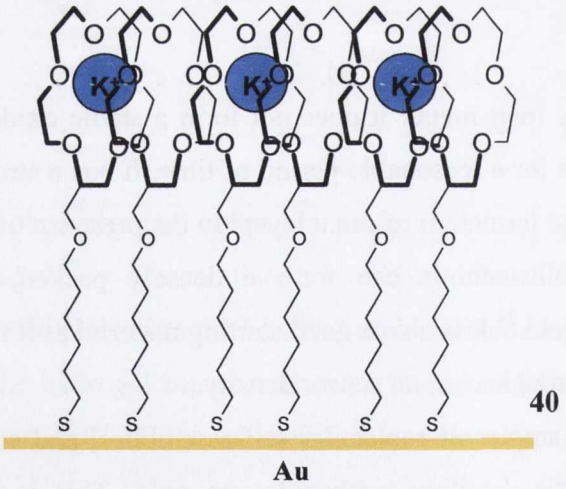

Figure 1.11 A high density SAM of 18-crown-4 tethered to a gold substrate, showing sandwich complexation to the K^+ ions.

SAMs on gold can also be used to anchor biosensors. The development of immunoassays for the determination of drugs or hormones requires the immobilisation of either the antibody or the antigen to the substrate.

Berggren and Johansson coupled monoclonal antibodies to SAMs of 6,8-dithiooctanoic acid (thioctic acid), **41**, to electrochemically detect antibody-antigen interactions, Figure 1.12.[87] Surface areas that were not covered were filled with 1-dodecanethiol to make the layer dense and insulating. The immunosensor was placed in a flow system, and a capacitance decrease could be observed after injection of an unlabeled antigen. Due to the selective binding of the corresponding antibody to the SAM, the average thickness of the layer increased upon detection. This method allowed for the detection of 1 pg/mL- 1 ng/mL, of a human hormone with a detection limit of 1.5×10^{-14} M.

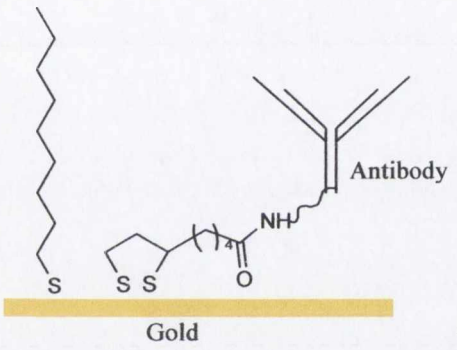

41

Figure 1.12 Antibodies immobilized on the gold sensor surface via an amide bond to the self-assembled thioctic acid. After the immobilization of the antibody a long hydrocarbon thiol, l-dodecanethiol, was introduced into the system to block any uncovered spots of the sensor surface.[87]

Roy and Mallik,[65] reported the synthesis of several polymerizable, metal-chelating thiols that were capable of complexing lanthanide ions, and self-assembling on gold, **42**, **43**, and **44**. Their goal was to immobilise proteins on the gold surface of a Quartz Crystal Microbalance (QCM) using metal-ligand interactions. For this purpose, a nonpolymerizable, metal-containing thiol, was synthesized and the SAM was fabricated. Proteins (myoglobin from horse heart and carbonic anhydrase from bovine erythrocyte) were found to bind to the metal ions of the surface of the SAM, however they also became embedded inside the monolayer which complicated the data analysis from QCM.

molecular interactions, and the corresponding very small mass changes. In the following section, quartz crystal microbalances will be briefly discussed, followed by microcantilevers.

1.3.1 Quartz Crystal Microbalance

A quartz crystal microbalance (QCM) measures mass per unit area by measuring the change in resonant frequency of a quartz crystal resonator. The resonance is shifted by the addition or removal of a small mass at the surface of the crystal. QCM is most commonly used under vacuum, however more recently it has also been used in liquid environments. It is useful for monitoring the rate of deposition in thin film deposition systems under vacuum. It is a very sensitive detection technique and it is possible to measure mass densities down to a level of below 1 $\mu g/cm^2$. It can also be combined with chemical hosts to monitor the interaction between host and guest when neither can report on this event in a way that can be instrumentally detected.

Interactions between molecules in the gas phase and SAMs have been studied by many groups using quartz crystal microbalances (QCMs). Willner *et al.* studied the binding of a photoisomerizable azobenzene derivatives **46**, and **47**, to an eosin **(45)** -modified, gold surface by QCM.

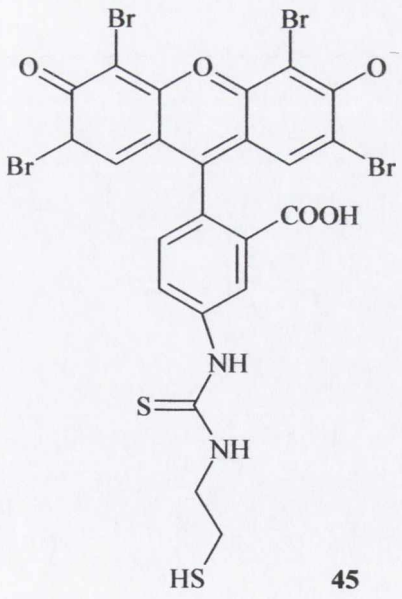

45

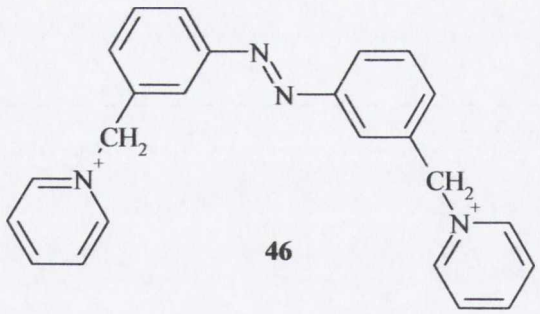

46 **(E)**

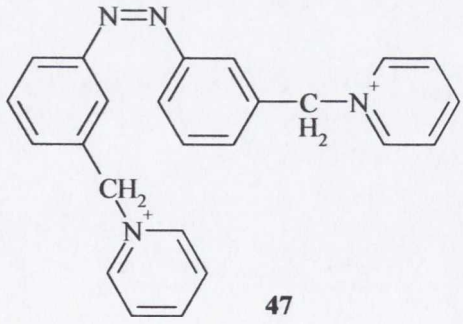

47 **(Z)**

They found that the E-isomer, **46** of the azobenzene had a substantially higher affinity for the eosin monolayer than the Z-isomer, **47**. By reversible photoisomerization of the

1.4 Work described in this thesis

Lanthanide metals form stable, luminescent complexes with many types of ligands. By using preorganised chelates, it is possible to build lanthanide-based supramolecular self-assemblies that retain both the properties of the ligand (such as chirality) and also the desired luminescent properties of the lanthanide metal. The initial focus of this thesis will be the design, synthesis, characterization and photophysical evaluation of a lanthanide templated self-assembly.

Chapter 2 will describe the synthesis and analytical studies performed on two chiral mono-dentate ligands **57** (*S,S*) and **58** (*R,R*), and their corresponding helical Eu^{III} complexes, in organic solvents. Several spectroscopic techniques will be employed to gain insight into the formation and structure of these complexes.

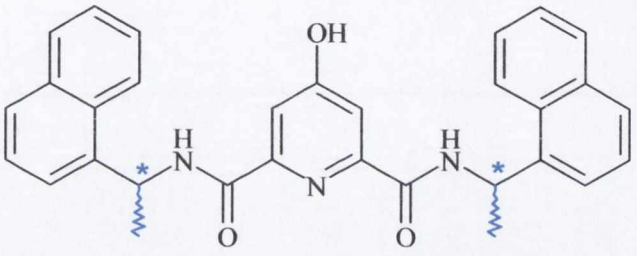

57: (*S,S*)
58: (*R,R*)

Chapter 3 will discuss the formation of SAMs on a gold substrate of a lanthanide-based sensor for flavin monophosphate that has been developed in the Gunnlaugsson group.[14] This complex has been studied extensively in solution and on gold nanoparticles. However to make use of the full potential of lanthanide-based sensors as diagnostic tools, it is preferable to have them incorporated in a solid matrix that can then be used as a device out of the laboratory and without specialized equipment. With this in mind, Chapter 3 will begin by describing the characterization and qualitative analysis of this complex on a flat gold substrate.

Although there are many examples of different types of cantilever sensors, one area has been left largely unexplored. Very little research has gone into the field of simultaneous mechanical and optical sensing. With this in mind, it is hoped that by functionalising lanthanide-based sensors on a cantilever surface, simultaneous mechanical and optical sensing could be achieved by combining the mechanical sensing abilities of the cantilever with the optical sensing abilities of the lanthanide complexes, thereby creating a self-verifying sensor. The results presented in Chapter 3, are the first step towards this kind of system, Scheme 1.1.

Chapter 2
Lanthanide-templated Supramolecular Assemblies

2 Lanthanide-Ion Templated Supramolecular Assemblies

2.0 Introduction

In general, supramolecular chemistry refers to the formation of large molecular structures from several smaller components, which may occur *via* spontaneous self-assembly. In going from pre-organized to predisposed receptors, one benefits from simplified synthetic procedures. When using lanthanides to template this self-assembly process, it is possible to take advantage of both the high electric field generated by the Ln^{III} ions and weak intermolecular interactions to self-assemble small co-ordinating units around the metal ion.[23]

By using chiral ligands, that will maintain their functionality upon complexation, it is possible to create chiral lanthanide complexes. These have the benefits discussed in the previous chapter however, they have the additional specificity of chirality. To date, many enantiomerically pure lanthanide complexes have been prepared and characterized, and have applications as, for example, chiral shift reagents for resolving NMR spectra of chiral compounds[107-109] (dating back to the 1970s) and more recently (dating from the early 1990s) as highly enantioselective catalysts and reagents[110-112] as well as chiral sensors.[113, 114]

The focus of this chapter, is the further development from ligands previously synthesised within the group, of a self-assembly of chiral ligands around a lanthanide centre, with a view to immobilising these systems on nanoparticles or substrates to extend their use to sensing and diagnostic applications, by means of adding a tethering molecule at the - 4 position on the pyridine central moiety. The characterisation of these complexes by NMR, electrospray mass spectrometry, and various optical techniques such as UV-Visible and steady state luminescence spectroscopy, circular dichroism, and circularly polarised luminescence will be detailed. This will be followed by a short section discussing the potential future applications of these systems. Firstly, the next section will discuss some examples of lanthanide templated chiral assemblies developed.

2.0.1 Chiral lanthanide self-assemblies

In addition to the classical separation of racemates, it is possible to synthesise specific stereoisomers from optically active starting materials or using chiral catalysts. However, with lanthanide metals this can be difficult since only small changes in reaction conditions can lead to addition or loss of coordinated solvent molecules and/or counter ions, which opens the

pathway for easy racemization.[115] The design of ligands that are predisposed to form only one of many possible stereoisomers is therefore a challenging task.

2,6-Pyridinedicarboxylic acid, **49**, also known as dipicolinic acid or DPA and its derivatives have been shown to be good candidates for the design of triple-stranded Ln^{III} building blocks with interesting luminescence properties.[116] Complexes in the form of $[Ln(DPA)_{1-3}]^{n+}$ have been shown, with $[Ln(DPA)_3]^{3-}$ being the most stable and luminescent. The weakly stable $[Ln(L)_3]^{3+}$ complexes exist as a mixture of rapidly interconverting conformers with Ln = Eu^{III}, Tb^{III} displaying fair quantum yields in acetonitrile. Moreover, $[Ln(DPA)]^{+}$ complexes are more stable than $[Ln(DPA)_2]^{-}$ but they are usually less luminescent.[50, 117] While these complexes are inherently chiral, they usually appear as racemic mixtures both in the solid state and in solution (often as fast interconverting isomers).[116] Some examples of ligands based on this structure are **50**, **51**, and **52**.

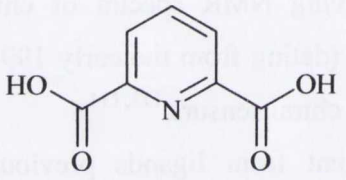

49

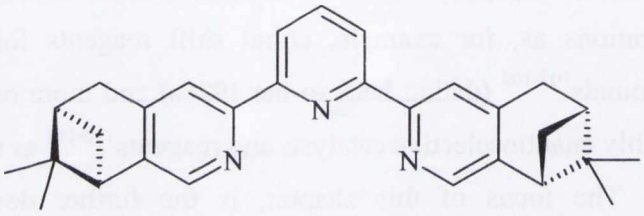

50

Müller *et al.*[115] reported the first selective formation of a single stereoisomer in a mononuclear lanthanide coordination compound resulting from the self-assembly of three independent tridentate chiral ligands. They began by using a chiral terpy ligand with pinene moieties attached in positions 9 and 10, respectively in **50**. This formed only ML_2 complexes with La^{III}, Eu^{III} and Lu^{III}. They thought that this low stoichiometry was most likely due to steric interactions, which were interfering with the coordination of the third ligand, as when they placed the pinene moieties facing away from the metal centre, in positions 10 and 11, respectively ML_3 complexes were formed in 80 – 90% yields. ^{1}H NMR studies showed that at room temperature, a nine-coordinate C_3 symmetric complex was predominant in solution and no additional resonances were observed at low temperature. Quantum yields of Φ_{Eu} = 4% and Φ_{Tb} = 0.022% were measured. Further investigation determined that these low values were due to inefficient intersystem crossing ($S_1 \rightarrow T_1$) in the ligand strands and that possibly some contribution from other photophysical processes such as photo induced electron transfer (PET) may also have been involved.[115]

Bünzli and co-workers[116, 118] developed ligands **51** and **52**. ES-MS spectra revealed that 1:1, 1:2, and 1:3; M:L complexes were all formed upon titration of **51**, with europium perchlorate ($Eu(ClO_4)_3$) in acetonitrile. A small amount of 1:4 species was also observed. Such species have been observed before for similar systems and were assigned to outer-sphere association of a fourth ligand with a 1:3 structure.[117] Of these, the 1:3; Eu:**51**, complex was by far the most abundant. Circularly polarised luminescence (CPL) studies indicated that there was a mixture of isomers in solution, as the spectra depended on the polarization of the excitation light.[116]

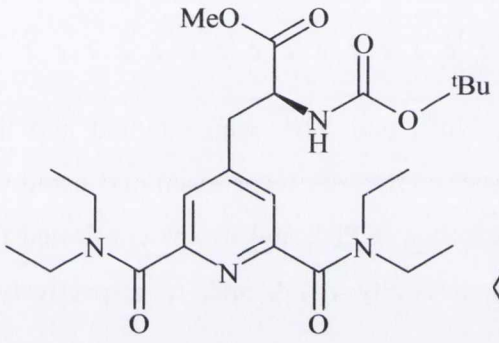

51

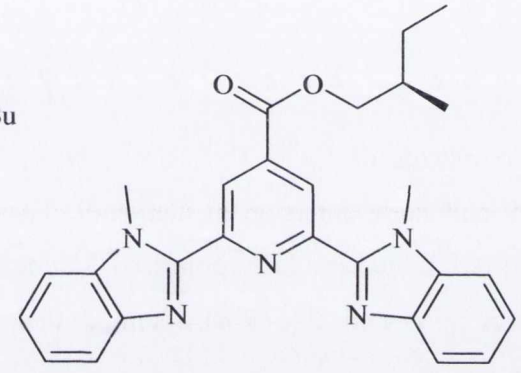

52

As with ligand **51**, the variety of ML_n species that formed in solution with ligand **52** and Eu^{III}, were identified by performing ES-MS and NMR titrations with europium perchlorate ($Eu(ClO_4)_3$) in acetonitrile.[118] Again, various stoichiometry of the complexes ML_n (n = 1 – 4) were observed, with the predominant species as ML_3. The introduction of a chiral neopentyl ester group in the 4-position of the central pyridine ring of **52,** leads to the formation of thermodynamically stable 1:3 complexes with lanthanide ions in acetonitrile. Chiro-optical data suggest the helical wrapping of the ligand strands around the Eu^{III} ions.

This work and those of the previous two examples show that structural chirality may be induced in triple helical lanthanide complexes by a suitable design of the ligand. This property opens new perspectives for the design of lanthanide triple helical complexes acting as probes for chiral recognition.[118]

The next section builds on ideas that were explored by Bünzli and co-workers and have just been discussed. It will describe some of the work previously completed within the Gunnlaugsson group on the topic of chiral lanthanide complexes.

2.0.2 Research from the Gunnlaugsson Group

One of the first examples of lanthanide templated self-assemblies from the Gunnlaugsson group was developed by Dr. Joseph Leonard, who used the chiral 2,6-pyridine diamide based ligands **53** (*S,S*) and **54** (*R,R*), respectively.[119]

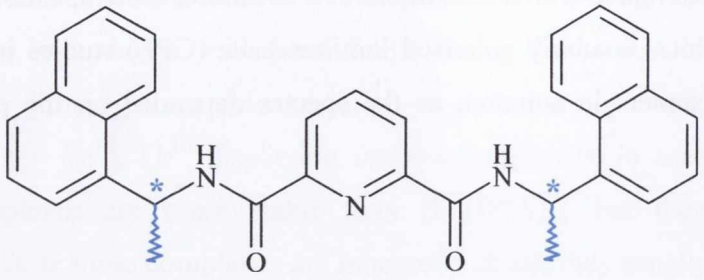

53: (*S,S*)
54: (*R,R*)

Complexes of Eu^{III}, Tb^{III}, Sm^{III}, Dy^{III}, Nd^{III}, and Yb^{III} were studied and they all produced lanthanide emission in methanol. These complexes were examined using circular dichroism (CD) and circularly polarised luminescence (CPL), and it was confirmed that the ligands **53** (*S,S*) and **54** (*R,R*) retained their chirality of Δ and Λ respectively upon complexation.

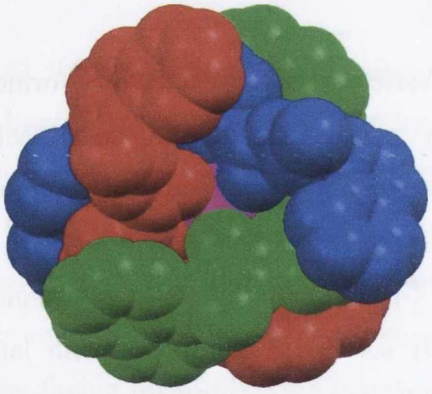

Figure 2.1 The X-ray crystal structure of the Tb.54 (*R,R*) complex showing the "helical" arrangement of the three ligands around Tb^{III} (pink) as viewed down the crystallographic a-axis. H-atoms, solvent molecules, and counter anions omitted for clarity.[119]

The crystal structure of ligands, **53** and **54**, for **Tb.54** (*R,R*) in Figure 2.1 showed the formation of 1:3 complexes with lanthanides, and coordinate to the metal ions through the central pyridine *N*-atom and two flanking oxygen atoms from the carboxamide groups. The ligands wrap around the Tb^{III} ion in a helical manner so that the central pyridine unit of each

ligand was sandwiched, or intercalated, in between the naphthalene units of the remaining two ligands to give a triple π-π stacking interaction that stabilizes the resulting bundle, called the Trinity Sliotar.

In these two ligands, the coordinating unit is the diamide derivative of DPA, which is known to form the propeller-shaped complex $[Ln(DPA)_3]^{3-}$, as shown above. These ligands not only sensitise their lanthanide centres efficiently, but also confer chirality onto the complex. Unfortunately these ligands and their behaviour with lanthanide metals in solution were never fully studied.

A second branch of this family of self assembly structures, **55** and **56** were synthesised and studied by Dr. Floriana Stomeo.[120] This work featured two tridentate chelating units, diamides derived from DPA, that are linked by the diamine 4,4'-diaminodiphenylmethane. As before, the antennae of the system, the (*S*) and (*R*) isomers of 1-(1-naphthyl)-ethylamine, confer chirality upon the ligands and corresponding complexes.

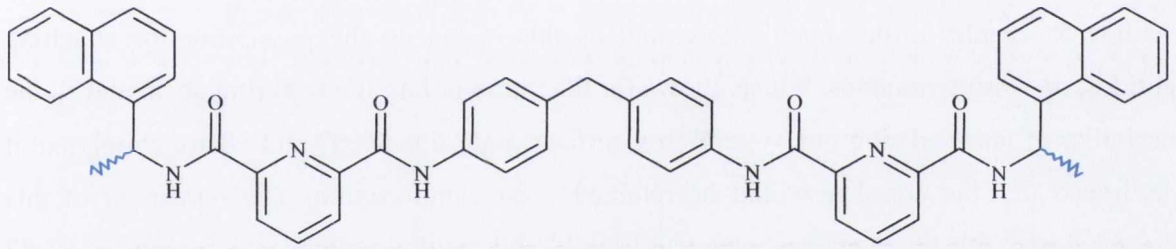

55: (*S,S*)
56: (*R,R*)

The Eu^{III}, Tb^{III}, and Sm^{III} complexes of **55** and **56** were characterised by NMR, mass spectrometry, CD, and CPL. Potentiometric studies of the Eu^{III} complexes were performed in a partially aqueous solution of CH_3CN/H_2O (80:20; v/v). Unfortunately, the determination of the metal complex stability constants proved unsuccessful, despite many attempts. The formation of **Eu.55** and **Eu.56** in organic media was also examined with a variety of spectroscopic techniques. ^1H NMR titrations indicated that complexation was fully achieved upon the addition of 0.6 equivalents of $Eu(CF_3SO_3)_3$, a result that is consistent with the formation of a 2:3 (M:L) complex, as predicted by the space-filling model shown in Figure 2.2. The retention of the ligand's chirality was confirmed by CD and CPL measurements.

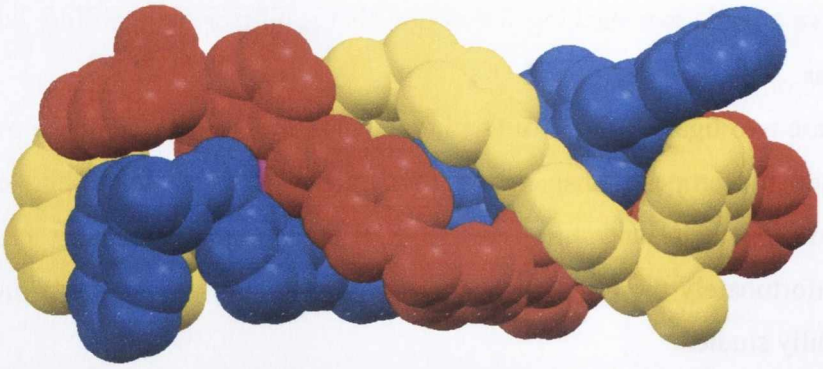

Figure 2.2 The space-filling model of the Eu.56 (*R,R*) complex showing the "helical" arrangement of the three ligands around Eu^{III} (pink).

2.1 Chiral Lanthanide Self-Assembly Complexes

Using the results obtained from the two examples described above, ligands **57** and **58** were designed. They are based upon **53** and **54**, but with a hydroxyl group on the back of the pyridine to enable further functionalisation, as this opens up the possibility for attaching peptides, or sensing moieties. It also allows for the introduction of a tethering chain and so the possibility of immobilising this system on a surface. Both ligands **57** and **58** are chiral, and it was hoped that the chirality would be retained upon complexation. The remainder of this Chapter deals with the synthesis, characterisation, and resulting lanthanide complexes of **57** and **58**. This discussion begins with the synthesis of the two ligands.

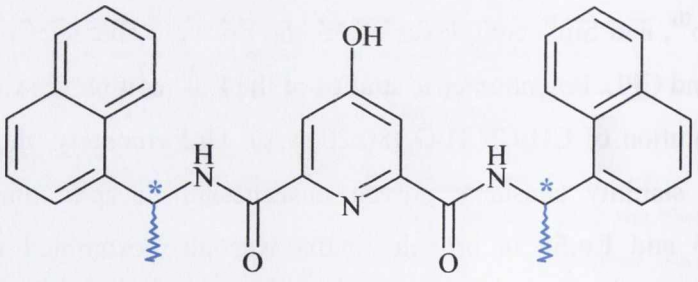

57: (*S,S*)
58: (*R,R*)

2.1.1 Synthesis and characterisation of Ligands 57 (*S,S*) and 58 (*R,R*)

The synthesis of ligands **57** (*S,S*) and **58** (*R,R*) involved a one step, peptide coupling reaction using EDCI·HCl (*N*-(3-Dimethylaminopropyl)-*N'*-ethylcarbodiimide hydrochloride), as shown in Scheme 2.1. The appropriate enantiomer (either *S*, or *R*) of 1-(1-naphthyl)-ethylamine which was commercially available, was stirred in anhydrous THF at 0 °C, and then HOBt (1-Hydroxybenzotriazole hydrate) and 4-Hydroxypyridine-2,6-dicarboxylic acid (Chelidamic acid, **59**) were added. This mixture was stirred for 30 minutes, before EDCI•HCl and triethylamine were added, and then stirred for a further 30 minutes under argon. The reaction was then left stirring for two days at room temperature under argon at room temperature. The insoluble residue was filtered off and the solvent removed under reduced pressure. The resulting crude product was dissolved in CH_2Cl_2 and washed twice with 0.1 M HCl, then with a saturated solution of $NaHCO_3$, and finally with water, to yield a very pale brown solid.

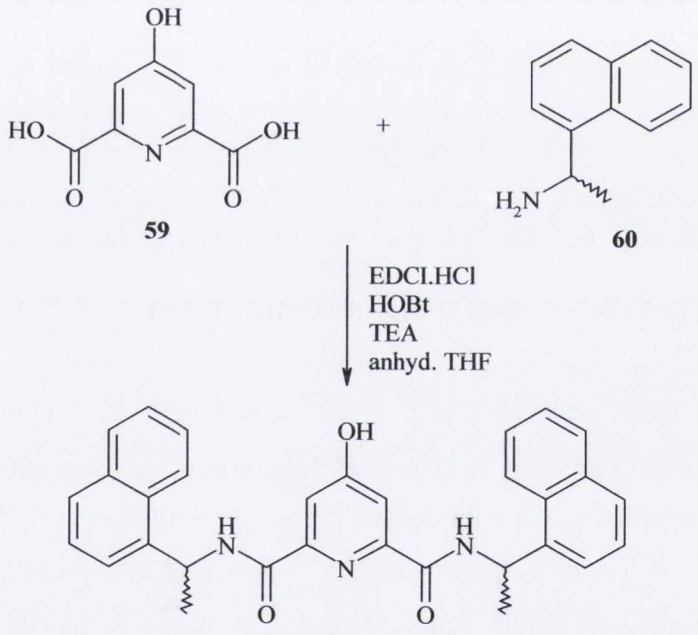

57: (*S,S*) 64% yield
58: (*R,R*) 49% yield

Scheme 2.1 Synthesis of ligands 57 (*S,S*) and 58 (*R,R*).

Interestingly, the *R,R* enantiomer consistently gave a lower yield than the *S,S* enantiomer, despite many attempts at increasing the yield of this product. The *S,S* enantiomer was achieved in 64% yield, while the *R,R* enantiomer was achieved in 49% yield. The product was then purified by flash column chromatography using neutral silica, 95:5; CH_2Cl_2:CH_3OH,

and precipitated by dissolving the product in a minimum volume of methanol and dropping it into water. The pure product was filtered off and dried over P_2O_5 prior to use. The product was characterized by ^{1}H-NMR, ^{13}C-NMR, IR, and elemental analysis (see Chapter 5).

A series of NMR experiments such as NOE, H-H COSY, C-H COSY, and N-H COSY (see ^{1}H-NMR spectrum shown in Figure 2.3, and 2-D spectra in Appendix **A1**, **A2**, and **A3**) were carried out to fully assign all the aromatic naphthalene peaks, as well as the rest of the structure of this molecule.

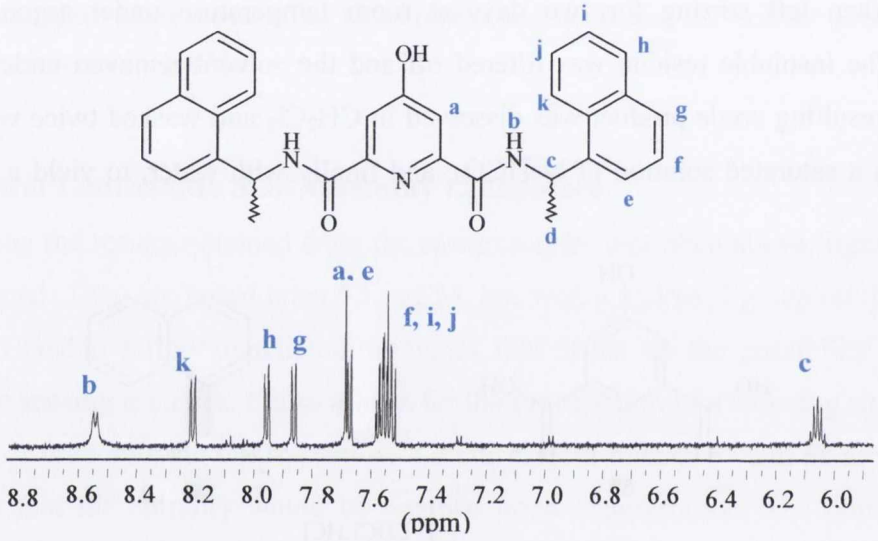

Figure 2.3 ^{1}H-NMR spectrum of Ligand 57 (*S,S*), (600 MHz, CD_3CN).

Ten resonances were observed, in agreement with C_2 symmetry of the ligand in solution. It was found that the CH proton of the chiral centre, **c**, a multiplet centred at 6.01 ppm, is strongly coupled to the naphthalene proton, **k**, a doublet at 8.25 ppm, but not to any other signal. The CH_3 protons, **d**, a singlet at 1.73 ppm (not shown in Figure 2.1), are strongly coupled to the naphthalene proton, **e**, at 7.68 ppm, and weakly to the NH proton, **b**, the doublet at 8.55 ppm. This indicates that there is no rotation around the chiral centre on the NMR time-scale, and that the structure is in fact rigid in its conformation. The spectra for isomers **57** and **58** were identical.

2.1.2 Synthesis of Eu^{III} and Tb^{III} complexes with ligands 57 (*S,S*) and 58 (*R,R*)

In order to form the final products, the Eu^{III} and Tb^{III} complexes of ligands **57** and **58**, **Eu.57**, **Eu.58**, **Tb.57**, and **Tb.58** respectively, were prepared. To achieve this the appropriate

ligand was dissolved in freshly distilled methanol (5 mL), and $Eu(CF_3SO_3)_3$ or $Tb(CF_3SO_3)_3$ added in the ratio of 1:3, M:L (Scheme 2.2), and this mixture was refluxed for 24 hrs under argon. The solution was then cooled, and dropped slowly onto diethyl ether (100 mL). The resulting pale brown solid was then filtered off and dried over P_2O_5. The desired products **Eu.57**, **Eu.58**, **Tb.57** and **Tb.58** [LnL_3] were collected in approximately quantitative yields, and characterised by ^{1}H-NMR, mass spectroscopy and elemental analysis.

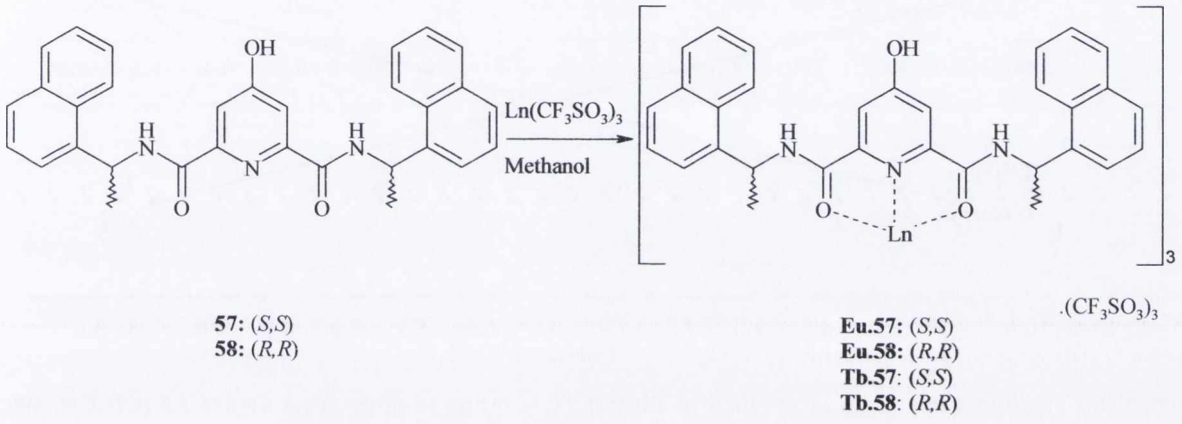

57: (*S,S*)
58: (*R,R*)

Eu.57: (*S,S*)
Eu.58: (*R,R*)
Tb.57: (*S,S*)
Tb.58: (*R,R*)

Scheme 2.2 Synthesis of Eu.57, Eu.58, Tb.57, and Tb.58

Again, the ^{1}H-NMR (600 MHz, CD_3CN) showed ten signals, in agreement with C_{2v} symmetry of the Eu^{III} complex in solution, in which the two carbonyls and the nitrogen of the pyridine are bound to the metal centre. As with their corresponding ligands, **57** and **58**, the spectra for **Eu.57** and **Eu.58** were identical.

The resonances are shifted due to the paramagnetic nature of the Eu^{III}. The protons closest to the Eu^{III} centre are more strongly affected by the presence of the Eu^{III} unpaired f-electrons, leading to paramagnetic relaxation and broadening of the resonances, as well as a shift in NMR frequency.[121] Signals have been attributed by H–H COSY experiments. The two signals that are most significantly shifted are the NH proton and the CH from the chiral centre, as shown in Figure 2.4, the ^{1}H NMR spectrum of **Eu.57** in CD_3CN depicted in Figure 2.4. These are quite dramatically shifted upfield, from 8.55 ppm to 3.27 ppm for the NH proton, and downfield from 6.07 ppm to 9.83 ppm for the CH proton.

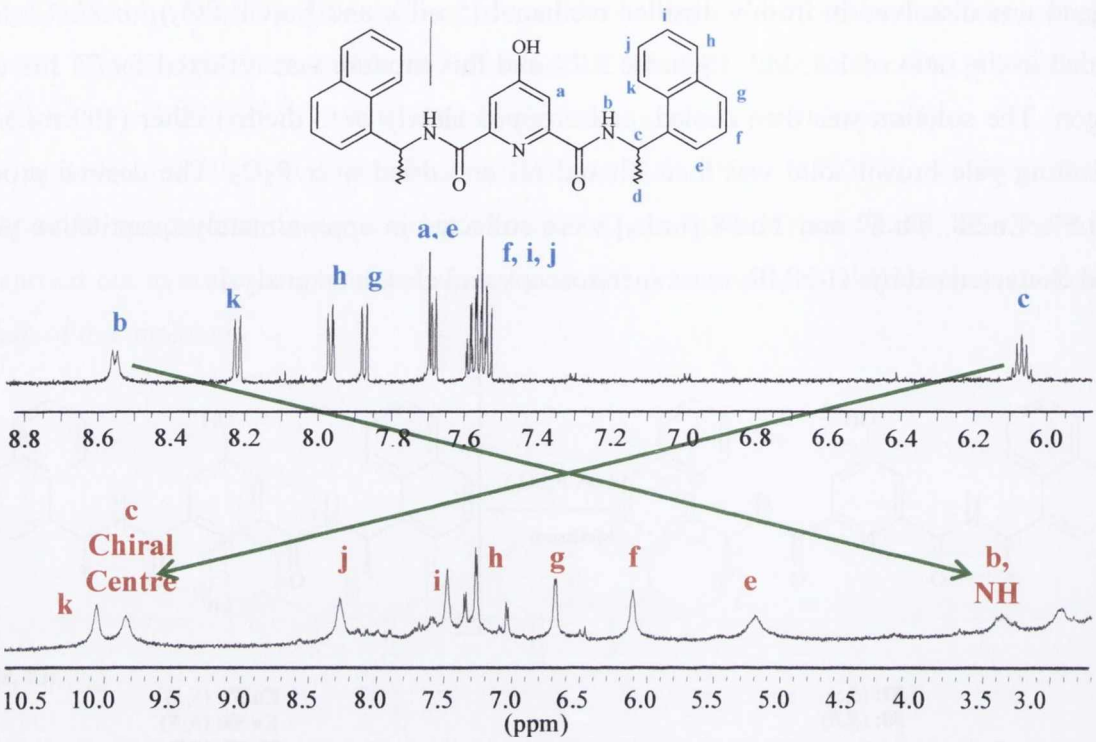

Figure 2.4 The upper spectrum is ^{1}H-NMR of Ligand 57, lettering assigned from Figure 2.3 (CD_3CN, 600 MHz); Lower spectrum is the ^{1}H-NMR spectra of Eu.57 (CD_3CN, 600 MHz), the peaks have been assigned, again using the nomenclature from Figure 2.3. Arrows indicate the shift of the NH proton and the proton at the chiral centre. [Eu.57] = $1x10^{-3}$ M.

The spectrum for the Tb^{III} complex **Tb.57** is shown in Figure 2.5. This spectrum is quite different to that of its Eu^{III} counterpart. The signals are shifted from 38 ppm down to -30 ppm. These signals could not be assigned however, so the spectrum is shown without assignment.

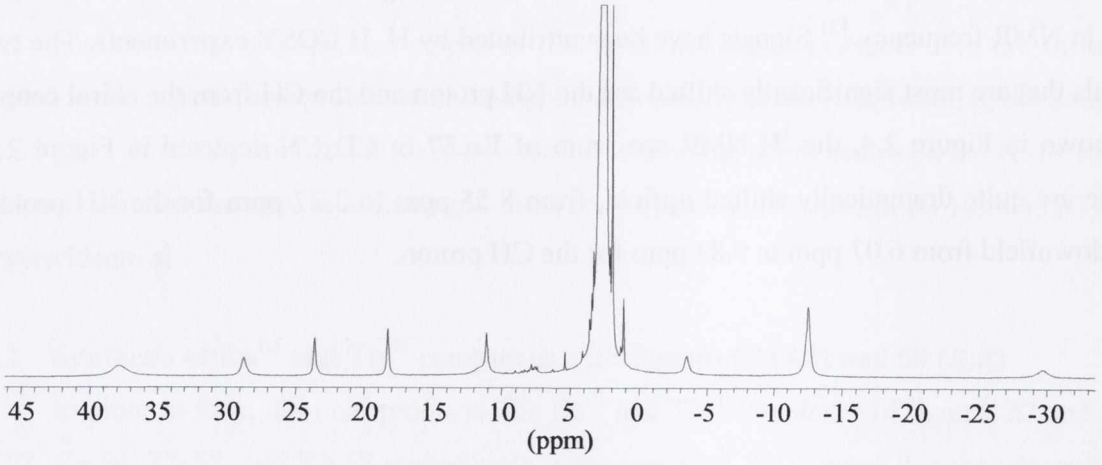

Figure 2.5 ^{1}H-NMR spectra of Tb.57 (CD_3CN, 600 MHz), [Tb.57] = $1x10^{-3}$ M.

2.1.3 Infra-Red analysis of 57(*S,S*) and 58(*R,R*)

IR Spectroscopy can be a useful method in investigating complex formation. The vibrational bands associated with the bonds involving the atoms that are directly coordinated to the lanthanide metal usually move to lower frequency (lower energy) upon complexation of a metal ion.[54] The simplest band to follow in this case is the carbonyl band (C=O) as it is directly bound to the lanthanide centre which will increase the bond length, and therefore decrease the IR stretching frequency. This was found to be the case for these complexes, as upon complexation the C=O band for **57** was shifted from 1653 cm^{-1} to 1619 cm^{-1} and 1618 cm^{-1} for **Eu.57** and **Tb.57**, respectively shown in Table 2.1 below.

Table 2.1. IR frequency for C=O stretch in 57, Eu.57, and Tb.57.

IR Stretch (cm^{-1})	57	Eu.57	Tb.57
C=O	1653	1619	1618

2.1.4 Spectroscopic Characterisation of ligands 57 and 58

The two ligands **57** and **58** were also characterised by using UV-Visible and fluorescence spectroscopy. The UV-Visible spectra of **57** (ε = 15853 $cm^{-1}M^{-1}$) was identical to that of **58** (ε = 15739 $cm^{-1}M^{-1}$) with a λ_{max} = 281 nm. Excitation at the λ_{max}, gave rise to a fluorescence emission with λ_{max} = 338 nm, and a shoulder at 332 nm. The UV-Visible and fluorescence spectra taken in CH_3CN are shown in Figure 2.6.

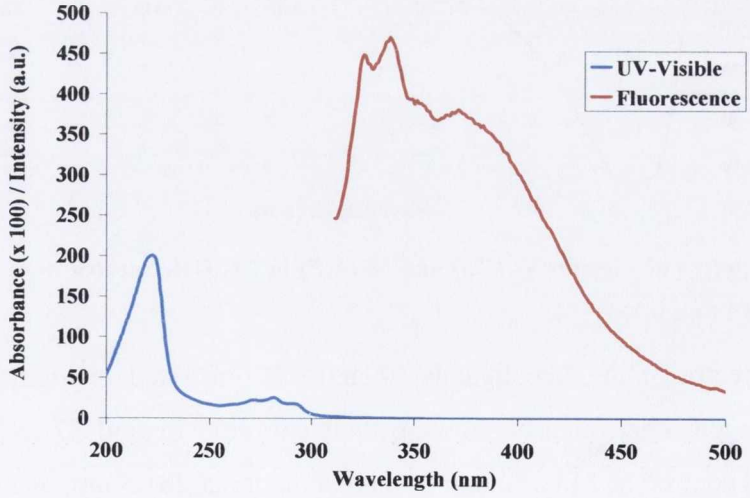

Figure 2.6 UV-Visible and fluorescence spectra of ligand 57 in CH_3CN, $\lambda_{excitation}$ = 281 nm.

2.1.5 Circular Dichroism Studies

In order to elucidate whether or not the chirality of ligands **57** and **58** were maintained in the corresponding complexes **Eu.57** and **Eu.58,** the circular dichroism spectra were recorded (see UV-Visible spectrum in Figure 2.6).

Circular dichroism (CD) spectroscopy measures differences in the absorption of left-handed polarized light versus right-handed polarized light which arise due to structural assymmetry. Every molecule will produce both positive and negative CD signals, as different electronic transitions involve electron distributions of different handedness and so achiral molecules will end up with little or no CD signal. Chiral molecules will absorb left and right polarized light to different magnitudes, and so will give different signals depending on its chirality. By measuring this signal over a range of wavelengths, a plot giving information on the chirality of a molecule is obtained.[122]

Circular dichroism spectra of the isomers **57** (*S,S*) and **58** (*R,R*) and their corresponding Eu^{III} and Tb^{III} complexes were recorded in methanol to investigate if the chirality of the ligands would be retained upon complexation, and to determine the chirality of the helicate. All spectra were recorded at an absorbance of 1 (a.u.).

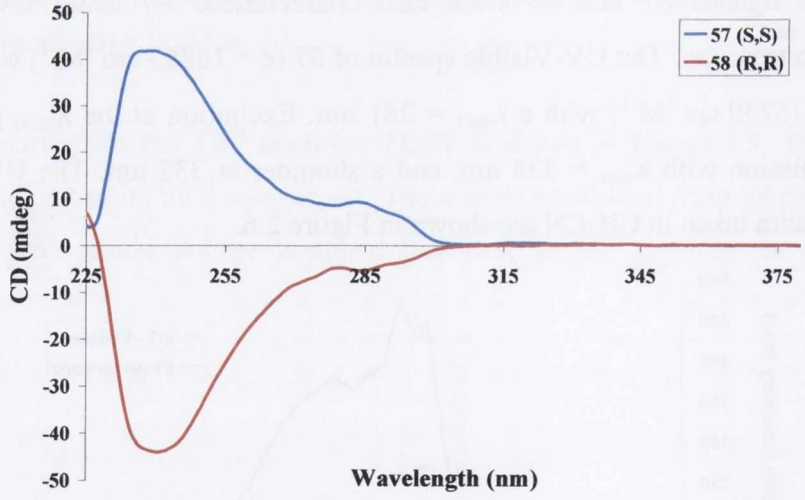

Figure 2.7 The CD spectra of Ligands 57 (*S,S*) and 58 (*R,R*) in CH_3OH. Spectra were recorded at a UV-Visible absorbance of 1 (a.u.).

The CD spectra of the free ligands **57** and **58,** illustrated in Figure 2.7 are almost mirror images of each other, clearly showing their chirality. Ligand **57** (*S,S*) exhibited one large positive band centred at 243 nm, and a small shoulder at 281.5 nm, as in the UV-Visible spectra (Figure 2.6). Ligand **58** (*R,R*) exhibited corresponding large negative band centred at 244.5 nm and a small shoulder at 281 nm. The slight discrepancy between the two signals, can

be attributed to the difference in concentration of each ligand used in this experiment, (*i.e.* [S,S] > [*R,R*]).

The CD spectra of the two Eu^{III} complexes, **Eu.57** (*S,S*) and **Eu.58** (*R,R*), were also recorded in methanol. As shown in Figure 2.8, there were two negative bands centred at 301 nm, and 270 nm, and a positive band at 249.5 nm detected for **Eu.57** (*S,S*). The spectrum for **Eu.58** (*R,R*) showed two positive bands at 302 nm and 269 nm, as well as one negative band at 246.5 nm. From this data, it is plausible to assume that the Eu^{III} complexes of each enantiomer, **Eu.57** (*S,S*) and **Eu.58** (*R,R*), retain their chirality upon complexation.

The spectrum of **Eu.57** is slightly different to that of **Eu.58**, in that there is a small shoulder present at 335 nm that is not observed in **Eu.58**. This suggests that binding between the ligand and the lanthanide metal occurs in a slightly different conformation for each isomer.

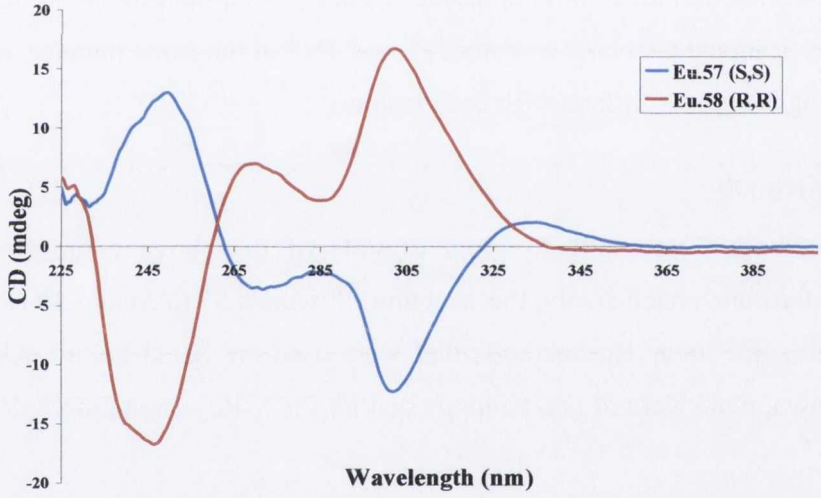

Figure 2.8 CD Spectra of Eu^{III} complexes Eu.57 (*S,S*) and Eu.58 (*R,R*) in CH_3OH.

The CD spectra of the two Tb^{III} complexes **Tb.57** (*S,S*) and **Tb.58** (*R,R*) were also recorded in methanol. As shown in Figure 2.9, for complex **Tb.57** (*S,S*), two negative bands centred at 302 nm, and 270 nm were detected, as well as a positive band at 244.5 nm. The spectrum for **Tb.58** (*R,R*) showed two positive bands at 302.5 nm and 269 nm, as well as one negative band at 243 nm. It appears from the spectra in Figure 2.7 that similarly to the Eu^{III} complexes, the Tb^{III} complexes of each enantiomer, **Tb.57** (*S,S*) and **Tb.58** (*R,R*), do not undergo significant conformational changes upon complexation, and that the conformations of both the Eu^{III} and Tb^{III} complexes are alike.

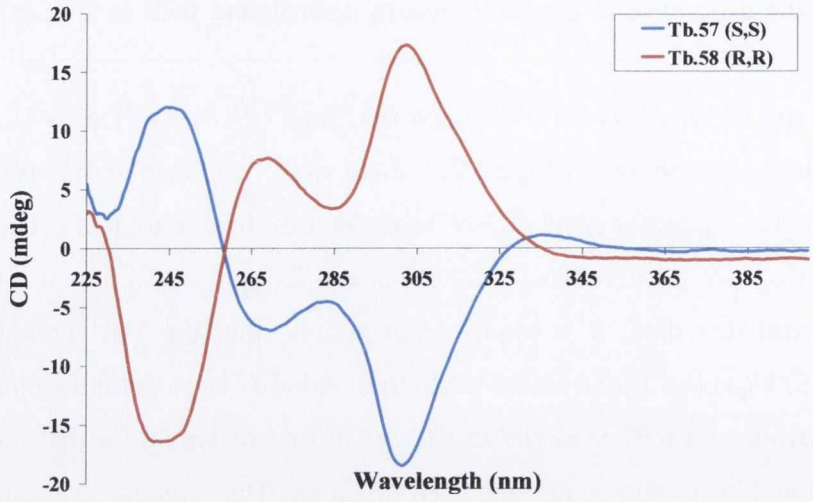

Figure 2.9 CD spectra of Tb^{III} complexes Tb.57 (*S,S*) and Tb.58 (*R,R*) in CH_3OH.

Again, the shoulder at 335 nm is present in **Tb.57**, but absent in **Tb.58**. It is reasonable to assume that each ligand will bind to both Eu^{III} and Tb^{III} in the same manner, and so as with **Eu.57**, the binding is slightly different for each isomer.

2.1.6 Crystal Growth

Many attempts were made to grow crystals of the above complexes for X-Ray diffraction, to determine, conclusively, the structure of ligands **57** (*S,S*) and **58** (*R,R*), and their complexes in the solid state. The methods that were used are listed below. Although many crystals were grown, none were of good enough quality for X-Ray crystallographic studies.

a) **Vapour diffusion:** The compound was dissolved in solvent A in a sample tube. This was then placed in a jar with a sealable lid that had some solvent B. The jar was then sealed. The solvents were chosen so that when solvent B diffused into the sample tube and mixed with solvent A as it diffused out of the sample tube, it would make the solute less soluble. Slow diffusion of solvent A into the jar, and solvent B into the sample tube should cause crystals to grow. Solvent A was CH_2Cl_2, CH_3OH, or EtOH, Solvent B was EtOAc or diethyl ether.

b) **Slow evaporation:** Saturated or nearly saturated solutions of the compounds were prepared. These solutions were then covered and the solvent allowed evaporate slowly.

Several solvents, and solvent mixtures were used, such as, CH_2Cl_2, EtOH, CH_3OH, CH_3CN, and H_2O.

2.1.7 Mass Spectrometry of 57, Eu.57 and Tb.57

The ligands were also characterised by mass spectrometry. The mass spectrum of ligands **57** (*S,S*) and **58** (*R,R*) showed the dominant peak at 512 m/z corresponding to [M+Na], and an accurate mass of 512.1961 was found corresponding to $C_{31}H_{27}N_3O_3Na$, ([M+Na]).

The mass spectra of ligand **57** and its complexes **Eu.57** and **Tb.57** are shown in Figure 2.10. The isotopic pattern in the complex spectra are clearly visible, showing m/z = $ML_3/2$. A similar result was also observed for the Eu^{III} and Tb^{III} complexes of ligand **58**. There were no other significant peaks observed in the spectra confirming that the ligand was fully complexed to ML_3 upon reflux.

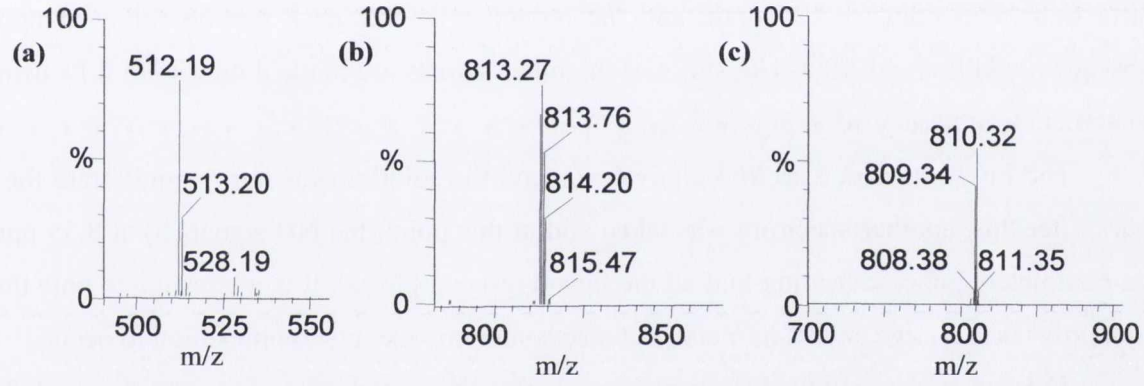

Figure 2.10 Magnified mass spectrometry spectra of (a) 57 m/z = M+Na, (b) Tb.57 and (c) Eu.57, m/z = $ML_3/2$.

Having characterized the complexes **Eu.57** and **Eu.58**, the next step was to examine the stoichiometry of these complexes in solution. As such, the following sections will focus on the use of two spectroscopic methods to determine the stoichiometric ratio between Eu^{III} and the ligands **57** and **58**, in solution; NMR spectroscopy and photophysical spectroscopy.

2.2 ^{1}H NMR Titrations

^{1}H NMR titration (600 MHz) was carried out to investigate the behavior of the complexation between Eu^{III} and ligand **57**(*S,S*) in CD_3CN, [**57**] = [1 x 10^{-3} M]. Figure 2.11 shows the gradual formation of the complex, upon addition of aliquots of $Eu(CF_3SO_3)_3$. Overall, the changes in the spectrum indicated the complexation occurs on the NMR timescale, in slow exchange. However, this is difficult to fully detect at low concentrations of Eu^{III}. From

these titrations, it became evident that no major changes occurred until the addition of 0.3 equivalents of Eu^{III}, the point at which the complex should be fully formed according to the synthesised complex (Section 2.1.2). After the addition of 0.3 equivalents of Eu^{III}, the appearance of two new resonances at 9.85 and 10.09 ppm was observed, along with the corresponding reduction in the resonances at 6.07 and 8.25, as the proton signal from the CH proton at the chiral centre (**c**) and the naphthalene CH, (**k**), start to shift upon complexation. The peak for (**k**) shifted dramatically and correlating with the assignment of the resonances showing that the stereochemistry of the ligand is as shown in Figure 2.4, with the naphthalene CH (**k**) positioned in proximity to the NH proton (**b**). Simultaneously the resonance corresponding to (**f**) a naphthalene CH resonance, begins to shift from the multiplet centred at 7.68 (which begins to decrease) to form a triplet at 6.07. For this reason, after the initial decrease in the resonance at 6.07 as the signal from (**c**) is shifted, it begins to increase again due to the formation of a new resonance peak corresponding to (**f**). The NH proton signal (**b**) shifts from 8.55 ppm to 3.24 ppm, and the reduction in this peak can be followed upon subsequent additions of Eu^{III}. The shifts of the other signals are marked on Figure 2.11 using the nomenclature assigned in Figure 2.4.

The Eu^{III} was added up to 3 equivalents, and the solution was left to equilibrate for 1 hour. After this, another spectrum was taken and at this point, the NH signal (**b**) at 8.55 ppm was completely gone, indicating that all the ligand has complexed. It is interesting to note that it not only takes a large excess of metal, but also some time for full complexation to occur.

The spectrum continued changing even after the supposed equilibrium point of 0.3 equivalents of metal has been added. This suggests that the system is dynamic in solution, at this concentration which is three orders of magnitude higher than the concentration used in the photophysical studies (Section 2.4). Spectra of the thermodynamically driven complex of **Eu.57** (*S,S*) were taken over a period of two weeks, in CD_3CN and no change was observed. The thermodynamically driven complex is therefore very stable in solution, however it does require energy (*via* heat, in refluxing the ligand and metal together) in order to form this stable 1:3, M:L complex.

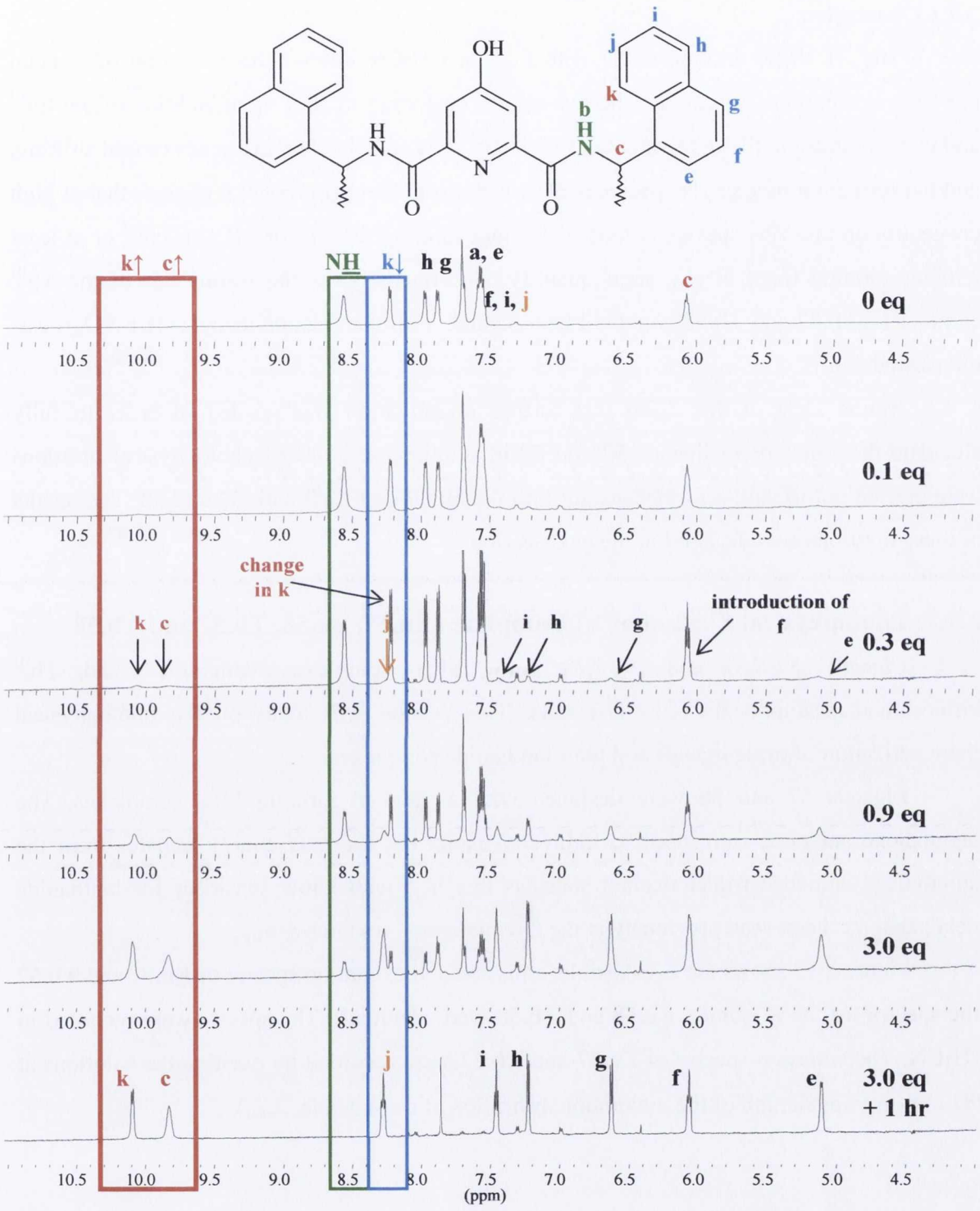

Figure 2.11 ^{1}H NMR spectra (600 MHz, CH_3CN) of ligand 57(*S,S*); [57(*S,S*)] = 1 x 10^{-3} M, upon titration of $Eu(CF_3SO_3)_3$; [$Eu(CF_3SO_3)_3$] = 1 x 10^{-1} M. This figure shows the appearance of two new peaks at 9.85 and 10.09 ppm, and the corresponding reduction in the peaks at 6.07 and 8.25 ppm as the proton signal from the CH at the chiral centre (c) and the naphthalene CH (k) shift upon complexation, highlighted by the red and blue boxes. The disappearance of the NH signal at 8.55 ppm is highlighted in green.

2.2.1 Conclusion

The ^{1}H NMR titration of **57** with Eu^{III} in CD_3CN follows the formation of a metal complex in solution. We can see the resonances beginning to shift upon addition of the Eu^{III} and this continues until 3 equivalents of Eu^{III} had been added, when the peaks ceased shifting, and the formation of a single species is observed. From these titrations, it appears that at high concentration the ML_3 species is formed without forming the ML or ML_2 species, or at least without forming them in any great quantity. Unfortunately, as the resonances of the Tb^{III} complexes, **Tb.57** and **Tb.58** could not be assigned, a similar titration using $Tb(CF_3SO_3)_3$ was not carried out.

It was clear at this point that further investigation was needed in order to fully elucidate the behavior of ligands **57** and **58** in solution. A series of photophysical titrations were carried out to gain a further insight into the binding of Eu^{III} with **57** and **58**. The results of these titrations are discussed in the next section.

2.3 Photophysical Evaluation of Complexes Eu.57, Eu.58, Tb.57 and Tb.58

Ligands **57**(*S,S*) and **58**(*R,R*) form ML_3 complexes with Eu^{III} and Tb^{III} trifluoromethanesulphonate (CF_3SO_3) salts. This section will focus on the photophysical characterization of these ligands and their lanthanide complexes.

Ligands **57** and **58** were designed with a view to forming ML_3 complexes. The naphthalene antennae were used to indirectly excite the Eu^{III} *via* energy transfer from the naphthalene antennae triplet excited state, as this is a well know sensitiser for lanthanide metals that has been used previously in the Gunnlaugsson research group.

Figure 2.12 shows the UV-Visible, emission and excitation spectra of **Eu.57** and **Tb.57** (the spectra for the *R* isomer, **Eu.58** and **Tb.58** were identical). The spectra were recorded in CH_3CN. The emission spectra of **Eu.57** and **Tb.57** were recorded by exciting the solutions at 281 nm (the wavelength of the maximum absorption of the antenna, λ_{max}).

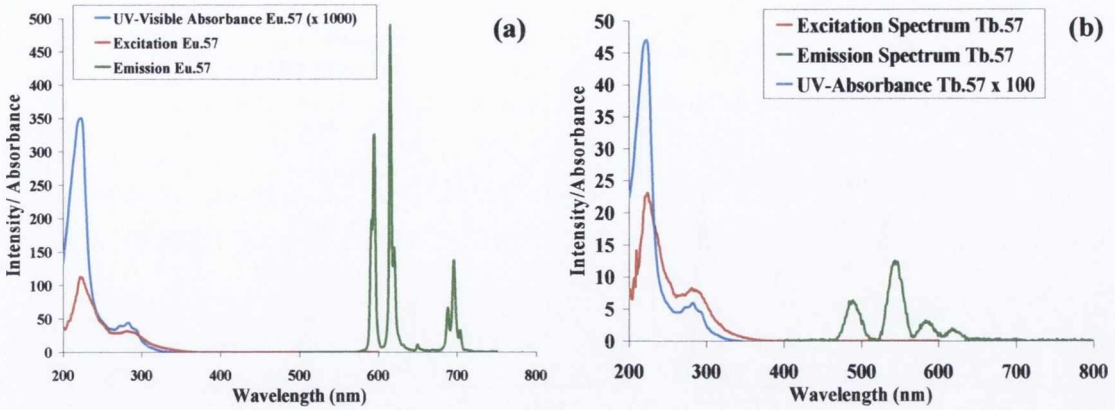

Figure 2.12 The UV-Visible, emission and excitation spectra of complexes Eu.57 (a) and Tb.57 (b) in CH_3CN, upon excitation at 281 nm. [Eu.57] = [Tb.57] =1 x 10^{-5} M.

The bands corresponding to the deactivation of the $^6D_0 \rightarrow {}^7F_J$ ground states of (J = 1 – 4) of the Eu^{III} spectrum are observed for **Eu.57** (J = 1, 595 nm; J = 2, 616 nm; J = 3, 650 nm; J = 4, 695 nm). The Tb^{III} emission observed by indirect population through the naphthalene antenna is weak in comparison to the emission intensity of the Eu^{III} complex. The emission did not increase when the sample was degassed which implies that the antenna is unable to populate the Tb^{III} excited state efficiently. It is known that naphthalene is not a good antenna for Tb^{III} as the naphthalene S_1 and Tb^{III} T_1 states are too close in energy for efficient intersystem crossing to occur, and close enough that back energy transfer from the Tb^{III} centre to the naphthalene can occur easily.[123, 124] For this reason it was decided not to pursue any further investigation into the complexation behaviour of **Tb.57** or **Tb.58**. Instead, the focus of the next sections will be on **Eu.57** and **Eu.58**, and determining how these complexes behave in solution and what, if any, differences are present between the *S* and *R* enantiomers.

As an initial test of how stable the complexes **Eu.57** and **Eu.58** were, a displacement assay was performed with EDTA, where ten equivalents of EDTA were added to a 1 x 10^{-5} M solution of **Eu.57** in methanol. The results of this are shown in Figure 2.13 (the resultant spectrum from **Eu.57** is shown as an example, however the results for **Eu.58** were identical). The measurement was done in methanol as EDTA is not soluble in organic solvents. The initial spectrum was taken and then ten equivalents of EDTA were added and the mixture was left stirring overnight, after which it was measured again. There is no significant decrease in emission intensity, however the spectrum has changed slightly which suggests that the EDTA is partially binding to the lanthanide centre but not fully displacing the ligand.

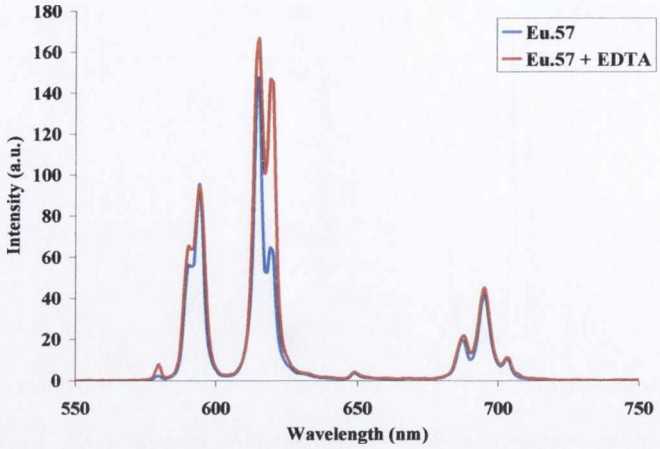

Figure 2.13 The luminescent spectra of complex Eu.57 in CH_3OH before and after the addition of 10 equivalents of EDTA, upon excitation at 281 nm. [Eu.57] =1 x 10^{-5} M.

2.4.1 Determination of bound water molecules of Eu.57 and Eu.58

Trivalent lanthanide ions have a high coordination number requirement, usually nine for Eu^{III}. If this requirement cannot be satisfied by coordinating ligands, any vacant coordination sites will be occupied by solvent molecules, such as water. The ^1H NMR studies (2.1.2) of ligands **57** and **58** suggest that binding to the Eu^{III} centre will occur through the nitrogen on the central pyridine moiety and through the two carbonyl groups. If the stoichiometry is ML_3, then nine coordination sites are available and the Eu^{III} will be coordinatively saturated and there should be no bound solvent molecules.

The lifetimes of the Eu^{III} complexes of **57** and **58** were examined to determine if this hypothesis was true, and to determine conclusively the number of solvent molecules within the first coordination sphere of the lanthanide centre, the results are listed in Table 2.2. Unfortunately due to solubility problems these measurements could not be carried out in pure water. Instead, they were carried out in H_2O:CH_3OH (80:20 v/v), and D_2O:CD_3OD (80:20 v/v). The mono-exponential luminescence decays were fitted to **Equation 1.1** (repeated here for clarity):[20]

$$q^{EuIII} = A\left[\left(\frac{1}{\tau_{H2O}} - \frac{1}{\tau_{D2O}}\right) - 0.25 - 0.075x\right] \qquad \textbf{Equation 1.1}$$

A value of τ_{H2O} = 1.53 ms and τ_{D2O} = 2.33 ms were obtained for **Eu.57** while values of τ_{H2O} = 1.43 and τ_{D2O} = 2.94 were obtained for **Eu.58**. The resulting values of q were; q = -0.22 ± 0.5 for **Eu.57** and q = - 0.13 ± 0.5 for **Eu.58**, indicating the presence of zero bound water molecules. The values are negative as the measurements were carried out in solutions of water

with methanol or D_2O/CD_3OD and not pure water or D_2O. Therefore the value of *A* is not completely accurate and so may lead to slightly anomalous results. However, as expected, there are no water molecules within the first coordination sphere of the complexes **Eu.57** and **Eu.58**. This result supports that the ML_3 species is the dominant species in solution.

Table 2.2 Lifetimes of complexes Eu.57 (*S,S*) and Eu.58 (*R,R*) upon direct excitation of Eu^{III} at 395 nm in H_2O:CH_3OH (80:20 v/v), and D_2O:CD_3OD (80:20 v/v).

Lifetimes			
Complex	τ_{H2O} **(ms)**	τ_{D2O} **(ms)**	**q (± 0.5)**
Eu.57	1.53 ± 0.08	2.33 ± 0.30	-0.22
Eu.58	1.43 ± 0.11	2.94 ± 0.27	-0.13

Figure 2.14 below shows the lifetime spectra for **Eu.57** in H_2O and D_2O. The mono-exponential decay can be seen from these spectra.

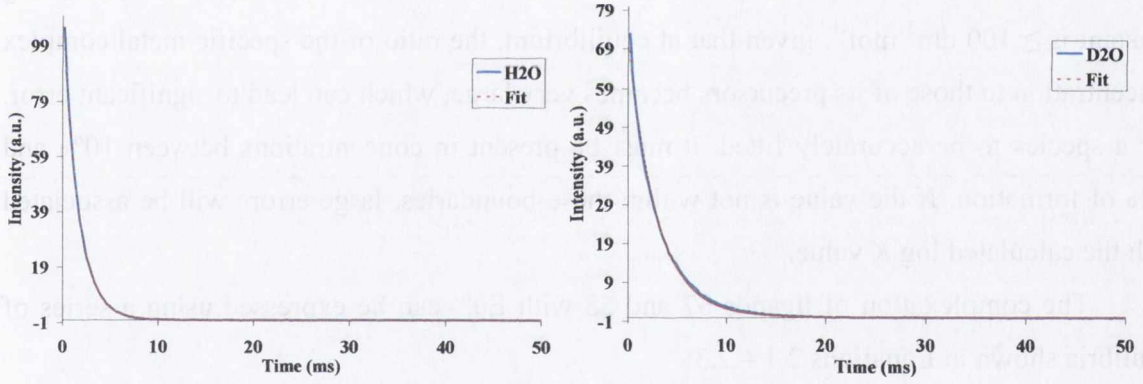

Figure 2.14 Lifetimes spectra of complex Eu.57 (*S,S*) (a) in H_2O:CH_3OH (80:20 v/v), and (b) D_2O:CD_3OD (80:20 v/v).

To further investigate the formation of the various complexes formed between the ligands **57** and **58**, with Eu^{III} in solution, a series of UV-Visible and luminescence titrations were performed. The results of these are discussed in the next section.

2.4 Photophysical Evaluation of Ligands 57 and 58

In order to fully investigate the behavior of **57** and **58** with Eu^{III}, a series of photophysical titrations were carried out. The ligands **57** and **58** are only sparingly soluble in

H_2O, as discussed previously (Section 2.4.1), so it was decided that all the spectroscopic measurements would be carried out in organic solvents. The titrations to determine the stoichiometry of the complexation process between ligands **57** and **58** were carried out in CH_3CN and $CH_3CN/CHCl_3$ (50:50; v/v). This combination was chosen for solubility reasons, and also to examine the behavior of the system in environments of different polarity.

The binding constants in the investigation were determined by fitting the data obtained from the changes in the UV-Visible and luminescence measurements. NMR spectroscopy was not a reasonable option for obtaining stability constants for these systems as the resulting spectra are quite complicated, and the fluorescence emission from ligands **57** and **58** did not change significantly upon addition of Eu^{III}, so it was decided to use only UV-Visible and luminescence measurements.

The data was fitted using the non-linear least-squares regression program SPECFIT.[125, 126] This method evaluates different stoichiometries between metal (Eu^{III}) and ligand (**57** and **58**) as well as their binding constants (log *K*). The program also takes into account the ability of the theoretical data to fit the experimental data, in the form of the sum of the squared standard deviation. However, the program is unable to fit the data accurately if the binding constant is ≥ 100 dm^3 mol^{-1}, given that at equilibrium, the ratio of the specific metal complex concentration to those of its precursors becomes very large, which can lead to significant error. For a species to be accurately fitted, it must be present in concentrations between 10% and 90% of formation. If the value is not within these boundaries, large errors will be associated with the calculated log *K* value.

The complexation of ligands **57** and **58** with Eu^{III} can be expressed using a series of equilibria shown in Equations 2.1 – 2.3:

$$Eu^{3+} + L \overset{K_{11}}{\rightleftharpoons} [EuL]^{3+} \qquad \textbf{Equation 2.1}$$

$$[EuL]^{3+} + L \overset{K_{12}}{\rightleftharpoons} [EuL_2]^{3+} \qquad \textbf{Equation 2.2}$$

$$[EuL_2]^{3+} + L \overset{K_{13}}{\rightleftharpoons} [EuL_3]^{3+} \qquad \textbf{Equation 2.3}$$

Although other groups with similar systems based on DPA reported that the EuL_4 system was found in their data fits,[115, 116] none of the titrations completed on ligands **57** and **58** could be fitted with a ML_4 species.

An overall stability constant, β_{13} can be derived from the product of the stepwise formation constants (K_{mn}), shown in Equations 2.4 and 3.5:

$$Eu^{3+} + 3\,L \overset{\beta_{13}}{\rightleftharpoons} [EuL_3] \qquad \textbf{Equation 2.4}$$

$$\beta_{13} = \frac{[EuL_3]]}{[Eu^{3+}][L]^3} = K_{11} \times K_{12} \times K_{13} \qquad \textbf{Equation 2.5}$$

The method used in the determination of the metal complex ion stability constants by UV-Visible and luminescence spectroscopy was the dilution method where the titration were carried out using a stock solution of ligand **57** or **58**, (3 mL, 1 x 10^{-5} M) with incremental additions of Eu^{III} as its trifluoromethanesulphonate salt ($Eu(CF_3SO_3)_3$), again in either CH_3CN or $CH_3CN/CHCl_3$ (50:50; v/v). Measurements were taken until no further changes in the spectra were observed, as this indicates the completion of the ligand-metal complexation process. A second method was also used as it had previously been successful in studying the helicate systems **55** and **56**. This method involved making twenty samples in volumetric flasks, each varying the metal ion concentration while keeping the ligand concentration constant. The resulting solutions were allowed to equilibrate overnight. The method will be discussed at the end of this section.

In the following sections, the results from the UV-Visible and luminescence titrations of ligands **57** (*S,S*) and **58** (*R,R*) against Eu^{III} in two solvent systems, along with their speciation and binding constants, will be described. All of the measurements reported were repeated and were fully reproducible.

2.4.1 Experimental Procedure

Measurements were carried out in CH_3CN and $CH_3CN/CHCl_3$ (50:50; v/v) with 1 x 10^{-5} M solutions of ligands **57** and **58**. The same solutions were used for both the UV-Visible, and luminescence measurements. The method used to perform these experiments was the dilution method. A stock solution (3 mL, 1 x 10^{-5} M) of each ligand, **57** and **58** was prepared, and a known volume of 1 x 10^{-3} M solution of $Eu(CF_3SO_3)_3$ was added. The UV-Visible absorbance and luminescence spectra were then recorded after an equilibration time of 3 minutes.

2.4.2 UV-Visible Titrations in $CH_3CN/CHCl_3$ (50:50; v/v)

2.4.2.1 (S,S) isomer

The UV-Visible absorption spectra and the corresponding titration profile are shown below in Figures 2.15 (a) and (b), for the titration of **57** with $Eu(CF_3SO_3)_3$ in $CH_3CN/CHCl_3$ (50:50; v/v).

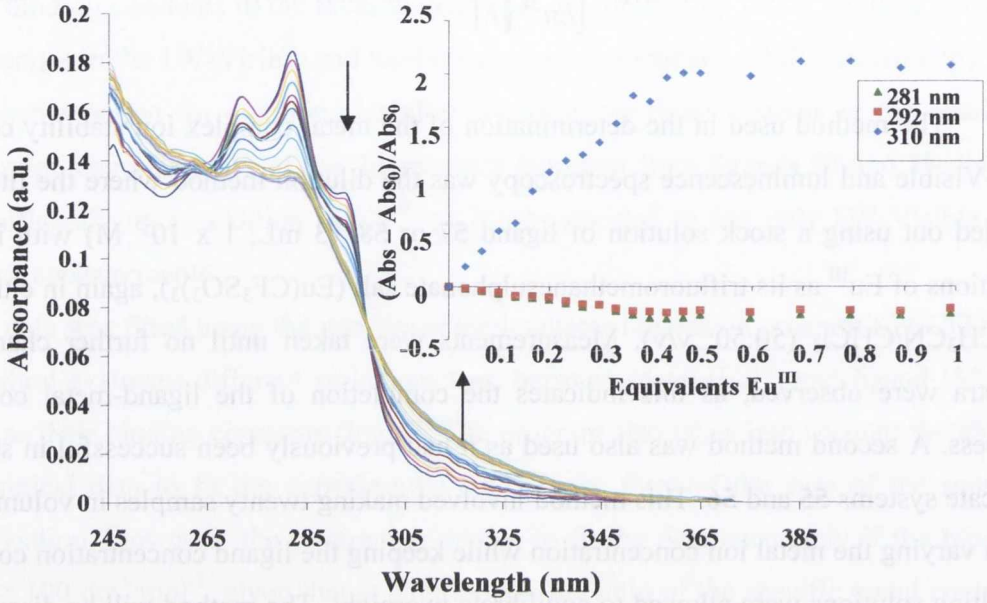

Figure 2.15 Overlaid UV-Visible spectra from the titration of ligand 57 [1 x 10^{-5} M] with $Eu(CF_3SO_3)_3$ in $CH_3CN/CHCl_3$ (50:50; v/v). Inset: Titration profile of the normalised absorbance at 310, 292, and 281 nm as a function of equivalents of Eu^{III} from the titration of ligand 57 [1 x 10^{-5} M] with $Eu(CF_3SO_3)_3$ in $CH_3CN/CHCl_3$ (50:50; v/v).

The UV-Visible spectrum in Figure 2.15 shows one main peak at 281 nm, with two small shoulders at 271 nm and 292 nm. This is characteristic of a substituted naphthalene derivative.[127] Upon addition of Eu^{III}, the band at 281 nm underwent a hypochromic shift, and simultaneously, a new band appeared at ~ 310 nm, with the concomitant formation of an isobestic point at 295 nm. Figure 2.15 shows the titration profile of normalised absorbance intensity at 310, 292 and 281 nm. The profile at 310 nm follows the formation of a new band, and so new species in solution. The profiles at 281 and 292 nm show a decrease in intensity upon the addition of Eu^{III}. The bands at 281 and 292 nm decrease with increasing equivalents of Eu^{III}. This is to be expected as these wavelengths correspond to the absorbance of the free antenna. As Eu^{III} is added, the ligand complexes with the metal and new species are formed. The absorbance forms a plateau upon reaching 0.4 equivalents of Eu^{III}. This is between the

0.33 equivalents for a ML_3 complex, and the 0.5 equivalents for a ML_2 complex. These results are reflected in the log *K* values calculated for this titration, as well as the speciation distribution diagram, shown in Table 2.3 and Figure 2.17, respectively.

2.3.2.2 (R,R) isomer

The same set of measurements as described above, were carried out for ligand **58**. The overlaid UV-Visible titration spectra, and the corresponding titration profile are shown below in Figure 2.16, obtained from the titration of ligand **58** with $Eu(CF_3SO_3)_3$ in $MeCN/CHCl_3$ (50:50; v/v). These were carried out using the same method as for the *S* isomer, ligand **57**.

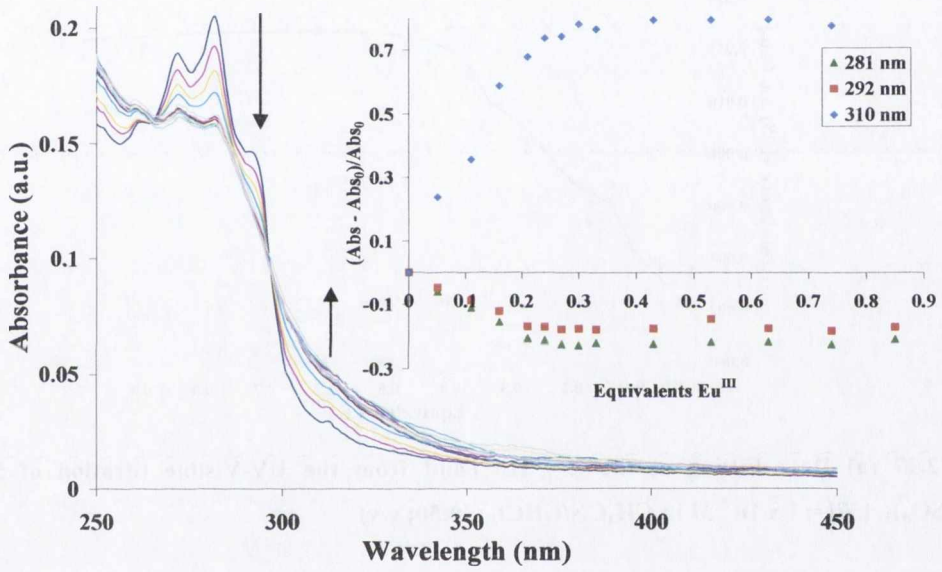

Figure 2.16 Overlaid UV-Vis spectra from the titration of ligand 58 (*R,R*) [1 x 10^{-5} M] with $Eu(CF_3SO_3)_3$ in $CH_3CN/CHCl_3$ (50:50; v/v). Inset: titration profile of the normalised absorbance at 281, 292, and 310 nm as a function of equivalents of Eu^{III} from the titration of ligand 58 (*R,R*) with $Eu(CF_3SO_3)_3$ in $CH_3CN/CHCl_3$ (50:50; v/v).

Both the *S* and *R* isomers display very similar spectra. However, the titration profile of the *R* isomer, **58**, shown inset in Figure 2.16, is somewhat different to that of the *S* isomer, **57**. The plateau begins at 0.3 equivalents for the *R* isomer, **58**. This suggests that the formation of the ML_3 complex as the dominant species.

2.4.2.3 Speciation Distribution Diagrams

Using metal ion stability constants, it is possible to calculate the concentration of the species present in solution at any concentration of Eu^{III}. The speciation diagrams for the Eu^{III} complexes formed for ligands **57** (*S,S*) and **58** (*R,R*) in $CH_3CN/CHCl_3$ (50:50; v/v), derived from the UV-Visible spectra of the respective titrations are shown in Figures 2.14 and 2.16. The fit on the data from the titration of **57** (*S,S*) with Eu^{III} in $CH_3CN/CHCl_3$ (50:50; v/v) is shown in Figure 2.17(a). The fit line does not correlate very well to the data, but it was acceptable.

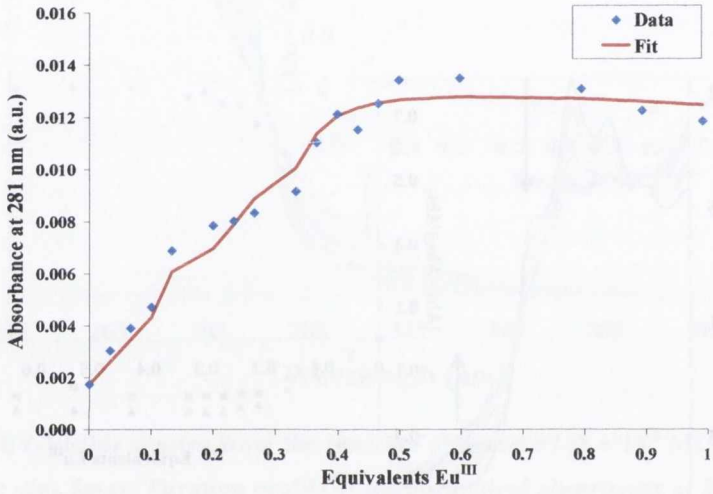

Figure 2.17 (a) Data Fitting at the λ = 310 band from the UV-Visible titration of 57 (*S,S*) with $Eu(CF_3SO_3)_3$. [57] = 1 x 10^{-5} M in $CH_3CN/CHCl_3$ (50:50; v/v).

Figure 2.17 (b) is the speciation diagram derived from UV-Visible titration **57** with $Eu(CF_3SO_3)_3$, showing the species present at various equivalents of Eu^{III} in $CH_3CN/CHCl_3$ (50:50; v/v). The predominant species present in solution after 0.33 equivalents of Eu^{III} have been added, is the EuL_3 complex which reaches a maximum after the addition of 0.33 equivalents. The EuL and EuL_2 complexes are also present but in much smaller amounts.

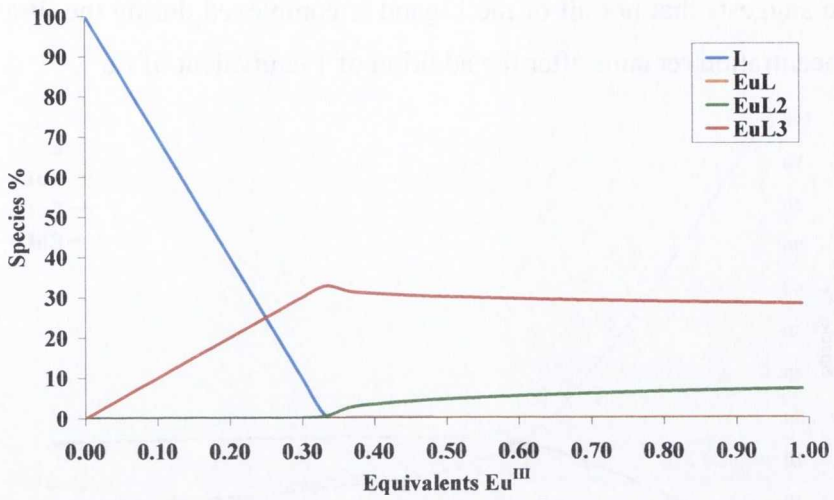

Figure 2.17 (b) Speciation diagram of ligand 57 (*S,S*) derived from UV-Visible data, showing the species present in $CH_3CN/CHCl_3$ (50:50; v/v) at various equivalents of $Eu(CF_3SO_3)_3$. [57] = 1 x 10^{-5} M.

The data fit for the UV-Visible titration of **58** with Eu^{III} is shown in Figure 2.18 (a), along with its corresponding speciation distribution diagram in 2.18 (b). The data fit line shown in Figure 2.18 (a) correlates with the data obtained in the titration.

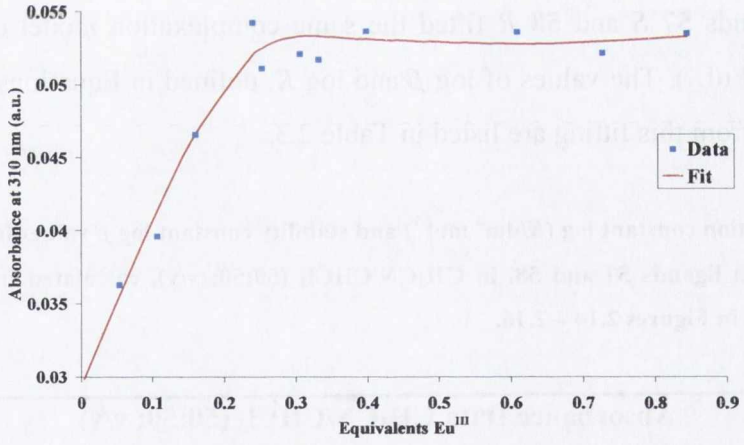

Figure 2.18 (a) Data Fitting at the absorbance band 310 nm, from the UV-Visible titration of 58 (*R,R*) with $Eu(CF_3SO_3)_3$. [58] = 1 x 10^{-5} M in $CH_3CN/CHCl_3$ (50:50; v/v).

The speciation diagram shows that a much larger percentage of the EuL species is formed towards the end of the titration, than was observed in the *S* isomer. This result correlates with the results from the titration profile and the log *K* values. The EuL_3 species is dominant in solution; however there is a significant contribution from the EuL and EuL_2

species. It also suggests that not all of the Ligand is complexed during the titration and that a significant concentration remains after the addition of 1 equivalent of Eu^{III}.

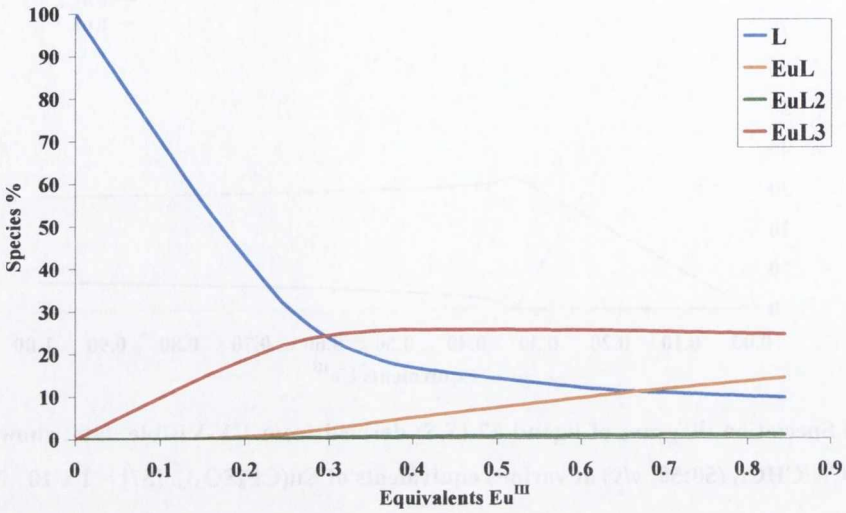

Figure 2.18 (b) Speciation diagram of ligand 58 (*R,R*) derived from UV-Visible data, showing the species present in $CH_3CN/CHCl_3$ (50:50; v/v) at increasing equivalents of $Eu(CF_3SO_3)_3$. [58] = 1 x 10^{-5} M.

2.4.2.4 Stability constants

Using the non-linear least squares regression program SPECFIT, the absorbance variation for ligands **57** *S* and **58** *R* fitted the same complexation model of 1:1 (EuL); 1:2 (EuL_2); and 1:3 (EuL_3). The values of log β and log *K*, defined in Equations 2.1 – 2.5, which were determined from this fitting are listed in Table 2.3.

Table 2.3 Complexation constant log (K/dm^3 mol^{-1}) and stability constant log β values for the complexation of $Eu(CF_3SO_3)_3$ with ligands 57 and 58, in $CH_3CN/CHCl_3$ (50:50; v/v), calculated from the UV-Visible titration data shown in Figures 2.14 – 2.16.

Absorbance Data $CH_3CN/CHCl_3$ (50:50; v/v)				
Species	**log β - 57 (*S,S*)**	**log *K* – 57 (*S,S*)**	**log β – 58 (*R,R*)**	**log *K* – 58 (*R,R*)**
EuL	(5.36)	(5.36)	(5.52)	(5.52)
EuL_2	12.74 ± 0.27	(7.38)	10.34 ± 1.72	4.82 ± 1.72
EuL_3	20.56 ± 0.51	(7.82)	17.79 ± 0.30	(7.46)
Overall log β	20.56		17.79	

The data fitting indicated that there were three species in solution; ML, ML_2, and ML_3. The highest stability constants were determined for the *S* and *R* ligands for the formation of the EuL_3 complex. Both constants were above 7 and so considered very high. Within error, the values of log K_{12}, for the EuL_2 species for both isomers were very similar, with log K_{12} for the *S* isomer only slightly higher. This suggests that the complex **Eu.57** is somewhat more stable in this mixed solvent system than the *R* isomer, **Eu.58**. The log K_{13} values for the *S* isomer reflect what is seen in the titration profile, Figure 2.17. The profile forms a plateau at a value between what is expected for the EuL_2 and EuL_3 complexes, and the log *K* values for these two species are the same (within error).

The overall stability constants, log β_{13}, for both *S* and *R* isomers are given in Table 2.3. The value of log β_{13} for the *S* isomer is higher than that for the *R* isomer indicating that in this solvent system and using the UV-Visible data, the *S* isomer forms a more stable complex with Eu^{III}.

2.4.3 UV-Visible Titrations in CH_3CN

2.4.3.1 (S,S) isomer

Having described the formation of the complex between **57** or **58** and Eu^{III} in mixed solvent media, the formation of ML_3 in pure CH_3CN was investigated next. Titrations were carried out as described before. The overlaid UV-Visible absorption spectra and the corresponding titration profile for the titration of ligand **57** with $Eu(CF_3SO_3)_3$ in CH_3CN, are shown in Figure 2.19. The UV-Visible spectra of the titration of **57** with $Eu(CF_3SO_3)_3$, in CH_3CN gives rise to spectral changes very similar to those obtained in $MeCN/CHCl_3$ (50:50; v/v) (see Figure 2.15). Upon addition of Eu^{III}, the band at 281 nm exhibits a hypochromic shift, and simultaneously, a new band centred at 310 nm forms, as in the previous titration. An isobestic point at 295 nm was again observed.

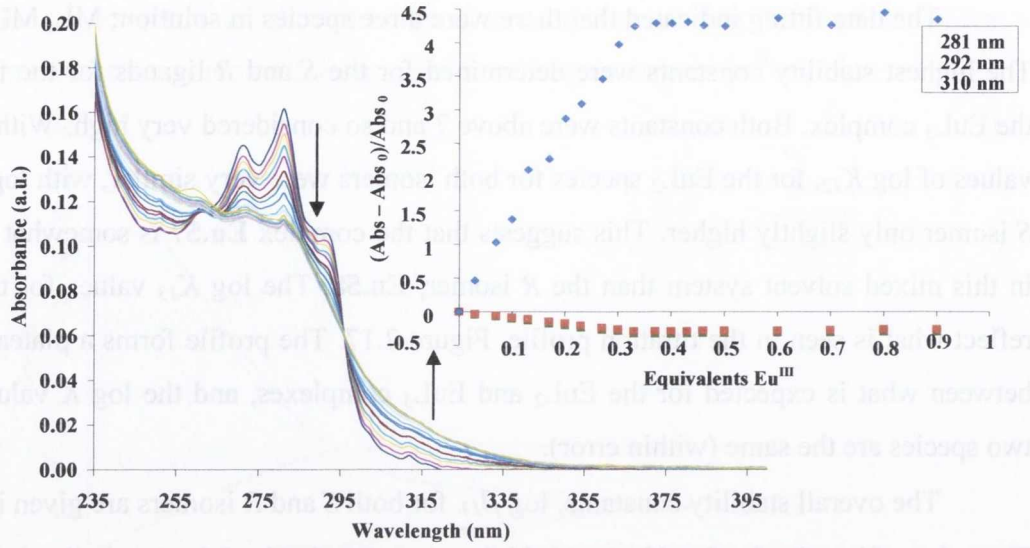

Figure 2.19 Overlaid UV-Vis spectra of the titration of 57 [1 x 10^{-5} M] with $Eu(CF_3SO_3)_3$ in CH_3CN. Inset: Titration profile plot of normalized absorbance at 281, 292, and 310 nm as a function of equivalents of Eu^{III} in the titration of 57 with $Eu(CF_3SO_3)_3$ in CH_3CN.

Examination of the titration profile (inset in Figure 2.19) shows that, as expected, **57** behaves somewhat differently in the more polar solvent system. The profile shows the plateau beginning at 0.33 equivalents of Eu^{III}, in contrast to the plateau at 0.4 equivalents observed in the $CH_3CN/CHCl_3$ (50:50; v/v) solvent system. This indicates that the polarity of the solvent system has an impact on the formation of the Eu^{III} complex in solution. The profiles for the bands at 281 and 292 nm both decrease at the same rate. This is because they both correspond to the absorbance of the free ligand, and so as the concentration of free ligand in solution decreases, these bands also decrease simultaneously.

2.4.3.2 (R,R) isomer

The UV-Visible absorption spectra and the corresponding titration profile for the titration of **58** with $Eu(CF_3SO_3)_3$ in CH_3CN, are shown below in Figure 2.20. The titration was carried out using the same method as the UV-Visible titration of **57** with $Eu(CF_3SO_3)_3$ in CH_3CN.

The UV-Visible spectra for the titration of **58** with $Eu(CF_3SO_3)_3$ in CH_3CN, showed the same features as that of the *S* isomer, **57** (Figure 2.20). As before, the main absorption was centred at 281 nm, with two small shoulders at 271 nm and 292 nm. As increasing equivalents of Eu^{III} metal ion was added, a hypsochromic shift at 281 nm was observed, as well as the formation of a new band at 310 nm, corresponding to a new species in solution.

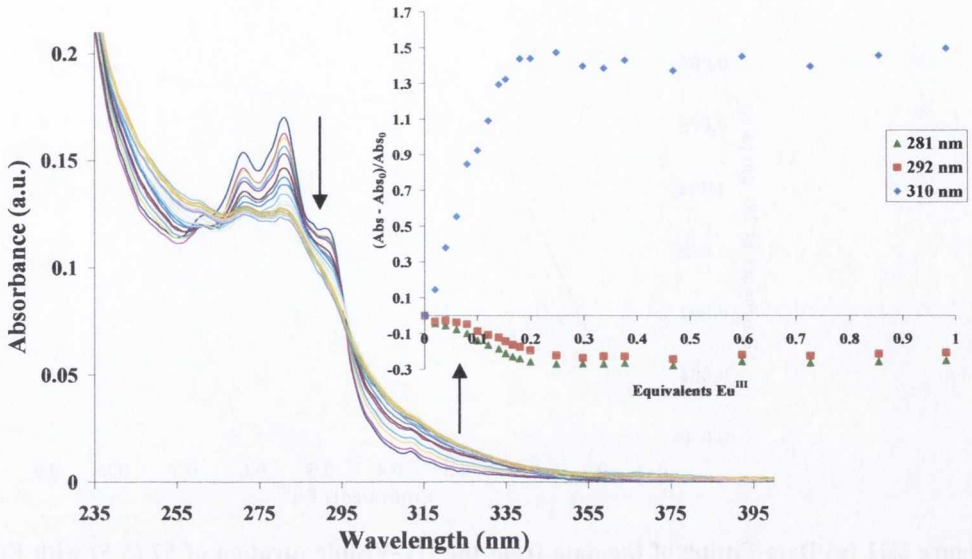

Figure 2.20 Overlaid UV-Vis spectra of the titration of 58 [1 x 10^{-5} M] with $Eu(CF_3SO_3)_3$ in CH_3CN. Inset: Absorbance at 310 nm as a function of equivalents of Eu^{III} in the titration of ligand 58 with $Eu(CF_3SO_3)_3$ in CH_3CN.

The titration profile of absorbance at 310 nm for **58**, inset in Figure 2.20, shows that a plateau is reached at 0.25 equivalents of Eu^{III}. This is slightly different to the titration profile of **58** in the mixed solvent system $CH_3CN/CHCl_3$ (50:50; v/v), where a plateau was reached at 0.3 equivalents of Eu^{III}. However it does correlate to the results observed for the *S* isomer, **57**, which saw a reduction in the number of equivalents of Eu^{III} needed to reach a plateau decrease from 0.4 to 0.3 upon changing from $CH_3CN/CHCl_3$ (50:50; v/v), to 100% CH_3CN. As before, a simultaneous decrease in the bands at 292 and 281 nm are observed.

2.4.3.3 Speciation Distribution Diagrams

The data fits, and speciation diagrams obtained from the fit for the UV-Visible titration of ligands **57** and **58** with $Eu(CF_3SO_3)_3$ in CH_3CN are shown in Figures 2.21 and 2.22.

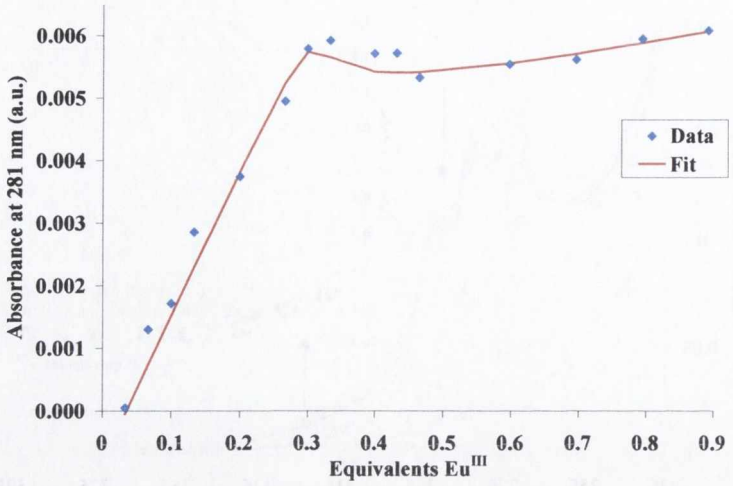

Figure 2.21 (a) Data Fitting of the data from the UV-Visible titration of 57 (*S,S*) with $Eu(CF_3SO_3)_3$ at 320 nm. [57] = 1 x 10^{-5} M in CH_3CN.

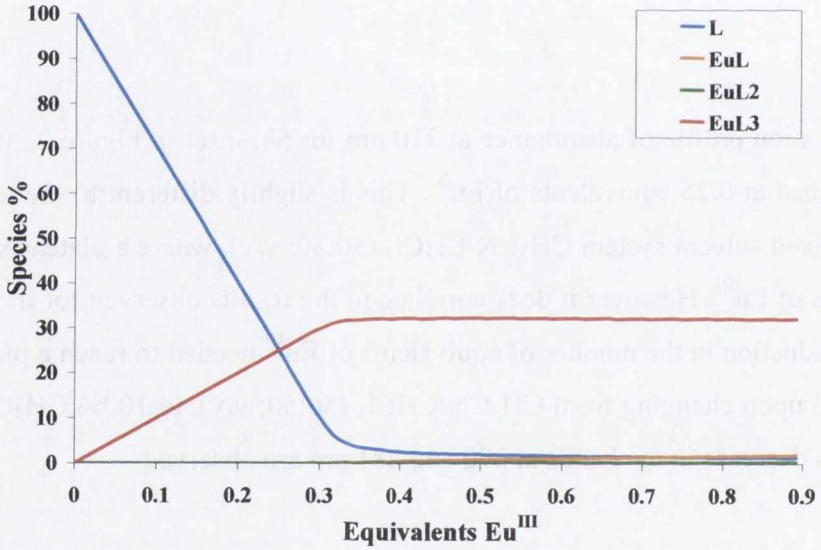

Figure 2.21 (b) Speciation diagram of ligand 57 (*S,S*) derived from UV-Visible data, showing the species present in CH_3CN at various equivalents of $Eu(CF_3SO_3)_3$. [57] = 1 x 10^{-5} M.

The fitting for the data, see Figure 2.21 (a) from this titration, shows a peak at 0.3 equivalents of Eu^{III} followed by a slight decrease and then a plateau. This may indicate that kinetic effects are occurring within the complexation process.

Figure 2.21 (b), the speciation distribution diagram of **57** in CH_3CN for the UV-Visible titrations shows that the EuL_3 species is the most dominant species present in solution after the addition of 0.33 equivalents of Eu^{III}, with only a small percentage of EuL and EuL_2 observed.

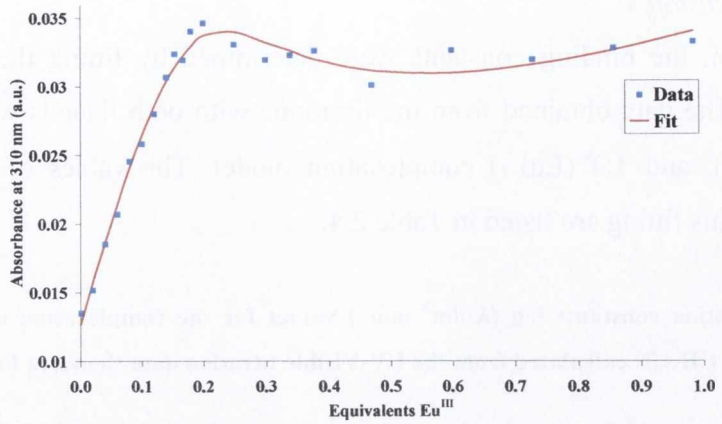

Figure 2.22 (a) Data Fitting of the data from the UV-Visible titration of 58 (*R,R*) with $Eu(CF_3SO_3)_3$ at 310 nm. [58] = 1 x 10^{-5} M in CH_3CN.

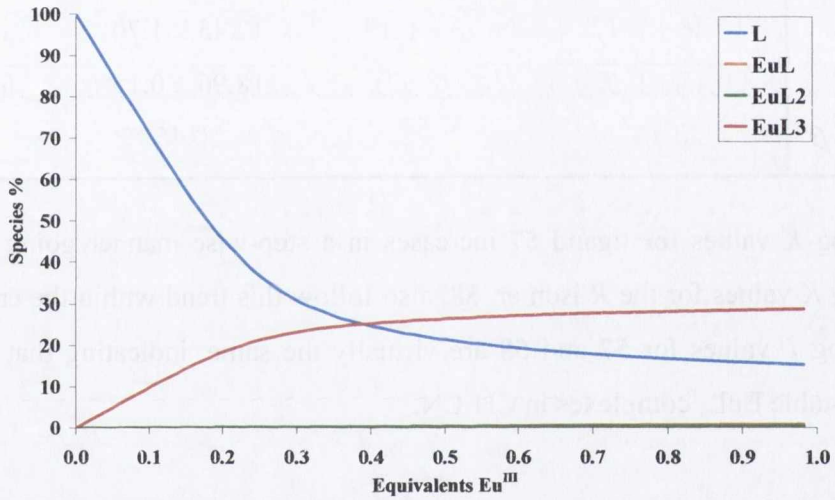

Figure 2.22 (b) Speciation diagram of ligand 58 (*R,R*) derived from UV-Visible data, showing the species present in CH_3CN at various equivalents of $Eu(CF_3SO_3)_3$. [58] = 1 x 10^{-5} M.

The titration data fit clearly shows that there is a slight decrease in absorbance after this point which suggests the influence of the kinetics of the system on the formation of the EuL_3 complex. The EuL_3 species is the most dominant species observed in solution after the addition of 0.4 equivalents of Eu^{III} to **58**, Figure 2.22 (b). There must be a contribution from the EuL and EuL_2 species that stabilise the increase in absorbance (as seen in the data fit graph shown in Figure 2.22 (a)) which occurs at 0.25 equivalents of Eu^{III}. There is quite a large proportion of free ligand left in solution by the end of the titration. This is may be due to the incomplete plateau in the Absorbance after the addition of 0.33 equivalents of Eu^{III}.

2.4.3.4 Stability constants

Once again, the binding constants were determined by fitting the spectral changes using SPECFIT. The data obtained from the titrations with both ligands were fitted to a 1:1 (EuL); 1:2 (EuL_2); and 1:3 (EuL_3) complexation model. The values of log β and log K determined from this fitting are listed in Table 2.4.

Table 2.4. Complexation constants log (K/dm^3 mol^{-1}) values for the complexation of $Eu(CF_3SO_3)_3$ with ligands 57 and 58, in CH_3CN calculated from the UV-Visible titration data shown in Figures 2.19 and 2.20.

Absorbance Data CH_3CN				
Species	**log β - 57 (*S,S*)**	**log K – 57 (*S,S*)**	**log β – 58 (*R,R*)**	**log K – 58 (*R,R*)**
EuL	5.33	> 5 (5.33)	5.39	> 5 (5.39)
EuL_2	11.46 ± 0.17	6.13 ± 0.17	12.45 ± 1.70	> 7 (7.06)
EuL_3	20.43 ± 0.37	>7 (8.97)	18.96 ± 0.15	6.51 ± 0.15
Overall log β	20.43		20.45	

The log K values for ligand **57** increases in a step-wise manner going from EuL to EuL_3. The log K values for the R isomer, **58**, also follow this trend within the errors outlined. The overall log β values for **57** and **58** are virtually the same, indicating that both isomers form equally stable EuL_3 complexes in CH_3CN.

2.4.3.5 Job's Plots from UV-Visible Data

The method of continuous variation, often known as Job's method, is an experimental technique used to determine the stoichiometry coefficients m and n in $\mathbf{M_mL_n}$.[128] The established procedure is to prepare a series of solutions of ligand and metal ion (Eu^{III} in this study) and vary the concentration of each, keeping the total concentration constant. The luminescence and absorbance will vary in solution as the ligand forms different species with the metal, and so it is possible to obtain the n/m ratio from either the maximum or minimum of one of these properties. All of the measurements described in this section were repeated and are fully reproducible. In this study, χ_{Eu} was used to determine the main stoichiometric coefficients, n, and m, from Equation 2.6:

$$\frac{n}{m} = \frac{\chi_{Eu}}{1-\chi_{Eu}}$$ **Equation 2.6**

where χ_{Eu} = [M]/([M]+[L]) is the molar fraction of the metal ($0 \leq \chi_{Eu} \leq 1$). This method was applied to the UV-Visible absorption data, see Figure 2.23.

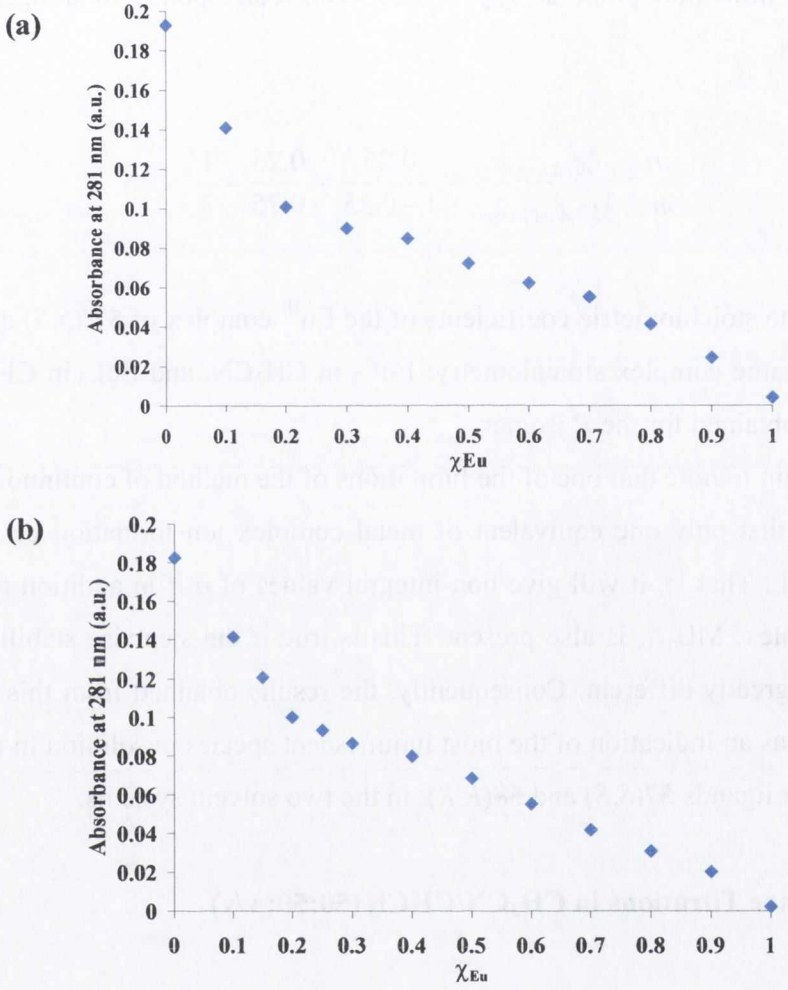

Figure 2.23 Job's Plot for the determination of the stoichiometry of the Eu^{III} complex of ligand 57; absorbance at 281 nm measured in (a) $CH_3CN/CHCl_3$ (50:50, v/v) , and (b) in CH_3CN 100%, *vs* χ_{Eu} ($0 \leq \chi \leq 1$); $[Eu^{III} + 57]_{total} = 1x10^{-5}$ M

From the plot in Figure 2.23 (a), an inflection point at χ_{Eu} = 0.2 was measured in $CH_3CN/CHCl_3$ (50:50, v/v), this corresponds to a ligand to metal stoichiometry of 4:1:

$$\frac{n}{m} = \frac{\chi_{\text{inf lection}}}{1-\chi_{\text{inf lection}}} = \frac{0.2}{1-0.2} = \frac{0.2}{0.8} = \frac{1}{4}$$

Therefore the stoichiometric coefficients of the Eu^{III} complex of **57**(*S,S*) are $m = 4$ and $n = 1$, EuL_4.

UV-Visible measurements were also used to determine the stoichiometry of the Eu^{III} complex of ligand **57** (*S,S*) using Job's method, were also carried out in CH_3CN, Figure 2.23 (b) resulted in an inflection point at $\chi_{Eu} = 0.25$. This corresponds to a ligand to metal stoichiometry of 3/1:

$$\frac{n}{m} = \frac{\chi_{\text{inf lection}}}{1-\chi_{\text{inf lection}}} = \frac{0.25}{1-0.25} = \frac{0.25}{0.75} = \frac{1}{3}$$

Therefore the stoichiometric coefficients of the Eu^{III} complex of **57** (*S,S*) are $n = 1$ and $m = 3$, EuL_3. The same complex stoichiometry: EuL_3 in CH_3CN, and EuL_3 in $CH_3CN/CHCl_3$ (50:50, v/v), were obtained for the *R* isomer.

It is important to note that one of the limitations of the method of continuous variations is the requirement that only one equivalent of metal complex ion formation be present in a solution of M and L. That is, it will give non-integral values of *n* if in addition to M, L, and ML_n, another complex, ML_{n+1}, is also present. This is true if the stepwise stability constants for the system are greatly different. Consequently, the results obtained from this method can only be considered as an indication of the most luminescent species in solution in the presence of $Eu(CF_3SO_3)_3$, for ligands **57**(*S,S*) and **58**(*R,R*), in the two solvent systems.

2.4.4 Luminescence Titrations in $CH_3CN/CHCl_3$ (50:50; v/v)

2.4.4.1 (S,S) isomer

The luminescent spectra were obtained by exciting the solution at 281 nm directly at the naphthalene antennae, and were carried out using the same samples used in the UV-Visible titrations, discussed in the previous section. The overlaid spectra and corresponding titration profiles are shown in Figures 2.24 and 2.25.

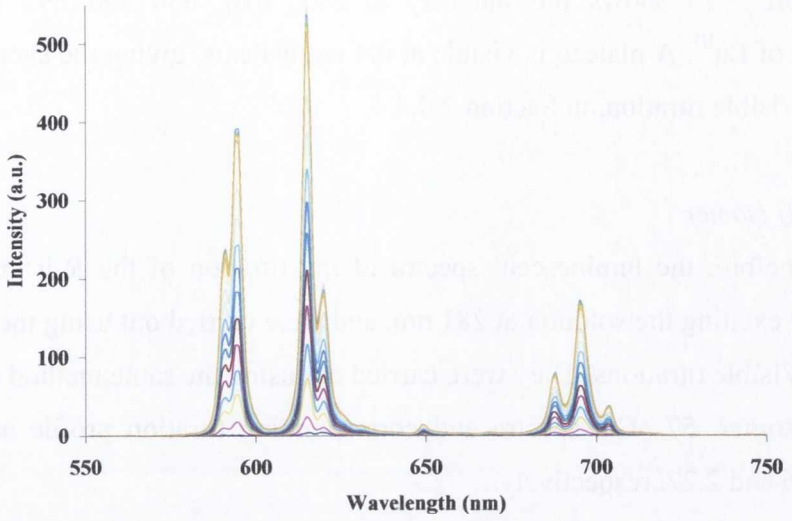

Figure 2.24 Luminescence emission spectra of the titration of ligand 57 [1 x 10^{-5} M] with $Eu(CF_3SO_3)_3$ in $CH_3CN/CHCl_3$ (50:50, v/v), upon excitation at 281 nm.

The spectra exhibit the characteristic Eu^{III} structure, with bands centred on 595 nm, 616 nm, 650 nm, and 695 nm, with the most intense band centred on 616 nm. These bands are representative of the deactivation of the $^5D_0 \rightarrow {}^7F_J$ ground states of (J = 1 – 4, respectively). The structure of these bands does not change during the titration. The two bands at 595 and 695 nm exhibit the largest change in intensity and not the band at 616 nm, even though it is the most intense (see Figure 2.25).

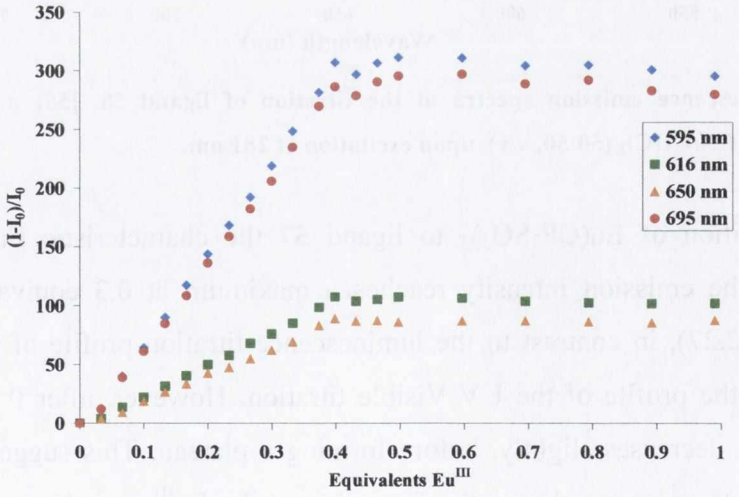

Figure 2.25 Plot of the change in luminescence emission intensity at 595, 616, 650 and 695 nm, from the titration of ligand 57 [57] = [1 x 10^{-5} M] as a function of equivalents of $Eu(CF_3SO_3)_3$ in $CH_3CN/CHCl_3$ (50:50, v/v), upon excitation at 281 nm.

Figure 2.25 shows the intensity at 595, 616, 650 and 695 nm plotted against equivalents of Eu^{III}. A plateau is visible at 0.4 equivalents, giving the same result as observed in the UV-Visible titration, in Section 2.4.4.1.

2.4.4.2 (R,R) isomer

As before, the luminescent spectra of the titration of the *R* isomer, ligand **58** were obtained by exciting the solution at 281 nm, and were carried out using the same samples used in the UV-Visible titrations. They were carried out using the same method as the data recorded for the *S* isomer, **57**. The spectra and corresponding titration profile are shown below in Figures 2.26 and 2.27, respectively.

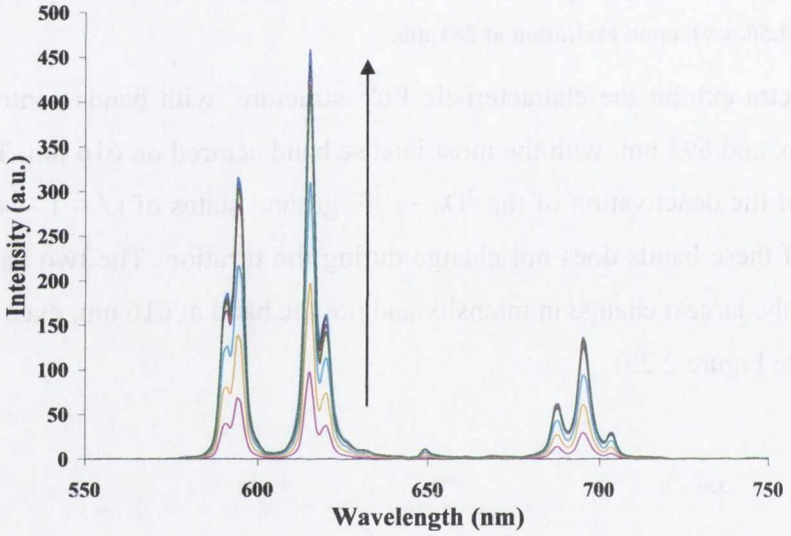

Figure 2.26 Luminescence emission spectra of the titration of ligand 58, [58] = [1 x 10^{-5} M] with $Eu(CF_3SO_3)_3$ in $CH_3CN/CHCl_3$ (50:50, v/v), upon excitation at 281 nm.

Upon addition of $Eu(CF_3SO_3)_3$ to ligand **57** the characteristic Eu^{III} emission was observed. Here, the emission intensity reaches a maximum at 0.3 equivalents of Eu^{III} (as shown in Figure 2.27), in contrast to the luminescence titration profile of the *S* ligand, and corresponding to the profile of the UV-Visible titration. However, after 0.3 equivalents the profile at 616 nm decreases slightly, before forming a plateau. This suggests that there are some kinetic effects occurring during the formation of the Eu^{III} complex, as the peak at 616 nm is indicative of the immediate coordination environment around the lanthanide ion

The profile taken at 595, 650 and 695 nm all appear to form a plateau between 0.25 and 0.3 equivalents of Eu^{III}. One explanation for this is that there may be other species in solution, but they are weakly luminescent and so the ML_3 species is principally observed even if others are present. Contrary to the results from the *S* isomer, the relative intensity of the band at 616 nm, is the highest, followed by the band at 595 nm ($J = 1$). The bands at 650 and 695 nm change significantly less again. It is interesting that these bands change at a different rates between isomers. This may be due to the slightly different formation of the various species in solution depending on the conformation of the ligand.

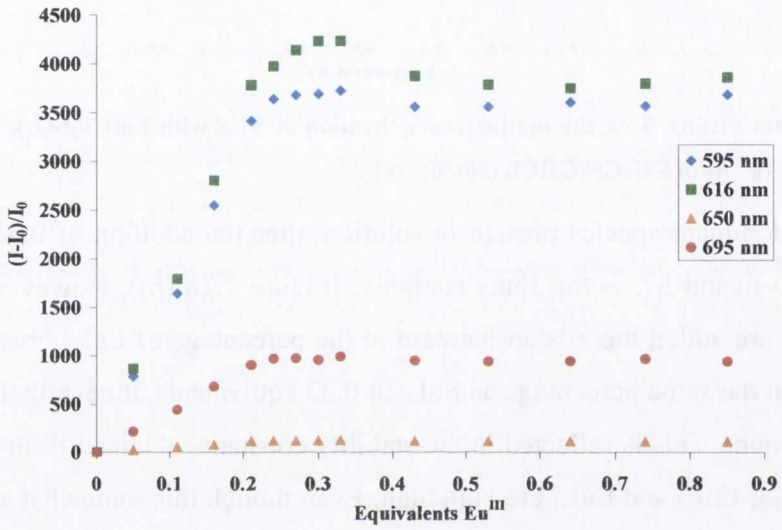

Figure 2.27 Plot of the change in luminescence emission intensity at 595, 616, 650, and 695 nm, from the titration of ligand 58 [58] = [1 x 10^{-5} M] as a function of equivalents of $Eu(CF_3SO_3)_3$ in $CH_3CN/CHCl_3$ (50:50, v/v), upon excitation at 281 nm.

2.4.4.3 Speciation Distribution Diagrams

The data fits, and speciation diagrams, derived using SPECFIT, from the luminescence titrations of **57** and **58** with $Eu(CF_3SO_3)_3$ in $CH_3CN/CHCl_3$ (50:50; v/v) are shown in Figures 2.28 and 2.29.

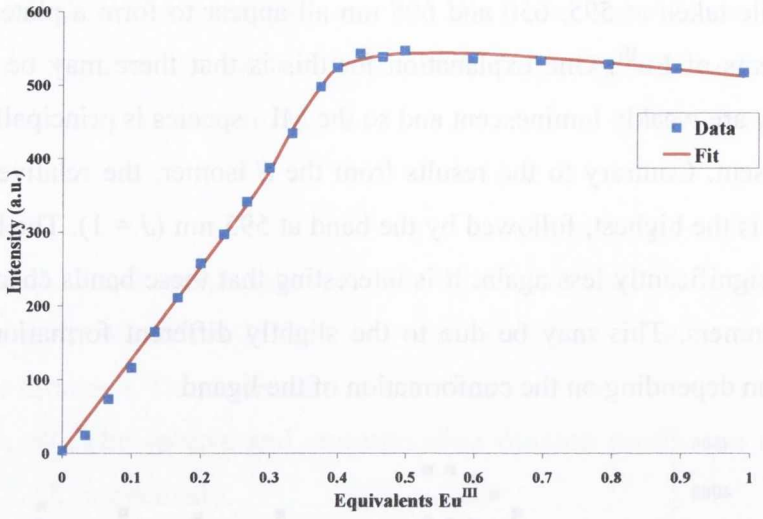

Figure 2.28 (a) Data Fitting from the luminescence titration of 57 *S* with $Eu(CF_3SO_3)_3$ at the intensity at 616 nm. [57] = 1 x 10^{-5} M in $CH_3CN/CHCl_3$ (50:50; v/v).

The predominant species present in solution after the addition of 0.33 equivalents of Eu^{III} is added to ligand **57**, is the EuL_3 complex, (Figure 2.28 (b)). However, as subsequent aliquots of Eu^{III} are added there is an increase in the percentage of EuL_2 present. Although it does not occur in the same percentage as EuL_3 at 0.33 equivalents, it nevertheless is present in a significant amount. This is reflected in the stability constants obtained from this titration, as log K_{12} and K_{13} for EuL_2 and EuL_3 are both high. Even though this somewhat anomalous result is obtained in the speciation distribution diagram, the fitting of the titration data corresponds very closely with the experimental data.

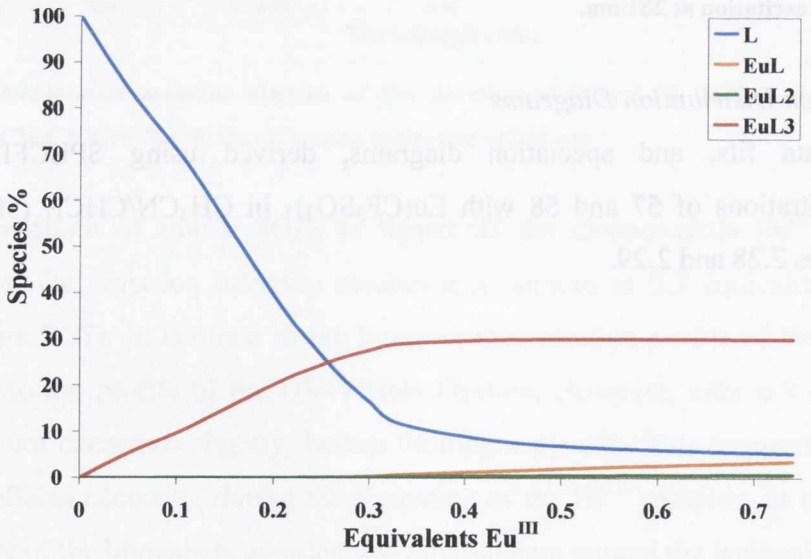

Figure 2.28 (b) Speciation diagram of ligand 57 (*S,S*) derived from luminescence data, showing the species present in $CH_3CN/CHCl_3$ (50:50; v/v) at various equivalents of $Eu(CF_3SO_3)_3$. [57] = 1 x 10^{-5} M.

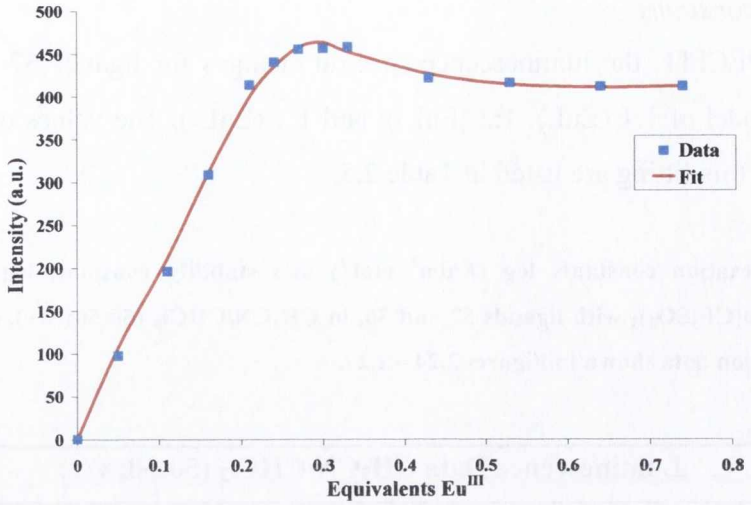

Figure 2.29 (a) Data Fitting from the luminescence titration of 58 (*R,R*) with $Eu(CF_3SO_3)_3$ of the intensity at 616 nm. [58] = 1 x 10^{-5} M in $CH_3CN/CHCl_3$ (50:50; v/v).

The data fit shown in Figure 2.29 (a), shows a good fit with the titration profile data. The speciation diagram of ligand **58**, *R,* (shown in Figure 2.29 (b)) shows that the dominant species in solution is EuL_3. Only a small percentage of EuL and EuL_2 are present. This is reflected in the stability constants calculated by SPECFIT. The log *K* values for EuL and EuL_2 are very similar at 5.22 and 5.57 respectively, while the log *K* value for EuL_3 is much larger (> 7).

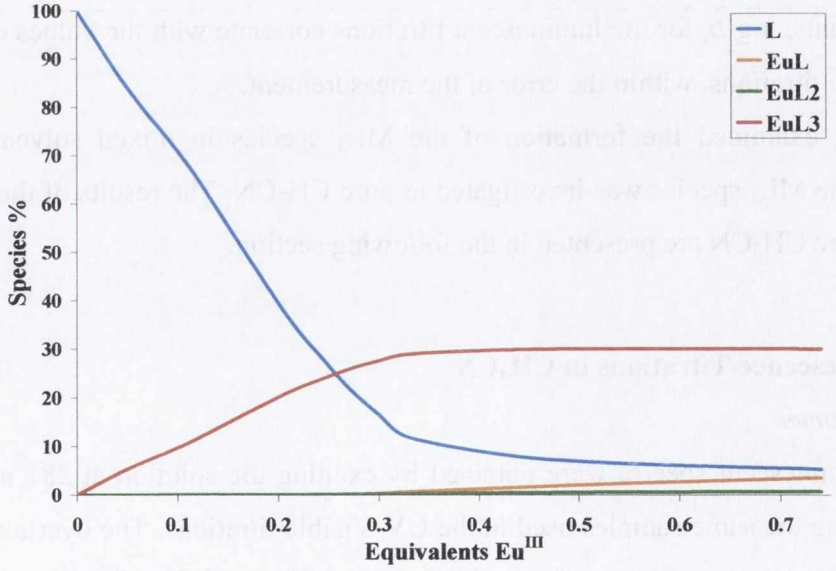

Figure 2.29 (b) Speciation diagram of ligand 58 (*R,R*) derived from luminescence data, showing the species present in $CH_3CN/CHCl_3$ (50:50; v/v) at various equivalents of $Eu(CF_3SO_3)_3$. [58] = 1 x 10^{-5} M.

2.4.4.4 Stability constants

Using SPECFIT, the luminescence spectral changes for ligands **57** and **58** fitted the complexation model of 1:1 (EuL); 1:2 (EuL_2); and 1:3 (EuL_3). The values of log β and log K determined from this fitting are listed in Table 2.5.

Table 2.5. Complexation constants log (K/dm^3 mol^{-1}) and stability constant, log β, values for the complexation of $Eu(CF_3SO_3)_3$ with ligands 57 and 58, in $CH_3CN/CHCl_3$ (50:50; v/v), calculated from the luminescence titration data shown in Figures 2.24 – 2.27.

Luminescence Data $CH_3CN/CHCl_3$ (50:50; v/v)				
Species	log β - 57 (*S,S*)	log K – 57 (*S,S*)	log β – 58 (*R,R*)	log K – 58 (*R,R*)
EuL	5.11 ± 0.63	5.11 ± 0.63	(5.22)	(5.22)
EuL_2	14.74 ± 0.30	(7.63)	10.79 ± 0.33	5.57 ± 0.33
EuL_3	22.17 ± 0.41	(7.43)	18.72 ± 0.10	(7.93)
Overall log β_{13}	22.17		18.72	

As with the results from the UV-Visible titrations, the *S,S* enantiomer isomer in general, exhibits higher stability constants than the *R,R* enantiomer, with an overall stability constant (log β) that is two orders of magnitude higher than the *R,R* enantiomer. The overall stability constants, log β, for the luminescent titrations correlate with the values calculated for the UV-Visible titrations, within the error of the measurement.

Having examined the formation of the ML_3 species in mixed solvent media, the formation of the ML_3 species was investigated in pure CH_3CN. The results of the luminescent titrations in pure CH_3CN are presented in the following section.

2.4.5 Luminescence Titrations in CH_3CN

2.4.5.1 (S,S) isomer

The luminescent spectra were obtained by exciting the solution at 281 nm, and were carried out using the same samples used in the UV-Visible titrations. The overlaid spectra and corresponding titration profile are shown in Figures 2.30 and 2.31. The spectra exhibit the characteristic Eu^{III} structure, with bands centred on 595 nm, 616 nm, 650 nm, and 695 nm, with the most intense band centred on 616 nm. These bands are representative of the

deactivation of the $^5D_0 \rightarrow {}^7F_J$ ground states of ($J = 1 - 4$, respectively). As such, changing to a more polar solvent does not appear to change the structure of the spectrum.

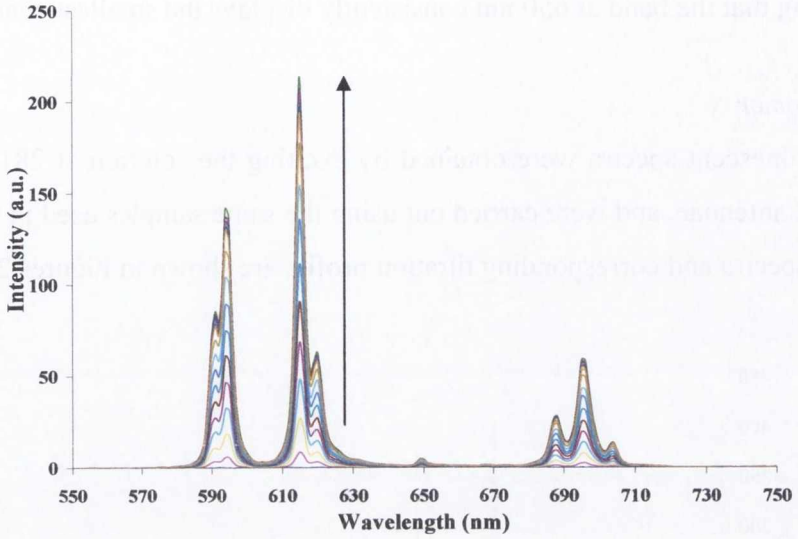

Figure 2.30 Overlaid luminescence spectra from the titration of ligand 57(*S,S*) [1 x 10^{-5}M] with $Eu(CF_3SO_3)_3$ in CH_3CN, upon excitation at 281 nm.

Figure 2.31 shows the change in emission intensity at 595, 616, 650 and 695 nm plotted against the number of equivalents of Eu^{III}. As can be observed, only minor changes occur at 616 nm after the addition of 0.33 equivalents of the metal ion. This gives the same result as observed in the UV-Visible titration. There is a small decrease in intensity, after 0.4 followed by a plateau. This decrease in emission intensity may be caused because of the formation of increasing amounts of the EuL_2 species which is less emissive than EuL_3. This can be seen in the speciation distribution diagram, Figure 2.34 (b).

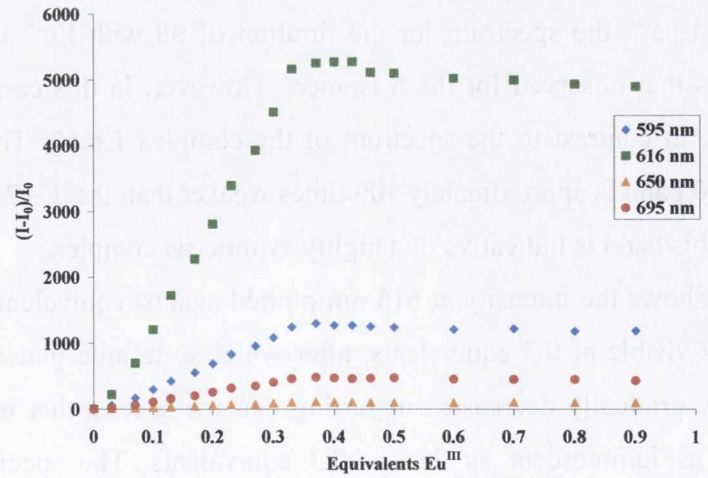

Figure 2.31 Titration profile of the change in Intensity at 595, 616, 650, and 695 nm as a function of equivalents of Eu^{III}, for the titration of 57(*S,S*) [1 x 10^{-5}M] with $Eu(CF_3SO_3)_3$ in CH_3CN.

The titration profile exhibits a different response to that seen for the luminescent titrations, in mixed solvent, in regard to the relative intensity of the $J = 1 - 4$, bands. The only correlation being that the band at 650 nm consistently displays the smallest change in emission.

2.4.5.2 (R,R) isomer

The luminescent spectra were obtained by exciting the solution at 281 nm directly at the naphthalene antennae, and were carried out using the same samples used in the UV-Visible titrations. The spectra and corresponding titration profile are shown in Figures 2.32 and 2.33.

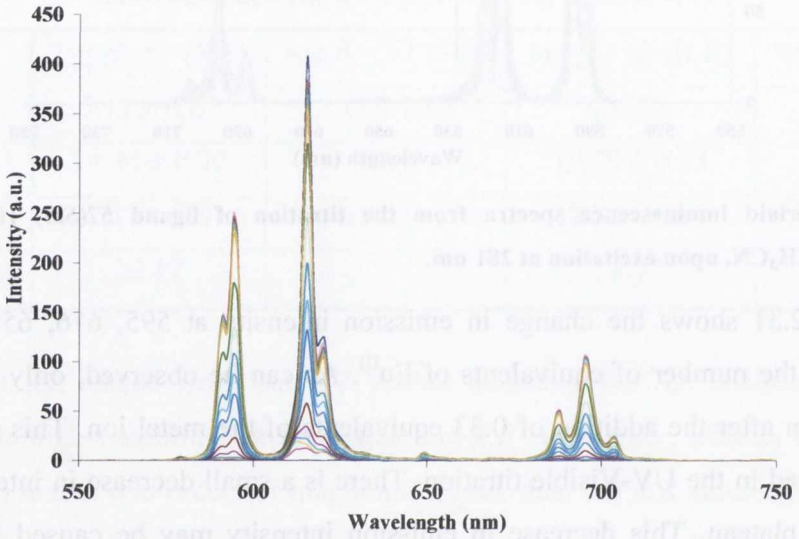

Figure 2.32 Overlaid luminescence spectra from the titration of 58 (*R,R*) [1 x 10^{-5}M] with $Eu(CF_3SO_3)_3$ in CH_3CN, upon excitation at 281 nm.

For the most part, the spectrum for the titration of **58** with Eu^{III} in CH_3CN (Figure 2.32) is the same as that observed for the *S* isomer. However, in this case alone, the $J = 0$ band was observed, in contrast to the spectrum of the complex **Eu.57**. The intensity of the emission of the $J = 0$ band is approximately 100 times weaker than the $J = 2$ band (at 616 nm). The appearance of this band is indicative of a highly symmetric complex.

Figure 2.33 shows the intensity at 616 nm plotted against equivalents of Eu^{III}. For the first time, a peak is visible at 0.3 equivalents, after which a definite plateau does not form. Rather, the intensity gradually decreases suggesting that the species that is formed after 0.3 equivalents is not as luminescent as that at 0.3 equivalents. The speciation distribution diagram shows that the percentage of ligand present after the addition of 0.3 equivalents of

Eu^{III} is much larger than seen in the other titrations, and this is possibly the reason for the unusual titration profile.

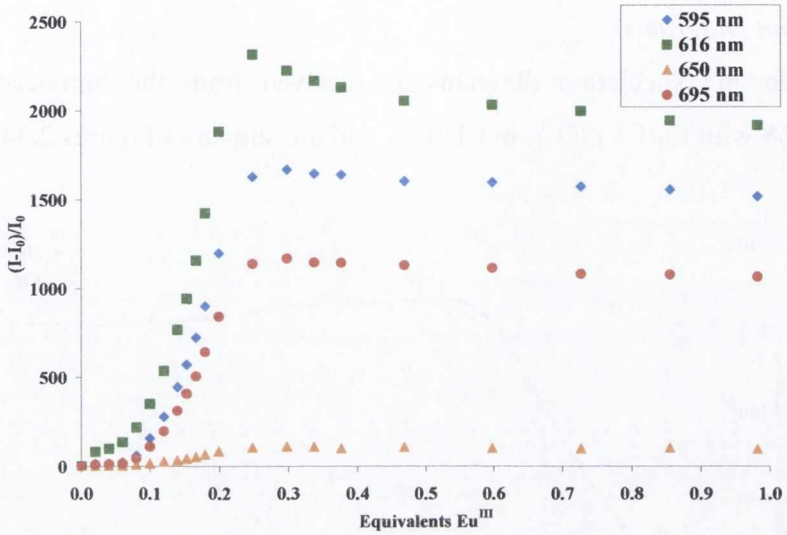

Figure 2.33 (a) Titration profile of the change in intensity at 595, 616, 650, and 695 nm as a function of equivalents of Eu^{III}, from the titration of 58 (*R,R*) [1 x 10^{-5}M] with $Eu(CF_3SO_3)_3$ in CH_3CN.

As for the *S* isomer, the $J = 2$ band displays the greatest change in intensity. This is followed by $J = 1$, $J = 3$ and $J = 4$.

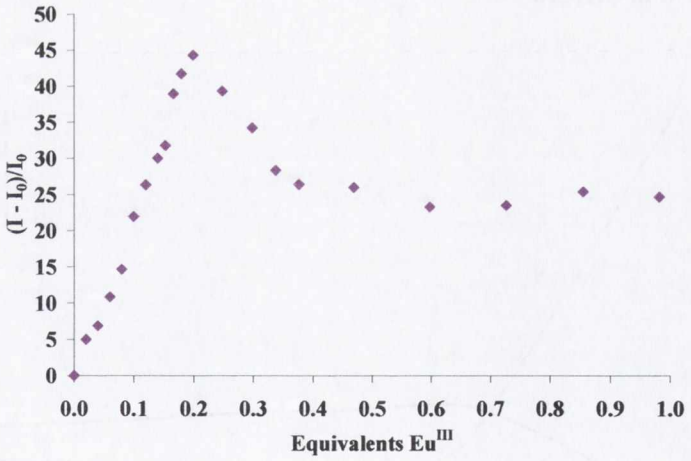

Figure 2.33 (b) Titration profile of the change in intensity at 580 nm as a function of equivalents of Eu^{III}, from the titration of 58 (*R,R*) [1 x 10^{-5}M] with $Eu(CF_3SO_3)_3$ in CH_3CN.

The titration profile for the change in intensity at 580 nm ($J = 0$) does not follow the same profile as the other bands. It peaks at 0.2 equivalents of Eu^{III}, then decreases to 0.33

equivalents, where it forms a plateau. This suggests the possibility that stacking between the chromophores, *i.e.* the naphthalene moieties of the ligand.

2.4.5.3 Speciation Diagrams

The following speciation diagrams are derived from the luminescent titration of ligands **57** and **58** with $Eu(CF_3SO_3)_3$ in CH_3CN, and are shown in Figures 2.34 and 2.35.

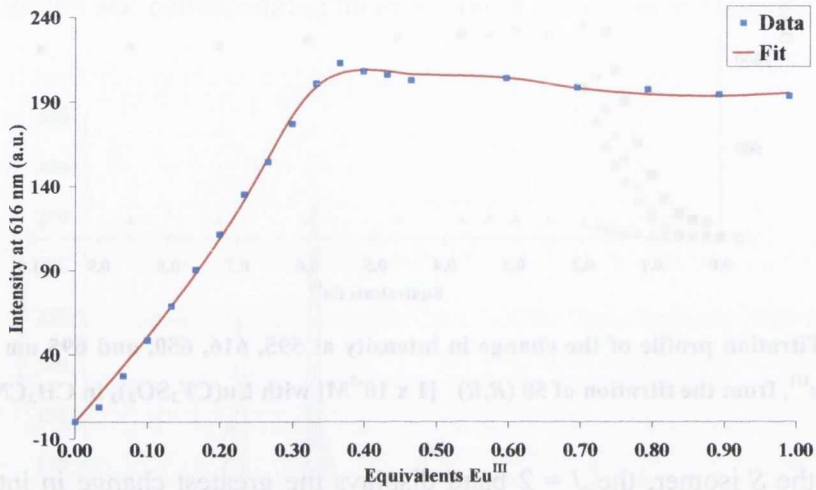

Figure 2.34 (a) Data Fitting of the luminescence titration of 57 (*S,S*) with $Eu(CF_3SO_3)_3$ intensity shown at 616 nm. [57] = 1 x 10^{-5} M in CH_3CN.

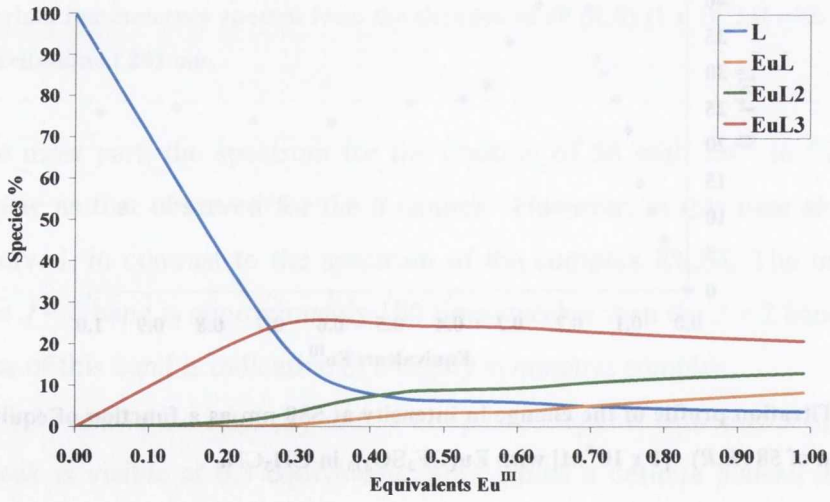

Figure 2.34 (b) Speciation diagram of ligand 57 (*S,S*) derived from luminescence data, showing the species present in CH_3CN at various equivalents of $Eu(CF_3SO_3)_3$. [57] = 1 x 10^{-5} M.

The speciation diagram of the luminescent titration of ligand **57** with $Eu(CF_3SO_3)_3$ in CH_3CN exhibits some interesting points. Although the dominant species in solution for the *S* isomer is EuL_3, which peaks after the addition of 0.33 equivalents of Eu^{III}, it then steadily decreases and the percentage of EuL and EuL_2 begin to increase. In Figure 2.34 (b), the speciation diagram for ligand **57**, by 1 equivalent of Eu^{III} the percentage of EuL_2 in solution is close to that of EuL_3. These results correlate with the log *K* values as log $K = 6.63$ for EuL_2 and 6.64 for EuL_3. These values are nearly identical indicating that both complexes are very stable in solution. The corresponding data fit is shown in Figure 2.34 (a).

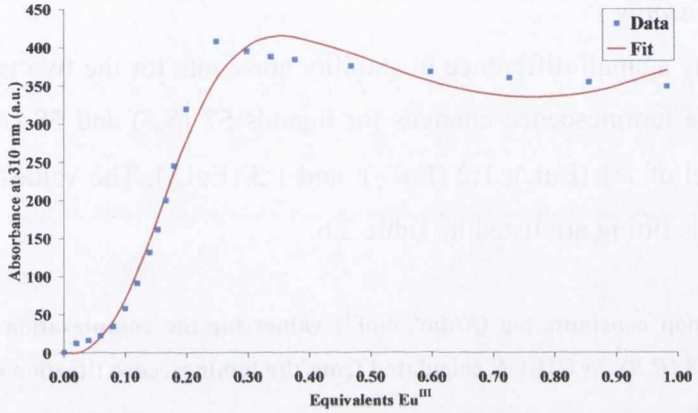

Figure 2.35 (a) Data Fitting of the luminescence titration of 58 (*R,R*) with $Eu(CF_3SO_3)_3$ fit shown of the emission at 616 nm. [58] = 1 x 10^{-5} M in CH_3CN.

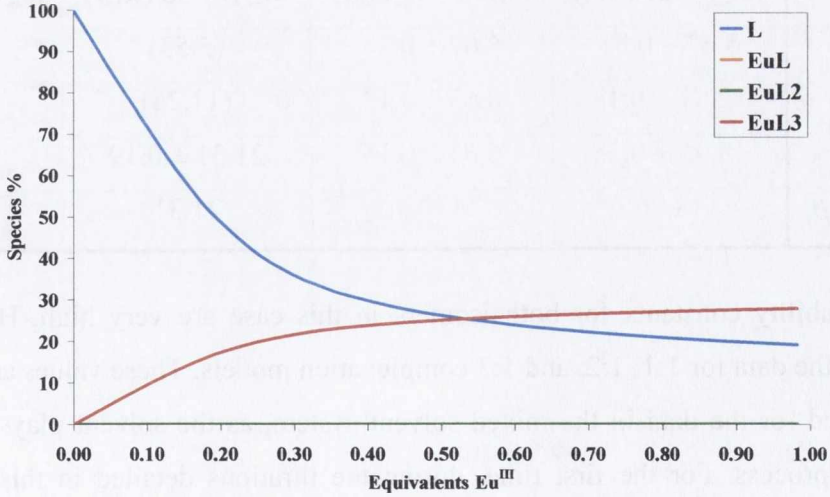

Figure 2.35 (b) Speciation diagram of ligand 58 (*R,R*) derived from luminescence data, showing the species present in CH_3CN at various equivalents of $Eu(CF_3SO_3)_3$. [58] = 1 x 10^{-5} M.

The speciation distribution diagram for **58**, in general, follows a much more conventional pattern than the corresponding diagram for **57**. However, the percentage of EuL_3 in solution only overtakes that of the free ligand after 0.5 equivalents of Eu^{III} have been added. This is not observed in the titration profile (Figure 2.33), which peaks at 0.25 equivalents of Eu^{III}. There is a decrease in the emission intensity observed after this point which may explain why the speciation diagram shows such a high percentage of free ligand. The log *K* value calculated for the EuL_3 species is very high, and the overall stability constant, log β, is higher for the *R* isomer than for the *S* isomer.

2.4.5.4 Stability constants

There is only a small difference in stability constants for the two isomers. When fitted using SPECFIT, the luminescence changes for ligands **57** (*S,S*) and **58** (*R,R*) fitted the same complexation model of 1:1 (EuL); 1:2 (EuL_2); and 1:3 (EuL_3). The values of log β and log *K* determined from this fitting are listed in Table 2.6.

Table 2.6. Complexation constants log (K/dm^3 mol^{-1}) values for the complexation of $Eu(CF_3SO_3)_3$ with ligands 57 (*S,S*) and 58 (*R,R*), in CH_3CN calculated from the luminescence titration data shown in Figures 2.30 and 2.32.

Luminescence Data CH_3CN				
Species	**log β - 57 (*S,S*)**	**log *K* – 57 (*S,S*)**	**log β – 58 (*R,R*)**	**log *K* – 58 (*R,R*)**
EuL	5.67 ± 0.31	5.67 ± 0.31	(5.53)	(5.52)
EuL_2	12.31 ± 0.13	6.63 ± 0.13	(11.24)	(5.71)
EuL_3	18.96 ± 0.15	6.64 ± 0.15	21.31 ± 0.19	(10.06)
Overall log β	18.96		21.31	

The stability constants for both isomers in this case are very high. However, both isomers fitted the data for 1:1, 1:2, and 1:3 complexation models. These values are higher than those calculated for the data in the mixed solvent system, as the solvent plays a role in the complexation process. For the first time, during the titrations detailed in this Chapter, the overall stability constant for the *R,R* enantiomer, **58** is higher than that of the *S,S* enantiomer, **57**.

2.4.5.5 Job's Plots from luminescence data

For this study, the emission at 616 nm ($J = 2$ band) was plotted against χ_{Eu} to find χ_{max}. The $J = 2$ band was chosen as it is most sensitive to the coordination environment of the Eu^{III} centre. To determine the stoichiometric ratios of complex **Eu.57** (*S,S*) and **Eu.58** (*R,R*) the emission at 616 nm of 12 samples, each containing the same total number of moles of ligand and Eu^{III}, but in different ratios, was measured. The emission of each was then plotted against the mole fraction of the metal (χ_{Eu}). Job's plots were taken in CH_3CN (100%) and $CH_3CN/CHCl_3$ (50:50, v/v). Figure 2.36 shows the Job's plot of emission at 616 nm of **Eu.57** (*S,S*) in (a) $CH_3CN/CHCl_3$ (50:50, v/v), and (b) CH_3CN. All of the measurements described in this section were repeated and are fully reproducible. The plots shown in Figure 2.36 is from the (*S,S*) isomer, however identical results were obtained for the *R* isomer. The stoichiometric ratio was calculated from Equation 2.6 as with the UV-Visible titration data.

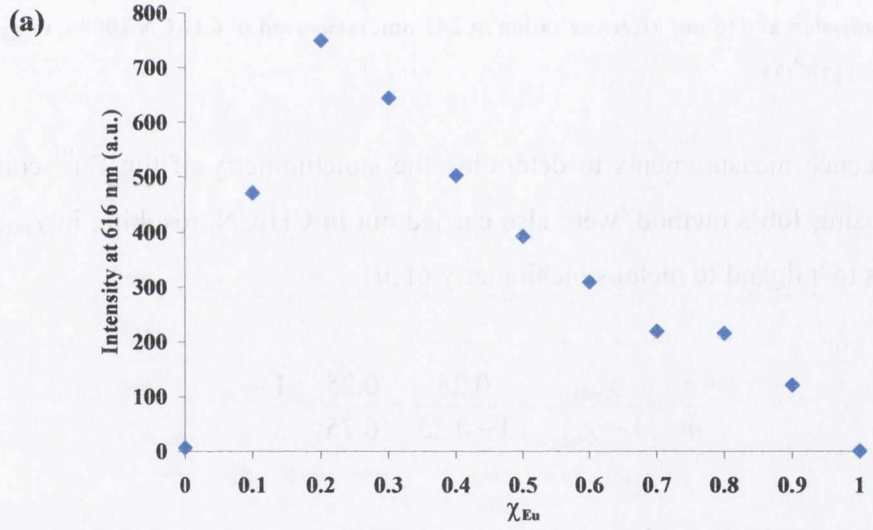

Figure 2.36 (a) Job's Plot for the determination of the stoichiometry of the Eu^{III} complex of ligand 57(*S,S*); phosphorescence emission at 616 nm after excitation at 281 nm, measured in $CH_3CN/CHCl_3$ (50:50, v/v) *vs* χ_{Eu} ($0 \leq \chi \leq 1$); $[Eu^{III} + 57]_{total} = 1x10^{-5}$ M

From the plot in Figure 2.36 (a), $\chi_{max} = 0.2$ was measured in $CH_3CN/CHCl_3$ (50:50, v/v), this corresponds to a ligand to metal stoichiometry of 4:1:

$$\frac{n}{m} = \frac{\chi_{max}}{1-\chi_{max}} = \frac{0.2}{1-0.2} = \frac{0.2}{0.8} = \frac{1}{4}$$

Therefore the stoichiometric coefficients of the Eu^{III} complex of **57**(*S,S*) are $m = 4$ and $n = 1$, EuL_4.

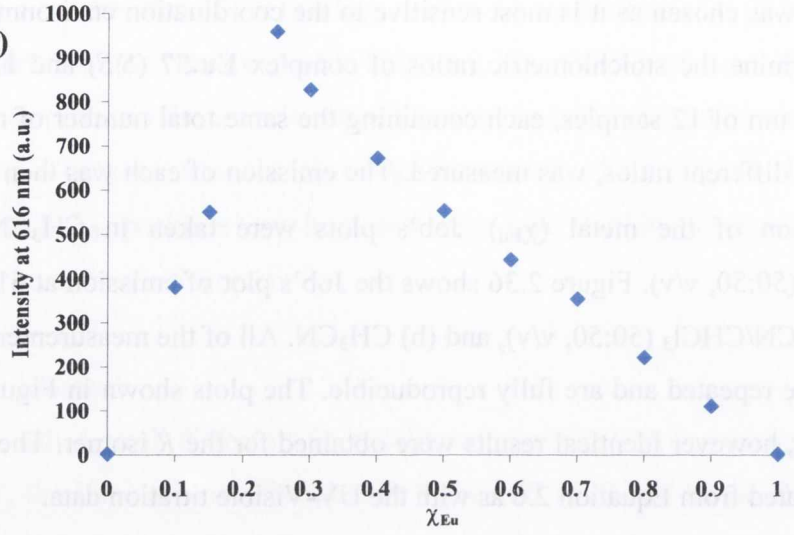

Figure 2.36 (b) Job's Plot for the determination of the stoichiometry of the Eu^{III} complex of ligand 57(*S,S*); phosphorescence emission at 616 nm after excitation at 281 nm, measured in CH_3CN 100%, *vs* χ_{Eu} ($0 \leq \chi \leq 1$); $[Eu^{III} + 57]_{total} = 1x10^{-5}$ M

Luminescence measurements to determine the stoichiometry of the Eu^{III} complex of ligand **57** (*S,S*) using Job's method, were also carried out in CH_3CN, resulting in $\chi_{max} = 0.25$. This corresponds to a ligand to metal stoichiometry of 3/1:

$$\frac{n}{m} = \frac{\chi_{max}}{1-\chi_{max}} = \frac{0.25}{1-0.25} = \frac{0.25}{0.75} = \frac{1}{3}$$

Therefore the stoichiometric coefficients of the Eu^{III} complex of **57** (*S,S*) are $n = 1$ and $m = 3$, EuL_3. The same complex stoichiometry: EuL_3 in CH_3CN, and EuL_3 in $CH_3CN/CHCl_3$ (50:50, v/v), were obtained for the *R* isomer. These results correlate with those of the UV-Visible Job's plots.

So far in this discussion of the photophysical measurement of the complex stoichiometry, the method used for all of the titrations described herein has been that of the dilution method. However, a second method was attempted and this will be discussed in the next section.

2.4.6 Photophysical Titration Method 2, Mole Fraction Method.

A second method, Method 2, was used to conduct the photophysical titrations described within this Chapter, the mole fraction method. Twenty samples (5 mL) of ligands **57** and **58** [1 x 10^{-5} M] were made with varying amounts of Eu^{III} (from 0 to 3 equivalents, as changes had been seen in the NMR titrations Section 2.2 up to 3 equivalents) and were then agitated using a mechanical shaker overnight, and the various spectra were recorded. This method had been used successfully for the helicate systems **55** and **56** by Dr. F. Stomeo and so it was decided to explore this method with **57** and **58** in addition to the titrations shown in previous sections. These investigations were carried out in the same solvent systems as for Method 1, and the changes observed in the lanthanide luminescence are shown in Figures 2.37 – 2.42, but in addition both the ground state and the singlet excited state changes were also recorded. The lanthanide luminescence spectra shown below are that of samples recorded using **57**, and the following discussion only focuses on the results obtained using this ligand. However, both **57** and **58** were examined using this method, and all measurements were repeated at least three times, and gave rise to identical results.

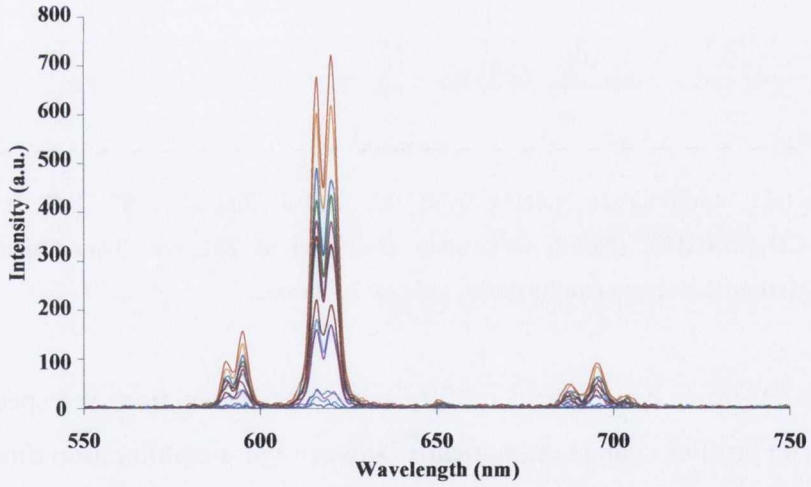

Figure 2.37 Overlaid luminescence spectra from the measurement of 57 (*S,S*) [1 x 10^{-5}M] with $Eu(CF_3SO_3)_3$ in $CH_3CN/CHCl_3$ (50:50, v/v), upon excitation at 281 nm. These results were obtained using Method 2, with an equilibration time of 3 minutes.

Figures 2.37 and 2.38 show the overlaid spectra for the various solutions of ligand **57** with Eu^{III} using Method 2. Figure 2.37 shows the luminescent spectra obtained after 3 minutes equilibration, while Figure 2.38 shows the luminescent spectra obtained after 24 hours equilibration. As in the case of Method 1, the J = 2 is split into two peaks. However, the first

thing to note is that the spectra appear quite different, as the relative intensity of these peaks (splitting) are very similar, in contrast to those seen using Method 1, where the first peak in the $J = 2$ band was significantly more intense than the second. Furthermore, as for Method 1, the characteristic Eu^{III} emission spectrum, seen in Figure 2.37, consists of the transitions from $J = 1 - 4$, only. However, although weak in intensity, in the corresponding spectrum taken after 24 hours equilibration time the $J = 0$ band is visible. This suggests that the equilibration time plays a large part in the formation of the species observed in solution, and that possibly other self-assembly processes occur within this time frame. Such observations are commonly seen for larger helical systems such as those developed by Bunzli and Piguet, discussed in Chapter 1.

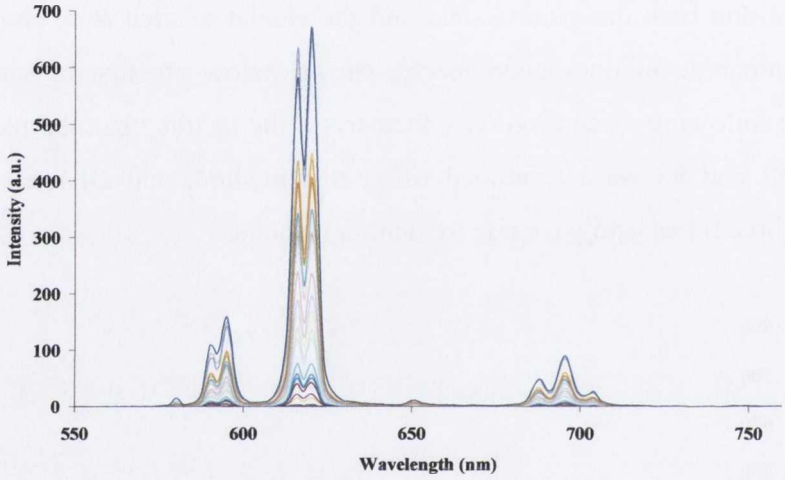

Figure 2.38 Overlaid luminescence spectra from the measurements of 57 (*S,S*) [1 x 10^{-5}M] with $Eu(CF_3SO_3)_3$ in $CH_3CN/CHCl_3$ (50:50, v/v), upon excitation at 281 nm. These measurements were performed using Method 2, with an equilibration time of 24 hours.

Figure 2.39 shows the overlaid profiles taken at 616 nm from the spectra in Figures 2.37 and 2.38. The profiles change dramatically between these equilibration times. The profile for the measurements recorded after 3 minutes shows very inconsistent increase in the luminescent intensity upon the increase in equivalents of Eu^{III}. However these were reproducible. In contrast, after equilibrating the solutions for 24 hours, these samples now show an increase in luminescence intensity that occurs in a steady manner. At present, we do not have an explanation for this behavior, which is strikingly different from that seen by using Method 1. It is worth mentioning, that using Method 1, always gave rise to reproducible results.

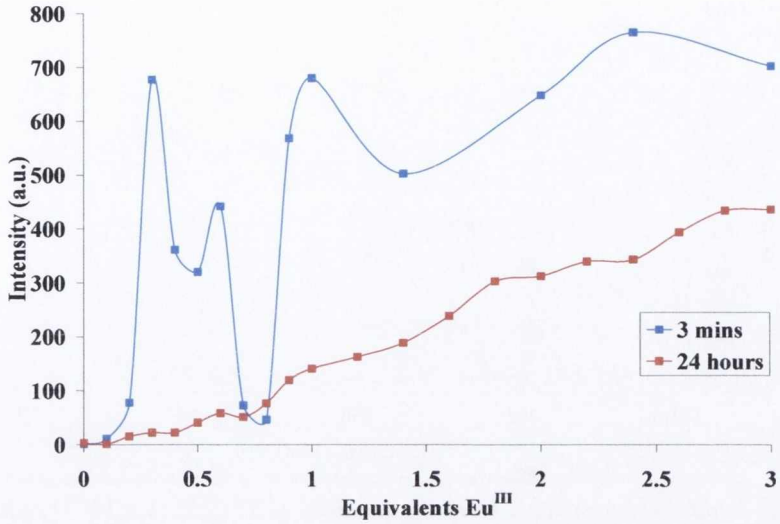

Figure 2.39 Titration profile of the change in intensity at 616 nm as a function of equivalents of Eu^{III}, from the titration of 57 (*S*,*S*) [1 x 10^{-5}M] with $Eu(CF_3SO_3)_3$ in $CH_3CN/CHCl_3$ (50:50, v/v), using Method 2.

Figures 2.40 and 2.41 show the overlaid emission spectra from the measurements of **57** with $Eu(CF_3SO_3)_3$ in CH_3CN. Again, the initial spectra, shown in Figure 2.40 is similar to that seen in the previous sections using Method 1. The relative intensity of the various transitions are similar to that observed before. However, after 24 hours equilibration the $\Delta J = 2$ transition appears significantly different (see Figure 2.41). Here, the general structure of the bands are similar to that seen in Figure 2.40, however, a new shoulder has appeared on the $J = 2$ band that was not observed before for this system using either Method 1 or 2. This suggests that the coordination sphere of the Eu^{III} metal ion has changed.

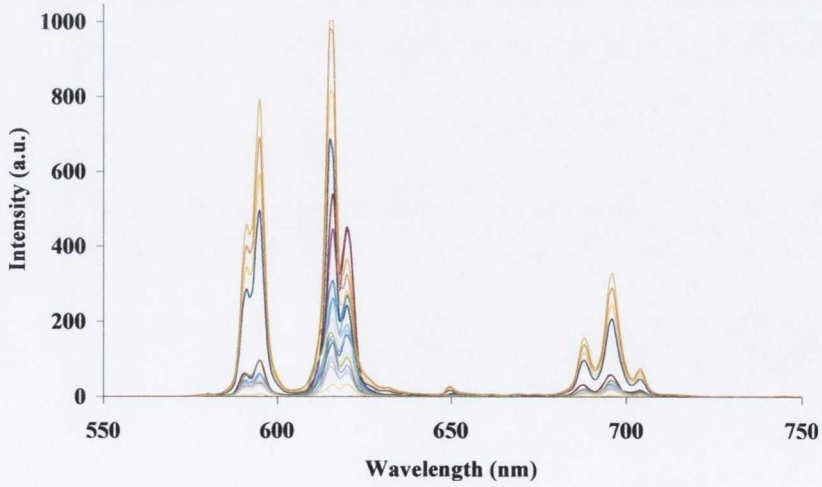

Figure 2.40 Overlaid luminescence spectra from the titration of 57 (*S*,*S*) [1 x 10^{-5}M] with $Eu(CF_3SO_3)_3$ in CH_3CN, upon excitation at 281 nm. This titration was performed using Method 2, with an equilibration time of 3 minutes.

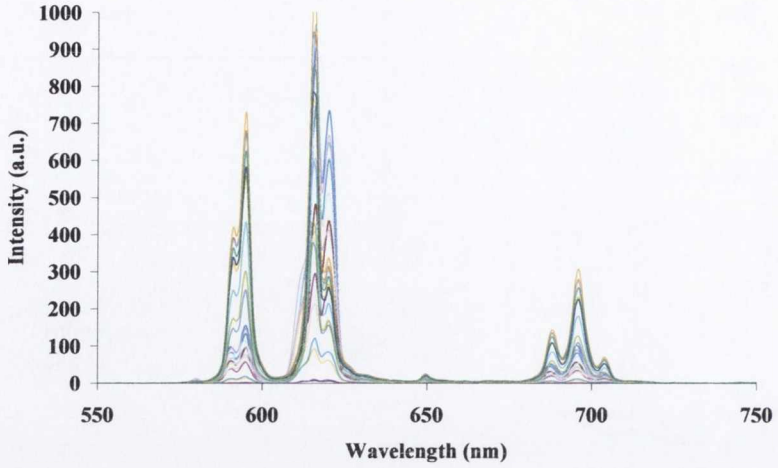

Figure 2.41 Overlaid luminescence spectra from the titration of 57 (*S*,*S*) [1 x 10^{-5}M] with $Eu(CF_3SO_3)_3$ in CH_3CN, upon excitation at 281 nm. This titration was performed using Method 2, with an equilibration time of 24 hours.

As before, the intensity of these different *J* transitions were analysed as a function of equivalents of Eu^{III}. Figure 2.42 shows the overlaid profile for the changes observed at 616 nm after 3 minutes, and 24 hours equilibration time, respectively. This time both profiles exhibit the inconsistent emission intensity with equivalents of Eu^{III}, unlike that seen in Figure 2.39. This suggests that the solvent also plays a major role in the self-assembly formation under these experimental conditions unlike that seen for Method 1. At present, it is not known why these results exhibit these strange profiles and consequently the data could not be fully analysed using SPECFIT. However, the results clearly indicate the complexity that such ligands can display and this phenomenon is under further investigation within the Gunnlaugsson group.

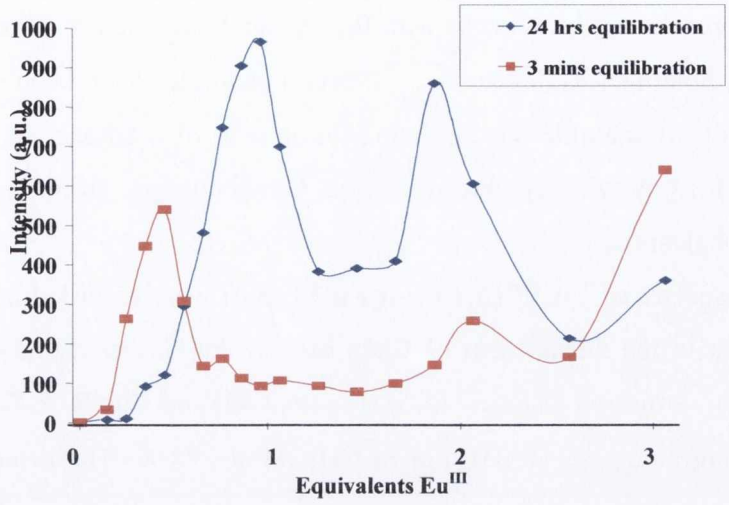

Figure 2.42 Titration profile of the change in intensity at 616 nm as a function of equivalents of Eu^{III}, from the titration of 57 (*S,S*) [1 x 10^{-5}M] with $Eu(CF_3SO_3)_3$ in CH_3CN, using method 2.

Before this Chapter is concluded, one more method was used to analyse the complexes **Eu.57** and **Eu.58** formed in Section 2.1, which involved the use of CPL studies of these two complexes in methanol and the results are presented in the following section.

2.4.7 Circularly polarized luminescence Studies

Circularly polarized luminescence (CPL) is the different emission of right circularly polarized light *vs* left circularly polarized light by chiral molecules. The principal information gained from CPL spectroscopy is the emission circular intensity differential" (ECID) which is calculated using Equation 2.7:

$$\Delta I(\lambda) = I_L(\lambda) - I_R(\lambda) \qquad \textbf{Equation 2.7}$$

Where $I(\lambda) = I_L(\lambda) + I_R(\lambda)$ and I_L and I_R denote the Intensity of the left (L) and right (R) circularly polarised components of the emitted radiation. CPL probes the chiral geometry of the excited states in the same way that CD probes the ground state structures. Secondly, CPL measurements also reflect molecular motions and energetics that take place between the excitation (absorption) and emission.[23]

CPL can be a very useful tool although it is still under development in the area of chiral lanthanide-based probes. Recently Parker and Peacock *et al.*[129] developed a Tb^{III} and Eu^{III} complex where the helicity of the (*SSS*)-Δ was inverted on reversible binding to 'drug site II' of serum albumin, which was signalled by a switch in its circularly polarised luminescence

emission. This behaviour did not occur with the (*RRR*)-Λ complexes. Therefore, a chiroptical probe of albumin binding was developed.[129] Several examples have been shown by Müller *et al.*[130-133] using CPL to examine the binding environment of a lanthanide centre for use in a chiral probe, and as previously described the Gunnlaugsson group have also used this technique in the analysis of

The CPL spectra of **Eu.57** (*R,R*) and **Eu.58** (*S,S*) were recorded in collaboration with Dr. R. D. Peacock in the Department of Chemistry at the University of Glasgow. The CPL spectra and the Eu^{III} emission of **Eu.57** (*S,S*) (Figure 2.43) and **Eu.58** (*R,R*) (Figure 2.44) were measured following a $\lambda_{excitation}$ at 310 nm in CH_3OH at 298 K. The detection of these CPL signals for both complexes confirms the presence of stable, chiral, emitting species on the luminescence time-scale. These Figures show that these two complexes were chiral, where the *J* transitions are of equal and opposite sign, as shown for clarity in Figure 2.45, showing that they are a pair of enantiomers, confirming that observed previously in the CD spectrum, a measure of the ground state chirality.

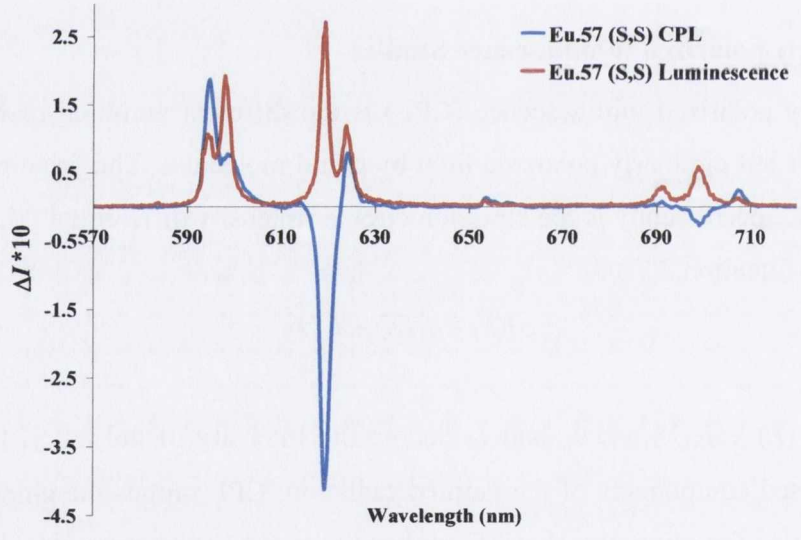

Figure 2.43 CPL and Eu^{III} emission spectra of Eu.57 (*S,S*) 1 x 10^{-5} M in CH_3OH at 298.2 K, $\lambda_{excitation}$ = 310 nm.

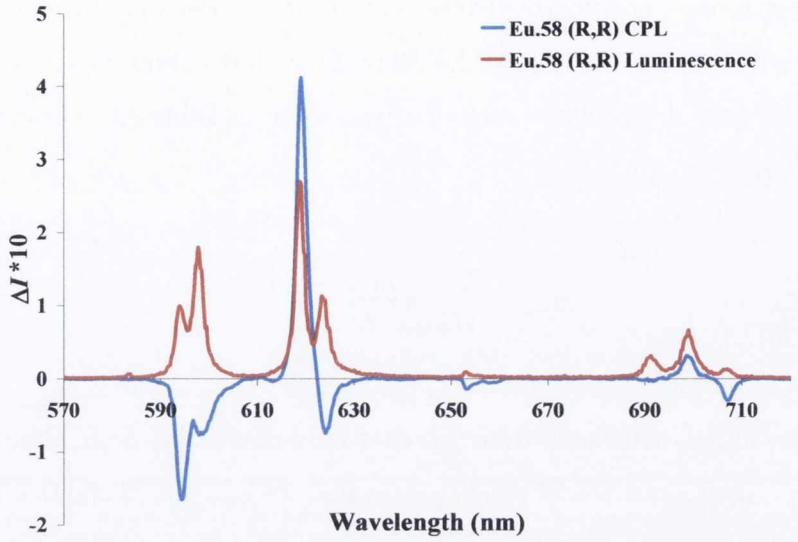

Figure 2.44 CPL and Eu^{III} emission spectra of Eu.58 (*R,R*) 1 x 10^{-5} M in CH_3OH at 298.2 K, $\lambda_{excitation}$ = 310 nm.

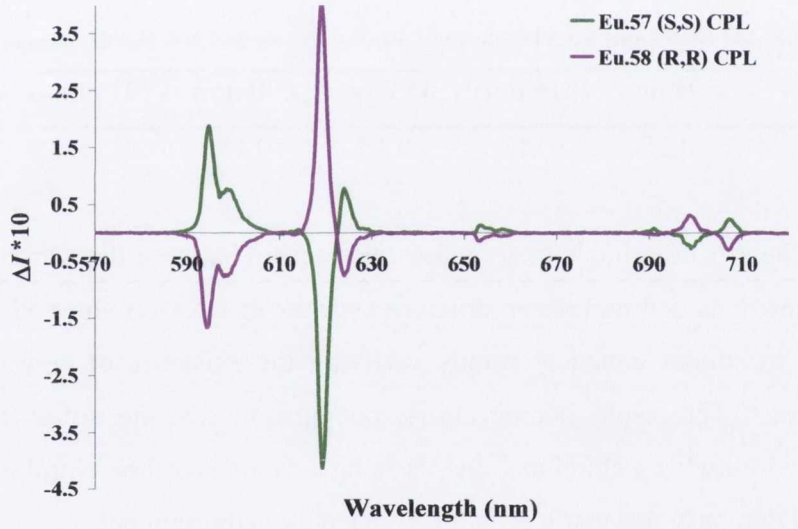

Figure 2.45 Composite CPL spectra of Eu.57(*S,S*) and Eu.58(*R,R*), 1 x 10^{-5} M in CH_3OH at 298 K, $\lambda_{excitation}$ = 310 nm.

The sign and magnitude of a CPL signal is affected by the degree of helical twist of the complex and the nature of the coordination of the ligand about the metal centre.[132] The observation of mirror images of the CPL signals (Figure 2.45) from **Eu.57** (*S,S*) and **Eu.58** (*R,R*) show that the emitted light is polarized in a direction determined by the helicity of the Eu^{III} ion which is in turn controlled by the absolute configuration of the chiral antenna. All of

the $^5D_J \rightarrow {}^7F_J$ transitions were clearly visible, with the $J = 2$ transition being the most intense. They also show that both **Eu.57** (*S,S*) and **Eu.58** (*R,R*) are homochiral in solution.

The signals gave dissymmetry factors of g_{lum} listed in Table 2.6. These were calculated using Equation 2.7.

$$g_{lum} = \frac{2\Delta I}{(I)} = \frac{2(I_L - I_R)}{I_L + I_R} \qquad \textbf{Equation 2.7}$$

The values of g_{lum} calculated from this data were reasonably high, although not as high as those found for **Sm.53** and **Sm.54** which gave values of g_{lum} = 0.28 and 0.5 for 600 and 560 nm respectively.

Table 2.7: g_{lum} values for Eu.57 and Eu.58 from the CPL data recorded in CH_3OH, $\lambda_{excitation}$ = 310 nm.

	595 nm	616 nm	653 nm	699 nm	707 nm
g_{lum}	-0.25	-0.11	-0.15	-0.18	-0.15

To date there is no reliable quantitative relationship between the sign or magnitude of g_{lum} for Eu^{III} transitions and molecular structure and, for that reason, the CPL measurements are most useful in studies aimed at simply verifying the existence of pure enantiomers or racemic mixtures.[115] The results herein, clearly demonstrate that the self-assemblies formed from **57** and **58** with Eu^{III} are chiral and that these ligands transfer their chiral properties to the metal ion, which demonstrates that it is "sitting" in a chiral environment.

2.5 Conclusions

This Chapter discussed the synthesis, characterization and analysis using a variety of spectroscopic studies, of ligands **57** and **58** and their corresponding Eu^{III} complexes, **Eu.57** and **Eu.58** in organic media.

The synthesis of ligands **57** and **58** was based upon that of their predecessors **53** and **54**. A peptide coupling reaction was used to link the chiral substituted naphthalene moiety to the central DPA derivative, the binding coordinating unit for the lanthanide metal. These ligands were characterized using mass spectrometry, NMR, and circular dichroism studies, the latter

two of which confirmed that the chirality of the ligand. The corresponding Eu^{III} and Tb^{III} complexes were synthesised and characterized using NMR, mass spectrometry, and circular dichroism studies. While the ^1H NMR of the Eu^{III} complexes were broad due to the paramagnetic nature of the lanthanides, and not much shifted in comparison to the ligand's NMR, the Tb^{III} complex gave rise to large changes in the NMR and demonstrated the formation of a single species with high symmetry in solution. Mass spectrometry confirmed the formation of the main species in solution as the ML_3, where three ligands wrap around a single metal ion. CD studies of these complexes confirmed that the chirality of the ligands was maintained upon formation of the ML_3 complexes.

^1H NMR titration of **57** with Eu^{III} showed the formation of the metal complex in solution, and that this was in slow exchange on the NMR timescale. Furthermore, it showed changes beyond 0.3 equivalents of the ion, where the formation of a single species was only confirmed after the addition of 3 equivalents of Eu^{III}. These studies were carried out at high concentration, [**57**] = 1 x 10^{-3} M in comparison to the luminescence titrations. This suggests that using NMR, a large excess of Eu^{III} is required to fully form a complex with the ligand, or possibly that other self-assembly processes can occur in competition with the 1:3 self-assembly formation. Unfortunately, the ^1H NMR of the Tb^{III} analogue, **Tb.57** was shifted so dramatically that it was not possible to fully assign the peaks and so a titration was not attempted.

The UV-Visible and luminescence behavior of isomers **57** and **58** was evaluated by studying the metal ion complexation in $CH_3CN/CHCl_3$ (50:50, v/v) and CH_3CN solution. The measurements were carried out using two different methods, conventional titration method (Method 1) dilution method, and Method 2; the mole fraction method. The results from the dilution method are reported extensively in Section 2.4, and they demonstrate the successful formation of the desired ML_3 systems. The data fits, and stability constants that were calculated from these titrations indicate that overall, the *S* isomer forms more stable species in solution than the *R* isomer. However, both isomers give similar log β_{13} values so even though the *S* isomer is more stable, it is not significantly so.

The use of two different solvent systems was designed to assess whether or not the polarity of the solvent system changed the complexation process. Although slight variations were noticed between solvent systems, the log β_{13} values obtained were very similar in these two solvent systems, and were approximately, log β_{13} = 20. This indicates that although there

were small local differences noted between titrations in different solvents, overall there was no significant effect. This stability was confirmed by carrying out competitive measurements using EDTA as a scavenging ligand. Comparing this result with the values of log β_{13} in CH_3CN for ligands **51** and **52**, (log β_{13} = 19.7 and 19 respectively) we can see that the value observed for 57 and 58 were slightly higher. Although all of these ligands are based upon the same motif of a central pyridine moiety functionalized at the 2,4, and 6 positions it appears that the addition of the hydroxyl group allows the formation of a resonance structure which may increase the basicity of the pyridyl nitrogen and so increases the binding constant.

Job's method of continuous variations (Job's plots) was also used to examine the stoichiometry of the most luminescent complex formed between **57** or **58** and Eu^{III} in $CH_3CN/CHCl_3$ (50:50, v/v) and CH_3CN solutions. Metal: Ligand stoichiometries of 1:4 and 1:3 were found in $CH_3CN/CHCl_3$ (50:50, v/v) and CH_3CN solutions, respectively.

Method 2 used to examine the complexation behaviour of ligands **57** and **58** with Eu^{III} in solution gave reproducible, but highly unusual results. The spectra obtained were different to those from the titrations carried out using Method 1, and their corresponding profiles gave results that could not be fully analysed using SPECFIT. However, these unusual results are currently under further investigations.

Finally, CPL studies of the complexes **Eu.57** and **Eu.58** were undertaken. These showed that the complexes not only retained the chirality of the ligands, but also gave rise to chiral luminescent signals which confirms that they are present as stable homochiral species in solution, and that the ligand conferred its chirality to the metal centres.

In summary, it is possible to conclude from the observations examined in this Chapter, that ligands **57** and **58** form stable, 1:3 (M:L) complexes with Eu^{III}. No crystal structures have been successfully isolated as yet, so this cannot be definitively proven. The formation of the 1:3 complex is affected by the timescale of the experiment as observed by utilising two methods for these titrations, by the concentration of the ligand and metal in solution (as observed from the ^1H NMR titration), and somewhat by the chirality of the ligand. However no significant effect is observed resulting from the polarity of the solvent system.

2.6 Future Work

The work reported so far, within this chapter is a useful step towards understanding how this ligand behaves. By functionalising the hydroxyl group with for example, a peptide chain, it would allow for its use as a probe for biological functions. This work is currently

being undertaken in the Gunnlaugsson group. A short summary of the most recent developments is shown below.

To achieve this aim, 4-chloro-pyridine-2,6-dicarboxilic acid bis-[(1-naphthalen-1-yl-ethyl)-amide], **59** (*S*,S) and **60** (*R,R*) analogues of **57** and **58** were synthesised by Elena Pazos Chantrero, a visiting PhD student in the Gunnlaugsson group (synthesis shown in Scheme 2.3). Ligand **57** or **58** was dissolved in $SOCl_2$ and DMF, and the reaction was heated at 80 °C for 1 h and then the solvent was removed. The crude product was purified by column chromatography.

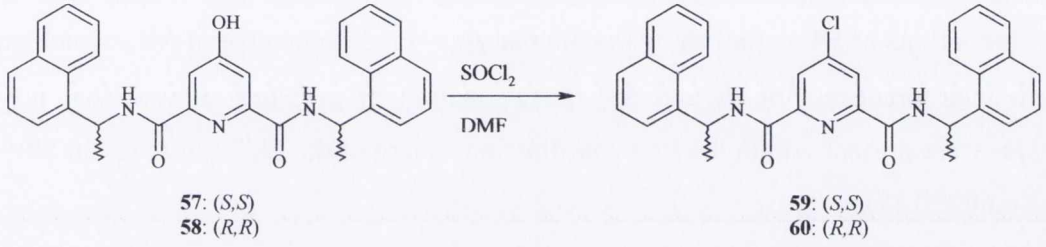

57: (*S,S*)
58: (*R,R*)

59: (*S,S*)
60: (*R,R*)

Scheme 2.3: Synthesis of chiral ligands 59 and 60, from 57 and 58.

Ligands **59** and **60** were complexed with Eu^{III} to form ML_3 complexes in the same manner as **57** and **58**. The ligands and their Eu^{III} complexes were characterised in the usual manner.

CD studies of **Eu.59** and **Eu.60** (Figure 2.46) indicate that the chirality of the ligand was maintained upon complexation. The CD spectra of ligands **59** and **60,** exhibit similar peaks to those of **57** and **58** (see Section 2.1.5). The CD of **59** (*S,S*) shows one main peak centred at 243 nm with a shoulder at 285.5 nm, and corresponding negative peaks for **60** (*R,R*), in a manner comparable to that of **57** and **58**.

However, the CD spectra of complexes **Eu.59** and **Eu.60** are markedly different to those of **Eu.57** and **Eu.58**. The CD spectrum of **Eu.57** has one large positive band at 249 nm, with a negative band centred at 301 nm, with a shoulder at 270 nm. Conversely, the CD of **Eu.59** exhibits its main peak at 240 nm with a shoulder at 255nm, and a single negative band at 325 nm. It is interesting that the two molecules, while appearing very similar, should bring about such different spectra. Clearly the presence of the Cl instead of the OH moiety on the back of the central pyridine ring has a substantial effect on the chiral environment about the Eu^{III} centre. The spectrum of **Eu.60** is a mirror image of **Eu.59**.

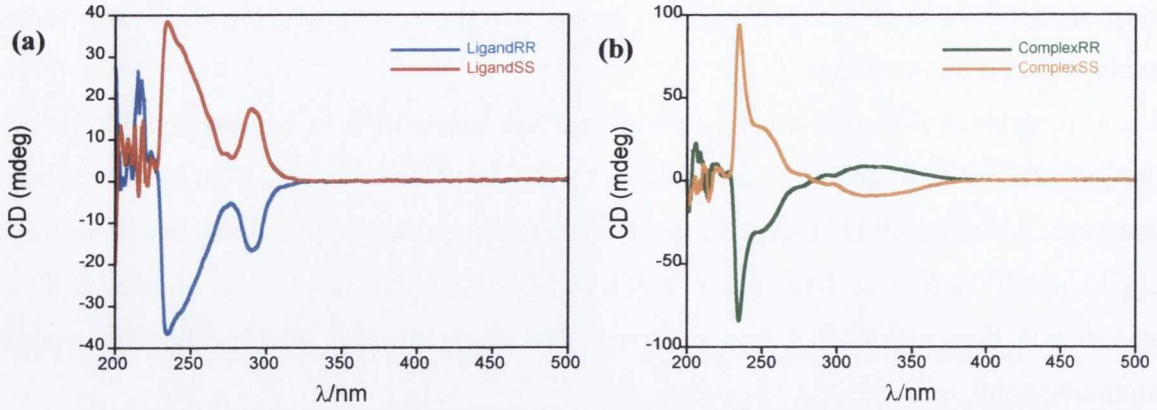

Figure 2.46: (a) CD spectra of ligands 59 and 60, (b) and their Eu^{III} complexes Eu.59 and Eu.60, in CH_3CN.

Job's Plots of **59** and **60** show maxima at $\chi_{Eu} = 0.25$, indicative of ML_3 stoichiometry. As with their predecessors **57** and **58**, the evaluation of q-values showed that no water molecules were present within the first coordination sphere of the Eu^{III} centre (q **Eu.59** = 0.13, and q **Eu.60** = 0.12).

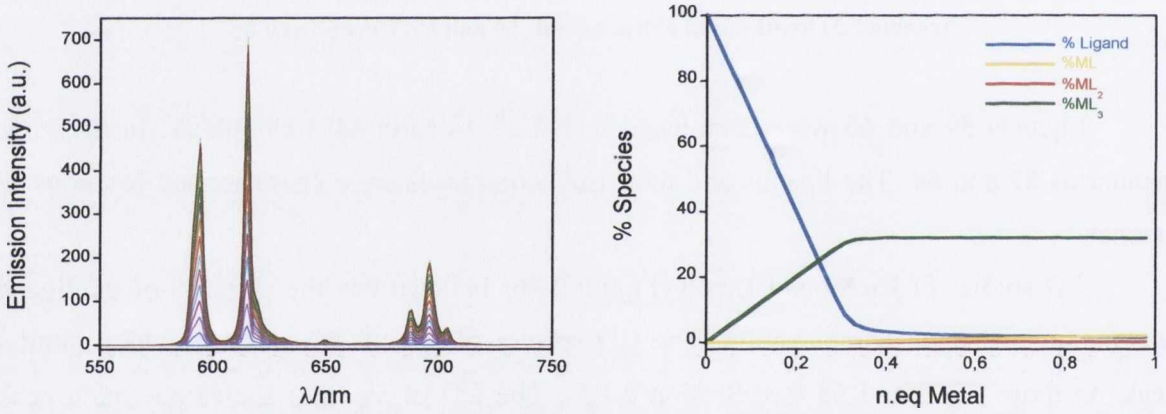

Figure 2.47: (a) Overlaid luminescence spectra from the titration of 59 (*S,S*) with $Eu(CF_3SO_3)_3$ in CH_3CN. (b) Speciation Diagram for the titration of 59 (S,S) with $Eu(CF_3SO_3)_3$ in CH_3CN.

Luminescent titrations of **59** (*S,S*) with Eu^{III} (Figure 2.47), resulted in a characteristic Eu^{III} spectrum with transitions $J = 1$ - 4 visible at 595 nm, 616 nm, 653 nm, and 695 nm, respectively. The titration profile revealed a plateau at 0.3 equivalents of Eu^{III}, and the corresponding speciation diagrams show the existence of three species in solution, with the predominant species being EuL_3. These titrations were carried out in CH_3CN. The titration for **60** (*R,R*) gave the same results. The UV-Visible and luminescent spectra from the titration of **53** with $Eu(CF_3SO_3)_3$ in CH_3CN are shown in Appendix, **A4**, **A5**, **A6**, and **A7**. The band at 616 nm, corresponding to the $J = 2$ transition has the same shoulder as that of **59**. This is in contrast to what is seen with ligand **57** and **58**, where two distinct peaks are observed. This

change in the shape of the $J = 2$ band indicates that the binding environment around the Eu^{III} has changed, further proof that the hydroxyl group at the 4 position on the central pyridyl unit affects the binding.

These results clearly compliment the work carried out in this Chapter, and clearly demonstrate the use of lanthanide directed synthesis of self-assembly complexes is highly attractive. It is hoped that in the future, functionalisation of the basic template with various functionalities such as a short peptide, will open up a route to the formation of a novel chiral, and potentially biologically mimicking, and bio-compatible lanthanide-based probes and self-assembly structures.

Chapter 3
Lanthanide-based Sensors on Gold: From Flat Gold to Functionalised Cantilevers

3. Lanthanide-Based Sensors on Gold: From Flat Gold to Functionalised Cantilevers

3.0 Introduction

Lanthanide-based systems make an excellent choice for use in supramolecular devices, such as luminescent sensors and switches, as discussed in Chapter 1.[15, 16, 28, 29, 37-39] While lanthanide based devices have been extensively studied in solution (e.g. Scheme 3.1, **Step 1**), or in soft materials, such as in hydrogels,[55] there are other supports such as nanoparticles[14] and various solid substrates that also offer an attractive means of immobilising these systems in order to form practical devices (Scheme 3.1, **Step 3** and **4**). However these have not been much explored to date. There are many advantages in developing such immobilised systems in contrast to solution-based systems. For instance, incorporating lanthanide-based sensors in, or immobilising them on solid substrates, could potentially make a highly sensitive detection device, and give rise to high population and hence, high local concentration which could allow for a much greater concentration of sensor species than would in general be present when in solution, as it is in an ordered assembly. It also allows for "wash-over" of the analyte for use in continuous monitoring such as in a flow cell.

Gold is an ideal surface to use as a model as it is relatively easy to form flat surfaces. Thiols on gold have been extensively researched, and are known to form well-defined and ordered monolayers.[78] Hence by conjugating lanthanide complexes using an alkyl thiol linker, the complex could be incorporated onto a solid surface. Extending this idea another step, incorporating an optical sensor with another type of sensor, such as a mechanical microcantilever sensor, would further allow for the possibility of creating a dual functioning, and self-verifying sensor using such lanthanide systems.

As previously discussed in Section 1.2.2.3, some research has been carried out within the Gunnlaugsson group by Dr. Massue, into incorporating a lanthanide-based sensor, **Eu.29**, onto gold nanoparticles (Au-NPs).[14] It was hoped that since this system had already been researched in solution and on Au-NPs, that we could further build upon this work and develop it for use on flat solid substrates. Using Scheme 3.1, **Step 1** is dealt with in the first section of this chapter, which discusses the results previously obtained by Dr. Massue a member of the Gunnlaugsson group, who examined the behavior of **Eu.29** in solution.[14] **Step 2**, also done by Dr. Massue, involved synthesising gold nanoparticles and attaching **Eu.29**, the results of

which are discussed briefly next.[14] This is followed by **Step 3**, an examination of **Eu.29** on a flat gold substrate, the subject of the current study.

This chapter is designed as a "proof of principle" study to show that **Eu.29** retains its properties when immobilized on a gold substrate and as such none of the experiments described in this chapter give quantitative data. To the best of the author's knowledge, this is the first time that lanthanide luminescence has been observed on a gold substrate. Finally, preliminary results of **Step 4** will be discussed at the end of the chapter.

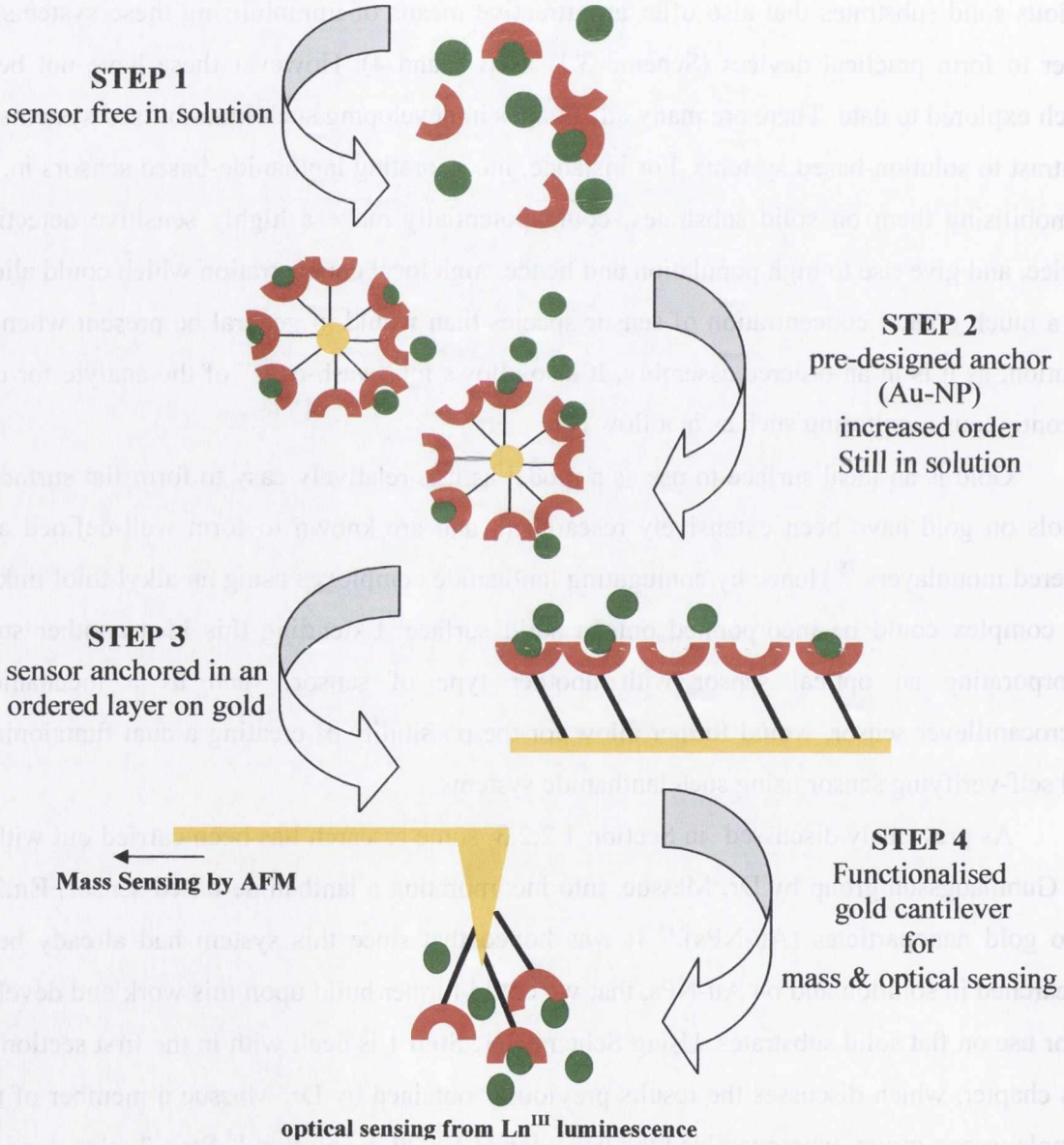

Scheme 3.1 Development of Eu.29 from solution to substrate.

Red shapes = Eu.29, green circles = antenna, 30.

3.1 Studies of Eu.29 in solution – STEP 1

3.1.1 Synthesis of Complex Eu.29

Complex **Eu.29** was synthesised by a method developed in the Gunnlaugsson group,[134] by initially forming **62** (as shown in Scheme 3.2). The remaining six amines of the cyclen macrocycle were alkylated in $CHCl_3$ using 2-chloro-*N,N*-dimethylacetamide, followed by reduction of the disulfide moiety using excess $NaBH_4$. Ligand **29** was obtained in 52% yield after precipitation from Et_2O. The Eu^{III} complex **Eu.29** was formed by refluxing **29** with 1.1 equivalents of $Eu(CF_3SO_3)_3$ overnight in CH_3CN. Analysis by ^1H NMR confirmed the formation of the paramagnetic complex **Eu.29**, and elemental analysis was consistent with the formation of **Eu.29** in which two water molecules were bound to the metal ion centre. The hydration state, q, was further confirmed by measuring the excited-state lifetimes of **Eu.29** in H_2O and D_2O, which gave $\tau_{H2O} = 0.39$ ms and $\tau_{D2O} = 0.89$ ms and $q \approx 1.5$, upon excitation at 396 nm, which was also consistent with two water molecules bound to the metal ion centre.[14]

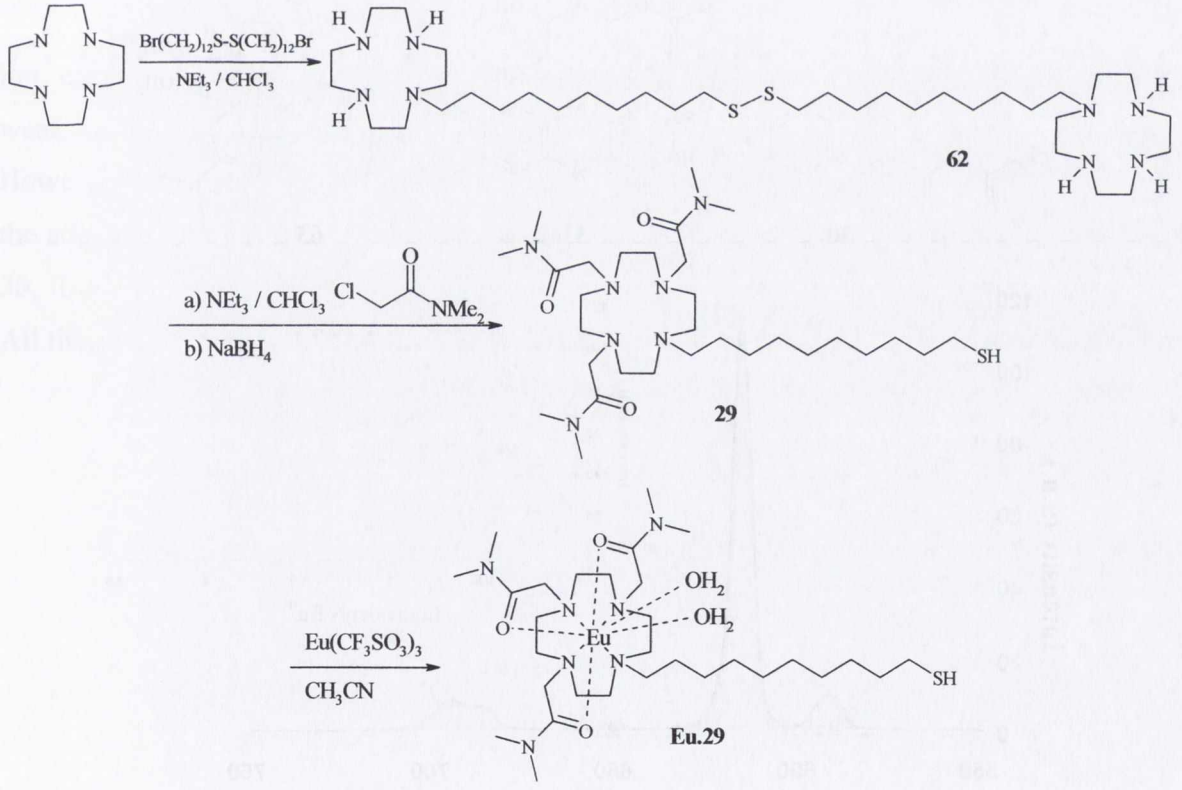

Scheme 3.2 Synthesis of Eu.29

3.1.2 Photophysical Studies

The complex **Eu.29** was based upon a design previously explored within the Gunnlaugsson group, **63**.[135] Figure 3.1 shows the results of the titration performed by Dr. Massue, of **Eu.29** with **30** a β-diketonate antenna. A characteristic Eu^{III} spectrum was observed with bands centred at 595 nm, 616 nm, 650 nm, and 695 nm, corresponding to $J = 1 - 4$, the bands for the deactivation of the $^5D_0$ excited state to the ^5F_J. The corresponding titration profile, inset in Figure 3.1, shows the change in intensity at the 616 nm transition *vs* equivalents of **30**. The diketonate moiety displaces the metal-bound water molecules and so removes their quenching effects, as well as populating the Eu^{III} excited state very effectively *via* indirect excitation, and so switches "*on*" the Eu^{III} emission. The titration profile shown as an inset in Figure 3.1 shows that **30** binds to **29** in a 1:1 stoichiometry. The titration was carried out in the presence of 0.1 M HEPES buffer at pH 7.4, to simulate physiological conditions.

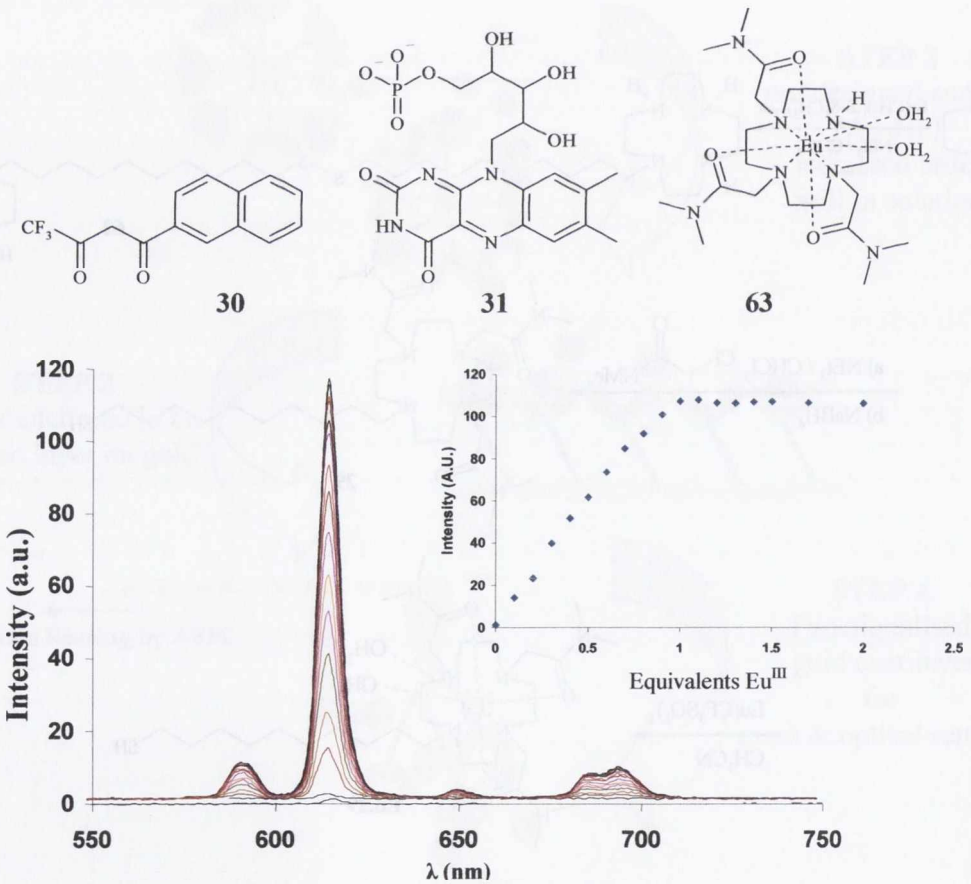

Figure 3.1 This spectrum shows the changes in the Eu^{III} emission of Eu.29 in the presence of 30 at pH = 7.4 (0.1M HEPES), in the presence of 0.1M TMACl and inset is a plot of the change in relative intensity upon the addition of 30, showing the emission being switched "*on*".[14]

The behaviour of this complex in solution was found to be the same as that observed for the analogous complex **Eu.63**. Once the behaviour of complex **Eu.29** had been established in solution, it was then immobilised onto gold nanoparticles and more measurements carried out by Dr. Massue to determine its behaviour in this environment. The results of this work are summarised in the next section.

3.2 Studies of Eu.29 on nanoparticles - STEP 2

3.2.1 Synthesis of Eu.29 on Nanoparticles

The nanoparticles were synthesised by means of two-phase Brust[136] method followed by the methods of Caruso *et al.*[137] and Lennox *et al.*,[138] which gave DMAP stabilized gold nanoparticles. The AuNPs were functionalised with **Eu.29** by exchanging the DMAP by stirring for 12 hours at room temperature. Any unbound **Eu.29** was then removed using Sephadex G15® size exclusion chromatography.

3.2.2 Photophysical Studies

These nanoparticles were not luminescent as there was no means to sensitise the Eu^{III} ion, except than by direct excitation of the Eu^{III} centre at 395 nm, which only gave rise to weak luminescence due to the effect of the OH quenching of the metal-bound water molecules. However, sensitisation was achieved using the same strategy as for the free complex **Eu.29** by the addition of the antenna **30**, and formation of a self-assembly. By exciting into the antenna, **30**, the Eu^{III} emission was 'switched on' and this was monitored by luminescence titrations. All titrations were done in buffered aqueous solution at pH 7.4.

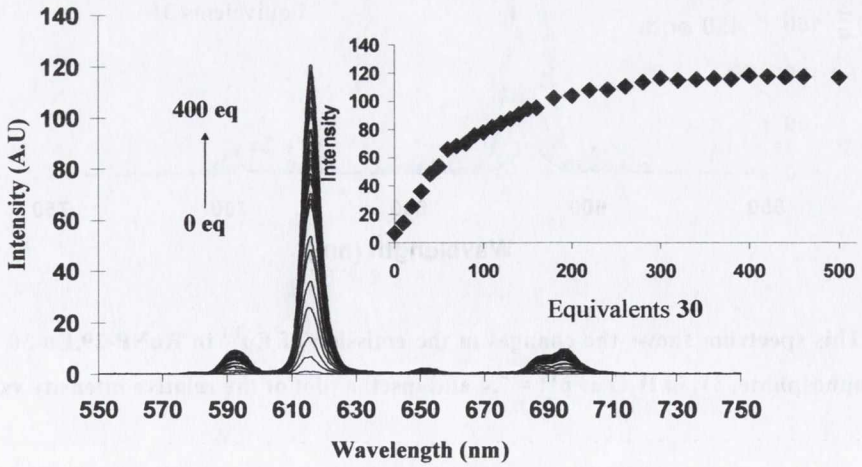

Figure 3.2 The changes in the Eu^{III} emission of AuNP-29.Eu (0.2 μM) upon titration with antenna 30 in H_2O at pH = 7.4 (0.1 M HEPES) with *Inset*: the changes in intensity at 616 nm *vs.* equivalents of 30.[14]

Upon addition of **30**, the hypersensitive $J = 2$ transition, centred at 616 nm, gave rise to the greatest changes in the Eu^{III} emission (see Figure 3.2). This is indicative of the direct coordination of the antenna to the Eu^{III} centre and the displacement of the two metal bound water molecules. The binding isotherm for the formation of **AuNP-29.Eu-30** is shown as an insert in Figure 3.2. Since the binding is in a 1:1 stoichiometry between each gold conjugated **29.Eu** and **30**, it was possible to estimate the number of bound Eu^{III} complexes per **AuNP** to be *ca.* 250.

The complex **30** was then investigated for use as a sensor for biologically relevant molecules. A selection of anions were tested by Dr. Massue using luminescence titrations, however the most effective was found to be flavin monophosphate, **31**, which plays a key role in many electron transfer, oxidation and dehydrogenation processes in the body. This anion was observed to effectively displace **30** from **AuNP-29.Eu-30** (shown in Figure 3.3). The displacement of **30** was monitored as a function of the decrease in emission upon addition of **31**, as **31** is not capable of sensitising Eu^{III}. Approximately 250 equivalents of **31** were required to fully '*switch off*' the luminescence. The binding constants for this recognition have been dertemined by using a modified Stern-Volmer equation.

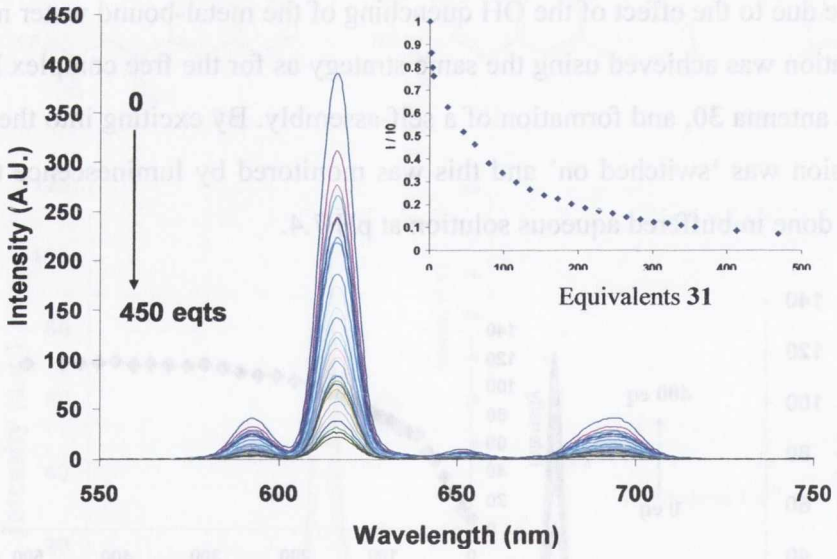

Figure 3.3 This spectrum shows the changes in the emission of Eu^{III} in AuNP-29.Eu-30 in the presence of flavin monophosphate, 31, in H_2O at pH = 7.4 and inset, a plot of the relative intensity vs. equivalents of 31 added.[14]

Although the results obtained from these studies showed very interesting and promising results, in order to create a functional sensor, it is desirable to have it immobilised

on a solid substrate. To this aim, it was decided to attempt to immobilise **Eu.29** onto a flat solid substrate, and evaluate the photophysical properties of the resulting assembly. The remaining part of this Chapter deals with results from this investigation.

3.3 Studies of Eu.29 on a Flat Gold Substrate – STEP 3

3.3.1 Preparation of Gold substrates and the Incorporation of Eu.29 onto a Flat Gold Substrate

Progressing along the path towards the ultimate aim of immobilising **Eu.29** onto the surface of a cantilever (**Step 4**), it was decided to conduct the surface studies on another flat substrate before any attempts were made to functionalise a cantilever, which we wished to examine by using simultaneous luminescence and mechanical sensing by an atomic force microscope (AFM) (**Step 3**). The preliminary measurements were conducted on samples of gold evaporated onto mica discs. Mica gives an atomically flat surface upon cleaving, and so is a good starting point for evaporation of gold. This approach was taken for a number of practical reasons. Firstly, it was easier to study samples with a large surface area such as those made using the mica sheets, than the small surface area of a microcantilever, using a fluorimeter. Secondly, cantilevers are quite expensive while mica is inexpensive. Using samples of gold evaporated onto mica allowed for the study of a model system with a view to understanding the photophysical behavior of the luminescent lanthanide complexes on a simple surface, before transferring the technique to a microcantilever. To the best of the author's knowledge, the simultaneous use of lanthanide luminescence and AFM mechanical sensing has never been demonstrated.

Self-assembled monolayer (SAM) formation involves a sequence of several structural phase transitions,[139] which are demonstrated schematically in Figure 3.4.

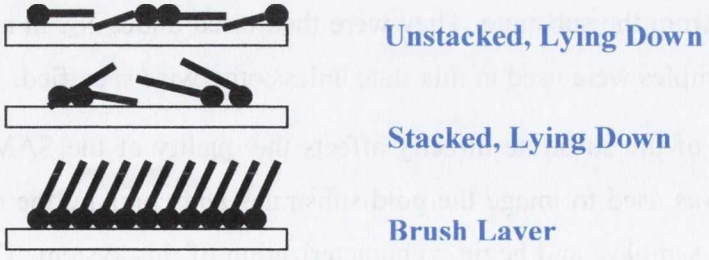

Figure 3.4 The three principle stages of self-assembly of a monolayer

Generally, at low concentration, the resulting SAM structure has the alkane chains lying down parallel to the surface. This is a rapid process, followed by the second much

slower process of the transition to an ordered brush phase,[140] characterised by the transition from lying-down phase to the stacked lying phase, before reaching the brush phase (other intermediate phases are not shown in Figure 3.4).

The standing-up phase for long-chain alkanethiols will generally not stand perpendicular to the surface, but at an angle. This is to reduce chain-to-chain separation and is driven by the chain's attractive intermolecular van der Waals interactions.[141] The optimal layer is a thin, uniform, and compact (to avoid interactions with the solid substrate beneath) layer of receptor molecules. When preparing a sensing device, the layer should be stable and robust, with the receptors covalently anchored to the surface while retaining enough freedom to interact with their specific ligand.[142]

Flat gold substrates were made by sonicating small discs (9 mm diameter) of mica in ethanol, and then evaporating a thin layer of gold (10 nm). Some of the samples were made by evaporating gold in an Auto 500 Edwards Electron Beam Evaporation System, and some were evaporated in a home-built thermal evaporation vacuum chamber. As mentioned before, immobilization on a substrate allows for a much higher concentration of sensor than would normally be used in solution. For example, a rough estimate of the number of Eu^{III} metal centres on a 9 mm disc of gold can be made. A typical thiol bond has a footprint of 22 $Å^2$. Since the approximate available surface area is 63 mm^2 = 63 x 10^9 $Å^2$, that allows for ~2.8 x 10^9 number of complexes, a number vastly in excess of what is used in solution measurements. For the experiments described in this Chapter, the gold samples were removed from the vacuum chamber and immediately immersed in 1 mmol solutions of **Eu.29**, **Eu.29-30** (1:1, **[Eu.29]**:**[30]**), and **Eu.29-30-31** (1:1:1, **[Eu.29]**:**[30]**:**[31]**), and then left overnight. When they were ready to be used, they were removed from the solution and rinsed thoroughly with ethanol. After this, it was assumed that a complete monolayer had formed and all excess thiol had been removed from the substrate. They were then dried under N_2. In all of the following experiments, the samples were used in this state unless otherwise specified.

The quality of the substrate directly affects the quality of the SAM,[143, 144] so atomic force microscopy was used to image the gold substrates and compare the clean gold and the functionalized gold samples, and begin a characterization of this system. This is discussed in the next section.

3.3.2 Atomic Force Microscopy Analysis of Eu.29 on Gold

In order to examine the surface structure of the samples used in this Chapter, they were imaged using an atomic force microscope. They were imaged in water, in contact mode, using silicon nitride cantilevers. The images obtained are displayed in Figures 3.5 and 3.6.

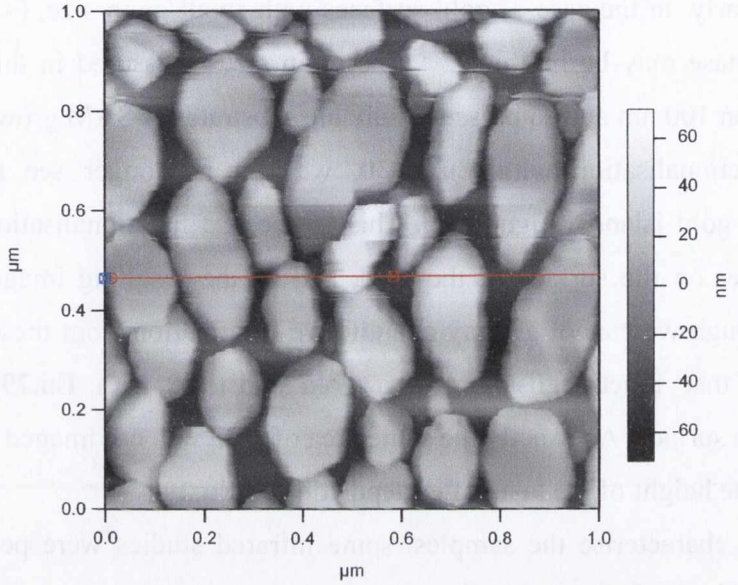

Figure 3.5 Sample of unfunctionalised gold evaporated onto mica. Imaged using AFM contact mode, in water.

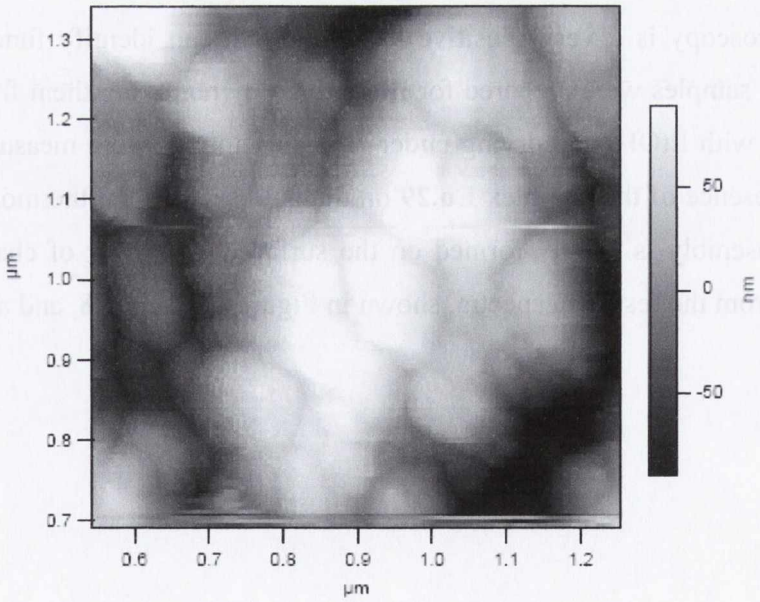

Figure 3.6 Sample of gold evaporated onto mica functionalised with Eu.29-30 [1 x 10^{-4} M] imaged using AFM in contact mode, in water.

The clearly defined shapes observed in Figure 3.5 are islands of gold formed when the gold cools after it is evaporated. The dimensions of these islands are dependent on the evaporation conditions, such as temperature, and pressure. It has been found that the formation and structure of a SAM is influenced strongly by the surface structure of the underlying gold substrate. Particularly, in the case of gold surfaces with small grain size, (<100 nm) the high coverage brush phase may be inhibited.[143] The grain sizes measured in this sample are, on average, larger than 100 nm and so present a suitable substrate for SAM growth.

Upon functionalisation with **Eu.29-30**, we can no longer see the well defined perimeters of the gold islands, Figure 3.6. This is because functionalisation with **Eu.29-30** creates a soft layer on the surface of the gold, and so the resulting image has a "cloudy" appearance. Although we cannot get any quantitative information from these images, we can qualitatively say that functionalisation of a gold substrate with **Eu.29-30** changes the morphology of the surface. As exactly the same area of gold was not imaged at both stages we cannot calculate the height of the layer after deposition of **Eu.29**.

To further characterise the samples, some infrared studies were performed, and the results are detailed in the following section.

3.3.3 Infrared Studies of Eu.29 on Gold

IR spectroscopy is a very sensitive technique that can identify functional groups in compounds. The samples were prepared for IR analysis by removing them from the particular solution, rinsing with EtOH, and drying under N_2. The samples were measured immediately, and show the presence of the complex **Eu.29** on the gold surface. Furthermore, upon addition of **30** the self-assembly is clearly formed on the surface. A number of characteristic bands were identified from the resulting spectra, shown in Figures 3.7 and 3.8, and are listed in Table 3.1.

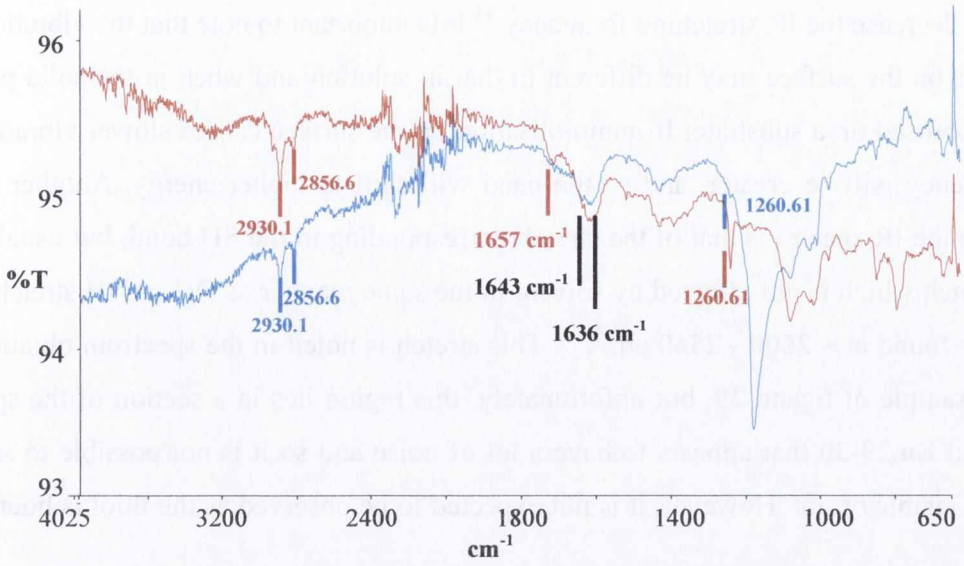

Figure 3.7 Infrared spectrum of Eu.29 (blue line) and Eu.29-30 (red line) immobilised on a gold sample.

The C=O stretch assigned to the carboxy amide for the complex **Eu.29** is at 1624 cm^{-1}, shifted down from 1644 cm^{-1} in the free ligand **29**. This is indicative of the direct binding of the C=O moiety in the complexation of the Eu^{III} to the ligand. There is also a clear stretch that corresponds to the C=O band for **Eu.29** on the gold sample, at 1636 cm^{-1}. Moreover, a new band is observed at 1657cm^{-1} upon formation of **Eu.20-30** on gold that may be due to the extra C=O groups from the antenna **30**, binding to the Eu^{III} centre.

Table 3.1 Peak assignments for ligand 29 and it Eu^{III} complex, Eu.29. The data for the KBr values are taken from the values listed in: Massue, J.; Quinn, S.; Gunnlaugsson, T.; *J. Am. Chem. Soc.* 2008, 130, 6900.

	Peak position cm^{-1}			
Vibrational Mode	**KBr 29**	**KBr Eu.29**	**Gold SAM Eu.29**	**Diamond IR Oil of Eu.29**
CH_2 (asymmetric stretching)	2927		2930	2920
CH_2 (symmetric stretching)	2855		2857	2881
S-H	2681			
C-C	1261	1255	1263	1266
C=O	1644	1624	1657	1638
CH (in-plane bending)	1069	1030	1034	1051
CH (out-of-plane bending)	782			784.5

One of the most useful bands to follow in this case was the carbonyl band of the amide, as it is directly bound to the lanthanide centre. Binding will increase the bond length, and

therefore decrease the IR stretching frequency.[54] It is important to note that the vibration of the molecules on the surface may be different to that in solution and when in the solid phase but not immobilised on a substrate. If immobilisation on the surface causes slower vibration, then the frequency will be greater, and so the band will shift to higher energy. Another defining feature in the IR spectra is that of the stretch corresponding to the SH bond, but usually it is a weak stretch which is not affected by solvent in the same manner as OH or NH stretches. This is usually found at ~ 2600 - 2550 cm^{-1}.[145] This stretch is noted in the spectrum obtained from the KBr sample of ligand **29**, but unfortunately, this region lies in a section of the spectra of **Eu.29** and **Eu.29-30** that appears to have a lot of noise and so it is not possible to say if the stretch is visible or not. However, it is not expected to be observed as the thiol is bound to the gold.

Furthermore, the asymmetric and symmetric CH_2 stretches from the alkyl thiol chain can be observed at 2930 and 2856 cm^{-1}, respectively and are shown in Figure 3.8.

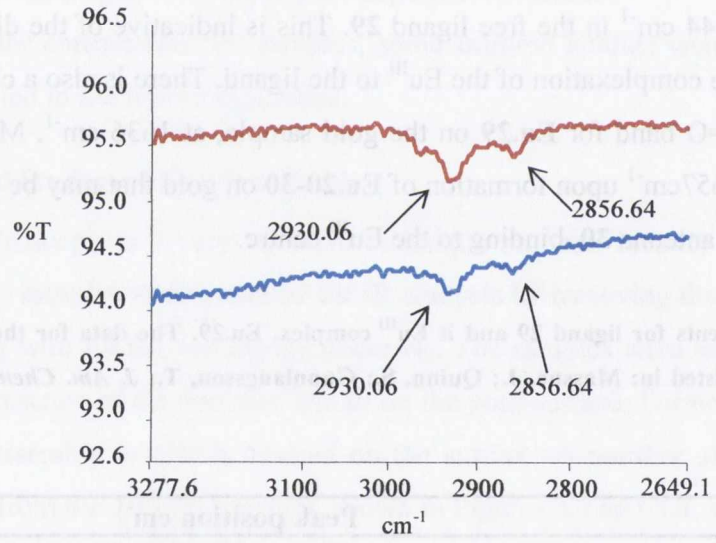

Figure 3.8 IR spectra of Eu.29 (blue line) and Eu.29-30 (red line) immobilised on a gold sample, between 3277.6 and 2649.1 cm^{-1} showing the CH_2 stretches from the alkyl chain.

From these results, we can conclude that **Eu.29** and **Eu.29-30** have been adsorbed onto the gold substrate. The next objective was to fully understand the photophysical properties of these complexes on the gold surface. These studies will help us to gain insight into the luminescent properties of the surface of these samples, and the results of these studies are shown in the next section.

3.3.4 Photophysical Studies of Eu.29 on Gold

Several photophysical measurements were performed on the samples prepared above, to determine if the behavior of **Eu.29** remained the same on flat gold subtrates as on nanoparticle and in solution. All measurements, unless otherwise stated, were taken in the absence of solvent. All measurements were performed at least twice, however they are qualitative and so the resulting trends observed were reproducible and that is what is described from here to analyse the behavior of complex **Eu.29** on a solid substrate.

In order to measure these samples in the fluorimeter, a home-modified fluorescence cell was used to hold the gold sample in the correct position in the beam and detector paths to optimise the luminescence output. The cell was fitted with a quatrz glass slide aligned so that it sat at a 90° angle to the beam path. Figure 3.9 shows a photograph and diagram of a functionalised gold sample in the home built fluorescence cell.

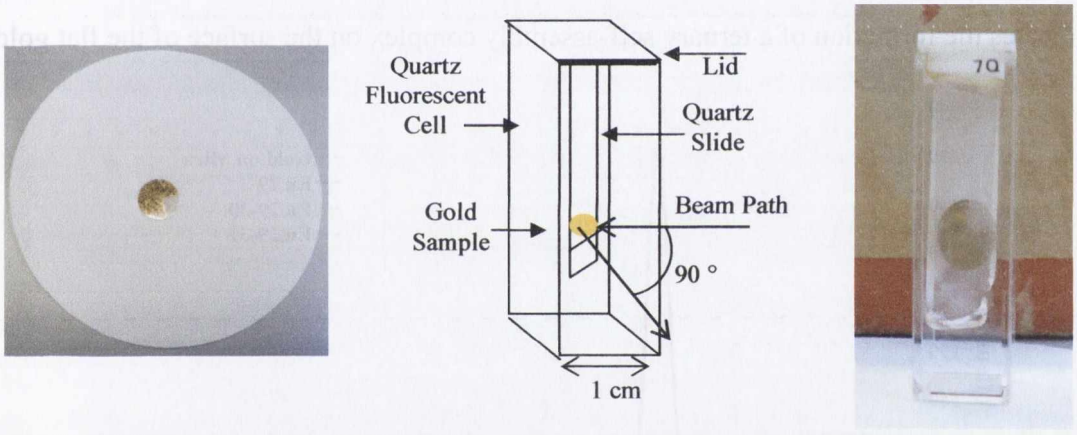

Figure 3.9 (a) Image of a gold sample. (b) Diagram and (c) Image of modified fluorescence cell holding a gold sample.

As a background test, a mica sample with a coating of gold was run in the fluorimeter, with excitation at 281 nm, and no emission was observed (see Figure 3.10). A band was present centred at 562 nm, however this corresponds to the second harmonic, $2\lambda_{excitation}$. Next, it was important to establish that it was possible to observe lanthanide luminescence on gold, as it has been previously reported that gold quenches lanthanide luminescence.[79] However, we proposed that our design might overcome this quenching as the complex **Eu.29** was synthesised with a C_{12} alkane chain linker between the cyclen head and thiol anchor. It was hoped that this chain would order the complex and keep it a sufficient distance from the surface to facilitate the lanthanide emission and hence prevent quenching. Although this complex had previously functioned on a nanoparticle, the spherical shape of the nanoparticles

help in distancing the Ln^{III} metal ion centre from the gold surface. This does not however, occur on a flat substrate, so it was not as obvious whether or not an emission would be detected after immobilisation onto the surface. To establish this, the phosphorescence emission spectra of the three complexes on gold *e.g.* **Eu.29**, **Eu.29-30**, and **Eu.29-30-31,** were recorded upon excitation at 281 nm, the maximum absorption wavelength of the antenna. The results are shown in Figure 3.10 and demonstrates that the lanthanide emission is indeed observed from the flat gold.

It is clear from Figure 3.10, that for these complexes an intense phosphorescence emission is only observed for the ternary complex **Eu.29-30**, where the line-like emission bands assigned to the deactivation of the Eu^{III} excited state $^5D_0 \rightarrow {}^7F_J$ (J = 1, 2, 3 and 4), at 595, 616, 685 and 700 nm, respectively, can be clearly seen. Here, just as in solution, the hypersensitive $J = 2$ is the most intense band visible in the spectrum. This transition is highly sensitive to the coordination environment of the metal ion. Therefore, this intense emission also indicates the formation of a ternary self-assembly complex on the surface of the flat gold.

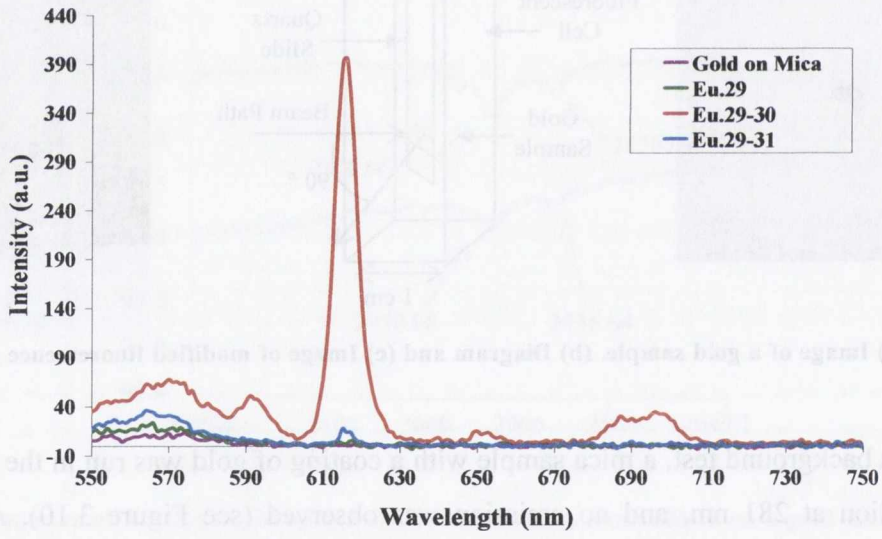

Figure 3.10 Plot of wavelength *vs* intensity of the phosphorescent emission of gold (purple line), the complex 29.Eu (green), the complex 29.Eu with two water molecules displaced by the β-diketonate antenna 30 (red), and the complex 29.Eu, with antenna, 30 displaced by riboflavin (blue) upon excitation at $\lambda_{excitation}$ = 281 nm.

As the *f-f* transitions of the lanthanides are shielded, no shifts are seen in the wavelength of the emission bands, therefore, immobilisation onto the gold substrate does not affect the emission pattern. In contrast to these results, no lanthanide emission was observed

from **Eu.29** when excited at 281 nm in the absence of **30**. However, a weak emission was observed at 616 nm from **Eu.29-31**. This example has a complex that fulfills the coordination requirements of the lanthanide ion, but lacks the ability to populate the lanthanide excited state. Consequently, one possible explanation for this weak emission is the incomplete displacement of the antenna which gives rise to the sensitisation of the Eu^{III} centre. However, it is important to point out that this is a very weak emission relative to the spectrum observed for **Eu.29-30**. These results are in good agreement with those previously observed with the same systems in solution and on nanoparticles.

In all spectra, a band at 562 nm that corresponds to a double harmonic at $2\lambda_{excitation}$ was observed. This was confirmed by varying the $\lambda_{excitation}$. This is shown in Figure 3.11 and clearly demonstrates that as $\lambda_{excitation}$ is varied, a new band at the corresponding $2\lambda_{excitation}$ appears. Interestingly, all of the $\lambda_{excitation}$ used gave rise to Eu^{III} emission clearly showing the ability of the antenna to sensitise the Eu^{III} excited state.

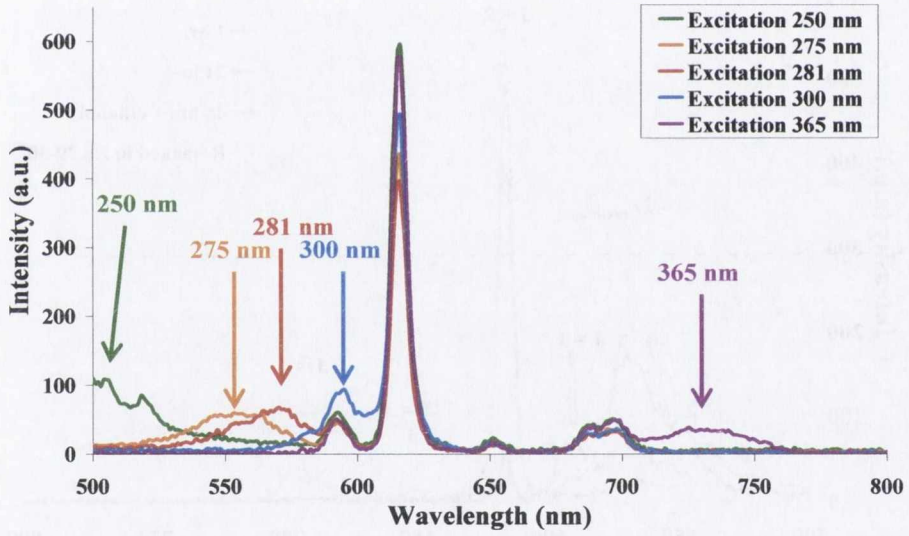

Figure 3.11 Plot of wavelength *vs* intensity of the emission of complex 29.Eu. The spectra are taken with $\lambda_{excitation}$ = 250, 275, 281, 300, and 365 nm. The arrows show the bands that correspond to $2\lambda_{exc}$.

With the aim of evaluating the stability of our system on a gold surface, the lanthanide emission was monitored as a function of time, the results of which are shown in Figure 3.12. The blue line spectrum represents a sample that had been functionalized with **Eu.29-30** overnight, and recorded one hour after rinsing with ethanol and drying with N_2. In contrast, the green line spectrum was recorded of the same sample 24 hours later, after being stored in a

loosely covered sample tube in the absence of solvent. It is clear that here the emission is significantly less intense (~83% of the initial value).

To investigate if this "loss" of emission was due to the dehydration of the monolayer, the sample was re-soaked in ethanol overnight after which, the spectrum was re-recorded (red line). This showed a further decrease in the intensity of the Eu^{III} emission. The sample was thus re-immersed in a solution of **Eu.29-30** overnight, and the resulting spectrum obtained is shown in purple, and clearly shows that the Eu^{III} emission is reinstated. This is probably due to re-population of the surface with **Eu.29-30**. This suggests that the decrease in intensity observed on Figure 3.12 was due to a reorganization of the SAM, which potentially allowed the emission to be quenched. To investigate the reproducibility of these results, several samples of **Eu.29-30** on gold were made, where the gold surface was of approximately the same size as used above, and on all occasions the samples exhibited approximately the same emission intensity.

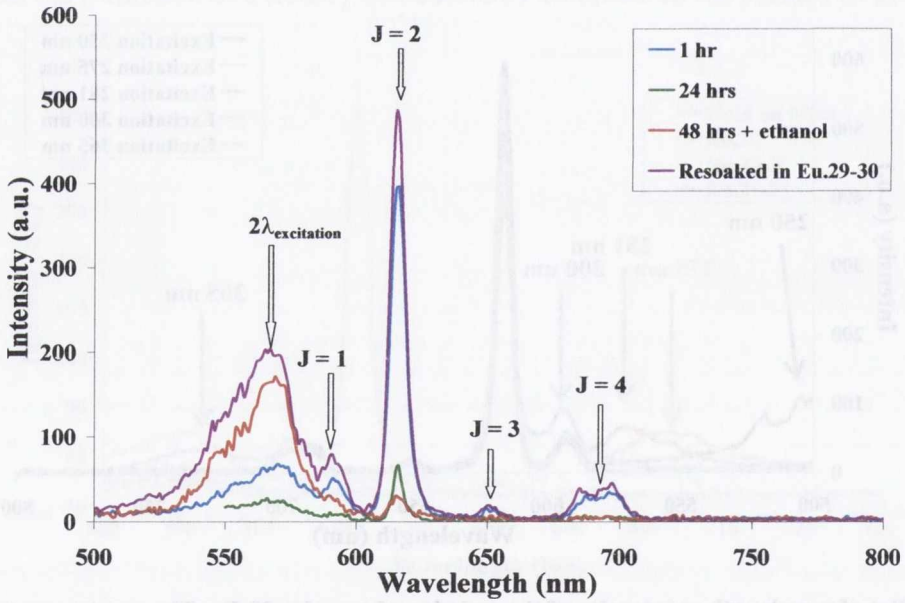

Figure 3.12 A series of overlaid luminescence spectra of one sample of Eu.29-30 on gold. This spectrum shows one sample, a) 1 hour after removing from a solution of Eu.29-30, rinsing with EtOH and drying under N_2, (blue spectrum); b) 24 hours after this (green spectrum); c) after immersion in EtOH for 24 hrs, followed by drying with N_2 (red spectrum); d) The sample was then re-immersed in a solution of Eu.29-30 overnight, rinsed in EtOH and dried under N_2 (purple spectrum).

Unfortunately, possibly due to the constraints of the equipment available, lifetime analyses of the **Eu.29-30** samples were not obtained as this technique did not give rise to excited state decay that could be fitted to a single or double exponential. An example of what was observed is shown below in Figure 3.13.

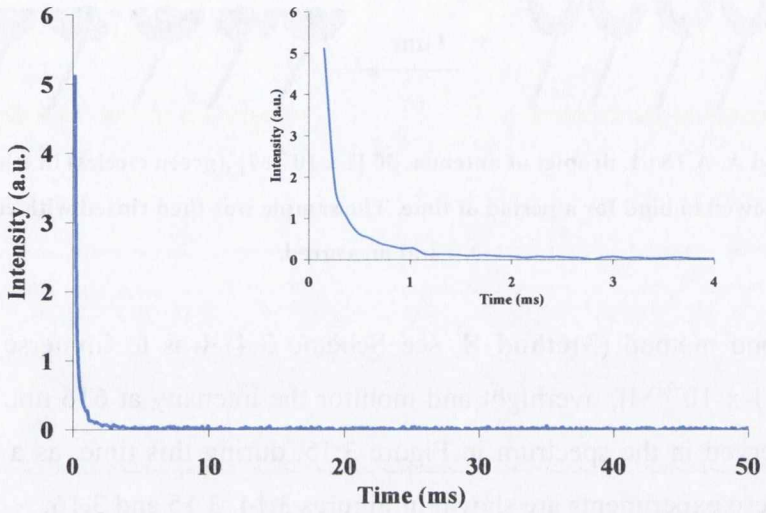

Figure 3.13 Spectrum showing the attempted lifetime measurement for Eu.29-30 on a gold substrate. Inset: The decay observed within the first 4 ms.

3.3.4.1 Functional Sensors on Gold – switching "on" luminescence

The aim of this chapter was to immobilise the lanthanide complex, **Eu.29** on a flat gold substrate, and yet retain its luminescent properties. The next two experiments were designed to determine if this could be achieved. Consequently, a gold sample was functionalised with **Eu.29** by immersing a freshly evaporated sample in a solution of **Eu.29** in ethanol overnight. Then, **30**, the β-diketonate antenna was introduced to the system using two methods.

The first method (**Method A**, see Scheme 3.3) was to place a droplet of **30** on the gold sample functionalised with **Eu.29**, leave it for a period of time, and then rinse it with ethanol and dry under N_2.

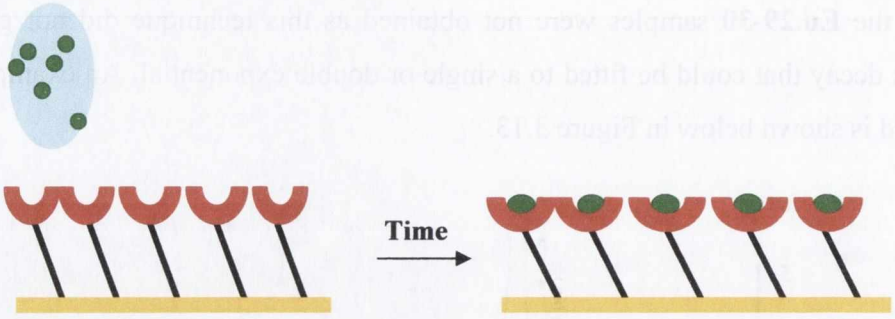

Scheme 3.3 Method A. A 15 μL droplet of antenna, 30 [1 x 10^{-4} M] ,(green circles) in ethanol was placed on the sample and allowed to bind for a period of time. The sample was then rinsed with ethanol, dried under N_2, and measured.

The second method (**Method B**, see Scheme 3.4) was to immerse the sample in a solution of **30,** [1 x 10^{-4} M], overnight and monitor the intensity at 616 nm, the most intense wavelength observed in the spectrum in Figure 3.15, during this time, as a function of time. The results of these experiments are shown in Figures 3.14, 3.15 and 3.16.

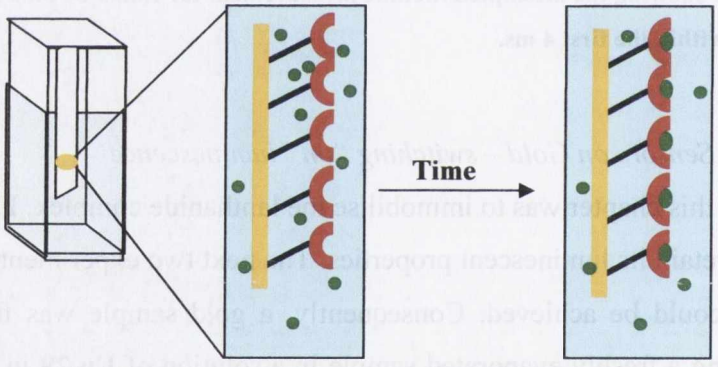

Scheme 3.4 Method B. The sample was placed in the cell filled with antenna, 30, (green circles) and allowed to bind for a period of time. The sample was then washed, dried, and measured.

Figure 3.14 shows the results of **Method A**, with the spectrum of **Eu.29**, the purple line, shows the lack of emission from the Eu^{III} centre due to the absence of the sensitising antenna. Upon dropping 15 μL of 1 x 10^{-4} M solution of **30** onto the sample followed by rinsing with ethanol after one minute, and drying under flowing N_2 to remove any excess ethanol, the emission is "switched *on*" upon excitation at 281 nm as shown in green in Figure 3.14. Furthermore, this emission increases after each subsequent addition of **30**. These results

clearly demonstrate that a self-assembly formation between the **Eu.29**-based gold surface and **30** is achieved.

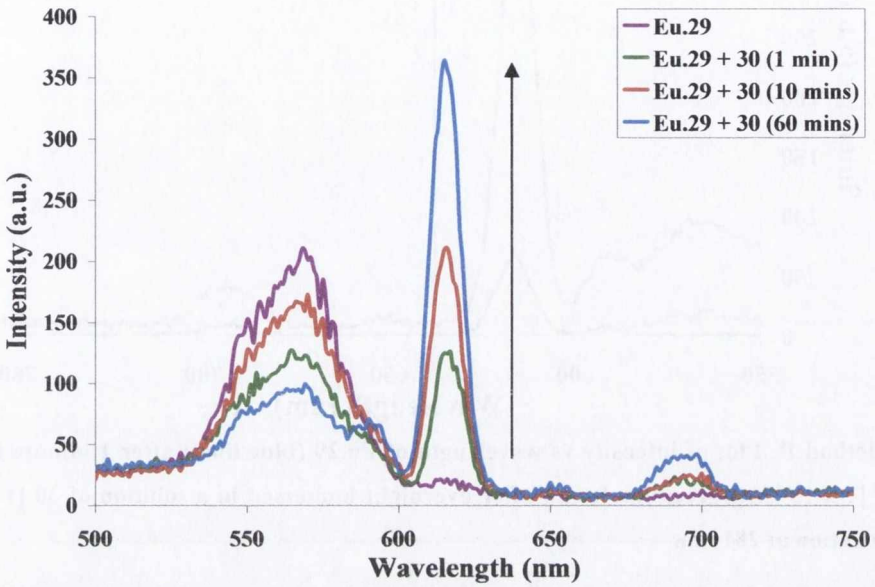

Figure 3.14 Method A: Plot of intensity *vs* wavelength of Eu.29 (purple line), with 1 minutes exposure to 15 μL 30 (green line), with 10 minutes exposure to 15 μL 30 (red line), and finally after an hour's exposure to 15 μL 30 (blue line), upon excitation at 281 nm.

Figure 3.15 shows the overlaid spectra resulting from **Method B**, when a gold sample functionalised with **Eu.29** was immersed into a solution of **30**, and the Eu^{III} emission was recorded as a function of time. Again the lanthanide luminescence is clearly observed. Here the initial increase in intensity was not as large as that of **Method A**. However, measurement of this sample after immersing it overnight in the solution indeed showed a large increase in the Eu^{III} emission intensity. Once more, the $J = 2$ band gives rise to the most intense emission while the $J = 1$ band was only visible as a shoulder in the $2\lambda_{excitation}$ band (red line in Figure 3.15), as in the spectra in Figure 3.14.

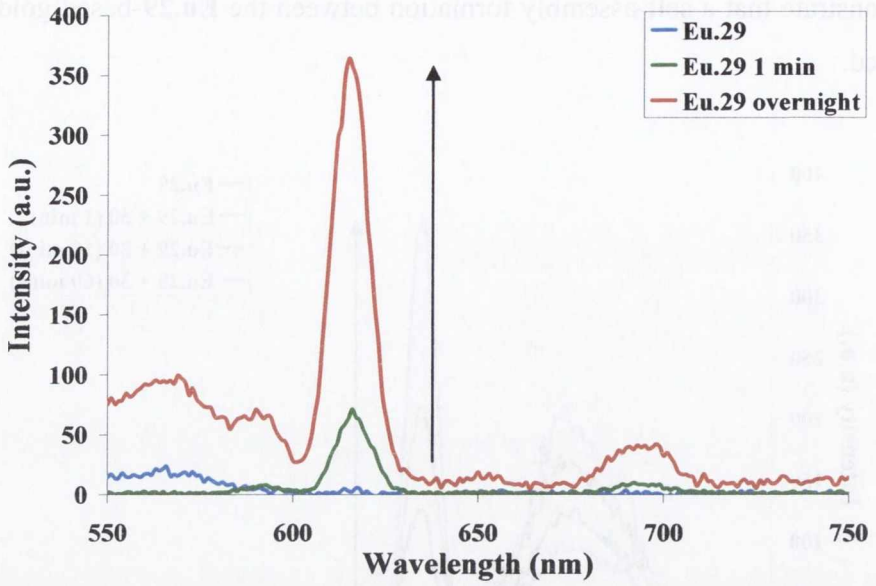

Figure 3.15 Method B: Plot of intensity vs wavelength of Eu.29 (blue line); after 1 minute immersed in a solution of 30 [1 x 10^{-4} M] (green line); and after overnight immersed in a solution of 30 [1 x 10^{-4} M] (red line), upon excitation at 281 nm.

Figure 3.16 shows a plot of emission intensity at 616 nm, as a function of time, upon excitation at 281 nm. This was measured overnight using **Method B**, where the gold sample **Eu.29**, was immersed in a solution of **30** overnight. Interestingly, this kinetics plot showed an initial decrease in the Eu^{III} intensity, followed by an increase in the spectrum seen in Figure 3.15 (red spectrum). This is possibly due to the initial reorganisation of the layer, followed by an efficient binding of the antenna to the metal complex, resulting in an increase in the Eu^{III} intensity.

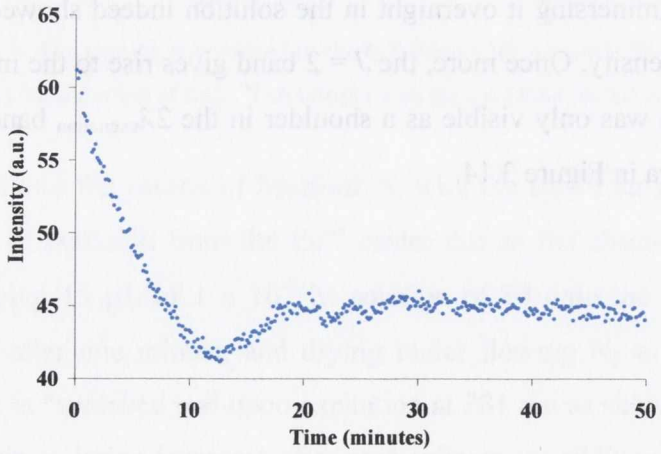

Figure 3.16 Method B: Plot of intensity at 616 nm of Eu.29 immersed in 30 as a function of time over 50 minutes, upon excitation at 281 nm.

The results presented and discussed in this section clearly demonstrate that not only is it possible to observe Eu^{III} emission on a flat gold substrate by using a sensitising antenna, but it is also possible to modify this response using different methods of introducing the antenna, **30**. This suggests that the structure of the layer of **Eu.29** on gold does not impede the binding of the antenna, **30**.

3.3.4.2 Functional Sensors on Gold – switching "off" luminescence

Having demonstrated Eu^{III} from a flat gold surface and that ternary luminescent self-assembly complexes could be successfully formed on a gold substrate with concomitant switching "*on*" of the Eu^{III} luminescence, the next step was to see if effective quenching could be observed by introducing flavin monophosphate, **31**, to the system (*e.g.* switching "*off*" the emission). As before, this was done *via* the same two experimental methods used in the previous section, except here a solution of **31** was used.

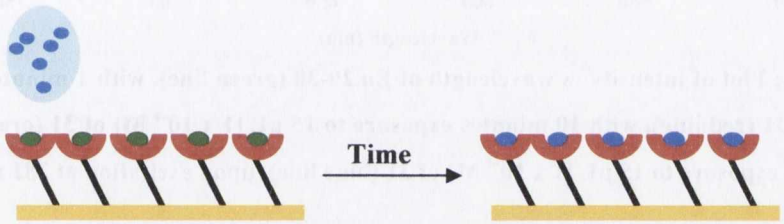

Scheme 3.5 Method A. A 15 μL droplet [1 x 10^{-4} M] of flavin monophosphate, 31, (blue circles) was placed on the sample and allowed to bind for a period of time.

The first method (**Method A**, see Scheme 3.5) was to place an aliquot of **31** (15 μL) on the gold sample functionalised with **Eu.29-30**, leave it for a period of time, and then rinse the surface with ethanol and dry it under N_2 before recording the Eu^{III} emission.

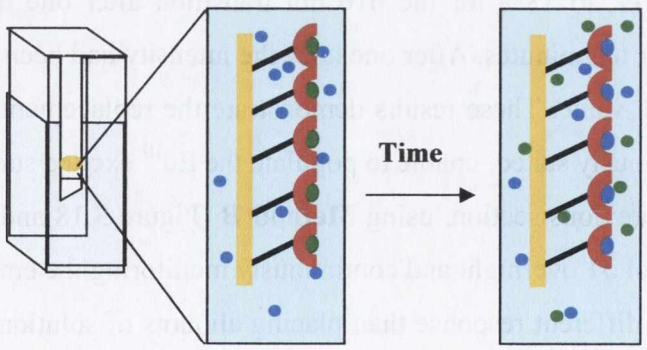

Scheme 3.6 Method B. The sample was placed in the cell filled with flavin monophosphate, 31, (blue circles) and allowed to bind for a period of time.

The second method (**Method B**, see Scheme 3.6) was to immerse the functionalised gold sample into a solution of **31** overnight and monitor the intensity every minute at 616 nm as a function of time, during this period. The results of these experiments are shown in Figures 3.17, 3.18 and 3.19.

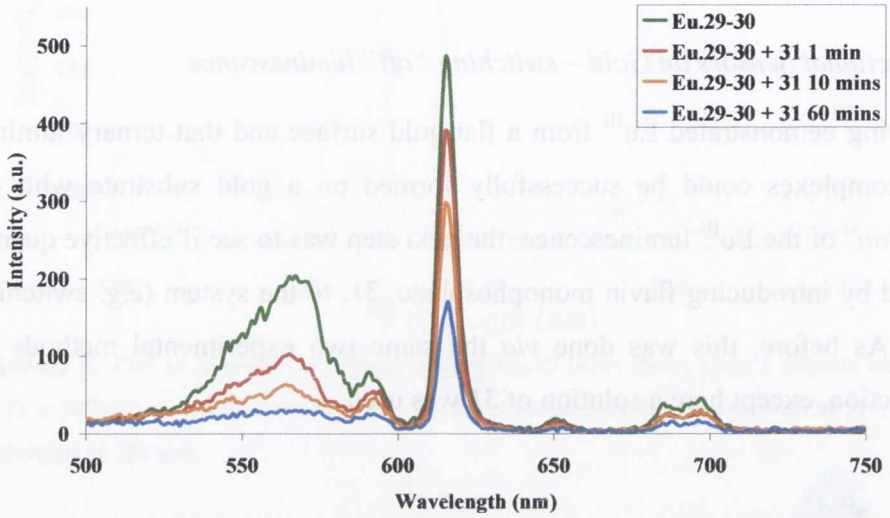

Figure 3.17 Method A: Plot of intensity *vs* wavelength of Eu.29-30 (green line), with 1 minutes exposure to 15 μL [1 x 10^{-4} M] of 31 (red line), with 10 minutes exposure to 15 μL [1 x 10^{-4} M] of 31 (orange line), and finally after an hour's exposure to 15 μL [1 x 10^{-4} M] of 31 (blue line), upon excitation at 281 nm.

Figure 3.17 shows the results of **Method A**. Initially, an aliquot of 15 μL of **31** was placed on the sample for 1 minute (red spectrum). The resulting luminescence spectrum was then recorded. This process was repeated, leaving the subsequent aliquots of 15 μL on the gold surface for 10 minutes and 1 hour. These results are shown as the orange and blue spectra, respectively in Figure 3.17. It is clear from these results, that the emission intensity is decreased, Figure 3.17, to 18% for the 616 nm transition after one minute, with a further decrease of 38% after ten minutes. After one hour the intensity had been reduced by two thirds (64%) from its initial value. These results demonstrate the replacement of the antenna **30** by **31**, which is, as previously stated, unable to populate the Eu^{III} excited state.

As with the previous section, using **Method B** (Figure 3.18 and 3.19); immersing the sample in a solution of **31** overnight and continuously monitoring the emission intensity at 616 nm, produces a very different response than placing aliquots of solution on the surface of the sample (Figure 3.18). Here, the decrease in luminescence intensity occurs much faster than for **Method A**, being ~ 77% for the $J = 2$ band at 616 nm, after one minute. With the aim of

further exploring this, the emission intensity at 616 nm was monitored overnight as a function of time, the results of which are shown in Figure 3.19.

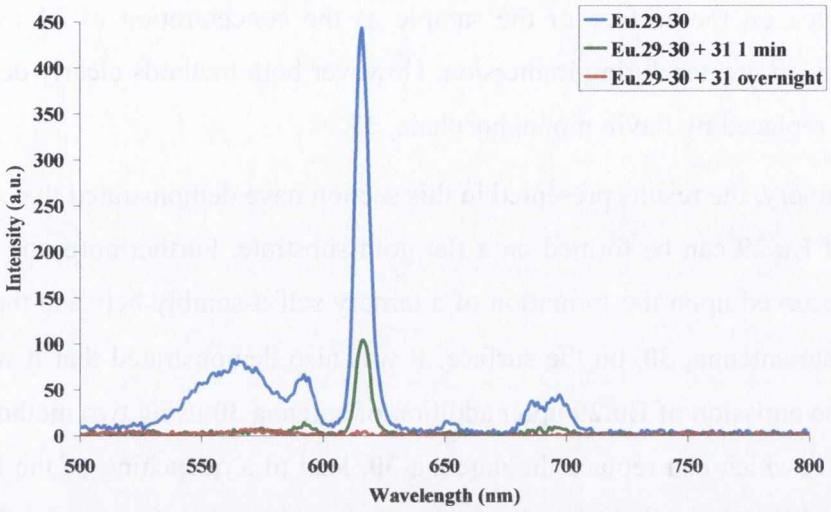

Figure 3.18 Method B: Plot of intensity *vs* wavelength of Eu.29-30 (blue line); after 1 minute immersed in a solution of 31 [1 x 10^{-4} M] (green line); and after overnight immersed in a solution of 31 [1 x 10^{-4} M] (red line), upon excitation at 281 nm.

Looking at Figure 3.19, it is clear that the emission is almost fully quenched after 1 hour. In Figure 3.12, we showed the loss of luminescence from the gold surface which we attributed to the possible reorganisation of the SAM, which resulted in an 83% reduction in intensity. Here however, it is important to notice that the decrease shown in Figure 3.18 and 3.19 is much greater, being ~ 99%. Therefore, it is reasonable to assume that this decrease was independent of the system's inherent emission decrease with time (see Figure 3.12). Therefore, this decrease can be attributed to the displacement of the antenna, **30**, with flavin monophosphate, **31**.

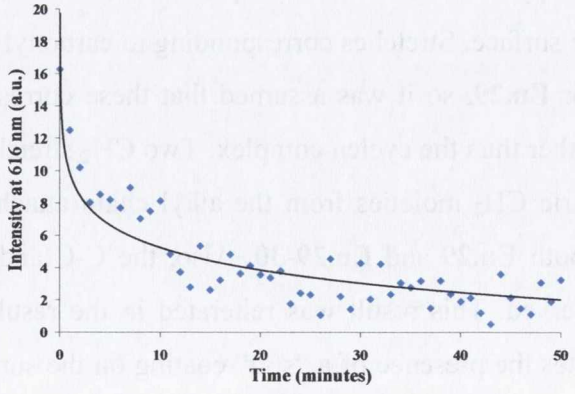

Figure 3.19 Method B: Plot of intensity at 616 nm of Eu.29-30 immersed in 31, [31] = 1 x 10^{-4} M, as a function of time, upon excitation at 281 nm.

One possible explanation for this effect is that because the sample is immersed in the solution it is easier for the layer to reorganize and for **30** to be displaced by **31** than when a droplet is placed on the surface of the sample as the concentration of **31** available to the sample is so much greater during immersion. However both methods clearly demonstrate that the antenna is replaced by flavin monophosphate, **31**.

In summary, the results presented in this section have demonstrated that self-assembled monolayers of **Eu.29** can be formed on a flat gold substrate. Furthermore, the Eu^{III} emission was clearly observed upon the formation of a ternary self-assembly between the complex and the β-diketonate antenna, **30**, on the surface. It was also demonstrated that it was possible to switch "*on*" the emission of **Eu.29** upon addition of antenna **30** using two methods. Moreover, additions of **31**, which can replace the antenna **30**, lead to a quenching of the Eu^{III} emission. These results, although qualitative and not quantitative, show that the complex **Eu.29** behaves in the same manner once immobilized on a flat substrate as in solution or on nanoparticles.

3.4 Conclusion to Analysis of Eu.29 on a Flat Gold Surface

One of the aims of this work was to combine the optical sensing abilities of lanthanide-based chemosensors with the mechanical properties of microcantilevers used commonly in scanning probe microscopies. The first step towards this aim, was to investigate whether or not lanthanide sensors could retain the luminescent properties that make them such good chemosensors when immobilised on a substrate. This chapter aimed to investigate and verify this, that is, it displays and discusses a series of preliminary experiments designed as a "proof of principle" study to show that lanthanide metals can luminesce on gold.

Infrared spectroscopy studies of these samples indicate that the complex **Eu.29** was indeed adsorbed onto the surface. Stretches corresponding to carbonyl moieties were observed for **Eu.29-30** and not for **Eu.29**, so it was assumed that these corresponded to the carbonyl groups in the antenna, rather than the cyclen complex. Two CH_2 stretches corresponding to the asymmetric and symmetric CH_2 moieties from the alkyl chain attaching the complex to the gold were observed in both **Eu.29** and **Eu.29-30**. Also, the C-C and CH stretches from the cyclen moiety were observed. This result was reiterated in the results from AFM imaging, which clearly demonstrates the presence of a "soft" coating on the surface of the gold, visible as cloudy, undefined islands on the functionalised surface. This is absent on the unfunctionalised gold, where clean island boundaries were observed.

Results showing that lanthanide-based sensors can retain their luminescent properties after immobilisation onto a solid substrate were also presented in this chapter, with a series of experiments showing the switching "*on*" of the lanthanide luminescence *via* the coordination of antenna **30** to the Eu^{III} centre. Self-assembly formation is essential for Eu^{III} luminescence to occur in this system. The phosphorescent emission from the Eu^{III} centre of **Eu.29** is clearly observed and emits with the same spectrum as seen in solution and on nanoparticles. Moreover, the subsequent displacement of **30** by **31**, which is unable to sensitise the Eu^{III} centre, results in the complete switching "*off*" of the luminescent emission.

All of the measurements carried out in this chapter give quantitative information on the behaviour and characterisation of **Eu.29** on a flat gold substrate. No qualitative data is presented. This work (to the best of the author's knowledge) represents the first example of lanthanide luminescence on a flat gold substrate.

3.5 Cantilever Functionalisation - STEP 4

As discussed before, **Step 4** (Scheme 3.1), one of the main objectives of this study was to functionalise a gold coated cantilever and examine the possibility of developing a novel dual functioning sensing method, by combining lanthanide optical sensing techniques with an AFM microcantilever mass sensor. At the time, work on **Eu.29** was being carried out in solution and on nanoparticles within the Gunnlaugsson laboratory. Consequently, it was decided to use another system for this aim. To this end, the Eu^{III} complex **Eu.66** was synthesised.

Complex **Eu.66** was designed with three naphthalene antennae and two metal-bound water molecules that quench the Eu^{III} luminescent emission as described previously. If these two water molecules are displaced, the emission is switched "*on*". In this system, the antennae are incorporated into the ligand and so a self-assembly process is not a prerequisite as for **Eu.29**, in order to generate sensitised Eu^{III} emission.

Ligand **66** was synthesised by refluxing **64**, **65**, and $NaHCO_3$ under argon in dry CH_3CN for two days.[146] This reaction produced a mixture of one-, two-, and three-armed products. The three-armed product was isolated by neutral silica flash column chromatography using CH_2Cl_2 containing 3% $CH_3OH(NH_3)$ as an eluent. The product, **66** was obtained as an oil, and was characterised by Mass spectrometry and NMR analysis. The Eu^{III} complex of **66** was formed by refluxing $Eu(CF_3SO_3)_3$ in dry methanol overnight, followed by precipitation into ether, Scheme 3.7. Analysis of the lanthanide excited state by excitation of the

naphthalene antenna, clearly demonstrated sensitised Eu^{III} emission and lifetime measurements showed that the complex indeed possessed two metal-bound water molecules.

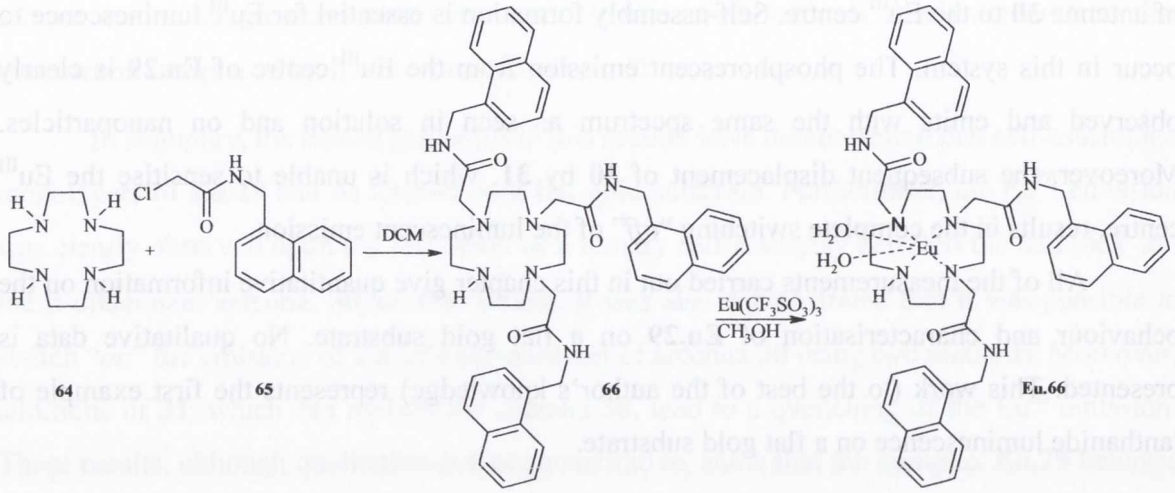

Scheme 3.7 Synthesis of Eu.66

The displacement of these water molecules was achieved in solution with 16-mercaptohexadecanoic acid, a long chain alkane thiol with a terminal carboxcylic acid head group. This resulted in a clear switching "*on*" of the emission (see Figure 3.20).

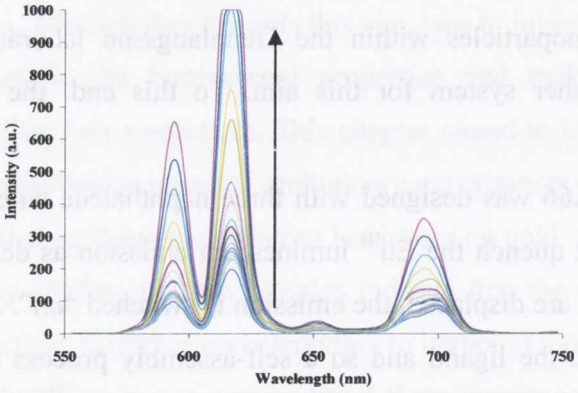

Figure 3.20 Plot of intensity *vs* wavelength of Eu.66 upon the addition of 16-mercaptohexadecanoic acid

Following the success of this result in solution, an experiment was devised whereby a silicon AFM cantilever was coated with gold using a home-built evaporation system, and then functionalised with the aim of developing a self-assembly complex between **Eu.66** and 16-mercaptohexadecanoic acid. We forecasted that this experiment would potentially detect a

change in mass on the cantilever using AFM, as well as changes in luminescence using a fluorescence microscope.

There were two possible routes to take as a means of incorporating this system onto a cantilever. Firstly, the complex could be tethered to the cantilever surface (in a similar manner to **Eu.29** as discussed in this chapter) and an appropriate carboxylic acid in solution would then bind to the cantilever and displace the water molecules and resulting in a switching "*on*" of the luminescent emission, (**Method 1**, Scheme 3.8).

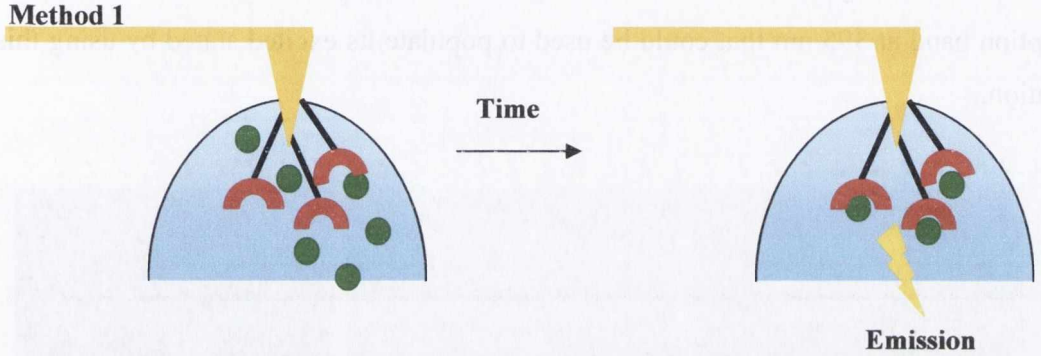

Scheme 3.8 Method 1 for combining a lanthanide luminescent sensor with an AFM microcantilever mass sensor.

Alternatively, a molecule with a carboxylic acid terminal group could be used to functionalise the cantilever surface, and then **Eu.66** would bind onto the cantilever, and switch "*on*". (**Method 2**, Scheme 3.9). It was decided in order to increase the mass added to the cantilever as much as possible, the second approach would be taken.

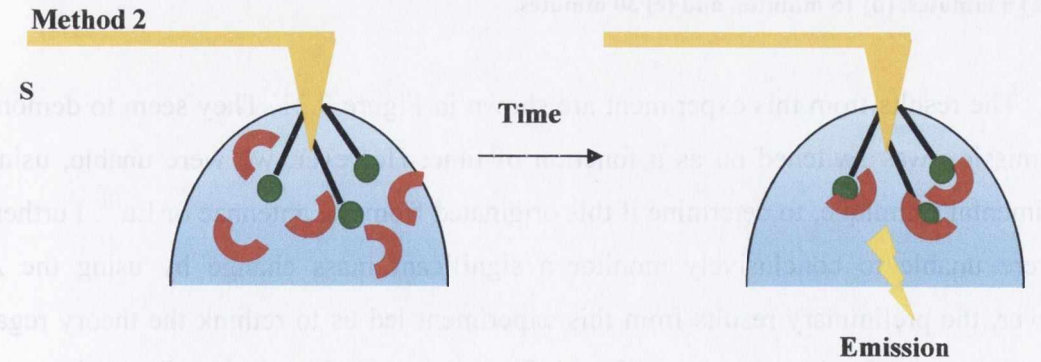

SScheme 3.9 Method 2 for combining a lanthanide luminescent sensor with an AFM microcantilever mass sensor.

The experiment involved placing the functionalised cantilever in a specially designed fluid cell that allowed the wash over of a solution containing **Eu.66**. It was designed such that the AFM head was sitting above an inverted fluorescence microscope so that the luminescence and mass change responses could be monitored simultaneously.

The cantilever coated with the 16-mercaptohexadecanoic acid SAM was mounted in the AFM head and then immersed in 50 μL solution of [5 x 10^{-4} M] **Eu.66**. This set-up was then monitored for 1 hour with a fluorescence microscope, using $\lambda_{excitation}$ = 400 nm. Although this was a much higher excitation wavelength than was used above, the Eu^{III} has a weak absorption band at 395 nm that could be used to populate its excited stated by using this laser excitation.

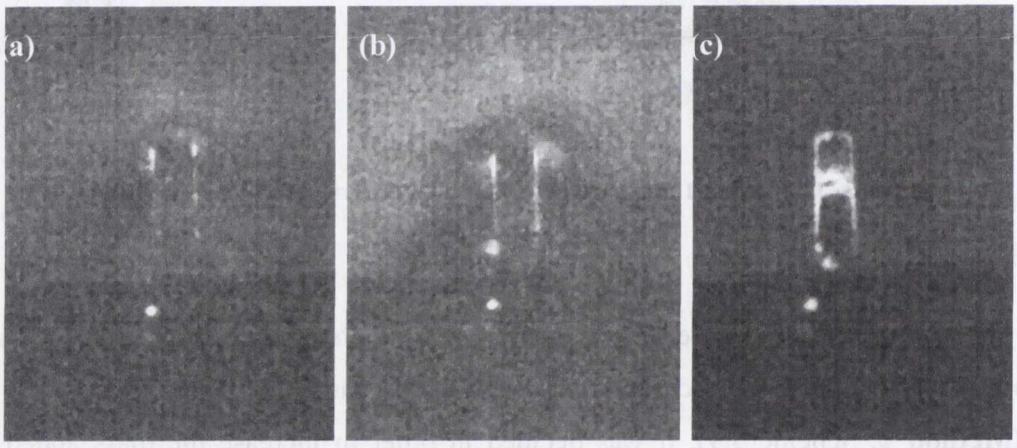

Figure 3.21: Images taken with the fluorescence microscope after the introduction of the carboxylic acid, after (a) 5 minutes, (b) 15 minutes, and (c) 30 minutes.

The results from this experiment are shown in Figure 3.21. They seem to demonstrate that emission was switched on as a function of time. However, we were unable, using our experimental technique, to determine if this originated from the antennae or Eu^{III}. Furthermore, we were unable to conclusively monitor a significant mass change by using the AFM. However, the preliminary results from this experiment led us to rethink the theory regarding cantilever sensors that is currently employed. Our reasons for this are described below.

As mentioned in Chapter 1, cantilever mass sensors rely on either deflection or resonant frequency measurements as their detection mechanism. As cantilever beams are miniaturised, their surface properties become increasingly important, and these surface

properties can affect both the deflection and resonant frequency. Changing the surface properties can alter the surface stress, for example, a SAM may swell or contract upon absorption or desorbtion of an analyte. An issue that recurred upon examination of the literature is that knowledge of the effect of surface stress on the stiffness, and therefore deflection and resonant frequency, of cantilever beams has never been experimentally verified.[147] At this point it was decided to explore this problem in greater detail and to attempt to experimentally resolve it.

3.6 Conclusion to Step 4

The aim of this work was to develop a new technique where lanthanide luminescent sensing was coupled with AFM cantilever-based mass sensing. While we were able to demonstrate the formation of a self-assembly between **Eu.66** and a thiol-based carboxylic acid in solution, with concomitant enhancement in the Eu^{III} emission, we were unable to demonstrate this phenomenon on a cantilever using the experimental setup developed in our laboratory. Nevertheless, the results from this preliminary experiment opened up serious issues with the current use of cantilever sensors, which resulted in a lengthy investigation into experimentally and theoretically examining this problem. The next Chapter, Chapter 4 will discuss this endeavour in detail. Due to time constraints, it was not possible to return to **Step 4** and functionalise a cantilever with either **Eu.66** or **Eu.29**, however this is a very interesting topic for future study within the Gunnlaugsson and Jarvis research groups.

properties can affect both the deflection and resonant frequency. Changing the surface properties can alter the surface stress, for example, a SAM may swell on contact upon absorption or desorption of an analyte. An issue that occurred upon examination of the literature is that knowledge of the effect of surface stress on the stiffness and therefore deflection and resonant frequency of cantilever beams has never been experimentally verified.[37] At this point it was decided to explore this problem in greater detail and to attempt to experimentally resolve it.

3.6 Conclusion to Step 4

The aim of this work was to develop a new technique where lanthanide luminescent sensing was coupled with AFM cantilever-based mass sensing. While we were able to demonstrate the formation of a self-assembly between Eu^{3+} and a thiol-based carboxylic acid in solution, with concomitant enhancement in the Eu^{3+} emission, we were unable to demonstrate this phenomenon on a cantilever using the experimental setup developed in our laboratory. Nevertheless, the results from this preliminary experiment opened up serious issues with the current use of cantilevers as sensors which resulted in a lengthy investigation into experimentally and theoretically examining this problem. The next Chapter (Chapter 4) will discuss this endeavour in detail. Due to time constraints it was not possible to return to Step 4 and functionalise a cantilever with either $Eu.6A$ or $Eu.2S$. However, this is a very interesting topic for future study within the Donnadieu and Jarvis research groups.

Chapter 4

An Experimental Study of the Effect of Surface Stress on the Stiffness of Cantilever Plates

4 An Experimental Study of the Effect of Surface Stress on the Stiffness of Cantilever Plates

4.0 Introduction

As discussed in Chapter 1, there are many examples of mechanical sensors. In order to measure very small quantities, a variety of miniaturised mechanical sensors have been developed. For example, the advent of inexpensive, mass-produced microelectromechanical systems (MEMS) devices has enabled the use of various microstructures for mechanical detection.[148] Advances in lithography and materials synthesis have enabled the fabrication of nanoscale mechanical resonators,[149, 150] which have been operated as precision force,[151] and mass sensors.[152] MEMS techniques are very popular for detecting small quantities, in low concentrations especially when integrated with, for example, biosensing applications.[153] These sensors employ a detector, which can range from chemical sensors of the type discussed in Chapter 1, to proteins or enzymes, as well as cells and microorganisms.[153] Sensors of this type typically make use of cantilevers that can translate a chemical signal into a mechanical one with high sensitivity. They provide a simple means for developing sensors that are smaller, more sensitive and lower in cost than traditional macroscopic sensors.[154]

4.1 Microcantilever Sensors

Cantilever-based sensors (CBS) are devices based upon the measured change of physical quantities of the cantilever such as resonance frequency, amplitude, deflection and quality factor.[155] There are many examples of CBS, as it is an area that has attracted a significant amount of interest since the development of microfabrication techniques for AFM cantilevers. The two methods most commonly employed involve monitoring cantilever bending and shifts in resonant frequency. However, the former is most commonly reported and easily measured, even though the latter tends to be more sensitive.

Surface stress alone can be used to induce bending in a cantilever, without the addition of mass. Butt[156] used microfabricated silicon nitride cantilevers with one side coated with gold and a hydrophobic self-assembled alkanethiol monolayer, in an experiment to monitor the effect of changing pH on the surface stress of a microcantilever. The use of alkanethiol monolayer was to ensure that interactions only occurred on one side, and so changing the pH would induce a bending of the microcantilever. Butt used a flow-through technique, changing

the pH with KOH or HNO_3 and calculated that even in flow-through experiments, changes in surface stress values as small as 0.005 Nm^{-2} could be detected reliably.

However, many systems rely on surface stress measurements when there is also a contribution from the addition of mass. Enzyme based biosensors have received more attention than any other type of sensors that employ biomolecules, because enzymes are unique in their high selectivity and their fast catalytic rates under normal conditions.[154] The basis for detection in most of these cases is that when the enzyme binds to the antibody on the surface of the cantilever, the chemical reaction between them creates a difference in surface stress that causes a deflection. Fritz *et al.*[157] reported an array of adjacent micromachined cantilevers to study the surface stress arising from Watson–Crick base pairing between unlabeled oligonucleotides and their surface-immobilized binding partners. Synthetic thio-modified oligonucleotides with different base sequences were covalently immobilized on the gold-covered side of the cantilevers. Then, the complementary 16-mer oligonucleotide solution was injected into the liquid cell followed by injection of a complementary 12-mer oligonucleotide solution. The hybridization between the oligonucleotides in solution and immobilized on the surface, results in a difference in surface stress between the functionalized gold and the nonfunctionalized Silicon surface, which bends the cantilever. This bending was monitored *in situ* using an optical beam deflection technique. The transduction of molecular recognition into surface stress occurs from electrostatic, steric, and hydrophobic interactions whose relative contributions depend on the molecules under investigation. All these interactions are repulsive and produce compressive surface stress during hybridization. From the bending data, they determined a surface coverage of 10^{10} oligonucleotides per cantilever, which is consistent with published densities. A major advantage of such a direct transduction is that it eliminates the requirement that the molecules under investigation have to be labelled, for example, with fluorescence or radioactive tags.

The results obtained in this experiment came from static measurements of the cantilever, and so it was impossible to quatitatively model the surface stress. As a result of this study, and many more like it, that do not differentiate between the contributions made by the addition of mass and the surface stress induced on a microcantilever system, it is important to establish a rigorous method of testing these two properties and deconvoluting their impact on measurements made with microcantilevers, in order to produce a functioning device for measuring mass.

4.2 The Relationship between Surface Stress and Cantilever Stiffness

As cantilever beams become smaller and thinner, there is a much greater surface to volume ratio. Therefore, the surface properties become increasingly more important upon miniaturisation. There has been considerable progress in designing and studying cantilever behaviour, yet knowledge of the effect of surface stress on the stiffness of cantilever plates remains an outstanding problem.[147]

In 1975 Lagowski *et al*,[99] first reported that the stiffness of a cantilever can be tuned by varying its surface stress. Lagowski's model was based on classical beam theory and describes the effect that changes in strain-independent stress have on the resonant frequency of the cantilever. This model was subsequently shown by Gurtin[100] to be incorrect, nevertheless, many of the models currently in use are still based upon the original model by Lagowski *et al*.[101-106] Indeed, such models have recently been used to argue that "in a viscous solution the frequency shift of the nanoscale cantilever is determined by surface stress generated by biomolecular interaction with negligible contributions from mass loading due to the biomolecules".[105] In other words, strain-independent surface stress dominates the dynamic response of microcantilevers in biomolecular recognition measurements[147]. As such, it is important to evaluate the accuracy of these models, and confirm conclusively the exact relationship between changes in surface stress and the stiffness of a cantilever beam, in order to correctly utilize them as sensitive dynamic sensors.

Before discussing the results from these measurements, it is important to explain the parameters and theory behind the experiment. The next section contains descriptions of the parameters and concepts used in reference to the microcantilever system discussed in this Chapter.

4.2.1 Definitions and Explanations

4.2.1.1 Resonant frequency

The resonant frequency of an oscillating beam (for the purpose of this chapter, a microcantilever) can be described by Hooke's Law (Equation 4.1):

$$\omega = \sqrt{\frac{k}{m^*}} \qquad \textbf{Equation 4.1}$$

where

$$m^* = n \times m \qquad \textbf{Equation 4.2}$$

where $n = 0.24$, a geometric correction factor for rectangular cantilevers and m is the mass of the cantilever,[158] and k is the normal spring constant. The method used to measure this was to monitor the vibrations of the cantilever due to ambient thermal motion (Brownian motion) using an AFM optical beam detection signal that was fed into a frequency spectrum analyser. Static measurements, *i.e.* monitoring the cantilever deflection using the optical lever technique as is commonly done, were not relied upon. As such, an intrinsic mechanical property of the cantilever was measured.

4.2.1.2 Q Value

Q value, or Quality factor, is a dimensionless parameter that can be described as:

$$Q = 2\pi \times \frac{\text{maximum energy}}{\text{average energy dissipated per cycle}} \qquad \textbf{Equation 4.3}$$

The quality factor can be deduced from the amplitude frequency response, see Figure 4.1, and Equation 4.4.

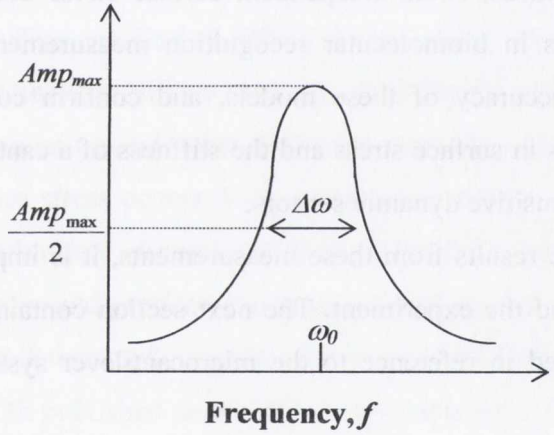

Figure 4.1 The bandwidth, $\Delta\omega$, of a damped oscillator is shown on a graph of Amplitude *vs* frequency.

$$Q = \frac{\omega_0}{\Delta\omega} \qquad \textbf{Equation 4.4}$$

where ω_0 is the resonant frequency and $\Delta\omega$ is the full bandwidth of the frequency spread at the half-power[2] point.

There are several points regarding Q values.

1. **A High Q system will have a narrow resonant peak**
2. **With high Q, there is low dissipation of energy per cycle so that little power is needed to maintain oscillation**
3. **With high Q, there is a narrow frequency band over which resonance occurs giving the sensor (in reference to the application of this chapter) high resolution**[159]

4.2.1.3 Surface Stress

Surface stress can be defined in various ways. It can be described as a measure of the average amount of force exerted per unit length and its units are N/m. The surface stress is called "tensile" when the surface stress is positive and "compressive" when the stress is negative.[160] See Figure 4.2.

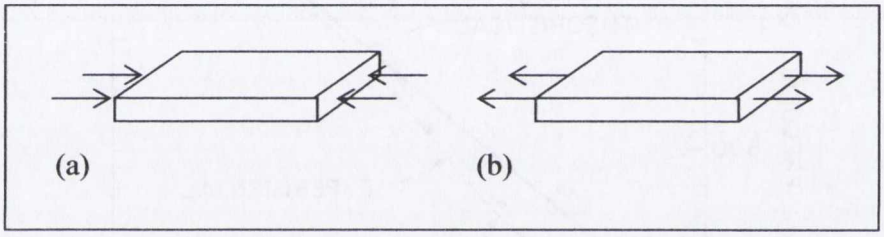

Figure 4.2 Two types of surface stress (a) compressive stress, and (b) tensile stress.

The total surface stress, σ_s, will have contributions from residual stress σ_0, as well as from the surface elasticity (a constant), b, and the relative strain, ε:

$$\sigma_S = \sigma_0 + b\varepsilon \qquad \textbf{Equation 4.5}$$

Gurtin *et al.* examined the effects of strain-dependent surface stress and showed theoretically that this can affect cantilever stiffness.[100, 161] However, they concluded that this effect was negligible. Therefore, for the rest of this chapter, the surface stress that is referred to is strain-independent surface stress.

The following section will discuss the background theory to the experiment presented in Section 4.4.

4.3 Experimental

4.3.1 Introduction

As discussed earlier, Lagowski *et al.*[99] performed a series of experiments where they measured the resonant frequency of thin GaAs crystal wafers. Their experiment showed that below a thickness of 15 μm the lowest natural frequency of the cantilever was noticeably below that predicted by classical beam theory. This is shown in Figure 4.3 where it can be clearly observed that the experimental (dashed) and theoretical (continuous) lines do not match.

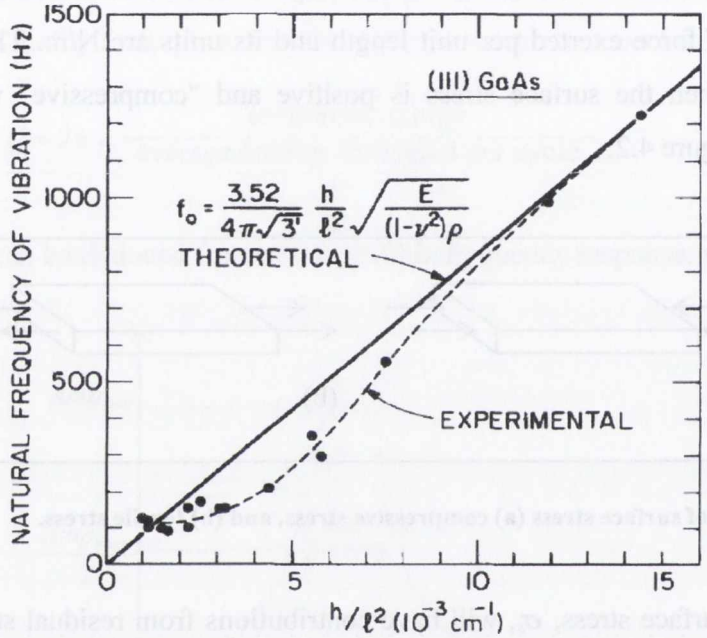

Figure 4.3 Resonant frequency of vibration of thin (111) GaAs crystals (in a cantilever configuration) as a function of crystal dimensions (h/l^2), where h = thickness, l = length, E = Young's modulus, ν = Poisson's ratio, and ρ = density. Reprinted with permission from Lagowski, J.; Gatos, H. C.; E. S. Sproles, Jr., Applied Physics Letters, 26, (9), 493-495, 1975. Copyright 1975, American Institute of Physics.

The authors hypothesised that the decrease in frequency was due to the presence of surface stress, and they presented a simplified model in which the surface stress was replaced by a compressive axial force $F=2\sigma b$, where σ is the surface stress, and b is the width of the beam,[99, 100] see Figure 4.3. Gurtin[100] in this work stated that "their (Lagowski) model is incorrect, because it fails to take into account the vertical loading due to surface stress. This loading which occurs during vibration and is distributed along the length of the beam, completely cancels the effects of F, at least within the framework of classical beam theory."

Further to this, the axial stress model bases its calculations on substituting the surface stress for an axial force that effectively "pulls" the end of the cantilever (see Figure 4.4). However, there is no such force and so this approach violates Newton's third law: *For a force there is always an equal and opposite reaction: or the forces of two bodies on each other are always equal and are directed in opposite directions.*[162]

The approach taken by Lachut *et al*,[147] and upon which the experiment described within this chapter was based, was to examine this problem within the framework of the theory of linear elasticity. Within this, differential surface stress, as used by many groups and in the well known *Stoney's Equation*[163], will not affect cantilever stiffness, since its only effect is to induce an effective bending moment at the edges[164]. As such, differential surface stress and bending are ignored. Instead, the focus is on the total surface stress, σ_s^T.

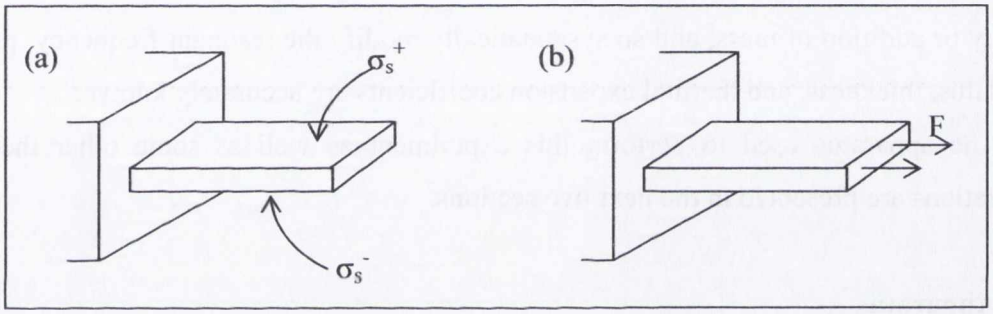

Figure 4.4 Diagram of the two surface stress models presented in this chapter. (a) Diagram shows the applied surface stresses, where σ_s^+ and σ_s^- are the isotropic strain-independent surface stress loading on the upper and lower faces of the cantilever, respectively. They are taken to be the changes in surface stress from their base (intrinsic) values. The differential surface stress is defined as, $\Delta\sigma_s = \sigma_s^+ - \sigma_s^-$, and the total surface stress is defined as, $\sigma_s^T = \sigma_s^+ + \sigma_s^-$. (b) The axial model of surface stress.

4.3.2 Modifying Surface Stress

Today, the axial stress model is widely used to determine the effect of stress on the resonant frequency[103-105], see Figure 4.4.

$$\frac{\omega}{\omega_0} = \left(1 + \frac{6\sigma_s}{\pi^2 k}\right)^{\frac{1}{2}} \qquad \textbf{Equation 4.6}$$

where ω_0 is the reference resonant frequency. The purpose of this experiment is to examine experimentally whether this model is valid or not. In order to do this we need a method of accurately modifying the surface stress in a predictable way.

A bi-metallic strip is used to convert a temperature change into a mechanical displacement. If a cantilever is made up of two strips of different metals which expand or contract at different rates as they are heated or cooled respectively, due to their different coefficients of thermal expansion, α, this displacement will induce a surface stress. The effect of temperature change on surface stress can be calculated directly by Equation 4.7:

$$\sigma_s = (\alpha_1 - \alpha_2)\Delta T \frac{E_1}{1-\nu} t_1 \qquad \textbf{Equation 4.7}$$

where ΔT is the temperature change, E is the Young's modulus, t is the thickness, and α_i is the thermal expansion coefficient of each layer. By utilizing the bimetallic effect, we can controllably tune the surface stress using temperature without any modifications to the surface chemistry or addition of mass, and so systematically modify the resonant frequency, provided the modulus, thickness, and thermal expansion coefficients are accurately known.

The apparatus used to perform this experiment as well as some other theoretical considerations are presented in the next two sections.

4.3.3 Apparatus

The beam is clamped rigidly at one end and is free at the other. L, b and t are the length, width, and thickness of a rectangular beam, respectively (see Figure 4.5).

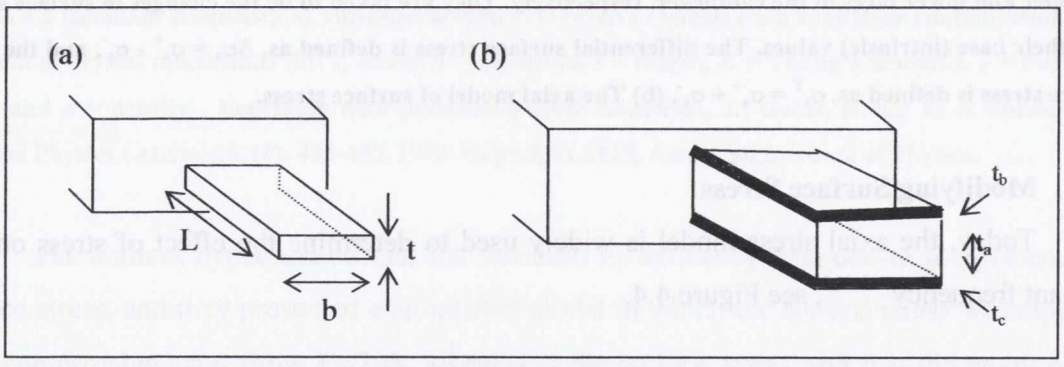

Figure 4.5 Geometry of a cantilever with rectangular cross section without coating (a) and two coats (b).

4.3.4 Materials and Methods

Commercially available, uncoated, undoped, single crystal silicon cantilevers were used in the experiments carried out herein, (Veeco, Nano Fabrication Centre, CA, USA). Aluminium was initially chosen as the coating material as its thermal expansion coefficient is very different to that of silicon. These cantilevers are rectangular, with dimensions and mechanical properties as listed in Table 4.1. The spring constant of each cantilever was measured at the beginning of each experiment using the calibration method of Sader *et al.*[165] In the discussion that follows, they will be referred to as cantilever A, B, C, and D. Their dimensions and mechanical properties are listed in Table 4.1a. The mechanical properties of the materials used in these "home-made" bimetallic strips are listed in Table 4.1b.

Table 4.1a Dimensions and mechanical properties of cantilevers A, B, C, and D

Cantilever	A	B	C	D
L (μm ± 1 nm)	84	185	85	185
w (μm ± 1 nm)	27	28	28	28

Table 4.1b Mechanical properties of the materials used. E is the Young's modulus, ρ is the density, and α is the thermal expansion coefficient.

Material	E (N/m^2)	ρ (kg/m^3)	α
Si	1.7×10^{11}	2300	2.49×10^{-6}
Al	7.03×10^{10}	2702	23.1×10^{-6}

These cantilevers were chosen as they are made from single crystal silicon and so have very well defined properties. The dimensions were also suitable, as we wish to examine micro-scale cantilevers. When cantilevers are miniaturized their surface to bulk thickness properties begin to change. That is, the ratio of the surface oxide layer, relative to the bulk increases. They need to be sufficiently thin (relative to their length and width) that maximum bending can occur and so their response becomes more sensitive and easier to measure. However, if they are too thin, they will respond more readily to noise (*e.g.* mechanical background noise) and so the signal will be correspondingly less accurate. However, the thinner they are the more readily they will respond to changes in temperature which, for the purpose of this experiment, is beneficial. It was important when choosing cantilevers for this study to consider these points carefully.

The experiments were carried out in an Asylum Research Bioheater cell that had been modified in-house to include three 5 μm diameter K-type thermocouples (see diagrams and photograph, Figure 4.6, and Image 4.1). These thermocouples were positioned one above and one below the chip onto which the cantilevers were mounted. The third thermocouple was attached to the heating coil of the cell. The thermocouples were attached to an InstaCal data acquisition meter to allow real time, continuous temperature monitoring. The cell was sealed at the beginning of each experiment to maintain a constant volume of air within the cell, to ensure the thermal spectra were measured at a constant temperature. The cantilevers were allowed to thermally equilibrate at each temperature point for 14 minutes.

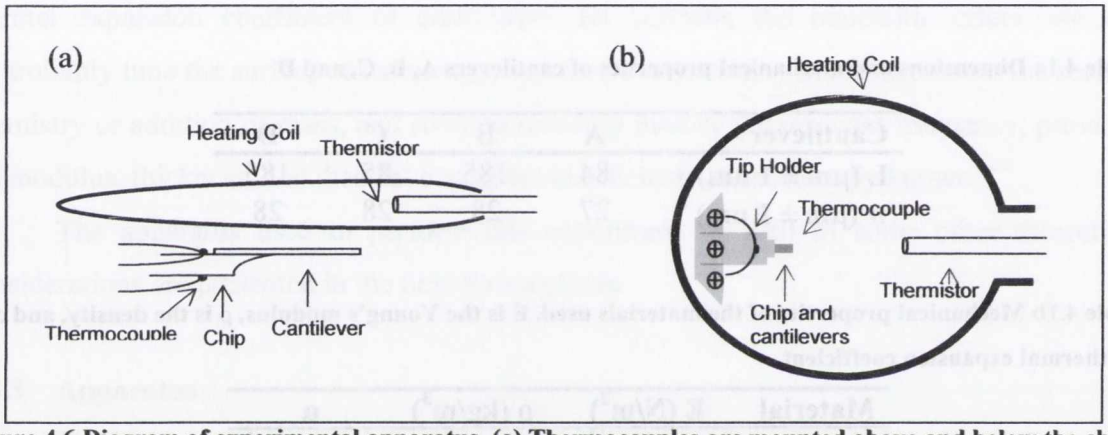

Figure 4.6 Diagram of experimental apparatus. (a) Thermocouples are mounted above and below the chip. The thermistor controls the feedback loop that maintains the temperature within the cell via the heating coil. (b) Top view of inside of the heating cell.

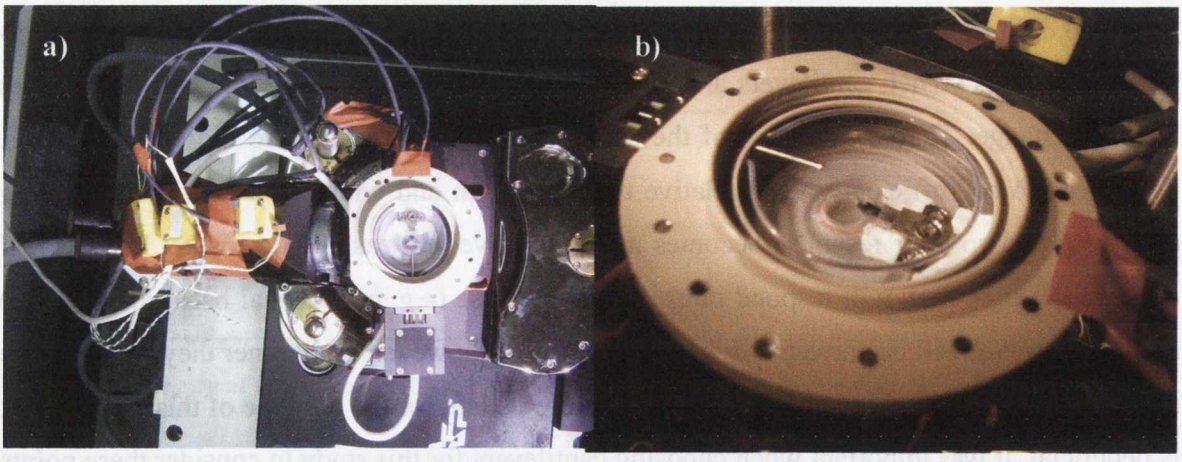

Image 4.1 Photographs of experimental apparatus. a) Top down view of the AFM head with home modified Asylum Research Bioheater Cell, and Agilent thermocouple metre. b) close up of home modified Asylum Research Bioheater Cell.

The cantilevers were coated with Aluminium using a Cressington 208HR sputter coater, and the deposited layer thicknesses were monitored *in situ* using a quartz crystal microbalance. The thicknesses of the cantilevers and coatings were accurately measured using a combination of focused ion beam (FIB) and scanning electron microscopy (SEM). The frequency measurements were performed using an Asylum Research MFP-3D AFM (Asylum Research, Santa Barbara, CA) and the frequency was measured by monitoring the thermal spectrum of the cantilever.

4.3.5 Other Considerations

There are many environmental effects that must also be considered when calculating the theoretical resonant frequency response. Within the heating cell, the properties of the ambient air will change as a function of temperature. These will not affect the resonant frequency of the cantilever as considerably as other effects e.g. the change in Young's Modulus of the cantilever, but they will make a contribution and so are worth considering when devising a model for this behaviour. These properties include pressure, density, humidity and most significantly viscosity. It is possible to calculate the effects of these parameters at each stage of the experiment.

4.3.6 Thermal Spectra

Thermal spectra were taken by allowing the cantilever to hang freely in space and monitoring its thermal fluctuations with time, see Figure 4.7. The data was fourier transformed into a power spectrum, with mean-square amplitude on the y axis and frequency on the x axis. The data was then fitted to a sum of 1/ f noise, white noise, and the simple harmonic oscillator (cantilever) response.[166] Matei *et al.*[166] describe an experiment to determine the accuracy of this method for determining the spring constant, and in doing so, the resonant frequency of a microcantilever.

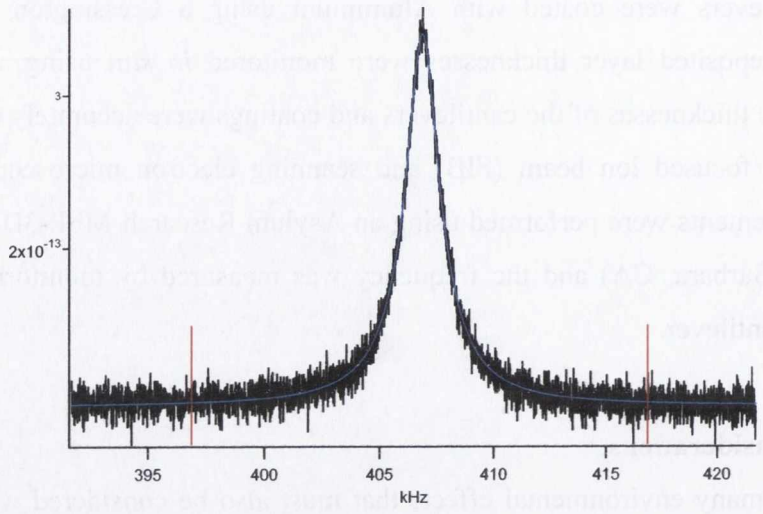

Figure 4.7 An example of a thermal spectrum. This is the spectrum of uncoated Cantilever A at 30 °C. The blue line is the fit, and the two red lines show the boundaries of the 20 kHz fit width.

Matei[166] performed three tests in order to establish the precision of this method. First, a series of ten runs on the same cantilever were performed, each with the laser spot on a different position near the end of the cantilever. One standard deviation of the variation in calculated stiffness was 4.3% of the average value.

Secondly, a coated cantilever was inverted such that the uncoated side faced the laser beam. The total signal at the photodiode was significantly weaker and the conversion factor, *s*, (obtained when pressing the beam against a stiff surface) was significantly greater, resulting in a power spectrum, and thus stiffness, that was only 5% different than that measured on the coated side. The third test was to add a mass, a 10 μm diameter sphere, to the cantilever. Adding the mass shifts the resonance peak from 10.74 to 10.24 kHz, and lowers the quality factor, *Q*, from 53.5 to 51.2. However, the measured spring constant was only changed by 1%, from 0.0331 to 0.0333 N/m upon these modifications. From these three tests, they claim 5% precision in the reproducibility of the data.[166]

Accuracy concerns how close the measured spring constant was to the true value. For this they took into account the accuracies in the individual measurements of dimensions, material properties of the cantilever, and frequency. Several systematic errors, both theoretical and experimental, were also accounted for, and they claimed an error of 5% in this measurement. In summary, the standard relative uncertainties of this method were estimated at 5% precision and 5% accuracy.[166]

The experiment to determine the effect of moving the laser spot on the cantilever was performed on the cantilevers used in this chapter, and the results are shown in Table 4.2, and graphed below in Figure 4.8. The values above 100% SUM signal are those measured as the laser spot is moved from the 100% SUM value towards the end of the cantilever. The graph shows that the error in frequency measurement due to the laser spot not being positioned identically for each experiment is low, at ± 2 Hz, or 0.003%.

Table 4.2 Percentage of the maximum SUM signal, and the corresponding resonant frequency and error.

Frequency (Hz)	% SUM Signal
81085	100
81085	110.9635
81084	105.3156
81086	94.68439
81087	88.37209

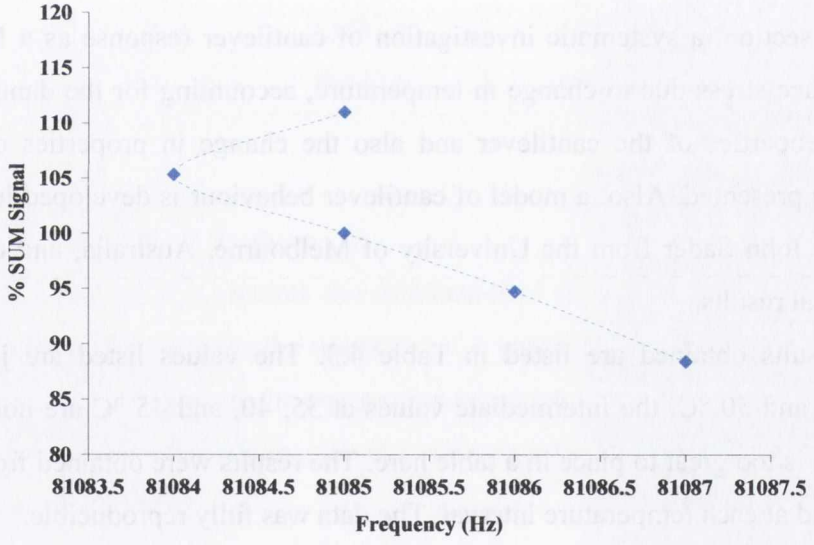

Figure 4.8 Graph of percentage SUM signal *vs.* resonant frequency at that SUM signal.

The last six sections have discussed the parameters and apparatus involved in the experiment described in this Chapter, and so the following section will describe the experimental procedure used to carry out this experiment.

4.3.7 Experimental Procedure

The frequency measurement experiments were carried out as follows: Each chip was prepared by cleaning it in an Argon plasma for 1 minute in a Gala Instrumente plasma cleaner. It was then mounted in the tip holder of the Bioheater cell (Asylum Research, Santa Barbara, CA), positioned in between two microthermocouples. The temperature was allowed to equilibrate at 30 °C before measurements were taken. Thermal spectra were then taken at 5 °C intervals between 30 °C and 50 °C, and then back to 30 °C.

The cantilevers were then sputter coated with a layer of Aluminium and re-mounted in the cell. Again, the resonant frequency was monitored at 5 °C intervals, between 30 and 50 °C, after which, the curvature of the cantilever was measured using interferometry. The underneath of the cantilevers was then coated with aluminium, and the process was repeated. Approximately twelve frequency measurements were taken per cantilever at each stage.

4.4 Results

In this section, a systematic investigation of cantilever response as a function of the change in surface stress due to change in temperature, accounting for the damping effects of the material properties of the cantilever and also the change in properties of the ambient environment is presented. Also, a model of cantilever behaviour is developed in collaboration with Professor John Sader from the University of Melbourne, Australia, and compared with the experimental results.

The results obtained are listed in Table 4.3. The values listed are just the values obtained at 30 and 50 °C, the intermediate values at 35, 40, and 45 °C are not shown as the volume of data is too great to place in a table here. The results were obtained from the thermal spectra recorded at each temperature interval. The data was fully reproducible.

The data was analysed by normalizing both the temperature and frequency shift so that the results could be compared between cantilevers. The data analysis is detailed in the next section.

Table 4.3 Frequency at 30 and 50° and average Q Data for each cantilever, at each coating step during the experiment. The average value of Q is the average of Q over the temperature range for each step of the experiment. Values taken at 35, 40 and 45° are not shown for concise reporting.

Cantilever	# Coatings	ω at 30 °C (Hz)	ω at 50 °C (Hz)	Average Q
A	0	406868	406679	361.473
A	1	424908	423878	274.813
A	2	425525	424214	269.76
B	0	89621.6	89579.7	165.148
B	1	93775.5	93535	169.202
B	2	94512.4	94515.6	212.182
C	0	367360	367191	330.342
C	1	377561	376765	279.808
C	2	380869	379793	255.82
D	0	81336.9	81301.6	139.662
D	1	83994.3	83825.2	158.306
D	2	86449.1	86150.8	162.69

4.4.1 Frequency Shift Data Analysis

The following section presents the mathematical theory developed in collaboration with Professor Sader, to describe the response of a cantilever to changes in surface stress caused by changes in temperature, the progression of which is shown in Equations 4.8 – 4.14. As such, we will begin by considering the material properties of the cantilever and how they will change with temperature.

The density of a material depends on its length, width, and thickness. The way these properties will change with temperature is described by the material's thermal expansion coefficient. As the temperature changes, the change in density will affect the Young's modulus of the material. For the temperature range used in this experiment we assume that dE/dT, the change in Young's modulus as a function of temperature, is constant.

We can calculate the flexural rigidity of a two layer beam of width b, Young's Modulus E_i, and thickness t_i. Layers are denoted by $i = a, b, c,$:

$$EI = \frac{b\left(E_a^2 t_a^4 + E_b^2 t_c^4 + 2E_a E_b t_a t_b \left(2t_a^2 + 3t_a t_b + 2t_b^2\right)\right)}{12\left(E_a t_a + E_b t_b\right)} \qquad \textbf{Equation 4.8}$$

and for a three-layer beam:

$$EI = \frac{b\left(E_a^2 t_a^4 + E_b^2 t_b^4 + E_c^2 t_c^4 + 2E_b E_c t_b t_c \left[2t_b^2 + 3tbtc + 2t_c^2\right]\right)}{12\left(E_a t_a + E_b t_b + E_c t_c\right)}$$

$$+ \frac{2b\left[E_a t_a \left(E_b t_b \left[2t_a^2 + 3t_a t_b + 2t_b^2\right] + E_c t_c \left[2t_a^2 + 3t_a\left(2t_b + t_c\right) + 2\left(3t_b^2 + 3t_b t_c + t_c^2\right)\right]\right)\right]}{12\left(E_a t_a + E_b t_b + E_c t_c\right)} \qquad \textbf{Equation 4.9}$$

Mass per unit length μ, with layers of density ρ_i is:

$$\mu = w\left(\rho_a t_a + \rho_b t_b + \rho_c t_c\right) \qquad \textbf{Equation 4.10}$$

In this model, the temperature dependence of all the properties is included, and so mass is conserved throughout. We can then calculate the resonant frequencies of the various modes of frequency of a cantilever using Equation 4.11:

$$\omega_n = \frac{C_n^{\,2}}{L^2}\sqrt{\frac{EI}{\rho A}} \qquad \textbf{Equation 4.11}$$

where L = length, A = cross-section, and C_1 = 1.875104… which is the smallest positive root of the function given in Equation 4.12:

$$1 + \cos C_n \cosh C_n = 0 \qquad \textbf{Equation 4.12}$$

where n = 1, 2, 3,…[167] By varying the temperature T, we can evaluate ω numerically and compare it to experimental results. These equations accurately describe how the cantilever behaves as a function of temperature.

The results of the experiment are displayed in Figure 4.9. It shows, that $\Delta\omega - \omega/\omega_0$ (the normalized shift in frequency) *vs* temperature is reproducible not only as you increase and decrease the temperature for each coating step, but also between cantilevers. This confirms that the experimental results are accurate, as they obey the rules of beam mechanics

$$\omega = \frac{t}{L^2}\sqrt{\frac{E}{\rho}} \qquad \textbf{Equation 4.13}$$

i.e. if E and ρ are consistent, then the value of ω will follow a predictable pattern as these parameters change with temperature.

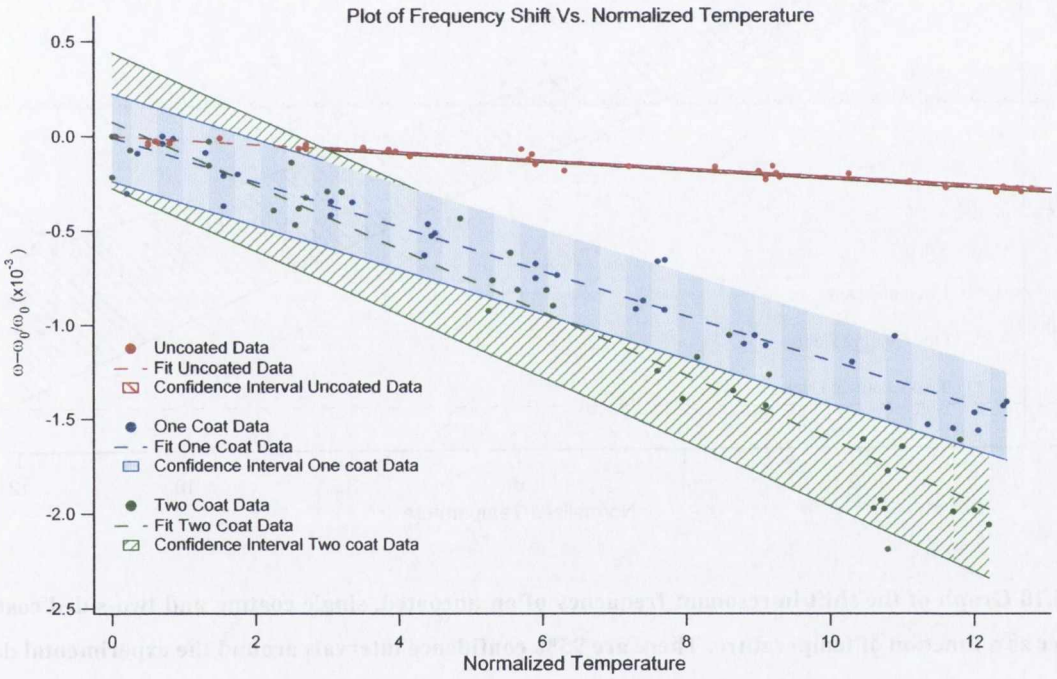

Figure 4.9 Plot of Frequency *vs* Temperature for 0, 1, and 2 coatings. The shaded areas correspond to a 95% confidence interval. The dotted lines are the the fit lines for the data, and the dots are the data points.

As mentioned previously, there will be a damping effect due to the environmental hydrodynamics within the heating cell. To account for this, a hydrodynamic function Γ is included and can therefore calculate the resultant resonant frequency, ω_{fluid}, Equation 4.14:

$$\omega_c = \omega_{fluid}\left(1+\frac{\pi\rho_f b}{4\rho_c}\Gamma_f\left(\omega_{fluid}\right)\right)^{1/2} \qquad \textbf{Equation 4.14}$$

where ρ_f and ρ_c are the densities of the fluid and the effective density of the cantilever, and Γ_f is a hydrodynamic function.[167] ω_{fluid} is solved numerically from the equations given above, using data processing software, to give the theoretical data lines in Figure 4.10.

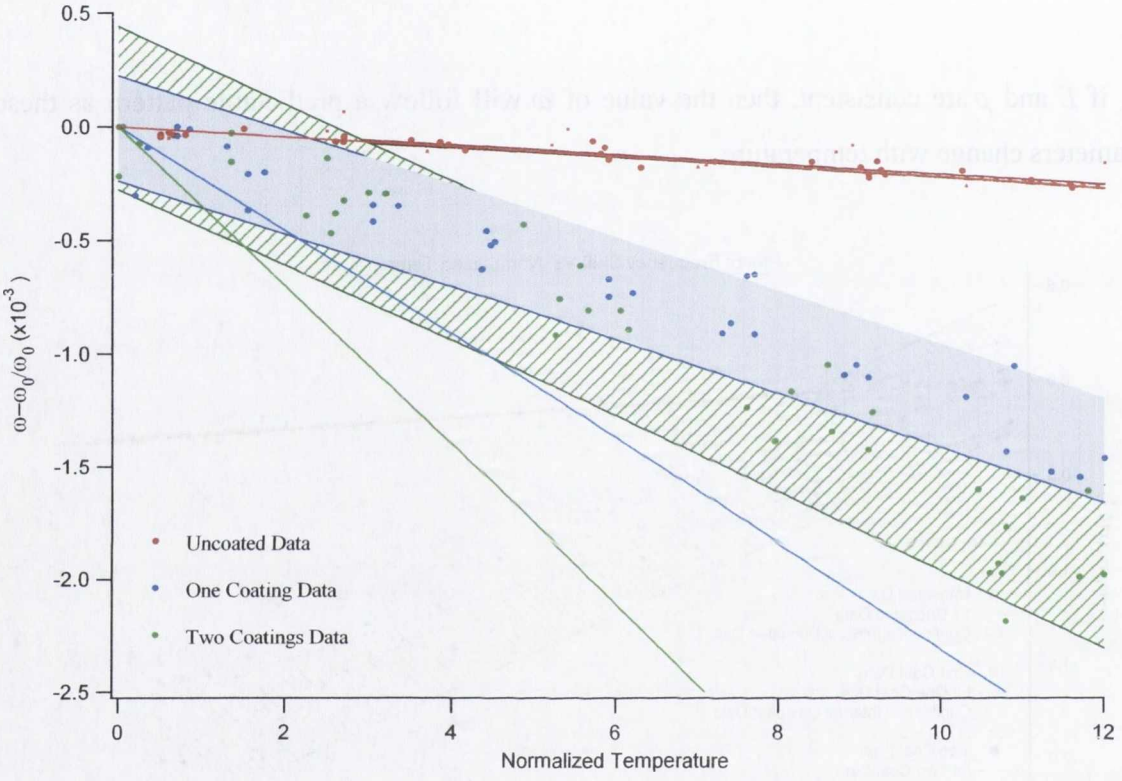

Figure 4.10 Graph of the shift in resonant frequency of an uncoated, single coating and two-sided coating cantilever as a function of temperature. There are 95% confidence intervals around the experimental data. The theory lines correspond to the calculated effect of changing the temperature on Young's modulus, air pressure, and air viscosity, and how this will affect the resonant frequency.

Figure 4.10 shows both the theoretical data lines and the experimental data points obtained through the measurement of the resonant frequency of the cantilevers at all stages throughout the experimental process. Figure 4.10 shows that the theoretical data correlates with the experimental data for the uncoated cantilevers. This is to be expected as all of the possible properties that change with temperature have been modeled into the theoretical response lines, listed in Equations 4.8 – 4.12 given previously. Upon examining the theoretical

response lines, listed in Equations 4.8 – 4.12 given previously. Upon examining the theoretical lines and experimental data points for the one- and two-coated cantilevers, the theoretical and experimental lines do not correlate. In order to deduce why this occurred, several factors were examined, and are discussed in the following sections.

4.4.2 Layer Thickness Calculations

It is possible to calculate the thickness value that corresponds to the frequency shifts that were observed, using Equation 4.15, and comparing this to the measured thickness obtained from the value given by the thickness metre in built in the sputter-coating system used to coat the cantilevers.

For the purpose of this comparison, it is acceptable to estimate that $E_{Al} \sim E_{Si}$, and $\rho_{Al} \sim \rho_{Si}$.

Therefore,

$$\frac{\omega_{layer}}{\omega_{uncoated}} \sim \frac{t_b}{t_a} \qquad \textbf{Equation 4.15}$$

and for example, for cantilever A:

$$1 \sim \frac{t_b}{t_a}$$

$$t_b \sim 100 \text{ nm}$$

That is, according to the shift in resonant frequency from the uncoated to the single coating of cantilever A, the thickness of the upper layer is approximately 100 nm. However the measured thickness is 1.2 μm. Thus, the frequency data tells us that the effective thickness is ~12 times less than the actual thickness. This result is consistent for the other three cantilevers, see Table 4.4.

Table 4.4. Thickness measurements and calculations for each cantilever. The thicknesses were measured by SEM.

	Cantilever A	Cantilever B	Cantilever C	Cantilever D
Beam Thickness, t_a	2.4×10^{-6} m	2.1×10^{-6} m	2.4×10^{-6} m	2.5×10^{-6} m
Measured t_b	1.2×10^{-6} m	1.2×10^{-6} m	0.8×10^{-6} m	0.8×10^{-6} m
Calculated t_b *(approximate values)*	0.01×10^{-6} m	0.01×10^{-6} m	0.07×10^{-6} m	0.08×10^{-6} m

There is clearly a problem with the layer that was deposited on the cantilevers and problem was further verified by examining the Q values obtained during the experiment, which is discussed in the next section.

4.4.3 Q Data Analysis

Upon further examination of the data it became apparent, that while the direction of change in frequency was qualitatively responding in the predicted manner, the values of Q were not (see Figure 4.11).

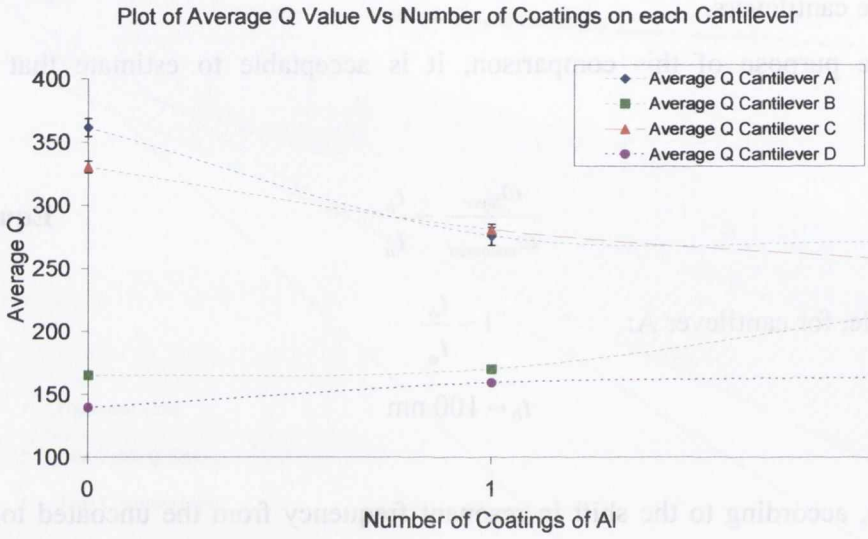

Figure 4.11 Plot of Average Q *vs* number of coatings

Ideally Q should increase as m^*, the effective mass, and ω, increase as shown in Equation 4.16:

$$Q = \frac{m^* \omega}{b} \qquad \textbf{Equation 4.16}$$

where b is a damping coefficient. However, cantilevers A and C (the two shorter cantilevers) exhibit decreasing Q with increasing m* (see Figure 4.11), *i.e.* the opposite behavior to that predicted. When there is damping only due to ambient air, this will typically give $b < m^*\omega$, which leads to an increase in Q as the effective mass, m^*, and the resonant frequency, ω, increase or *vice versa*. For Q to decrease it indicates that there is a much greater damping

present than just that from the surrounding air. The only other source of damping in this system is from the cantilever itself. This result and that from the calculation of the effective thickness of the layer, indicated that there was a problem with the quality of the layer and the way in which it was bonded to the surface of the cantilever. So at this point, the cantilever was broken at the base and imaged with an SEM. From these images it was determined that the nature of the layer was not pure Aluminium as was initially thought and upon which the calculations were based, but a porous material, as shown in Image 4.2. This may have been caused by heating effects in the instrument during deposition which resulted in this discrepancy between the target thickness and the actual thickness.

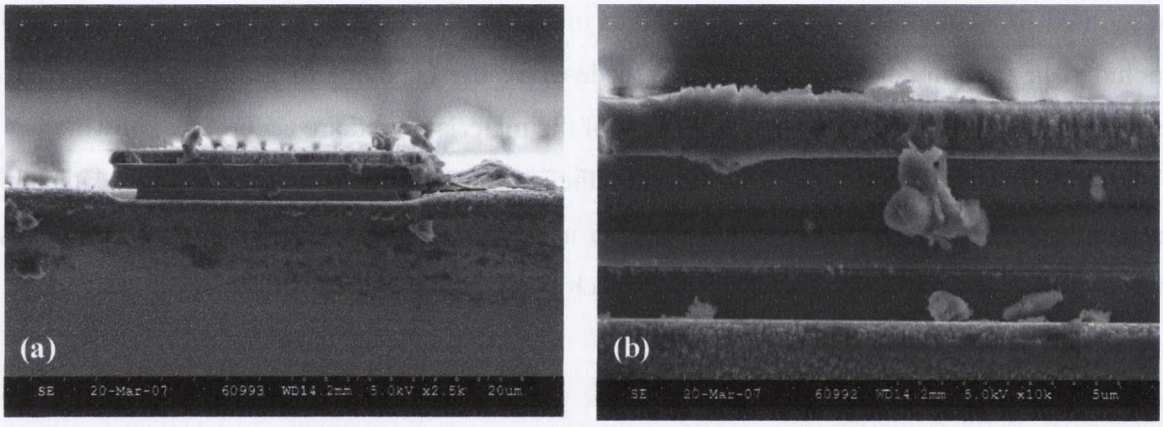

Image 4.2 Image of broken cantilever. The porous nature of the coating material can be seen from this picture. (a) A view of the end of the cantilever and some of the chip upon which it is mounted. (b) A close up view of the end of the cantilever.

As the coatings are not pure Aluminium, the calculations shown in Figures 4.9 and 4.10 are invalid as we do not accurately know the mechanical properties of the coating material. Since it is not known with any accuracy what E and ρ are for this porous material, we cannot predict what $\Delta\omega$ will be.

From Figure 4.11, it is clear that only the Q for the two short cantilevers (A and C) decreases. The Q for cantilevers B and D stays approximately the same throughout the experiment. The longer cantilevers have a low Q value and so quite large damping, thus the damping effect from the porous layer is not that considerable in comparison. However, the short cantilevers have high Q values and correspondingly much lower damping and so the additional damping from the layer has a considerable effect on the Q value.

4.5 Conclusion

In order to asses the validity of Lagowski's model, the layer properties must be accurately known so that the $\Delta\sigma^T$ can be calculated. For this, a clean, homogeneous layer with a clean mechanical attachment to the surface of the cantilever is necessary.

There were several problems with this experiment that resulted in unexpected resonant frequency and Q responses. Firstly, the exact composition of the coatings is not known, due to problems with the equipment as discussed previously. Secondly, that the layer is inhomogeneous suggests that it will not be strongly attached to the cantilever surface. This will induce less surface stress than that accounted for within the proposed theoretical model. Finally, the porous nature of the layer leads to additional damping which again, is not accounted for within the theoretical model as previously discussed. These variables cannot be included in this model as it is designed to describe the behavior of homogeneously coated cantilevers, where the mechanical properties of the materials used are accurately known.

In order to examine fully if this theory represents the experimental data, this experiment will have to be repeated, using an improved deposition technique. Unfortunately, due to time constraints, this has not yet been achieved. However, it is topic for future work.

Chapter 5
Experimental

5 EXPERIMENTAL

5.0 General Experimental Details

All chemicals were obtained from Sigma-Aldrich, Fluka, or Lancaster and were used without further purification. Deuterated solvents for NMR were purchased from Apollo. Dry solvents were prepared using standard procedures according to Vogel, with distillation prior to each use. Chromatographic columns were run using silica gel 60 (230-400 mesh ASTM) or Aluminium Oxide (activated, Neutral, Brockman I STD grade 150 mesh). Solvents for synthetic purposes were used at GPR grade unless otherwise stated. Analytical TLC was performed using Merck Kieselgel 60 F_{254} silica plates or Polygram Alox N/UV_{254} Aluminium Oxide plates. Visualisation was by UV light (254 nm), or by immersion in aqueous alkaline $KMnO_4$ solution. NMR spectra were recorded at 400 MHz using a Bruker Spectrospin DPX-400 instrument that operates at 400.13 MHz or at 600 MHz, using a Bruker Avance II that operates at 600.13 MHz, for ^{1}H-NMR and 150.9 MHz for ^{13}C NMR. Tetramethylsilane (TMS) was used as an internal reference standard, with chemical shifts expressed in parts per million (ppm) downfield from the standard. Multiplicities are abbreviated as follows: singlet (s), doublet (d), triplet (t), quintet (q) and multiplet (m). NMR titrations were performed at 293 °K. Mass Spectra were determined by detection using electrospray on a Mass Lynx NT V 3.4 on a Waters 600 Controller connected to a 996 photodiode array detector with HPLC-grade methanol, water, or acetonitrile as carrier solvents. Accurate molecular weights were determined by a peak-matching method, using leucine enkephaline(H-Tyr-Gly-Gly-Phe-Leu-OH) as the standard internal reference (m/z = 556.2771); all accurate mass were calculated to $\leq$ 5 ppm. Samples were prepared as solutions in methanol or acetonitrile. Melting points were determined using an electrothermal 1A9000 melting point apparatus in an unsealed capillary tube. Infrared spectra were recorded on a Perkin Elmer Spectrum One FT-IR spectrometer fitted with a Universal ATR Sampling Accessory. Atomic force microscopy work was performed on an Asylum Research Atomic Force Microscope. The gold samples were made by thermally evaporating gold using an Auto 500 Electron Beam Evaporation System. This system was also used to thermally evaporate copper to coat the cantilevers in Chapter 5. Elemental analysis was carried out at the microanalysis laboratory, School of Chemistry and Chemical Biology, University College Dublin.

5.1 General physical methods

The lanthanide metal salts $Eu(CF_3SO_3)_3$, $Tb(CF_3SO_3)_3$, and $Sm(CF_3SO_3)_3$ were purchased from Aldrich and were dried under high vacuum over P_2O_5. The ligands were prepared as described in Chapter 2 and they were dried over P_2O_5 under vacuum prior to use.

5.2 UltraViolet-Visible spectroscopy

UV-Visible absorption spectra were recorded with a Varian CARY 50 spectrophotometer. The solvents used were of HPLC grade. The wavelength range was 230 - 540 nm with a scan rate of 600 nm min^{-1}. The blank used was a sample of the solvent system the titration was undertaken in, either CH_3CN or $CH_3CN/CHCl_3$ (50:50, v/v). Baseline correction measurements were used in all spectra. The ligand concentration was 1 x 10^{-5} M for all of the UV-Vis titrations described. All stock solutions were prepared freshly before measurement.

5.3 Luminescence Measurements

Fluorescence and luminescence measurements were recorded in a Varian Carey Eclipse Fluorimeter with a 1.0 cm path length quartz cell. The solvents used were all of HPLC grade. The data in the luminescence titrations was obtained between 550 and 750 nm. The concentrations of the ligands and complexes examined were the same as those used for the UV-Visible absorption measurements (Section 5.2). The settings of the fluorimeter for the luminescence measurements carried out in chapters 2 and 3 are shown in Tables 5.1 – 5.2.

Table 5.1 Luminescence settings for the titrations described in Chapter 2 (CH_3CN 100% and $CH_3CN/CHCl_3$ (50:50, v/v)).

Luminescence Settings		
Mode: Phosphorescence	**Excitation:** 280 nm	**Scan:** 550 – 750 nm
Excitation Slit: 20 nm	**Emission Slit:** 2.5 nm	**PMT Voltage:** 700 V
Flash Count: 1	**Gate Time:** 5 ms	**Delay Time:** 0.2 ms
Averaging Time: 0.05 s	**Total Decay Time:** 0.02 s	**Data Interval:** 1.0 nm

Table 5.2 Luminescence settings for the titrations described in Chapter 3

Luminescence Settings		
Mode: Phosphorescence	**Excitation:** 280 nm	**Scan:** 550 – 750 nm
Excitation Slit: 20 nm	**Emission Slit:** 20 nm	**PMT Voltage:** 1000 V
Flash Count: 1	**Gate Time:** 5 ms	**Delay Time:** 0.2 ms
Averaging Time: 0.1 s	**Total Decay Time:** 0.02 s	**Data Interval:** 1.0 nm

5.4 Lifetime determination for Ln^{III} complexes

Luminescence lifetime measurements of **Eu57** (*S,S*) and **Eu58** (*R,R*) were carried out in CH_3CN/H_2O and CD_3CN/D_2O, and CH_3OH/H_2O (80:20, v/v) and CD_3OD/D_2O (80:20, v/v), on a Varian Carey Eclipse Fluorescence spectrophotometer. The settings for the Varian Carey Eclipse Fluorescence spectrophotometer are shown in Table 5.3.

Table 5.3 Settings for the Varian Carey Eclipse Fluorescence spectrophotometer for measuring lifetimes.

Lifetime Settings			
Direct Excitation:	Eu^{III} – 395 nm	**Emission:**	616 nm
Total Decay:	200, 100 or 50 ms	**Delay:**	0.5 ms
No. Cycles:	100	**Gate:**	0.2 ms
Flash Count:	1	**PMT Voltage:**	600 V
Excitation Slit width:	20 nm	**Emission Slit width:**	10 nm

5.5 CD measurements

CD spectra were recorded on a Jasco J-810-150S spectropolarimeter. All CD spectra are reported as mdeg *vs* λ (nm). The baseline solvent was taken and removed from the spectra shown. These spectra were recorded in methanol, HPLC grade, at a concentration of 1×10^{-4}M.

5.6 CPL measurements

Circularly polarised luminescence spectra were recorded at the University of Glasgow. Excitation of the Eu^{III} (560 – 581 nm) was accomplished using a Coherent 599 tuneable dye laser (0.03 nm resolution) with an argon ion laser as a pump source. The laser dye used in the measurement was Rhodamine 100 in ethylene glycol. Calibration of the emission monochromator (and subsequently the dye laser) was accomplished by passing scattered light from a low power He-Ne laser through the detection system. The error in the dye laser wavelength was assumed to be equal to the resolution of the emission detection. Optical detection consisted of a photoelastic modulator (PEM, Hinds Int.) operating at 50 kHz and a liner polariser, which together act as a circular analyser, followed by a long pass filter, focusing lens and a 0.22 m double monochromator. The emitted light was detected by a cooled EM1-9558QB photomultiplier tube operating in photon counting mode. The output pulses from the photomultiplier tube were passed through a variable gain amplifier/discriminator and input into a purpose built differential photon counter. The 50 kHz reference signal from the photoelastic modulator was used to direct the incoming pulses into two separate counters, an up-counter, which counts every photon pulse and thus is a measure of the total luminescence signal $I = I_{left} + I_{right}$, and an up/down counter, which adds pulses when the analyser is transmitting left circularly polarised light and subtracts when the analyser is transmitting right circularly polarised light. This second counter provides a measure of the differential emission intensity $\Delta I = I_{left} - I_{right}$. The differential photon counter allows for the selection of a time window for counting, which is centred around the maximum in the modulation cycle. For the measurements reported in this thesis, the window was set to 50%.

5.7 General Synthetic Procedures for Chapter 2

Procedure 1: Coupling Reaction of chelidamic acid with an amine using EDCI•HCl

To a stirred solution of 1-(1-naphthyl)-ethylamine (2 equivalents) in anhydrous THF, HOBt (2 equiv) and the 2,6-pyridinedicarboxylic acid derivative (1 equivalent) were added. The solution was stirred for 30 minutes at 0 °C before EDCI•HCl (2.05 equivalents) and triethylamine (2.05 equivalents) were added, and then stirred for a further 30 minutes under argon. The reaction was allowed to reach room temperature and the mixture left stirring for 48 h. The insoluble residue was removed by filtration suction and the solvent removed under

reduced pressure. DCM was added to the crude oil and washed twice with 0.1 M HCl, a saturated solution of $NaHCO_3$, and water. The organic layer was then dried over $MgSO_4$, filtered, and the solvent removed under reduced pressure. The product was then purified by column chromatography using flash silica, 95:5; DCM:MeOH.

(57) 4-hydroxy pyridine-2,6-dicarboxylic acid bis-(*S*) [(1-naphthalen-1-yl-ethyl)-amide]

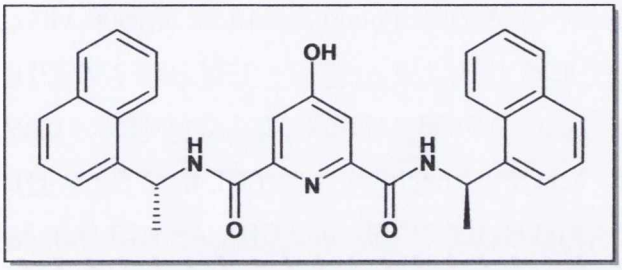

Compound **57** was synthesised by stirring a solution of (*S*)-(-)-1-(1-Naphthyl)ethylamine (1.04 g, 6.08 mmol) in anhydrous THF (50 mL), HOBt (0.78g, 5.79 mmol) and chelidamic acid (0.4 g, 2.89 mmol) for 30 minutes at 0 °C before EDCI•HCl (1.14 g, 5.9 mmol) and TEA (0.83 mL, 5.9 mmol) were added according to **Procedure 1**. A pale brown solid was obtained. The product was then purified by column chromatography using flash silica, 95:5; DCM:MeOH, and a cream coloured solid was obtained (1.41 g, 2.89 mmol, 64% yield). m.p. 158 – 160 °C; Calculated for $C_{31}H_{27}N_3O_3 \cdot \frac{1}{3}\ CH_3OH \cdot \frac{1}{3}\ H_2O$: C, 74.3; H, 5.77; N, 8.30% Found $C_{31}H_{27}N_3O_3 \cdot \frac{1}{3}\ CH_3OH \cdot \frac{1}{3}\ H_2O$: C, 74.50; H, 5.74; N, 8.74%; Calculated for $C_{31}H_{27}N_3O_3$: (M + Na) m/z = 512.1946; Found 512.1950; δ_H (600 MHz, CD_3CN, 298 K) 8.55 (1H, d, N-H, J = 1.25 Hz), 8.25 (2H, d, 2 Ar-H, J = 1.38 Hz), 7.97 (2H, d, 2 naph-H, J = 1.56 Hz), 7.87 (2H, d, 2 naph-H, J = 1.38 Hz), 7.70 (2H, d, 2 py-H, J = 0.69 Hz), 7.68 (2H, d, 2 naph-H, J = 1.19 Hz), 7.58 (2H, m, 2 naph-H), 7.55 (2H, m, 2 naph -H), 7.54 (2H, m, 2 naph -H), 6.07 (2H, q, 2 CH, J = 3.63 Hz), 1.73 (6H, d, 2 CH_3, J = 1.13 Hz); δ_C (100 MHz, CD_3CN, 298 K) 167.0 (C - py) 163.6 (C=O), 152.0 (C-OH), 140.3, 134.9, 131.9, 129.8, 128.8, 127.3, 126.7, 126.4, 124.2, 123.9, 113.0 (CH-py), 112.4 (NH), 46.1 (CH), 21.4 (CH_3). IR υ_{max} (cm^{-1}) 3283.12, 1652.91, 1600.16, 1520.94, 1448.98, 1354.83, 1237.73, 1178.26, 1135.91, 996.73, 888.64, 856.76, 799.25, 775.07, 691.07.

(58) 4-hydroxy pyridine-2,6-dicarboxylic acid bis-(*R*) [(1-naphthalen-1-yl-ethyl)-amide]

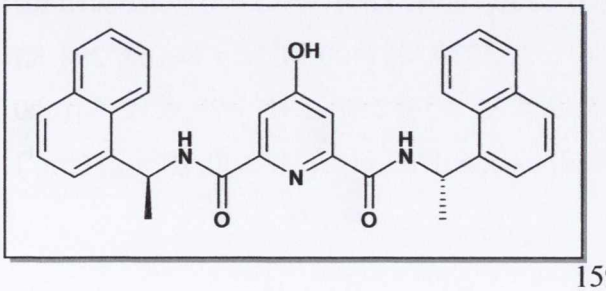

Compound **58** was synthesised by stirring a solution of (*R*)-(+)-1-(1-Naphthyl)ethylamine, (1.04 g, 6.08 mmol) in anhydrous THF (50 mL), with HOBt (0.78g, 5.79 mmol) and

chelidamic acid (0.4 g, 2.89 mmol) for 30 minutes at 0 °C before EDCI•HCl (1.14 g, 5.9 mmol) and TEA (0.83 mL, 5.9 mmol) were added according to **Procedure 1**. A pale brown solid was obtained. The product was then purified by flash column chromatography using neutral silica, 95:5; DCM:MeOH, and a cream coloured solid was obtained. (1.08 g, 2.20 mmol, 49% yield). m.p. 158 – 160 °C; Calculated for $C_{31}H_{27}N_3O_3 \cdot \frac{1}{3}\ CH_3OH \cdot \frac{1}{3}\ H_2O$: C, 74.30; H, 5.77; N, 8.30% Found $C_{31}H_{27}N_3O_3 \cdot \frac{1}{3}\ CH_3OH \cdot \frac{1}{3}\ H_2O$: C, 74.73; H, 5.75; N, 8.55%; Calculated for $C_{31}H_{27}N_3O_3$: (M + Na) m/z = 512.1946; Found 512.1950; δ_H (600 MHz, CD_3CN, 298 K) 8.55 (1H, d, N-H, J = 1.25 Hz), 8.25 (2H, d, 2 Ar-H, J = 1.38 Hz), 7.97 (2H, d, 2 naph-H, J = 1.56 Hz), 7.87 (2H, d, 2 naph-H, J = 1.38 Hz), 7.70 (2H, d, 2 py-H, J = 0.69 Hz), 7.68 (2H, d, 2 naph-H, J = 1.19 Hz), 7.58 (2H, m, 2 naph-H), 7.55 (2H, m, 2 naph -H), 7.54 (2H, m, 2 naph -H), 6.07 (2H, q, 2 CH, J = 3.63 Hz), 1.73 (6H, d, 2 CH_3, J = 1.13 Hz); δ_C (100 MHz, CD_3CN, 298 K) 167.0 (C - py) 163.6 (C=O), 152.0 (C-OH), 140.3, 134.9, 131.9, 129.8, 128.8, 127.3, 126.7, 126.4, 124.2, 123.9, 113.0 (CH-py), 46.1 (CH), 21.4 (CH_3). IR υ_{max} (cm^{-1}) 3283.12, 1652.91, 1600.16, 1520.94, 1448.98, 1354.83, 1237.73, 1178.26, 1135.91, 996.73, 888.64, 856.76, 799.25, 775.07, 691.07.

Procedure 2: General Synthesis of Ln^{III} Complexes

Compound **57**, 4-hydroxy pyridine-2,6-dicarboxylic acid bis-(*S*) [(1-naphthalen-1-yl-ethyl)-amide] or **58**, 4-hydroxy pyridine-2,6-dicarboxylic acid bis-(*R*) [(1-naphthalen-1-yl-ethyl)-amide] (0.083 mmol) and Ln^{III} Trifluoromethanesulphonate (0.027 mmol) were added to a 10 mL RBF that contained freshly dried MeOH (5 mL). The solution was freeze-thawed three times, placed under an argon atmosphere, and left stirring at reflux for 24 hrs. The resulting solution was cooled to room temperature and then precipitated slowly in diethyl ether (100 mL). The solid was filtered off, recrystallised from MeOH, and dried under vacuum.

(Eu.57) (*S,S*) 4-hydroxy pyridine-2,6-dicarboxylic acid bis-(*S*) [(1-naphthalen-1-yl-ethyl)-amide] Eu^{III}

m.p. 230 - 232°C; Calculated for $C_{96}H_{81}EuF_9N_9O_{18}S_3 \cdot (CH_3CH_2)_2O$: C, 55.44; H, 4.51; N, 6.06% Found $C_{96}H_{81}EuF_9N_9O_{18}S_3 \cdot (CH_3CH_2)_2O$: C, 56.76; H, 4.30; N, 6.35%; Calculated for $C_{31}H_{27}O_3N_3Eu$: $(M/2)^+$ m/z = 1620.5448; Found 1620.5370; δ_H (400 MHz, CD_3OD, 298 K) 10.30, 10.28, 8.29, 7.43, 7.18, 7.16, 6.56, 6.55, 5.99, 4.92, 3.36, 2.97, 2.31, 1.29, 0.11; δ_H (600 MHz, CD_3CN, 298 K) 10.09, 9.85, 8.27, 7.46, 7.22, 6.63, 6.07, 5.11, 3.24, 2.30. IR υ_{max} (cm^{-1})

330.05, 2975.28, 1616.80, 1555.10, 1450.91, 1373.92, 1239.72, 1165.27, 1023, 961.47, 878.79, 798.51, 774.99.

(Eu.58) (*R,R*) 4-hydroxy pyridine-2,6-dicarboxylic acid bis-(*R*) [(1-naphthalen-1-yl-ethyl)-amide] Eu^{III}

m.p. 230 - 232°C; Calculated for $C_{96}H_{81}EuF_9N_9O_{18}S_3 \cdot (CH_3CH_2)_2O$: C, 55.44; H, 4.51; N, 6.06% Found $C_{96}H_{81}EuF_9N_9O_{18}S_3 \cdot (CH_3CH_2)_2O$: C, 53.48; H, 4.16; N, 5.69%; Calculated for $C_{31}H_{27}O_3N_3Eu$: $(M/2)^+$ m/z = 1620.5448; Found 1620.5370; δ_H (400 MHz, CD_3OD, 298 K) 10.30, 10.28, 8.29, 7.43, 7.18, 7.16, 6.56, 6.55, 5.99, 4.92, 3.36, 2.97, 2.31, 1.29, 0.11; δ_H (600 MHz, CD_3CN, 298 K) 10.09, 9.85, 8.27, 7.46, 7.22, 6.63, 6.07, 5.11, 3.24, 2.30. IR υ_{max} (cm^{-1}) 330.05, 2975.28, 1616.80, 1555.10, 1450.91, 1373.92, 1239.72, 1165.27, 1023, 961.47, 878.79, 798.51, 774.99.

(Tb.57) (*S,S*) 4-hydroxy pyridine-2,6-dicarboxylic acid bis-(*S*) [(1-naphthalen-1-yl-ethyl)-amide] Tb^{III}

m.p. 230 - 232°C; Calculated for $C_{96}H_{81}TbF_9N_9O_{18}S_3$: C, 55.25; H, 4.49; N, 6.04% Found $C_{96}H_{81}TbF_9N_9O_{18}S_3$: C, 55.36; H, 4.13; N, 6.32%; Calculated for $C_{31}H_{27}O_3N_3Tb$: $(M/2)^+$ m/z = 1626.5346; Found 1626.5411; δ_H (400 MHz, CD_3OD, 298 K) 39.81, 38.00, 30.64, 25.25, 19.76, 12.47, 10.25, 9.94, 7.16, 5.54, 4.86, 4.41, 3.79, 3.55, 3.07, 2.41, -1.99, -9.97, -28.07; IR υ_{max} (cm^{-1}) 3295.96, 1617.87, 1598.06, 1554.79, 1450.73, 1372.67, 1237.59, 1164.30, 1022.31, 961.12, 880.00, 799.35, 774.67.

(Tb.58) (*R,R*) 4-hydroxy pyridine-2,6-dicarboxylic acid bis-(*R*) [(1-naphthalen-1-yl-ethyl)-amide] Tb^{III}

m.p. 230 - 232°C; Calculated for $C_{96}H_{81}TbF_9N_9O_{18}S_3$: C, 55.25; H, 4.49; N, 6.04% Found $C_{96}H_{81}TbF_9N_9O_{18}S_3$: C, 50.74; H, 3.87; N, 5.51%; Calculated for $C_{31}H_{27}O_3N_3Tb$: $(M/2)^+$ m/z = 1626.5346; Found 1626.5411; δ_H (400 MHz, CD_3OD, 298 K) 39.81, 38.00, 30.64, 25.25, 19.76, 12.47, 10.25, 9.94, 7.16, 5.54, 4.86, 4.41, 3.79, 3.55, 3.07, 2.41, -1.99, -9.97, -28.07; IR υ_{max} (cm^{-1}) 3295.96, 1617.87, 1598.06, 1554.79, 1450.73, 1372.67, 1237.59, 1164.30, 1022.31, 961.12, 880.00, 799.35, 774.67.

5.8 Synthesis for Chapter 3

(66) 1, 4, 7-tris(N-naphthalene-1-yl-acetamide)-1,4,7,10-tetraazacyclododecane

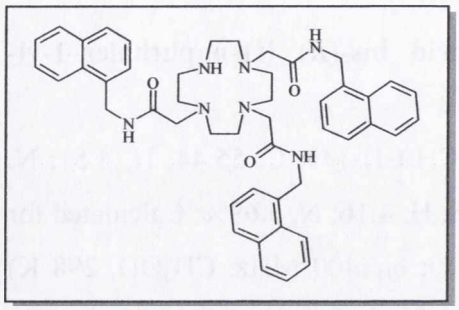

Compound **66** was synthesised by refluxing Cyclen, (0.34 g, 2 mmol), 2-chloro-*N*-naphthalen-1-yl-acetamide, (0.94 g, 6 mmol) and $NaHCO_3$ (0.5 g, 6 mmol) under argon in dry CH_3CN (100 mL) for two days. The mixture was then filtered through celite and the solvent removed under reduced pressure. The product was then purified by flash column chromatography using neutral silica, with a gradiated eluent 1%-5% $CH_3OH(NH_3)$ in DCM. The product was collected as a brown oil. (0.9g, 1.1 mmol, 59%) ^{1}H NMR ($CDCl_3$) δ 8.00 (1H, d, C<u>H</u>) 7.91 (1H, d, C<u>H</u>) 7.86 (1H, dd, C<u>H</u>) 7.57 (2H, q, C<u>H</u>C<u>H</u>) 7.48 (2H, s, C<u>H</u>C<u>H</u>) 4.9 (6H, d, (C<u>H</u>$_2$)$_3$) 3.5 (6H, d, (C<u>H</u>$_2$)$_3$) 2.06 (s, cyclen) Calculated for $C_{47}H_{53}N_7O_3$: (M) m/z = 764.41; Found 764.43.

5.9 Gold Substrate Preparation

Flat gold substrates were prepared by sonicating circular discs of mica (9 mm diameter) in ethanol and then freshly cleaving them, before evaporating 10 - 15 nm of gold onto the cleaved surface. The mica discs were coated using either a home-built gold evaporator, or an Auto 500 Electron Beam Evaporation System. The gold source used was gold wire that had been sonicated in ethanol. Both evaporation systems used a tungsten basket as the heating element, and a quartz crystal thickness metre to determine the thickness of gold deposited. Upon removing the gold substrates from the vacuum chamber, they were immediately immersed in 1 mmol solution of the appropriate complex and left for a minimum time of twelve hours.

5.10 Measurements of Gold Substrates

In order to take luminescent measurements of the lanthanide complexes on the gold substrates, a home-modified quartz fluorescence cell was used. This included a quartz glass slide that was positioned at a 90° angle to the incoming beam and also to the detector. Luminescence measurements on gold substrates were carried out on a Varian Cary Eclipse Fluorescence Spectrophotometer, the parameters for this are listed in Table 5.2. The Infrared measurements were carried out on a Perkin Elmer Spectrum One FT-IR spectrometer fitted

with a Universal ATR Sampling Accessory. Atomic Force Microscopy images were taken in ethanol with and NSC-15 cantilever from Mikromasch on a home modified Asylum Research MFP-3D atomic force microscope.

5.11 Formation of Self Assembled Monolayers of Eu.29$_3$ in Chapter 3

Self-assembled monolayers of **Eu.29**, **Eu.29** and **30**, and **Eu.29**, **30** and **31** on gold were formed by immersing a freshly evaporated gold sample in a 1 mmol solution of the appropriate compound(s) in HPLC grade ethanol, overnight (unless otherwise stated). The sample was then removed, rinsed thoroughly with HPLC grade ethanol, and dried under flowing N_2.

5.12 Characterisation of Cantilevers in Chapter 4

The cantilevers used in the experiments described in Chapter 4, were Veeco Force Calibration cantilevers, CLFC-NOBO. Their dimensions were accurately measured by a scanning electron microscope. The spring constants were determined by using the Sader method.[165] The thicknesses of the coatings on the cantilevers were determined initially by SEM and the internal quartz crystal monitor within the vacuum chamber, and finally by cutting a section from the corner of the cantilever using a focused ion beam, and then measuring the thicknesses of the layers and cantilever using a scanning electron microscope.

All frequency measurements were carried out in an Asylum Research Bioheater cell that had been home-modified with three thermocouples to measure the temperature. The thermocouples were attached to an Agilent metre that converted the thermocouple reading into temperature. All frequencies were measured by monitoring the vibrations of the cantilever due to ambient thermal motion (Brownian motion) using an AFM optical beam detection signal fed into a frequency spectrum analyser.

5.13 Coating of Cantilevers in Chapter 4

The cantilevers used in the experiments described in Chapter 4 were prepared by firstly plasma cleaning them for one minute, in an Argon Plasma, using a Gala Instrumente plasma cleaner. They were then removed from the chamber and positioned on a clean glass slide over

a square sheet of mica (10 mm x 10 mm x <1 mm). They were not fixed using tape or any other adhesive. They were then coated using a Cressington 208HR sputter coater. Once a sufficient thickness had been deposited, the cantilevers were removed from the chamber and placed immediately in the modified Asylum Research BioHeater Cell, which was then sealed. To coat the underside of the cantilevers, they were carefully removed from the Asylum Research BioHeater Cell and placed upside down on the edge of a mica square, such that the cantilever was not in contact with anything, and only the chip upon which it was mounted was in contact with the mica. The coating procedure was then completed as before.

References

6 REFERENCES

1. Bünzli, J.-C., *Acc. Chem. Res.* **2006,** 39, 53 - 61.
2. Cotton, S., *Lanthanides and Actinides.* 1 ed.; Macmillan Education Ltd.: London, 1991; p 192.
3. Piguet, C.; Bünzli, J.-C., *Chem. Soc. Rev.* **1999,** 28, 347 - 358.
4. Aspinall, H. C., *Chemistry of the f-block elements.* Australia ; [Great Britain] : Gordon & Breach: 2001.
5. Schultz, R. A.; White, B. D.; Dishong, D. M.; Arnold, K. A.; Gokel, G. W., *J. Am. Chem. Soc* **1985,** 107, 6659-6668.
6. Beer, P. D.; Dent, S. W.; West, T. J., *J.Chem. Soc., Dalton Trans.* **2001**, 2341-2346.
7. Parker, D., *Coord. Chem. Rev.* **2000,** 205, 109-130.
8. Alpha, B.; Ballardini, R.; Balzani, V.; Lehn, J.-M.; Perathoner, S.; Sabbatini, N., *Photochem. & Photobiol.* **1990,** 52, (2), 299-306.
9. Parker, D.; Williams, J. A. G., *J. Chem. Soc., Dalton. Trans.* **1996,** 123, 201-228.
10. Sabbatini, N.; Guardigli, M.; Lehn, J.-M., *Coord. Chem. Rev.* **1993,** 123, 201-228.
11. Beeby, A.; Faulkner, S.; Parker, D.; Williams, J. A. G., *J. Chem. Soc., Perkin. Trans, 2* **2001**, 1268-1273.
12. Forster, T., *Discuss. Faraday Soc.* **1959,** 27, 7 - 17.
13. Dexter, D., *J. Phys. Chem.* **1953,** 21, 836.
14. Massue, J.; Quinn, S.; Gunnlaugsson, T., *J. Am. Chem. Soc.* **2008,** 130, (22), 6900-6901.
15. Bruce, J. I.; Dickins, R. S.; Govenlock, L. J.; Gunnlaugsson, T.; Lopinski, S.; Lowe, M. P.; Parker, D.; Peacock, R. D.; Perry, J. J. B.; Aime, S.; Botta, M., *J. Am. Chem. Soc.* **2000,** 122, 9674-9684.
16. Dickins, R. S.; Gunnlaugsson, T.; Parker, D.; Peacock, R. D., *Chem. Commun.* **1998,** 18, 1643 - 1644.
17. Beeby, A.; Clarkson, I. M.; Dickens, R. S.; Faulkner, S.; Parker, D.; Royle, L.; Sousa, A. S. d.; Williams, J. A. G.; Woods, M., *J. Chem. Soc., Perkin Trans. 2.* **1999**, 493-503.
18. Horrocks, W. D. J.; Sudnick, D. R., *Journal of the American Chemical Society* **1979,** 101, 334 - 340.
19. Horrocks, W. D.; Sundick, D. R., *Acc. Chem. Res.* **1981,** 14, 384-392.
20. Supowski, R. M.; Horrocks, W. D., *Inorganica Chimica Acta* **2002**, (340), 44 - 48.

21. Beeby, A.; Dickins, R. S.; Faulkner, S.; Parker, D.; Williams, J. A. G., *Chem. Commun.* **1997**, 1401 - 1402.

22. Ji, H.-F.; Dabestani, R.; Brown, G. M.; Hettich, R. L., *Photochem. & Photobiol.* **1999,** 65, (5), 513-516.

23. Bünzli, J.-C. G.; Piguet, C., *Chem. Soc. Rev.* **2005,** 34, 1048 - 1077.

24. Caravan, P.; Ellison, J. J.; McMurry, T. J.; Lauffer, R. B., *Chem. Rev.* **1999,** 99, (9), 2293-2352.

25. FDA, U. S., FDA Requests Boxed Warning for Contrast Agents Used to Improve MRI Images. In U.S.; Department; of; Health; and; Human; Services, Eds. 2007.

26. Montalti, M.; Prodi, L.; Zaccheroni, N.; Charbonnie`re, L.; Douce, L.; Ziessel, R., *J. Am. Chem. Soc.* **2001,** 123, (50), 12694-12695.

27. Yamada, T.; Shinoda, S.; Tsukube, H., *Chem. Commun.* **2002,** 11, 1218 - 1219.

28. Hanaoka, K.; Kikuchi, K.; Kojima, H.; Urano, Y.; Nagano, T., *Angew. Chemie Int. Ed.* **2003,** 42, (26), 2996-2999.

29. Hanaoka, K.; Kikuchi, K.; Kojima, H.; Urano, Y.; Nagano, T., *J. Am. Chem. Soc.* **2004,** 126, 12470 - 12476.

30. Cotton, F. A.; Wilkinson, G., *Advanced Inorganic Chemistry.* 5th ed.; Wiley Interscience: 1988.

31. Bünzli, J.-C. G., *Journal of Alloys and Compounds* **2006,** 408 - 412, 934 - 944.

32. Bünzli, J.-C. G.; Andr´e, N.; Elhabiri, M.; Muller, G.; Piguet, C., *Journal of Alloys and Compounds* **2000,** 303/304, 66.

33. Gunnlaugsson, T.; Davies, R. J. H.; Nieuwenhuyzen, M.; O'Brien, J. E.; Stevenson, C. S.; Mulready, S., *Polyhedron* **2003,** 22, (5), 711 - 724.

34. Gunnlaugsson, T.; O'Brien, J. E.; Mulready, S., *Tetrahedron Letters* **2002,** 43, 8493-8497.

35. Gunnlaugsson, T.; Davies, R. J. H.; Kruger, P. E.; Jensen, P.; McCabe, T.; Mulready, S.; O'Brien, J. E.; Stevenson, C. S.; Fanning, A.-M., *Tetrahedron Letters* **2005,** 46, (21), 3761-3766.

36. Zucchi, G.; Ferrand, A. C.; Scopelliti, R.; Bünzli, J.-C., *Inorganic Chemistry* **2002,** 41, (9), 2459 - 2465.

37. Parker, D.; Senanayake, P. K.; Williams, J. A. G., *J. Chem. Soc., Perkin Trans. 2.* **1998,** 2129-2139.

38. Wang, E.; Meyerhoff, M. E., *Analytica Chimica Acta* **1993,** 283, (2), 673-682.

39. Gunnlaugsson, T.; Harte, A. J.; Leonard, J. P.; Nieuwenhuyzen, M., *Chem. Commun.* **2002**, 2134.
40. Bretonnière, Y.; Cann, M. J.; Parker, D.; Slater, R., *Chem. Commun.* **2002,** 17, 1930 - 1931.
41. Pal, R.; Parker, D., *Chem. Commun.* **2007**, 474.
42. Senechal-David, K.; Leonard, J. P.; Plush, S. E.; Gunnlaugsson, T., *Org. Lett.* **2006,** 8, 2727.
43. Pope, S. J.; Laye, R. H., *Dalton Trans.* **2006**, 3108 - 3113.
44. B¨unzli, J.-C. G.; Piguet, C., *Chem. Rev.* **2002,** 102, 1897.
45. Michels, J. J.; Huskens, J.; Reinhoudt, D. N., *J. Am. Chem. Soc.* **2002,** 124, (9), 2056 - 2064.
46. dos Santos, C. M. G.; Harte, A. J.; Quinn, S. J.; Gunnlaugsson, T., *Coord. Chem. Rev.* **2007**.
47. Bünzli, J.-C. G.; Comby, S.; Chauvin, A. S.; Vandevyver, C. D. B., *Journal of Rare Earths* **2007,** 25, 257 - 274.
48. Piguet, C.; Williams, J. A. F.; Bernardinelli, G.; Bunzli, J.-C., *Inorg. Chem.* **1993,** 32, 4139-4149.
49. Borgne, T. L.; Benech, J. M.; Floquet, S.; Bernardinelli, G.; Aliprandini, C.; Bettens, P.; Piguet, C., *Dalton Trans.* **2003**.
50. Renaud, F.; Piguet, C.; Bernardinelli, G.; G., B.-C.; Hopfgartner, G., *Chem. Eur. J.* **1997,** 3, 1646.
51. Bünzli, J.-C. G.; Piguet, C., *Chem. Rev.* **2002,** 102, 1897.
52. Leonard, J. P.; Nolan, C. B.; Stomeo, F.; Gunnlaugsson, T., *Photochemistry and Photophysics of Coordination Compounds: Lanthanides, Topics in Current Chemistry.* 2007.
53. Gunnlaugsson, T.; Glynn, M.; Tocci, G. M.; Kruger, P. E.; Pfeffer, F. M., *Coord. Chem. Rev.* **2006,** 250, 3094-3117.
54. Parker, D.; Dickson, R. S.; Puschmann, H.; Crossland, C.; Howard, J. A. K., *Chem. Rev.* **2002,** 102, (6), 1977-2010.
55. Gunnlaugsson, T.; McCoy, C. P.; Stomeo, F., *Tetrahedron Letters* **2004,** 45, 8403 - 8407.
56. Niemeyer, C. M., *Angew. Chem. Int. Ed.* **2001,** 40, (4128).

57. Medintz, I. L.; Uyeda, H. T.; Goldman, E. R.; Mattoussi, H., *Nat Mater* **2005,** 4, (6), 435-446.
58. Ipe, B. I.; Yoosaf, K.; Thomas, K. G., *J. Am. Chem. Soc.* **2006.**
59. Lewis, D. J.; Day, T. M.; MacPherson, J. V.; Pikramenou, Z., *Chem. Commun.* **2006,** 1433.
60. Chen, Y.; Lu, Z., *Analytica Chimica Acta* **2007,** 587, 180–186.
61. Langmuir, I., *J. Am. Chem. Soc.* **1917,** 39, 1848.
62. Blodgett, K. B., *J. Am. Chem. Soc.* **1935,** 57, 1007.
63. Flink, S.; Veggel, F. C. M. v.; Reinhoudt, D. N., *Adv. Mater.* **2000,** 12, (8), 1315-1328.
64. Bigelow, W. C.; Pickett, D. L.; Zisman, W. A., *J. Colloid Interface Sci.* **1946,** 1, 513.
65. Roy, B. C.; Mallik, S., *Org. Lett.* **2001,** 3, (12), 1877-1879.
66. Blair, S.; Kataky, R.; Parker, D., *New J. Chem.* **2002,** 26, 530-535.
67. Allara, D. L.; Nuzzo, R. G., *Langmuir* **1985,** 1, 45.
68. de Bettencourt-Dias, A., *Dalton Trans.* **2007,** 2229.
69. Kido, J.; Okamoto, Y., *Chem. Rev.* **2002,** 102, 2357-2368.
70. Kido, J.; Nagai, K.; Okamoto, Y., *Journal of Alloys and Compounds* **1993,** 192, 30-33.
71. Li, S.; Zhong, G.; Zhu, W. H.; Li, F.; Pan, J.; Huang, W.; Tian, H., *J. Mater. Chem* **2005,** 15, 3221.
72. Armelao, L.; Bottaro, G.; Quici, S.; Cavazzini, M.; Raffo, M. C.; Barigellettic, F.; Accorsi, G., *Chem. Commun.* **2007,** 2911 - 2913.
73. Kopecek, J., *Eur. J. Pharm. Sci.* **2003,** 20, 1.
74. Wichterle, O.; Lim, D., *Nature* **1960,** 185, 117.
75. Tew, G. N.; Sanabria-DeLong, N.; Agrawalb, S. K.; Bhatia, S. R., *Soft Matter* **2005,** 1, 253–258.
76. Yaung, J.-F.; Kwei, T. K., *J. Appl. Pol. Sci.* **1997,** 69, (5), 921 - 930.
77. Bekiari, V.; Lianos, P., *Langmuir* **2006,** 22, (20), 8602-8606.
78. Bain, C. D.; Troughton, E. B.; Tao, Y.-T.; Evall, J.; Whitesides, G. M.; Nuzzo, R. G., *J. Am. Chem. Soc.* **1989,** 111, 321-335.
79. Kuhn, H., *J. Chem. Phys.* **1970,** 53, 101.
80. Kittredge, K. W.; Fox, M. A.; Whitesell, J. K., *J. Phys. Chem. B* **2001,** 105, (43), 10594-10599.
81. Rubenstein, I.; Steinberg, S.; Tor, Y.; Shanzer, A.; Sagiv, J., *Nature* **1988,** 332, 426.
82. Steinberg, S.; Tor, Y.; Sabatini, E.; Rubenstein, I., *J. Am. Chem. Soc.* **1991,** 113, 5176.

83. Steinberg, S.; Rubenstein, I., *Langmuir* **1992,** 8, 1183.

84. Gafni, Y.; Weizman, H.; Libm, a., J.; Shanzer, A.; Rubenstein, I., *Chem. Eur. J.* **1996,** 2, 759.

85. Stora, T.; Hovius, R.; Dienes, Z.; Pachoud, M.; Vogel, H., *Langmuir* **1997,** 13, 5211.

86. Flink, S.; van Veggel, F. C. J. M.; Reinhoudt, D. N., *J. Phys. Chem. B.* **1999,** 103, 6515.

87. Berggren, C.; Johansson, G., *Anal. Chem.* **1997,** 69, (18).

88. Ebright, Y. W.; Chen, Y.; Ludescher, R. D.; Ebright, R. H., *Bioconj. Chem. Commun.* **1993,** 4, 219-225.

89. Ma, W.; Hwang, K. J.; Lee, V. H. L., *Pharm. Res.* **1993,** 10, 204-207.

90. Schierbaum, K. D.; Weiss, T.; Thoden van Veizen, E. U.; Engbersen, J. F. J.; Reinhoudt, D. N.; Göpel, W., *Science* **1994,** 265, (5177), 1413 - 1415.

91. Hosaka, S.; Chiyoma, T.; Ikeuchi, A.; Okano, H.; Sone, H.; Izumi, T., *Current Applied Physics* **2006,** 6, 384 - 388.

92. Lavrik, N. V.; Datskos, P. G., *Applied Physics Letters* **2003,** 82, (16), 1697-2699.

93. Jianqiang, H.; Changchun, Z.; Junhua, L.; Yongning, H., *Sensors and Actuators A: Physical* **2002,** 101, (1-2), 37-41.

94. Kim, S.; Kihm, K. D., *Applied Physics Letters* **2006,** 89, 061918.

95. McLoughlin, N.; Lee, S. L.; Hahner, G., *Applied Physics Letters* **2006,** 89, 184106.

96. Sandberg, R.; Svandsen, W.; Molhave, K.; Boisen, A., *Journal of Micromechanics and Microengineering* **2005,** 15, 1454 - 1458.

97. Thundat, T.; Chen, G. Y.; Warmack, R. J.; Allison, D. P.; Wachter, E. A., *Anal. Chem.* **1995,** 67, 519 - 521.

98. Mertens, J.; Finot, E.; Thundat, T.; Fabre, A.; Nadal, M.-H.; Eyraud, V.; Bourillot, E., *Ultramicroscopy* **2003,** 97, 119 - 126.

99. Lagowski, J.; Gatos, H. C.; E. S. Sproles, Jr., *Applied Physics Letters* **1975,** 26, (9), 493-495.

100. Gurtin, M. E.; Markenscoff, X.; Thurston, R. N., *Applied Physics Letters* **1976,** 29, (9), 529-530.

101. Chen, G. Y.; Thundat, T.; Wachter, E. A.; Warmack, R. J., *Journal of Applied Physics* **1995,** 77, 3618 - 3622.

102. Zhang, Y.; Ren, Q.; Zhao, Y.-p., *Journal of Physics D: Applied Physics* **2004,** 15, (37), 2140.

103. Hwang, K. S.; Eom, K.; Lee, J. H.; Chun, D. W.; Cha, B. H.; Yoon, D. S.; Kim, T. S.; Park, J. H., *Applied Physics Letters* **2006,** 89, 173905.

104. McFarland, A. W.; Poggi, M. A.; Doyle, M. J.; Bottomley, L. A.; Colton, J. S., *Applied Physics Letters* **2005,** 87, 053505.

105. Dorignac, J.; Kalinowski, A.; Erramilli, S.; Mohanty, P., *Physical Review Letters* **2006,** 96, 186105.

106. Wang, G. F.; Feng, X. Q., *Applied Physics Letters* **2007,** 90, 231904.

107. Whitesides, G. M.; Lewis, D. W., *J. Am. Chem. Soc.* **1971,** 93, (22), 5914-5916.

108. Sullivan, G. R.; Ciavarella, D.; Mosher, H. S., *J. Org. Chem.* **1974,** 39, (16), 2411-2412.

109. Adams, C. M.; Ghosh, I.; Kishi, Y., *Org. Lett.* **2004,** 6, (25), 4723-4726.

110. Furuno, H.; Hanamoto, T.; Sugimoto, Y.; Inanaga, J., *Org. Lett.* **2000,** 2, (1), 49-52.

111. Kobayashi, S.; Hamada, T.; Nagayama, S.; Manabe, K., *Org. Lett.* **2001,** 3, (2), 165-167.

112. Aspinall, H. C., *Chem. Rev.* **2002,** 102, 1807-1850.

113. Yamada, T.; Shinoda, S.; Sugimoto, H.; Uenishi, J.-I.; Tsukube, H., *Inorg. Chem.* **2003,** 42, 7932-7937.

114. Tsukube, H.; Hosokubo, M.; Wada, M.; Shinoda, S.; Tamiaki, H., *Inorg. Chem.* **2001,** 40, (4), 740-745.

115. Muller, G.; Bünzli, J.-C.; Riehl, J. P.; Suhr, D.; von Zelewskyc, A.; Mürner, H., *Chem. Commun.* **2002**, 1522–1523.

116. Muller, G.; Schmidt, B.; Jiricek, J.; Hopfgartner, G.; Riehl, J. P.; Bünzli, J.-C. G.; Piguet, C., *J. Chem. Soc., Dalton Trans.* **2001**, 2655–2662.

117. Renaud, F.; Piguet, C.; Bernardinelli, G.; Bünzli, J.-C.; Hopfgartner, G., *Chem. Eur. J.* **1997,** 3, 1660.

118. Muller, G.; Riehl, J. P.; Schenk, K. J.; Hopfgartner, G.; Piguet, C.; Bünzli, J.-C., *Eur. J. Inorg. Chem.* **2002,** 12, 3101-3110.

119. Leonard, J. P.; Jensen, P.; McCabe, T.; O'Brien, J. E.; Peacock, R. D.; Kruger, P. E.; Gunnlaugsson, T., *J. Am. Chem. Soc.* **2007,** 129, 10986-10987.

120. Stomeo, F. Design, Synhthesis and Physical Evaluation of Luminescent Lanthanide-based Supramolecular Systems. University of Dublin, Trinity College, Dublin, 2006.

121. Akitt, J. W., *NMR and Chemistry: an Introduction to modern NMR spectroscopy*. 4th ed.; 2000.

122. Rodger, A.; Nordén, B., *Circular dichroism and linear dichroism*. Oxford University Press: Oxford, New York, 1997; p 150.

123. Steemers, F. J.; Verboom, W.; Reinhoudt, D. N.; van der Tal, E. B.; Verhoeven, J. W., *J. Am. Chem. Soc.* **1995,** 117, 9408.

124. Latvaa, M.; Takalob, H.; Mukkala, V.-M.; Matachescuc, C.; Rodriguez-Ubisd, J.-C.; Kankarea, J., *J.Lumin.* **1997,** 75, 149.

125. Gampp, H.; Maeder, M.; Meyer, C. J.; Zuberbuhler, A. D., *Talanta* **1985,** 32, 95 - 101.

126. Maeder, M.; Zuberbuhler, A. D., *Anal. Chem.* **1990,** 62, 2220-2224.

127. Berlman, I. B., *Handbook of Fluorescence Spectra of aromatic Compounds*. Academic Press: London, 1965.

128. Job, A., *Annales de Chemie* **1928,** 9, 113.

129. Montgomery, C. P.; New, E. J.; Parker, D.; Peacock, R. D., *Chem. Commun.* **2008**, 4261 - 4263.

130. Do, K.; Muller, F. C.; Muller, G., *J. Phys. Chem. A.* **2008,** 112, 6789-6793.

131. Seitz, M.; Moore, E. G.; Ingram, A. J.; Muller, G.; Raymond, K. N., *J. Am. Chem. Soc.* **2007,** 129, 15468-15470.

132. Lunkley, J. L.; Shirotani, D.; Yamanari, K.; Kaizaki, S.; Muller, G., *J. Am. Chem. Soc.* **2008,** 42, (130), 13814–13815.

133. Petoud, S.; Muller, G.; Moore, E. G.; Xu, J.; Sokolnicki, J.; Riehl, J. P.; Le, U. N.; Cohen, S. M.; Raymond, K. N., *J. Am. Chem. Soc.* **2007,** 129, 77-83.

134. Massue, J.; Plush, S. E.; Bonnet, C. S.; Moore, D. A.; Gunnlaugsson, T., *Tetrahedron Letters* **2007,** 48, 8052.

135. Leonard, J. P.; dos Santos, C. M. G.; Plush, S. E.; McCabe, T.; Gunnlaugsson, T., *Chem. Commun.* **2007**, 129.

136. Brust, W. M.; Bethell, D.; Schiffrin, D. J.; Whyman, R., *J. Chem. Soc., Chem. Commun.* **1994**, 801.

137. Gittins, D. I.; Caruso, F., *Angew. Chem. Int. Ed.* **2001,** 40, 3001.

138. Gandubert, V. J.; Lennox, R. B., *Langmuir* **2005,** 21, 6532.

139. Poirier, G. E., *Langmuir* **1999,** 15, 1167.

140. Schreiber, F.; Eberhardt, E.; Leung, T. Y. B.; Schwartz, P.; Wetterer, S. M.; Lavrich, D. J.; Berman, L.; Fenter, P.; Eisenberger, P.; Scoles, G., *Phys. Rev. B* **1998,** 57, 12476.

141. Berger, R.; Delamarche, E.; Lang, H. P.; Gerber, C.; Gimzewski, J. K.; Meyer, E.; Guntherodt, H.-J., *Science* **1997,** 276, (5321), 2021-2024.

142. Raiteri, R.; Grattarola, M.; Berger, R., *Materials Today* **2002,** 5, (1), 22-29.

143. Godin, M.; Williams, P. J.; Tabard-Cossa, V.; Laroche, O.; Beaulieu, L. Y.; Lennox, R. B.; Grutter, P., *Langmuir* **2004,** 20, (17), 7090-7096.

144. Han, J.; Wang, X.; Kwok, D. Y. In *Structure and Stability of SAMs for octadecane thiol adsorbed on flame annealing gold substrate and its potential application to microfluidics*, PROC. ICMENS 2004, 2004; 2004; p 2189.

145. Chan, Y.-H.; Schuckman, A. E.; Perez, L. M.; Vinodu, M.; Drain, C. M.; Batteas, J. D., *J. Phys. Chem. C* **2008,** 112, 6110.

146. Aoki, S.; Kawatani, H.; Goto, T.; Kimura, E.; Shiro, M., *J. Am. Chem. Soc* **2001,** 123, 1123 - 1132.

147. Lachut, M., J.; Sader, J., E., *Physical Review Letters* **2007,** 99, (20), 206102.

148. Datskos, P. G.; Sepaniak, M. J.; Tipple, C. A.; Lavrik, N., *Sensors and Actuators B: Chemical* **2001,** 76, (1-3), 393-402.

149. Cleland, A. N.; Roukes, M. L., *Appl. Phys. Lett.* **1996,** 69, 2653–2655.

150. Ekinci, K. L.; Roukes, M. L., *Rev. Sci. Instrum.* **2005,** 76, 061101.

151. Mamin, H. J.; Rugar, D., *Appl. Phys.Lett.* **2001,** 79, 3358–3360.

152. Ekinci, K. L.; Huang, X. M. H.; Roukes, M. L., *Appl. Phys. Lett.* **2004,** 84, 4469–4471.

153. Raiteri, R.; Grattarola, M.; Butt, H.-J.; Skládal, P., *Sensors and Actuators B: Chemical,* **2001,** 79, (2-3), 115-126.

154. Jeetender, A.; Stiharu, I.; Packirisamy, M. In *Micro-opto mechanical biosensors for enzymatic detection*, Photonic Applications in Biosensing and Imaging, Toronto, ON, Canada, 2005; International Society for Optical Engineering, Bellingham WA, WA 98227-0010, United States: Toronto, ON, Canada, 2005.

155. Ren, Q.; Zhao, Y.-P., *Microsystem Technologies* **2004,** 10, 307-314.

156. Butt, H.-J., *J. Colloid Interface Sci.* **1996,** 180, 251–260.

157. Fritz, J.; Baller, M. K.; Lang, H. P.; Rothuizen, H.; Vettiger, P.; Meyer, E.; Güntherodt, H.-J.; Gerber, C.; Gimzewski, J. K., *Science* **2000,** 288, 316.

158. Chen, G. Y.; Warmack, R. J.; Thundat, T.; Allison, D. P.; Huang, A., *Rev. Sci. Instrum.* **1994,** 65, 2532.

159. Jackson, R. G., *Novel Sensors and Sensing*. Institute of Physics Publishing: 2004; p 299.

160. Ibach, H., *Surface Science Reports* **1997,** 29, 193-263.

161. Gurtin, M. E.; Murdoch, A. I., *Archive of Rational Mechanical Analysis* **1975,** 57, 529.

162. Newton, I., *Philosophiae Naturalis Principia Mathematica*. 1687.

163. Stoney, G. G., *Proc. R. Soc.* **1909,** 9, 172-5.

164. Sader, J. E., *Journal of Applied Physics* **2001,** 89, (5), 2911 - 2921.

165. Sader, J. E.; Chon, J. W. M.; Mulvaney, P., *Rev. Sci. Inst.* **1999,** 70, (10), 3967.

166. Matei, G. A.; Thoreson, E. J.; Pratt, J. R.; Newell, D. B.; Burnham, N. A., *Rev. Sci. Instrum.* **2006,** 77, 083703.

167. Sader, J. E., *Journal of Applied Physics* **1998,** 84, (1), 64-76.

Appendix

7 Appendix

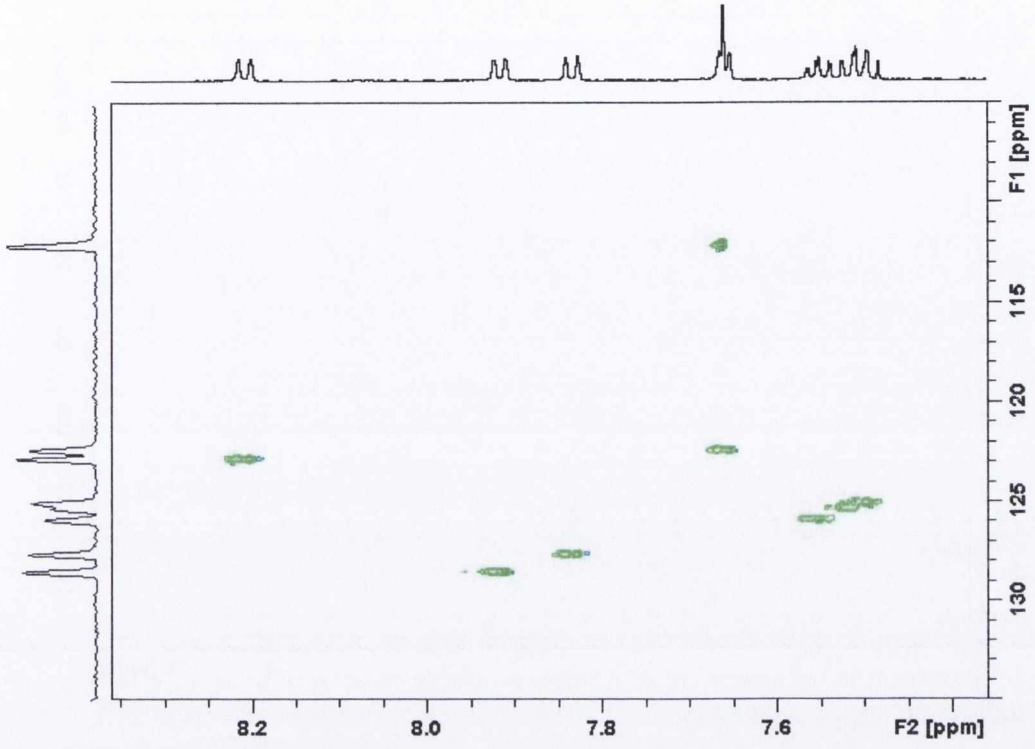

A1. hsqc nmr of ligand **57** (*S,S*)

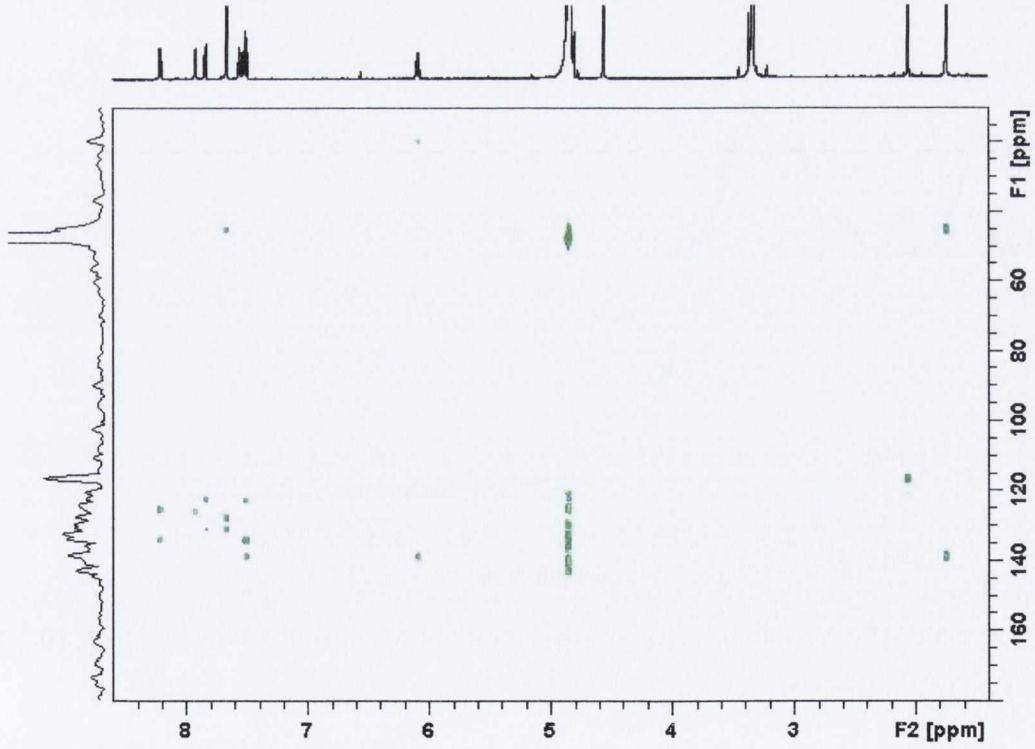

A2. hsqc nmr of ligand **57** (*S,S*)

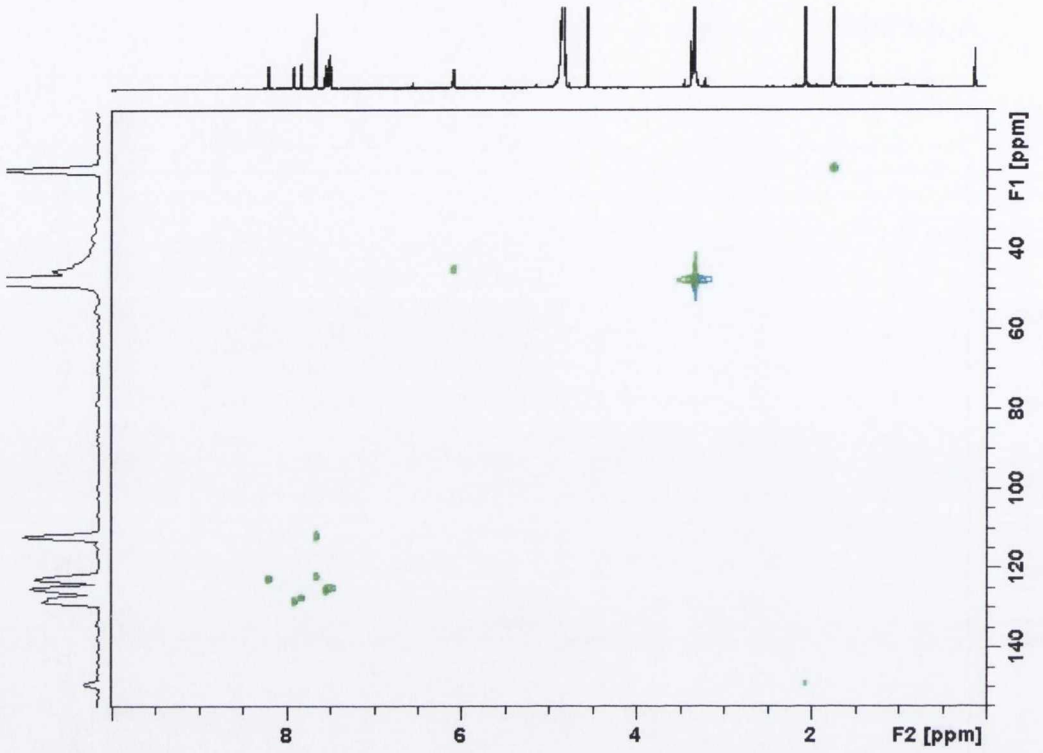

A3. hsqc nmr of ligand **57** (*S,S*)

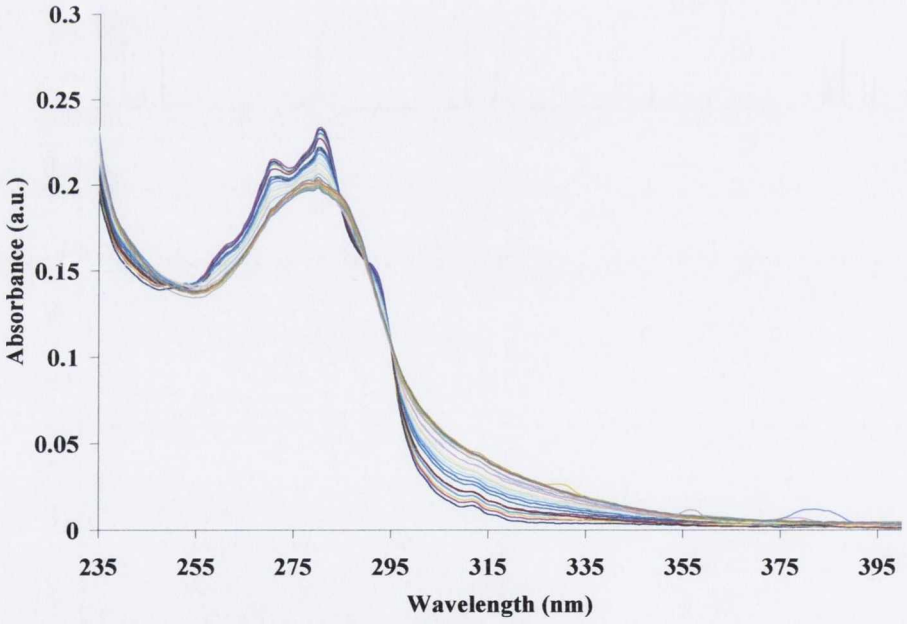

A4. Overlaid UV-Visible spectra of the titration of ligand **53** (*S,S*) [1 x 10^{-5} M] with $Eu(CF_3SO_3)_3$ in CH_3CN.

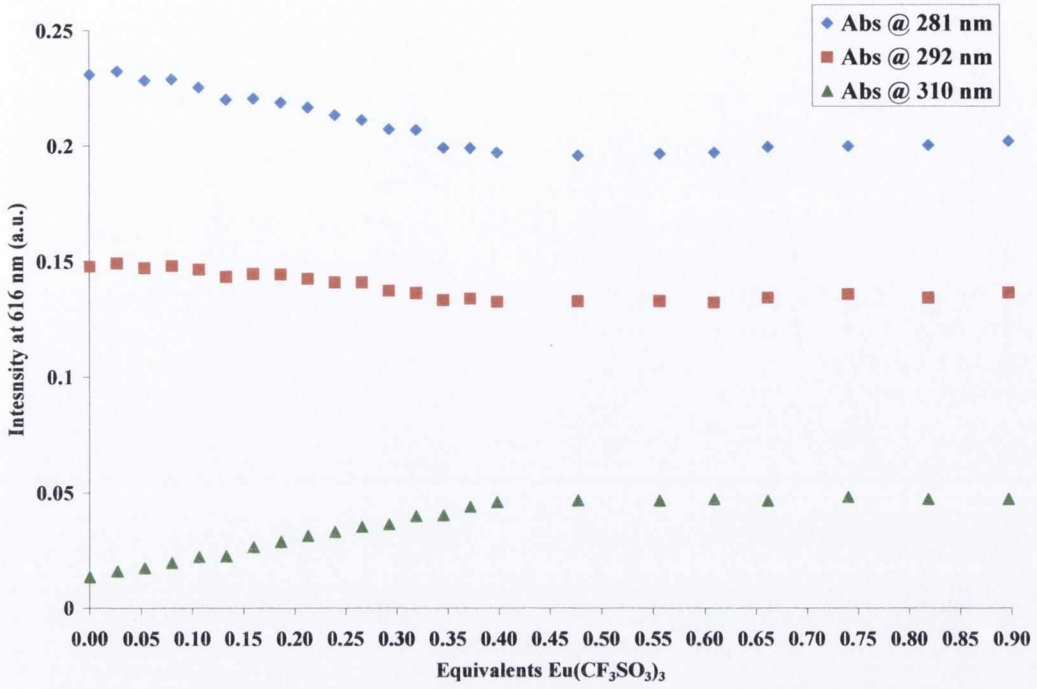

A5. Absorbance at 281 nm, 292 nm, and 310 nm as a function of equivalents of Eu^{III} in the titration of ligand **53** (*S,S*) with $Eu(CF_3SO_3)_3$ in CH_3CN.

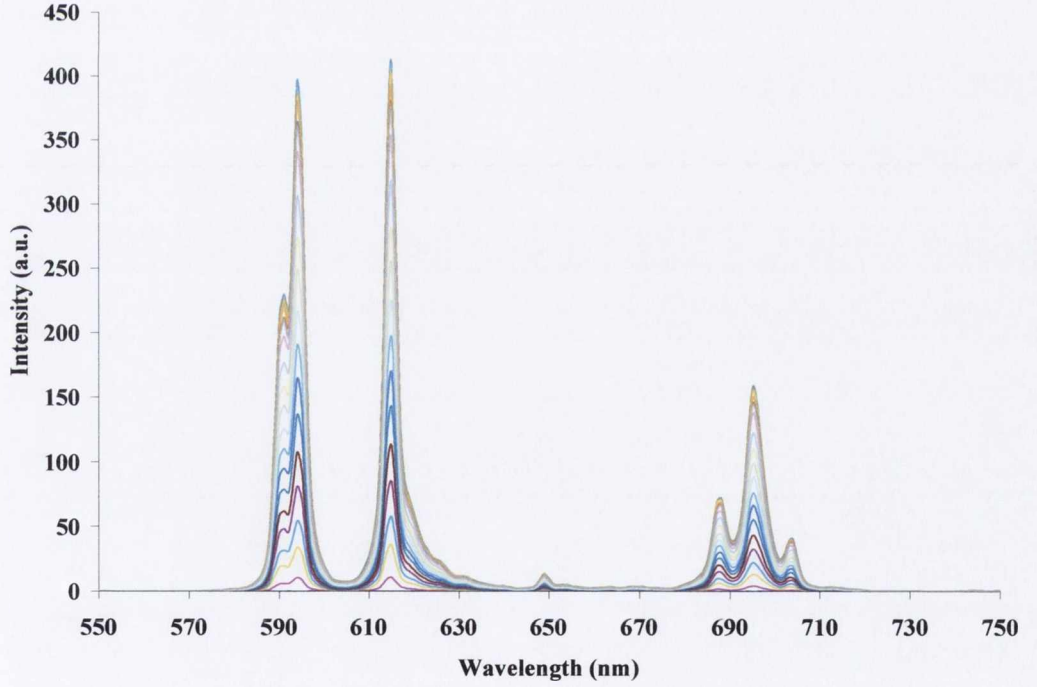

A6. Overlaid luminescence spectra from the titration of ligand **53** (*S,S*) [1 x 10^{-5} M] with $Eu(CF_3SO_3)_3$ in CH_3CN, upon excitation at 281 nm.

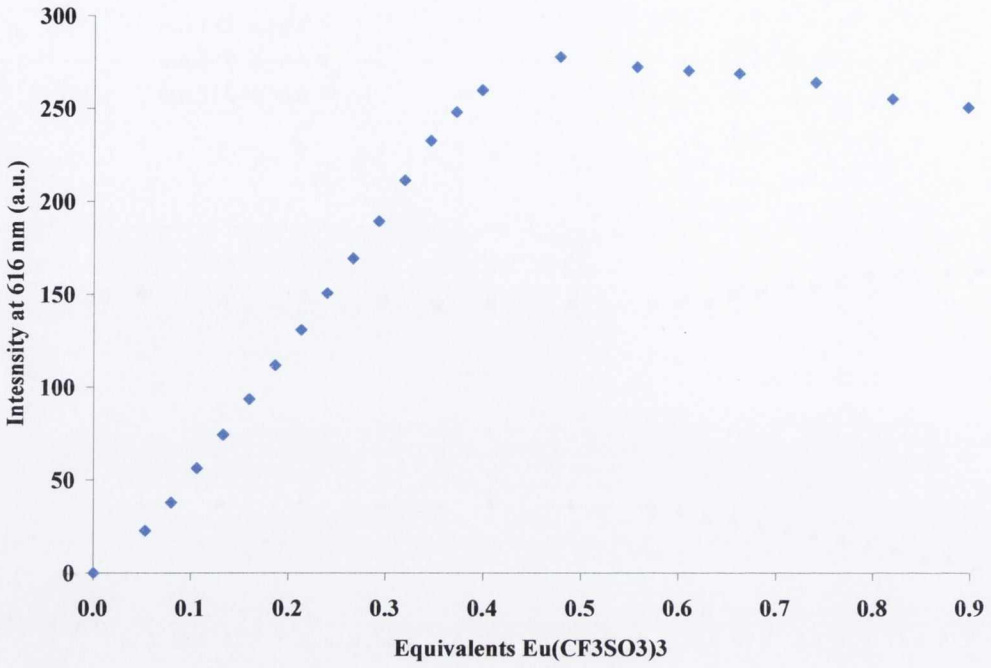

A7. Intensity at 616 nm as a function of equivalents of Eu^{III} in the titration of ligand **53** (*S,S*) with $Eu(CF_3SO_3)_3$ in CH_3CN.